



2D-materials Enabled Printed Flexible RF and Microwave Antennas and Wireless Sensors

A thesis submitted to The University of Manchester for the degree of
Doctor of Philosophy
in the Faculty of Science and Engineering

2019

Kewen Pan

**Faculty of Science and Engineering
Department of Electrical and Electronic Engineering**

List of contents

| | |
|--|----|
| List of contents..... | 1 |
| List of figures..... | 4 |
| List of tables..... | 10 |
| Abstract..... | 11 |
| Declaration..... | 12 |
| Copyright statement | 13 |
| Acknowledgments..... | 14 |
| Publications..... | 15 |
| Abbreviations..... | 18 |
| Statement of novelty..... | 21 |
| 1 Introduction..... | 22 |
| 1.1 Motivation | 22 |
| 1.2 Thesis outline..... | 24 |
| References | 28 |
| 2 Background theory and concepts | 30 |
| 2.1 Graphene modeling | 30 |
| 2.2 Basic theories..... | 35 |
| 2.2.1 Sheet resistance | 35 |
| 2.2.2 Skin depth and surface resistance..... | 35 |
| 2.2.3 Antenna gain measurement..... | 36 |
| 2.2.4 Permittivity and permeability measurement (Nicolson-Ross-Weir (NRW) method)..... | 38 |
| References | 41 |
| 3 Sustainable production of highly conductive multilayer graphene ink for wireless connectivity and IoT applications | 43 |
| Abstract..... | 44 |
| 3.1 Introduction | 44 |
| 3.2 Results | 46 |
| 3.2.1 Ink characterization. | 46 |
| 3.2.2 Antennas design and fabrication. | 55 |
| 3.2.3 NFC battery-free temperature sensor..... | 59 |
| 3.2.4 Long read range UHF RFID antenna. | 60 |
| 3.2.5 Ultra-wideband antenna and energy harvesting applications. | 62 |
| 3.3 Discussion..... | 67 |
| 3.4 Methods | 68 |
| 3.4.1 Liquid exfoliation of graphene with high concentration. | 68 |
| 3.4.2 Screen-printing high concentration graphene ink preparation..... | 69 |
| 3.4.3 FTIR. | 69 |
| 3.4.4 Raman..... | 70 |
| 3.4.5 Atomic force microscopy..... | 70 |
| 3.4.6 Scanning electron microscopy. | 70 |

| | | |
|--------|---|-----|
| 3.4.7 | Conductivity measurement. | 71 |
| 3.4.8 | Antenna reflection coefficient measurement. | 71 |
| 3.4.9 | Radiation pattern measurement. | 71 |
| 3.4.10 | RFID antenna measurement. | 72 |
| 3.4.11 | Antenna efficiency measurement. | 73 |
| | References | 74 |
| 3.5 | Supplementary figures..... | 78 |
| 3.6 | Supplementary notes | 80 |
| 4 | 3D graphene/polymer porous spongy for sensing and microwave absorbing applications | 87 |
| | Abstract..... | 88 |
| 4.1 | Introduction | 88 |
| 4.2 | Results | 92 |
| 4.3 | Conclusion | 116 |
| 4.4 | Method | 117 |
| 4.4.1 | Shear Mixing exfoliation of graphene..... | 117 |
| 4.4.2 | Preparing Gp&Gr loaded conductive sponge. | 118 |
| 4.4.3 | Atomic force microscopy | 119 |
| 4.4.4 | Scanning electron microscopy | 119 |
| 4.4.5 | Raman..... | 119 |
| 4.4.6 | TGA and DSC | 119 |
| | References | 120 |
| 4.5 | Supplementary information | 125 |
| 5 | Controlled reduction of graphene oxide laminate and its applications for ultra-wideband microwave absorption..... | 126 |
| | Abstract..... | 127 |
| 5.1 | Introduction | 127 |
| 5.2 | Experimental detail | 131 |
| 5.2.1 | Material preparation | 131 |
| 5.2.2 | Preparation of rGO laminates | 132 |
| 5.2.3 | Characterization | 132 |
| 5.3 | Results and discussion..... | 134 |
| 5.4 | Conclusions | 154 |
| | References | 156 |
| 5.5 | Supplementary figures..... | 161 |
| 5.6 | Supplementary tables | 162 |
| | Supplementary reference | 163 |
| 5.7 | Supplementary Matlab program for absorber optimization | 164 |
| 6 | Soft wireless battery-free UHF RFID stretchable sensor based on microfluidic technology..... | 166 |
| | Abstract..... | 167 |
| 6.1 | Introduction | 168 |
| 6.2 | Design of metamaterial inspired liquid metal soft antenna..... | 170 |
| 6.3 | Soft antenna fabrication..... | 172 |

| | | |
|-------|---|-----|
| 6.4 | Antenna measurement | 176 |
| 6.5 | Results and discussions | 177 |
| 6.6 | Conclusion | 186 |
| | References | 188 |
| 7 | Soft radio-frequency identification sensors: wireless long-range strain sensors using radio-frequency identification | 190 |
| | Abstract | 191 |
| 7.1 | Introduction | 192 |
| 7.1.1 | Soft sensors | 192 |
| 7.1.2 | Design of a new soft RFID sensor | 194 |
| 7.1.3 | RFID technology | 196 |
| 7.1.4 | Sensor constitutes | 197 |
| 7.2 | Working principles | 198 |
| 7.3 | Implementation in soft robotics | 199 |
| 7.4 | Antenna design | 200 |
| 7.4.1 | Selection and design of the antenna | 200 |
| 7.4.2 | Antenna matching | 201 |
| 7.4.3 | Materials and Fabrication Methods | 203 |
| 7.4.4 | Experimental Design | 205 |
| 7.5 | Results | 208 |
| 7.5.1 | Permittivity of Ecoflex 00-50 | 208 |
| 7.5.2 | Simulation of antenna efficiency | 208 |
| 7.5.3 | Resonant frequency upon strain | 211 |
| 7.5.4 | Repeatability and reliability test | 213 |
| 7.5.5 | Radiation pattern | 215 |
| 7.6 | Discussion | 216 |
| 7.7 | Conclusion | 217 |
| | References | 218 |
| 8 | Conclusions and future works | 222 |

List of figures

| | |
|---|----|
| Figure 1-1: The thesis outline..... | 25 |
| Figure 2-1: The surface conductivity tunability of graphene in microwave and THz frequency [14].... | 32 |
| Figure 2-2: The relationship between applied voltage and chemical potential [16]..... | 33 |
| Figure 2-3: The structure of the constructed CPW graphene switch in vertical cross view (left) and top view (right) [16]. | 34 |
| Figure 2-4: The magnitude of measured transmission S_{21} over the frequency range 0–110 GHz respectively [16]. | 34 |
| Figure 2-5: Antenna measurement methods [23]. | 37 |
| Figure 3-1: Quality of exfoliated graphene flakes in Cyrene: Measured average sheet resistance values (left axis, measured 5 times per point) and variation (right axis) of sheet resistance as function of sonication time (black line: NMP, red line: Cyrene). | 49 |
| Figure 3-2: Sheet resistance variation (measured 5 times per point) with different CAB concentration and the insert sample of 10 mg mL ⁻¹ graphene ink with 1 mg mL ⁻¹ CAB. | 50 |
| Figure 3-3: AFM image of graphene flakes on silicon substrate; scale bar is 1 μ m. | 51 |
| Figure 3-4: (a) Thickness histograms and (b) flake size. | 52 |
| Figure 3-5: FTIR characterization of Cyrene graphene ink with and without CAB. | 52 |
| Figure 3-6: Raman spectra of Cyrene graphene ink with and without CAB. | 53 |
| Figure 3-7: SEM images of screen printed graphene on paper (a Uncompressed and c Compressed screen-printed graphene laminates with 300X magnification; scale bar is 30 μ m, b Uncompressed and d Compressed screen-printed graphene laminates with 10kX magnification; scale bar is 1 μ m.)..... | 54 |
| Figure 3-8: Graphene antenna fabrication using screen printing technology. Screen-printing steps: a Patterning graphene ink via exposed screen and squeegee, b Annealing printed patterns and c Compressing dried pattern with steel rolling machine..... | 55 |
| Figure 3-9: Cyrene based graphene ink and high concentrated (70 mg mL ⁻¹) screen printing ink..... | 56 |
| Figure 3-10: a Demonstration of printed antennas on A4 paper. b SEM cross-section view of the printed graphene antenna; scale bar is 1 μ m. | 56 |
| Figure 3-11: Flexibility of the printed graphene antenna. | 57 |
| Figure 3-12: a-c Printed graphene antennas' geometric parameters (mm): a NFC antenna (without NFC chip and jumper), b UHF RFID antenna, c wideband slot antenna. | 58 |
| Figure 3-13: a-c Healthcare applications (a Illustration of graphene printed NFC temperature sensing system, b Demonstration of measurement and c recorded data of body temperature)..... | 59 |
| Figure 3-14: a-c UHF RFID tag applications demonstration (a Illustration of printed graphene RFID antenna system, b Read range and c radiation pattern (E-field, at 915 MHz)). | 60 |
| Figure 3-15: Measured reflection coefficient (S_{11}) of the graphene printed slot antenna..... | 62 |
| Figure 3-16: Measured slot antenna gain (three-antenna method)..... | 63 |
| Figure 3-17: a-d Measured radiation pattern at a 4 GHz, b 8 GHz, c 12 GHz and d 14 GHz..... | 64 |
| Figure 3-18: a Illustration of RF energy harvesting system, b Measurement set up..... | 65 |
| Figure 3-19: Measured efficiencies and output DC voltage as a function of different RF power levels. | 66 |
| Figure 4-1: Schematic illustration of Gp&Gr loaded high conductive sponge fabrication process. | 92 |

| | |
|--|-----|
| Figure 4-2: High conductive Gp&Gr ink characterization. (a) AFM image of 2K RPM centrifuged Gp&Gr dispersion on silicon dioxide substrate; scale is 5 μm ×5 μm . (b) Height distribution of flakes. | 95 |
| Figure 4-3: Optical image of the AFM sample, scale bar is in the image..... | 96 |
| Figure 4-4: DSC analysis of pure NC. | 96 |
| Figure 4-5: TGA results of dried dispersion samples with different centrifuge speed and NC content. The less weight loss at high temperature represents higher Gp&Gr flakes concentration. | 97 |
| Figure 4-6: Calculated graphene concentration from Figure 4-5..... | 98 |
| Figure 4-7: The derivative of the 3K RPM TGA results with different NC contents..... | 99 |
| Figure 4-8: Measured temperature ramping in annealing process. | 99 |
| Figure 4-9: Post-processing of the dried conductive laminates and sponges. (a) SEM image of the dried Gp/Gr dispersion. Flakes have been enveloped in NC. (b) SEM image of the annealed sample, NC has been completely removed and graphite fragment can be clearly observed. | 100 |
| Figure 4-10: Conductivity measurement of the annealed laminates as a function of centrifuge speeds. | 101 |
| Figure 4-11: (a) Magnified cross-section view of the fabricated sponge, the white part is not conductive (polymer) and the grey part are conductive (Gp&Gr flakes). (b) The cross-section SEM image of the sponge under low magnification, clear cube shaped holes can be seen. (c) The magnified SEM image of the conductive surface, flakes have been well covered by cross-linked Ecoflex polymer. | 102 |
| Figure 4-12: (a) The optical image at 50×. (b) Mapping of the intensity ratio of 2707 cm^{-1} (Graphene 2D band) and 2896 cm^{-1} (Ecoflex C-H). | 103 |
| Figure 4-13: Raman results of the sponge cross-section, where mark 1,2 and 3 are corresponded to the area in Figure 4-12b..... | 103 |
| Figure 4-14: X-band sponges' permittivity and permeability measurement set up. | 104 |
| Figure 4-15: Measured real part (a) and imaginary part (b) of permittivity..... | 105 |
| Figure 4-16: (a) and (b) is the real part and imaginary part of permeability, respectively. | 106 |
| Figure 4-17: Corresponded wave impedance of the sponges with different graphene content..... | 106 |
| Figure 4-18: (a) Transmission line equivalent circuit model of the microwave absorber. (b), (c) 3D illustration of the proposed four and two layers' microwave absorber. Thickness and Gp&Gr contents are marked. | 107 |
| Figure 4-19: (a) Simulated reflection results of four layers absorber at perpendicular and angled incident conditions. (b) Simulation results for two layers absorber with the same incident angles. | 109 |
| Figure 4-20: Calculated microwave absorptions, effective absorption generally above 0.9..... | 110 |
| Figure 4-21: (a) Cyclic voltammetry (C-V) curves of the fabricated supercapacitor with varied charge speeds. (b) Measurement of equivalent series resistance (ESR), the small schematic in (b) is the DC equivalent circuit for ESR measurement. | 111 |
| Figure 4-22: (a) Galvanostatic charge-discharge (GCD) profile of the supercapacitor. (b) Measured leakage currents versus applied voltage and time..... | 113 |
| Figure 4-23: (a) Leakage currents after 8 hrs stabilization. (b) Calculated specific capacitance from GCD results..... | 114 |
| Figure 4-24: (a) Measured capacitor retention with full charge (2 V) and discharge (<50 mV) cycles. (b) Stretch test of the supercapacitor. Only 1.7% capacitance lost after 100 times cyclic test. (c) | |

| | |
|--|-----|
| The demonstration of a fully charged supercapacitor can work effectively to power up an electric circuit for a short period even though it has been bent. | 115 |
| Figure 4-25: Electronic circuit schematic for supercapacitors' GCD measurement..... | 125 |
| Figure 4-26: Circuit diagram for ESR and leakage current tests. | 125 |
| Figure 5-1: (a) AFM image of GO sheets on silicon dioxide substrate; scale bar is 1 μm . (b) Height of GO sheets in AFM image (green line). (c) Measured viscosity of the screen printable GO ink with the concentration of 25 mg mL^{-1} | 134 |
| Figure 5-2: (a) Raman spectra of rGO laminate with different reduction times (0 hr, 1 hr, 3 hr, 5 hr, 9 hr, 15 hr and 27 hr). (b) I_D/I_G intensity ratio of Raman spectra in (a). | 135 |
| Figure 5-3: FTIR characterization of rGO laminates with different reduction times. | 136 |
| Figure 5-4: XRD spectra of rGO laminate with different reduction times. | 137 |
| Figure 5-5: (a) Wide scan XPS spectra of rGO laminate with different reduction times. (b) The calculated carbon/oxygen ratio from XPS..... | 138 |
| Figure 5-6: (a) TGA results of rGO laminate with different reduction times. The less weight loss at high temperature represents better reduction. (b) Weight ratio of GO and rGO laminates from TGA results at different temperatures (300°C and 100°C)..... | 139 |
| Figure 5-7: Sheet resistance measurement of rGO laminate (from 1 printed layer to 6 printed layers) with different reduction times. | 140 |
| Figure 5-8: 1 st derivative of Raman, XPS, XRD and sheet resistance results..... | 141 |
| Figure 5-9: (a,b) SEM images of rGO laminates (1 printed layer (a), 6 printed layers (b)), scale bar is 10 μm . (c) SEM cross-sectional view of the rGO laminate with 3 printed layers and scale bar is 100 nm..... | 142 |
| Figure 5-10: (a) Bending test setup (upper: initial state, lower: banded state). (b) Bending test results of the rGO laminate with 6 printed layers. | 143 |
| Figure 5-11: Absorber structure and fabrication (a) Cross-section illustration of the proposed three-layer microwave absorber. (b) Transmission line equivalent circuit model of the microwave absorber..... | 144 |
| Figure 5-12: Performance comparison of calculated results from Figure 5-11b and simulated ones using full wave simulator CST. | 146 |
| Figure 5-13: Image of the fabricated three-layer microwave absorber..... | 147 |
| Figure 5-14: (a) Printed GO laminates. (b) L-AA reduced rGO laminates..... | 148 |
| Figure 5-15: (a) Perpendicular incident experiment setup. (b) 45° incident experiment setup (θ represents incident angle)..... | 149 |
| Figure 5-16: Microwave absorber measurement and comparison with simulation. (a) Measured transmission at perpendicular incident (solid lines) and RCS (dash lines). (b) Comparing calculated, simulated and measured reflection coefficients (solid lines) and absorptions (dash lines) at perpendicular incident. (c) Measured transmission TE wave at 45° incident condition (solid lines) and RCS (dash lines). (d) Comparing simulated and measured reflection coefficients (solid lines) and absorptions (dash lines) at different incident angles..... | 151 |
| Figure 5-17: Simulated surface power loss density of the absorber in different layers at 1, 3, 5, 9 GHz from left to right respectively. | 152 |
| Figure 5-18: (a) TEM image of 1-layer printed sample under low magnification, wrinkles of rGO sheets can be observed. (b) TEM image under high magnification. | 161 |
| Figure 6-1: Meandered SRR RFID sensor. (a) Antenna structure (red corn is feed port). (b) Fabricated | |

| | |
|---|-----|
| device (3.3cm×3.5cm). (c) Geometry parameters. | 170 |
| Figure 6-2: Antenna equivalent circuit model (Left is RFID chip side and right is antenna side). | 171 |
| Figure 6-3: (a) Top view of the Ecoflex liquid metal SRR antenna with detailed cross-section drawing of the RFID chip insertion. The initial length, width and thickness of the antenna are $L_x=33$ mm, $L_y=35$ mm and $L_z=2.5$ mm respectively. The channels with filled Galinstan in the Ecoflex substrate are 1 mm in the width. The RFID chip was bonded on an aluminum film then inserted in the fluidic channels to connect with Galinstan; (b) when the antenna is under stretching, the length in X direction, the width in Y direction and the thickness in Z direction become $L_x+\Delta L_x$, $L_y+\Delta L_y$ and $L_z+\Delta L_z$ respectively. | 173 |
| Figure 6-4: Schematic illustration of the fabrication process and photograph of the stretchable fluidic antenna; (a) the soft-lithography mold made with 0.15 mm vinyl film (red) and 2 mm Acrylic substrate and frame (white); (b) uncured Ecoflex with height of 2 mm was poured into the soft-lithography mold; (c) the casted piece of Ecoflex was sealed with another 0.2 mm Ecoflex film; (d) the RFID chip bonded on an aluminum film was inserted into the channels in Ecoflex substrate; (e) two needles were used to inject Galinstan into the channels. (f) Photograph of the final prototype. | 175 |
| Figure 6-5: RFID measurement set up with Voyantic Tagformance. | 176 |
| Figure 6-6: (a) Simulated antenna impedance under different stretch conditions. (b) Measurement results of RFID tag read range and resonance frequency under different stretching conditions. (c) Antenna resonance frequency verses antenna stretching ratio (stretched length/ original length), the red line is linear fits of scatters. | 179 |
| Figure 6-7: Measured RFID antenna radiation pattern under different stretching length in E-plane (a) and H-plane (b) (0%, 30% and 60%). | 180 |
| Figure 6-8: (a) Antenna resonance frequency variation with different bending angle (0°, 45°, 90°). (b) Antenna resonance variation under rolling ($r=0.7, 1.5, 3, \infty$). | 181 |
| Figure 6-9: (a) Cyclability test of the RFID stretchable sensor. The sensor was stretched from its initial state to 200% of the original length (X direction) with 1000 cycles. (b) Demonstration of the measured backscattered power where the RFID stretchable sensor is placed in normal office environment with a fixed distance. | 183 |
| Figure 6-10: Soft pneumatic actuator with RFID stretchable sensor attached on the Ecoflex side. | 185 |
| Figure 6-11: Soft pneumatic actuator bending process when air pressure increasing (0°, 15°, 30°, 45°, 60°, 75° and 90°) and corresponded measured RFID antenna resonance frequencies. | 186 |
| Figure 7-1: (a) Schematic diagram of the stretchable microfluidic sensor. Galinstan is enclosed in Ecoflex substrate while an RFID chip is bonded on a piece of aluminium foil which is inserted in the channels. Detailed and cross-section figures of the part near RFID chip are presented. Directions of x , y , and z axis are indicated; (b) Initial state of the antenna when it's not stretched. The effective antenna length on x -direction and y -direction is defined as l_x and l_y respectively. Notice: The electrical length of the entire antenna is $l_x+10l_y+l_m$. The non-symmetric part, l_m is used for fine impedance matching between the antenna and the RFID chip; (c) When the soft antenna is stretched, the effective antenna length on x -direction and y -direction is defined as $l_x+\Delta l_x$ and $l_y+\Delta l_y$ respectively. | 198 |
| Figure 7-2: The electronic system for measuring data from a pneumatic soft robot that contains four embedded microfluidic strain sensors. | 200 |
| Figure 7-3: (a) Equivalent circuit of the RFID chip and the transporter antenna. Z_a is the total | |

impedance of the transport antenna whereas Z_c is impedance of the RFID chip; (b) Schematic diagram of T-matching for a dipole antenna. The l represents length of the original dipole antenna. This antenna is connected at the centre to a short second dipole. The close distance between matching stub and the original antenna is b , whereas w and w' are the widths of the original dipole antenna and the mating stub respectively; (c) Equivalent circuit at the source point of the dipole antenna after T-matching. Z'_a is the impedance of the first dipole antenna without T-matching while Z_t is the impedance that the matching stub created. The α in the ratio is the current division factor between the two connectors..... 203

Figure 7-4: Fabrication process and prototype of the stretchable microfluidic sensor (RFID tag antenna). (a) cut the sensor profile on a piece of self-adhesive vinyl attached on an Acrylic substrate. Notice: the red and pink parts are a same piece of vinyl. Two different colours are used here to show the laser-cut profile clearer; (b) the unwanted part of vinyl was peel off, a 2 mm-thick Acrylic frame was stuck on the substrate to form a soft-lithography mould; (c) uncured Ecoflex with a controlled height of 2 mm was poured into the soft-lithography mould; (d) the casted piece of Ecoflex was sealed with another 0.15 mm Ecoflex film and the RFID chip bonded on aluminium film was inserted into the channels; (e) two needles were used to inject Galinstan into the channel; (f) Photograph of the final prototype. 205

Figure 7-5: (a) We used Voyantic Tagformance system to measure characteristics of the proposed antenna. This measurement system sends input signals to the tag antenna with transmitted power. The power received on tag is the transmitted power minus cable loss and free space loss. RFID chip in the tag antenna receives the input signals, absorbs energy in the signals, and then sends backscattered signals back to the measurement system. According to the results of the measurement system, we can know the resonant frequency and the theoretical reading range of the tag antenna, as well as the phase of the backscattered signals. We affixed the two edges of the tag antenna with clips made of rigid foam. In order to stretch the tag antenna and hold its position for measurement, we stuck grip tape on the surface of the foam clips, and on the measurement platform. (b) Experimental setup for measurement of the permittivity of Ecoflex 00-50 with the Agilent 85070E dielectric probe kit system. (c) Photograph of the experimental setup of the soft antenna and the Voyantic Tagformance system. 206

Figure 7-6: Radiation pattern measurement in H-plane and E-plane in an anechoic room with Diamond Engineering Automated measurement system and an automatic turntable. In the measurement, the reader antenna holds its position while the strain sensor (transporter antenna) turn with the turntable. 207

Figure 7-7: Permittivity of Ecoflex type 00-50 in the frequency range of 200 MHz~1.2 GHz. Measured with Agilent 85070E dielectric probe kit system. 208

Figure 7-8: Finite elements simulation results. Under 0% strain condition, simulated resonant frequency of the antenna is 856 MHz. The simulated resonant frequency continuously goes down to 827 MHz when the antenna is under 50% strain. 210

Figure 7-9: (a) Transmitted power. The minimum transmitted power recorded for the sensor under 0% - 50% strain, with a step of 5%. (b) The power received on tag, which was calculated based on the transmitted power and cable and free space loss. (c) Theoretical reading range forward, which was calculated based on the power received on tag. (d) Backscattered phase in the frequency band of 800-880MHz (with a step of 1 MHz) when the sensor was under 0% - 50% strain, with a step of 5%. 212

Figure 7-10: (a) Resonant frequency change upon different strain conditions. In the experiment, we did 7 tests on the same prototype. Error bars represent standard deviation. (b) Resonant frequency change upon different strain conditions. In the experiment, we did one test on 3 different prototypes with same design and same fabrication method. Error bars represent standard deviation. (c) Hysteresis test. A prototype was tested from 0% to 50% of strain, leave for 24 hours, then from 50% back to 0%. (d) Cyclic stretching test. The sample was stretched to 50% of strain then back to 0% for 240 times. Resonant frequency of the sample was measured each 20 times of stretching. 214

Figure 7-11: Theoretical reading range of the antenna in H-plane (left) and E-plane (right) with 0%, 25% and 50% length stretching in x-direction. The data were recorded for every 5-degree rotation in H-plane and every 10-degree rotation in E-plane. 215

List of tables

| | |
|---|-----|
| Table 1-1: Journals, manuscripts and the corresponding chapters in the thesis..... | 26 |
| Table 5-1: Comparison between non-hybrid microwave absorbers based on graphene/rGO as absorption material..... | 162 |
| Table 5-2: RCS Comparison between reported functional radar absorbers..... | 162 |

Abstract

As graphene has been discovered since 2004, a large amount of papers investigating the fundamental physical and chemical properties of graphene has been published. However, the applications that perfect taking advantage of graphene's properties are bare. This thesis focused on the development of graphene and graphene oxide (GO) based materials and their applications for electromagnetic ranges such as antennas, absorbers, wireless energy harvesting devices, sensors, and so on.

In this thesis, physical exfoliation of graphene from graphite particles has been well discussed and compared. Both popular bath sonication and mechanical shear-mixing methods have been used and compared. The cost, concentration and conductivity of exfoliated graphene have been optimized. Moreover, the graphene based low-cost screen printing inks have been developed and discussed in this thesis. Excellent conductivity property allows engineers to produce wireless connectivity antenna operational from MHz to tens of GHz. Applications of printed, flexible Near Field Communication antenna (NFC), ultra high frequency Radio Frequency Identification (RFID) tags, wireless NFC sensors and ultra-wideband energy harvesting system have been designed, fabricated and demonstrated in this thesis.

Due to the advances of ink preparation, cost and electrical properties, chemically exfoliated GO is used to replace physical exfoliated graphene on certain occasions. Printing and novel reduction process which can control reduced graphene oxide's (rGO) conductivity has been demonstrated as well. The fabricated rGO laminate not only can be used in flexible electronic circuits as conductors or resistors but also highly efficient to absorb microwave radiations with proper design. A printed Jaumann structured microwave absorber has been characterized and compared with standard absorber which is consisted by graphene loaded composites.

This thesis also presents the latest microfluidic RFID sensors for stretch sensing. The liquid, high conductive alloy based conductor has excellent sensitivity and repeatability comparing with lossy, rigid graphene based materials.

Declaration

No portion of the work referred to in the thesis has been submitted in support of an application for another degree or qualification of this or any other university or other institute of learning.

Copyright statement

The following four notes on copyright and the ownership of intellectual property rights must be included as written below:

- i. The author of this thesis (including any appendices and/or schedules to this thesis) owns certain copyright or related rights in it (the “Copyright”) and s/he has given The University of Manchester certain rights to use such Copyright, including for administrative purposes.
- ii. Copies of this thesis, either in full or in extracts and whether in hard or electronic copy, may be made only in accordance with the Copyright, Designs and Patents Act 1988 (as amended) and regulations issued under it or, where appropriate, in accordance with licensing agreements which the University has from time to time. This page must form part of any such copies made.
- iii. The ownership of certain Copyright, patents, designs, trademarks and other intellectual property (the “Intellectual Property”) and any reproductions of copyright works in the thesis, for example graphs and tables (“Reproductions”), which may be described in this thesis, may not be owned by the author and may be owned by third parties. Such Intellectual Property and Reproductions cannot and must not be made available for use without the prior written permission of the owner(s) of the relevant Intellectual Property and/or Reproductions.
- iv. Further information on the conditions under which disclosure, publication and commercialisation of this thesis, the Copyright and any Intellectual Property and/or Reproductions described in it may take place is available in the University IP Policy (see <http://documents.manchester.ac.uk/DocuInfo.aspx?DocID=24420>), in any relevant Thesis restriction declarations deposited in the University Library, The University Library’s regulations (see <http://www.library.manchester.ac.uk/about/regulations/>) and in The University’s policy on Presentation of Theses

Acknowledgments

First, and most of all, I would like to thank my PhD supervisor Prof. Zhirun Hu, for his expertise, assistance, guidance, and patience throughout the process of writing this thesis. He leads me to the right directions and guides me to think independently. I am extremely grateful for the opportunity to do the research and it was a great privilege and honor to work and study under his guidance. I would also like to thank him for his friendship, empathy, and great sense of humor.

I have achieved so much in the past four years at the University of Manchester, not just academically. I cannot express enough thanks to my friends, family and supervisors. Without all of you, I could never have reached this level of success.

In addition, I would sincerely thank Miss Lan Guang, Dr. James Yu from Scottish Power, Prof. Linghao and Prof. John Gallop from NPL who has given me endless support on my PhD study and life. I would also like to express my deepest gratitude to those who patiently taught and supported me from the beginning of my PhD study: Dr. Jiawei Zhang, Dr. Jiashen Li, Prof. Konstantin Novoselov, Dr. Qi Chen, Dr. David Zhang, Dr. Xianjun Huang, Dr. Xiao Zhang, Dr. Ting Leng, Dr. Zhen Li, Dr. Zeyu Long and Dr. Zhaozhong Meng, etc.

I am grateful to all of those whom I have had support and encouragement from during the last four years. They are Miss. Huan Gao, Mr. Jiwen Zhu, Mr. Jason Ye, Mr. Liang Peng, Mr. Yangyang Fan, Mr. Jun Song, Dr. Lijun Teng, Miss. Zhiying Xin, Miss. Zihan Lu, Mr. Shimeng Wang, Miss. Yutong Jiang, Miss. Yixian Fang and Miss. Xinyao Zhou, Miss. Luying Cui etc.

Last but not least, I would like to express my eternal appreciation towards my parents and family who have always been with me no matter where I am, for all unconditional supports and patience. Thank you for being ever so understanding and never ending motivations I've been getting all this while.

Publications

- **Kewen Pan**, et al. "graphene/polymer porous spongy for sensing and microwave absorbing applications." Submitted to Advanced Functional Materials.
- **Kewen Pan**, et al. "Controlled reduction of graphene oxide laminate and its applications for ultra-wideband microwave absorption." Carbon Volume 160, 30 April 2020, Pages 307-316.
- **Kewen pan**, et al. "Sustainable production of highly conductive multilayer graphene ink for wireless connectivity and IoT applications." Nature communications 9.1 (2018): 5197.
- **Kewen Pan**, et al. "Soft Wireless Battery-free UHF RFID Stretchable Sensor based on Microfluidic Technology." IEEE Journal of Radio Frequency Identification (2019).
- **Kewen Pan**, et al. "Soft Radio-Frequency Identification Sensors: Wireless Long-Range Strain Sensors Using Radio-Frequency Identification." Soft robotics 6.1 (2019): 82-94.
- Leng, T., **Pan, K.**, Zhang, Y., Li, J., Afroj, S., Novoselov, K. S., & Hu, Z. (2019). "Screen-Printed Graphite Nanoplate Conductive Ink for Machine Learning Enabled Wireless Radiofrequency-Identification Sensors". ACS Applied Nano Materials, 2(10), 6197-6208.
- Leng, Ting, **Kewen Pan**, and Zhirun Hu. "Printed Graphene Radio Frequency and Sensing Applications for Internet of Things." Handbook of Graphene: Technology and Innovations (2019): 11.
- Jiang, Y., **Pan, K.**, Leng, T., & Hu, Z. (2019). "Smart Textile Integrated Wireless Powered Near Field Communication (NFC) Body Temperature and Sweat Sensing System". IEEE Journal of Electromagnetics, RF and Microwaves in Medicine and Biology.
- Huang Xianjun, **Kewen Pan**, and Zhirun Hu. "Experimental demonstration of printed graphene nano-flakes enabled flexible and conformable wideband radar absorbers". Scientific reports, 6 (2016): 38197.
- Lu, Z., Song, J., **Pan, K.**, Meng, J., Xin, Z., Liu, Y., ... & Li, J. (2019). "EcoFlex sponge with ultrahigh oil absorption capacity". ACS applied materials & interfaces.

- **Kewen Pan**, et al. "Graphene Printed UWB Monopole Antenna for Wireless communication applications." 2019 IEEE International Symposium on Antennas and Propagation and USNC-URSI Radio Science Meeting. IEEE, 2019.
- **Kewen Pan**, Ting Leng, David Zhang, Habiba Ouslimani and Zhirun Hu. "Metamaterial Inspired Long Read Range UHF RFID Tag Antenna". PIERS 2018, Toyama.
- **Kewen Pan**, Ting Leng, Xiao Zhang and Zhirun Hu, "Design and modeling of back gated graphene based RF switch with CPW transmission line on a high resistivity silicon substrate," 2017 10th UK-Europe-China Workshop on Millimetre Waves and Terahertz Technologies (UCMMT), Liverpool, 2017, pp. 1-2.
- **Kewen Pan**, Ting Leng, and Z. Hu, "Printed Graphene Antennas: Near and Far (Field) ", LAPC (2017 Loughborough Antennas & Propagation Conference).
- Leng, T., **Pan, K.**, Jiang, Y., Hu, Z., OUSLIMANI, H., & Abdalla, M. A. (2019, July). "Dual Band Graphene Nanoflakes Printed Compact Monopole Antenna for Low Cost WIFI Applications". In 2019 IEEE International Symposium on Antennas and Propagation and USNC-URSI Radio Science Meeting (pp. 1287-1288). IEEE.
- Ting Leng, **Kewen Pan**, Zhirun Hu, "Design of Reconfigurable Meandered Line Dipole Antenna for Printed Graphene Applications". IEEE AP-S International Symposium, 2017.
- Ting Leng, **Kewen Pan**, Zhirun Hu, "Graphene Nanoflakes Conductive Ink Printed Near Field Communication". IEEE International Microwave Symposium, 2017.
- Ting Leng, **Kewen Pan** and Zhirun Hu, "Printed Graphene for Chipless RFID Applications". EuMW 2018, Madrid, Spain.
- Xiao Zhang, **Kewen Pan**, Weisheng Yue, Ernie Hill, Habiba Ouslimani and Zhirun Hu, "A Graphene-based Electromagnetic Switch at Microwave Frequencies", 2016 IEEE 5th Asia-Pacific Conference on Antennas and Propagation, Kaohsiung, Taiwan, July 2016.

- Dai, Xuewu, Fei Qin, Zhiwei Gao, **Kewen Pan**, and Krishna Busawon. "Model-based on-line sensor fault detection in Wireless Sensor Actuator Networks". In Industrial Informatics (INDIN), 2015 IEEE 13th International Conference on, pp. 556-561. IEEE, 2015.

Abbreviations

| | |
|------------|--|
| 2D | Two dimensional |
| 3D | Three dimensional |
| AFM | Atomic force microscopy |
| AgNW | Silver nanowire |
| CAB | Cellulose acetate butyrate |
| CMOS | Complementary metal–oxide– semiconductor |
| CVD | Chemical vapor deposition |
| CPW | Coplanar waveguide |
| CNTs | Carbon nanotubes |
| DC | Direct current |
| DEMMA-TFSI | Diethylmethyl(2- methoxyethyl)ammonium bis(trifluoromethylsulfonyl)imide |
| DMF | Dimethylformamide |
| DSC | Differential scanning calorimetry |
| DUT | Device under test |
| EM | Electromagnetic |
| EMI | Electromagnetic interference |
| FLG | Few layer graphene |
| FTIR | Fourier-transform infrared spectroscopy |
| FSS | Frequency selective surface |
| GCD | Galvanostatic charge/discharge |
| GNPs | Graphene nano pellets |
| Gp | Graphite flakes |
| Gr | Graphene flakes |
| GO | Graphene oxide |

| | |
|------|---|
| IOT | Internet of things |
| ISO | International organization for standardization |
| LNA | Low noise amplifier |
| NC | Nitrocellulose |
| NFC | Near field communication |
| NMP | N-Methyl-2-pyrrolidone |
| NP | Nanoparticles |
| NRW | Nicolson Ross Weir |
| PCB | Printed circuit board |
| PDMS | Polydimethylsiloxane |
| PEC | Perfect electronic conductor |
| RFID | Radio frequency identification |
| RF | Radio frequency |
| RPM | Revolutions per minute |
| rGO | Reduced graphene oxide |
| RCS | Radar cross section |
| SEM | Scanning electron microscope |
| SE | Shielding effectiveness |
| SMA | Subminiature version A |
| SRR | Split ring resonator |
| TL | Transmission line |
| TE | Transverse electric |
| TGA | Thermo gravimetric analysis |
| TM | Transverse magnetic |
| TEM | Transmission electron microscopy or transverse electromagnetic |
| UAVs | Unmanned aerial vehicles |
| UHF | Ultra high frequency |

| | |
|------|-----------------------------------|
| UWB | Ultra wideband |
| VNA | Vector network analyzer |
| WSNs | Wireless sensor networks |
| XPS | X-ray photo-electron spectrometry |
| XRD | X-ray diffraction |

Statement of novelty

In chapter 3, very high concentration graphene ink with the highest conductivity so far was proposed. Pure graphene printed long range UHF RFID tag, low loss NFC coil antenna and wideband slot antennas were first reported.

In chapter 4, a novel graphene coated, multi-functional elastic sponge structure was proposed. Based on the conductive sponge, a practical wide band microwave absorber and an elastic supercapacitor were demonstrated.

In chapter 5, the conductivity of reduced graphene oxide laminates under different reduction levels was monitored. The first light weight, printed rGO based microwave absorber was proposed.

In chapter 6 and 7, two different types of stretchable antenna were designed and fabricated for wireless stretch sensing. This is the first attempt to replace wired stretchable sensors on soft robotics by using RFID technology.

1 Introduction

1.1 Motivation

The research of wearable electronics, health care and internet of things (IoT) has been accelerated since ten years ago. Various electronic devices ranging from sensors to wireless antennas are connected together. Due to the flexible requirement of wearable devices, traditional PCB technology cannot satisfy. The novel printed electronic technology is growing up because of the flexibility, fast production, low cost and less waste. The total market of the printed electronics industry in 2024 is estimated to \$ 13.35 billion. Among these, flexible monitors, touch screens, stretchable circuits and printed NFC, RFID tags are widely used in practical applications [1,2].

Since the development of inkjet printing technology [3], the silver nanoparticle-based conductive inks have received much attention because of the highest conductivity [4]. However, polymers and surfactants which would severely degrade conductivity [1] must be added to avoid the aggregation problem. Secondly, the raw material is expensive silver. Therefore, researchers are trying to use alternative conductive metals such as aluminum and copper. Unlike conductive silver oxide, aluminum oxide and copper oxide are excellent insulating materials that would cover the surface of these metal nanoparticles and then block electron flow [5]. The electronic devices that printed by these active metal typically have poor durability. Moreover, the annealing process is also required to sinter metal nanoparticles. But most polymer substrates such as paper and plastic film cannot tolerate high temperatures [6]. In order to replace expensive

metal particles, metal nanowire was developed [7] with lower contact resistance and better transparency. A stretchable patch antenna was fabricated by silver nanowire [8] and a conductive line was printed by copper nanowire [9]. Many works have solved the problems of metal nanowires from laboratory to industry except the expensive raw materials. Another approach is using conductive polymers rather than metal. As some of the conductive polymers behave like semiconductors [10], conductive sensors have been printed and fabricated in [11,12]. However, the cost, chemical instability [13] and low conductivity still limit their application on conductors. Benefit from the excellent conductivity and stable structure, carbon-based materials have attracted more attention since the invention of carbon nanotubes (CNT). The electrical conductivity of single-wall CNT is close to metal [14]. However, the single-wall CNT is challenging to be prepared and van der Waals force makes CNTs extremely easy to get aggregated. Any stabilization method would degrade CNT's conductivity [15,16]. Although many outstanding works have demonstrated the conductive printing of CNT [17,18], there is still a long way to go before practical.

Graphene, which is a planar atomic layer of carbon atoms is the latest promising carbon-based material and related to CNT in which a single-walled CNT can be thought as monolayer graphene flakes rolled into a cylinder. Graphene has all the advantages for conductive ink, such as oxide free, highly conductive and low cost, etc. Previous works have demonstrated that graphene conductive ink can be printed by many popular printing methods: screen printing [19], inkjet printing [20], gravure printing and sputtering [21]. To prepare the graphene inks, graphene flakes must be exfoliated from

graphite particles. Manual exfoliation and CVD growth are not possible because of low efficiency. Only mechanical (ultrasonic, shear exfoliation, etc.) and chemical (graphene oxide-reduced graphene oxide) routes are possible. For mechanical routes, the concentrations of graphene flakes are quite low and poisoned solvents are used. For chemical routes, the conductivity of reduced graphene oxide is relatively low due to its defects. Current works are still mainly focusing on the ink preparation and printing areas. Well designed and practical applications are barely reported.

This thesis first studies the high concentration and conductivity graphene ink preparation through both ultrasonic exfoliation, shear exfoliation and chemical exfoliation. Graphene-based conductors, antennas, absorbers, sensors and supercapacitor were designed and fabricated by using the prepared graphene inks. After being inspired by the wireless sensor and graphene RFID antenna, battery-free, soft RFID stretch sensors were fabricated in the last chapter 6 and 7.

1.2 Thesis outline

The thesis includes eight chapters. Chapter 1 introduced the motivations. In chapter 2, some fundamental theories and background knowledge are listed for the analyses of graphene, antenna test and microwave parameters measurement. The detailed results are presented from chapter 3 to 7 with the format of journal publications. Figures in this thesis have been rearranged. The thesis structure and relations of chapters are shown in Figure 1-1.

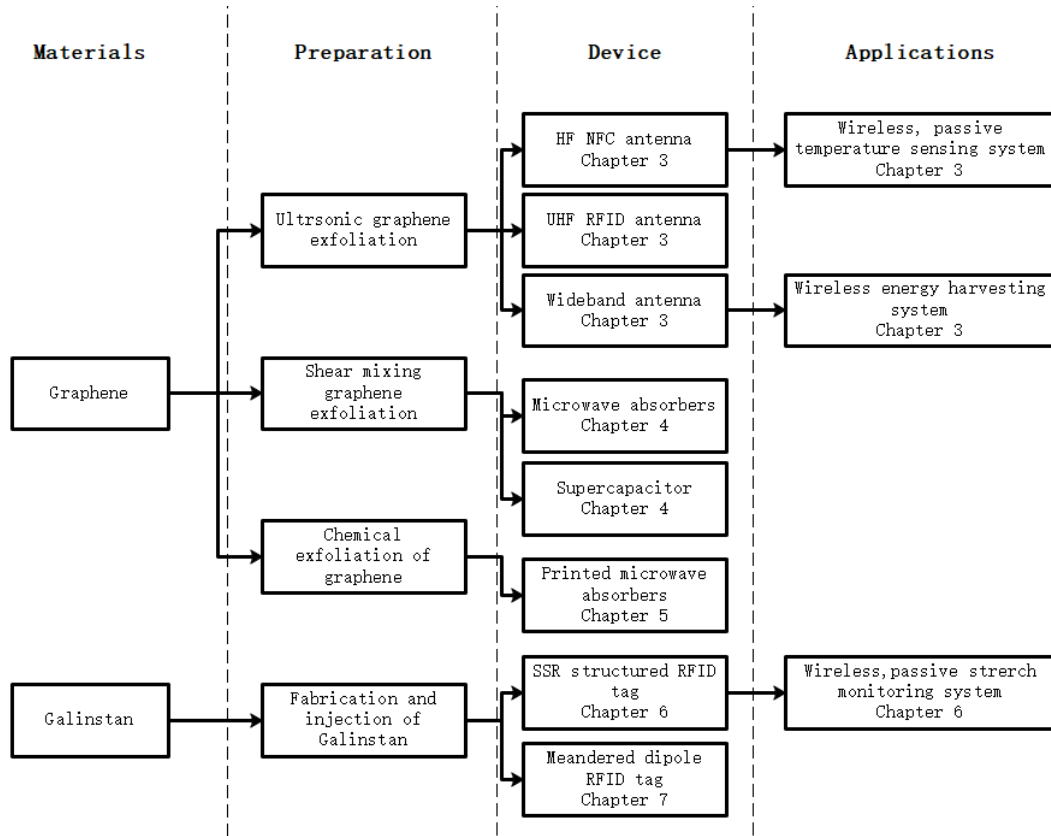


Figure 1-1: The thesis outline.

In chapter 3, the concentration of graphene ink has been dramatically increased by using the novel, environmentally friendly solvent: Cyrene. Antennas from high frequency band to microwave band have been printed and characterized. A graphene printed NFC temperature sensor and a wireless energy harvesting system were demonstrated in this chapter. As the ultrasonication method still requires long processing time, shear exfoliation was discussed in chapter 4 with concentration and conductivity optimization. A graphene loaded sponge was prepared and its electrical and microwave applications have been presented. In chapter 5, reduced graphene oxide was prepared and discussed. The rGO laminates' conductivity can be controlled accurately for EM shielding or absorption applications. Chapter 6 and 7 demonstrated

stretchable RFID sensor tags and the whole measurement system. Galinstan was applied as conductor to ensure the continuity of antennas. Journal papers according to the sequence of chapters are listed in Table 1-1.

Table 1-1: Journals, manuscripts and the corresponding chapters in the thesis.

| Chapter | Publications |
|---------|--|
| 3 | <p>"Sustainable production of highly conductive multilayer graphene ink for wireless connectivity and IoT applications." <i>Nature communications</i> 9.1 (2018): 5197.</p> <p>Kewen Pan, Yangyang Fan, Ting Leng, Jiashen Li, Zhiying Xin, Jiawei Zhang, Ling Hao, John Gallop, Kostya S. Novoselov & Zhirun Hu</p> |
| 4 | <p>"3D graphene/polymer porous spongy for sensing and microwave absorbing applications" Submitted to <i>Advanced Functional Materials</i></p> <p>Kewen Pan, Ting Leng, Jiashen Li, Kostya S. Novoselov & Zhirun Hu</p> |
| 5 | <p>"Controlled reduction of graphene oxide laminate and its applications for ultra-wideband microwave absorption." <i>Carbon</i> Volume 160, 30 April 2020, Pages 307-316.</p> <p>Kewen Pan, Ting Leng, Jun Song, Chengyu Ji, Jiawei Zhang, Jiashen Li, Kostya S. Novoselov & Zhirun Hu</p> |
| 6 | <p>"Soft Wireless Battery-free UHF RFID Stretchable Sensor based on Microfluidic Technology." <i>IEEE Journal of Radio Frequency Identification</i> 3:4, 252-258 (2019).</p> <p>Kewen Pan, Lijun Teng, Leng Ting, Xinyao Zhou, Adam A. Stokes and</p> |

Zhirun Hu

- 7 "Soft Radio-Frequency Identification Sensors: Wireless Long-Range Strain Sensors Using Radio-Frequency Identification." *Soft robotics* 6.1 (2019): 82-94.

Lijun Teng, Kewen Pan, Markus P. Nemitz, Rui Song, Zhirun Hu, and Adam A. Stokes

References

- [1] Kamyshny A, Magdassi S. Conductive nanomaterials for printed electronics. *Small* 2014;10:3515–35.
- [2] Layani M, Kamyshny A, Magdassi S. Transparent conductors composed of nanomaterials. *Nanoscale* 2014;6:5581–91.
- [3] Singh M, Haverinen HM, Dhagat P, Jabbour GE. Inkjet printing—process and its applications. *Adv Mater* 2010;22:673–85.
- [4] Layani M, Magdassi S. Flexible transparent conductive coatings by combining self-assembly with sintering of silver nanoparticles performed at room temperature. *J Mater Chem* 2011;21:15378–82.
- [5] Campbell T, Kalia RK, Nakano A, Vashishta P, Ogata S, Rodgers S. Dynamics of oxidation of aluminum nanoclusters using variable charge molecular-dynamics simulations on parallel computers. *Phys Rev Lett* 1999;82:4866.
- [6] Han L, Zhao Y-X, Liu C-M, Li L-H, Liang X-J, Wei Y. The effects of nanoparticle shape on electrical conductivity of Ag nanomaterials. *J Mater Sci Mater Electron* 2014;25:3870–7.
- [7] De S, Higgins TM, Lyons PE, Doherty EM, Nirmalraj PN, Blau WJ, et al. Silver nanowire networks as flexible, transparent, conducting films: extremely high DC to optical conductivity ratios. *ACS Nano* 2009;3:1767–74.
- [8] Rai T, Dantes P, Bahreyni B, Kim WS. A stretchable RF antenna with silver nanowires. *IEEE Electron Device Lett* 2013;34:544–6.
- [9] Rathmell AR, Wiley BJ. The synthesis and coating of long, thin copper nanowires to make flexible, transparent conducting films on plastic substrates. *Adv Mater* 2011;23:4798–803.
- [10] Shirakawa H, Louis EJ, MacDiarmid AG, Chiang CK, Heeger AJ. Synthesis of electrically conducting organic polymers: halogen derivatives of polyacetylene, (CH)_x. *J Chem Soc Chem Commun* 1977:578–80.
- [11] Cochrane C, Lewandowski M, Koncar V. A flexible strain sensor based on a conductive polymer composite for in situ measurement of parachute canopy deformation. *Sensors* 2010;10:8291–303.
- [12] Cochrane C, Koncar V, Lewandowski M, Dufour C. Design and development of a flexible strain sensor for textile structures based on a conductive polymer composite. *Sensors* 2007;7:473–92.
- [13] Richardson-Burns SM, Hendricks JL, Foster B, Povlich LK, Kim D-H, Martin DC. Polymerization of the conducting polymer poly (3, 4-ethylenedioxythiophene)(PEDOT) around living neural cells. *Biomaterials* 2007;28:1539–52.
- [14] Hu L, Hecht DS, Gruner G. Carbon nanotube thin films: fabrication, properties, and applications. *Chem Rev* 2010;110:5790–844.
- [15] Lu KL, Lago RM, Chen YK, Green MLH, Harris PJF, Tsang SC. Mechanical damage of carbon nanotubes by ultrasound. *Carbon N Y* 1996;34.
- [16] Azoubel S, Magdassi S. The formation of carbon nanotube dispersions by high pressure homogenization and their rapid characterization by analytical centrifuge. *Carbon N Y* 2010;48:3346–52.
- [17] Jo JW, Jung JW, Lee JU, Jo WH. Fabrication of highly conductive and transparent thin films

- from single-walled carbon nanotubes using a new non-ionic surfactant via spin coating. *ACS Nano* 2010;4:5382–8.
- [18] Hecht DS, Hu L, Irvin G. Emerging transparent electrodes based on thin films of carbon nanotubes, graphene, and metallic nanostructures. *Adv Mater* 2011;23:1482–513.
- [19] Pan K, Fan Y, Leng T, Li J, Xin Z, Zhang J, et al. Sustainable production of highly conductive multilayer graphene ink for wireless connectivity and IoT applications. *Nat Commun* 2018;9:5197.
- [20] Li J, Ye F, Vaziri S, Muhammed M, Lemme MC, Östling M. Efficient inkjet printing of graphene. *Adv Mater* 2013;25:3985–92.
- [21] Huang X, Pan K, Hu Z. Experimental demonstration of printed graphene nano-flakes enabled flexible and conformable wideband radar absorbers. *Sci Rep* 2016;6:38197.

2 Background theory and concepts

2.1 Graphene modeling

Graphene has unique outstanding proprieties since Geim and Novoselov discovered the new material in 2004 [1]. Some excellent proprieties, including high electron mobility [1] and electrical conductivity [2] are very useful for electronic applications. The band structure of monolayer graphene is well discussed [3]. The conduction and valence bands of graphene touch at Dirac point where the energy is zero. For low energies, the dispersion relation is linear near the Dirac point. The charge carriers behave like massless Dirac fermion. Therefore, the band gap of ideal graphene is zero which means graphene is neither semiconductor nor metal but semimetal. This unique property makes the charge carriers can be continuously turned between electrons and holes by shifting energy levels electrically or magnetically. The carrier mobility limitation in graphene is $200,000 \text{ cm}^2\text{V}^{-1}\text{s}^{-1}$ with the carrier density of 10^{12} cm^{-2} [4]. The corresponded conductivity is 10^8 S/m , which is the highest conductivity that we know at room temperature [5]. The measured carrier mobility peak of suspended graphene flake is $230,000 \text{ cm}^2\text{V}^{-1}\text{s}^{-1}$ [6]. However, suspended graphene is difficult to be fabricated as practical devices. The measured highest mobility of graphene on the top of SiO_2 is much lower because of the electron scattering phenomenon of the substrate [7]. Moreover, the manual exfoliated graphene is not fabrication friendly. Chemical vapour deposition (CVD) method is more commonly used for the large area synthesis of graphene. The mobility dropped to approximately $4000 \text{ cm}^2\text{V}^{-1}\text{s}^{-1}$ [8]. In

conclusion, both substrate, doping from the air, chemical residual or defects would significantly affect the mobility and conductivity of graphene.

Apart from the excellent mobility, the tenability of carrier density under an external electrical field makes graphene a good candidate for designing tunable components. Novoselov and Geim [1] found the graphene-based back gated transistor structure can be turned by voltage. Also, microwave propagation performance of graphene has been reported [9,10]. Therefore, graphene is possible to be applied as reconfigure antennas [11], filter [12], frequency selective surface [13], etc. To accurately describe the tunable behavior, graphene can be modeled as a thin layer conductor with surface conductivity σ . By using Kubo's formula [9], the surface conductivity of graphene can be described as the sum of inter-band and intra-band. The intra-band can be expressed as [9]:

$$\sigma_{intra}(\omega) = \frac{e^2 k_B T \tau}{\pi \hbar^2 (1 + j\omega\tau)} \left\{ \frac{U_c}{k_B T} + 2 \ln(e^{-U_c/k_B T} + 1) \right\} \quad (2.1)$$

while $k_B T \ll |\mu_c|$, the conductivity of inter-band can be approximated as:

$$\sigma_{inter}(\omega) = \frac{-je^2}{4\pi\hbar} \ln\left(\frac{2|U_c| - (\omega - 2\Gamma)\hbar}{2|U_c| + (\omega - 2\Gamma)\hbar}\right) \quad (2.2)$$

ω is the radian frequency, τ is the scattering time, e is the charge of an electron, k_B is Boltzmann's constant, T is temperature, $\hbar = h/2\pi$ is the reduced Planck's constant, and U_c is the chemical potential. The final conductivity can be expressed as:

$$\sigma = \sigma_{intra} + \sigma_{inter} \quad (2.3)$$

In the microwave region, the transition of inter-band threshold $\hbar\omega < 2|E_F|$, therefore the intra-band contribution of conductivity dominates and the surface impedance can be simplified as:

$$Z_s = 1/\sigma_{intra} \quad (2.4)$$

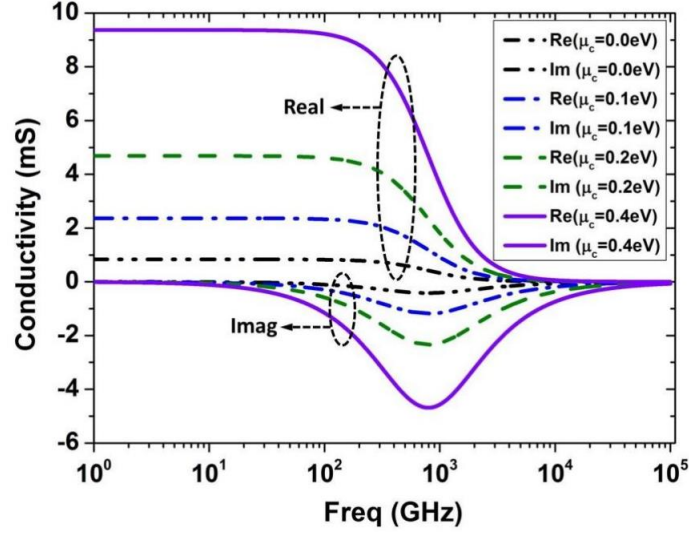


Figure 2-1: The surface conductivity tunability of graphene in microwave and THz frequency [14].

From above analysis, the surface conductivity of monolayer graphene is the function of chemical potential U_c . As seen in Figure 2-1, the surface conductivity of graphene under room temperature, ranging from low frequency to infrared bands has been plotted with different chemical potentials 0, 0.1, 0.2 and 0.4 eV. For the higher frequency (>100 GHz but <10 THz), the imaginary part of conductivity changes dynamically with the increasing of chemical potentials. However, for the microwave band (<100 GHz), the imaginary part is not responding to the varying of chemical potentials. The real part seems more sensitive. Therefore, graphene behaves more like a tunable resistor in microwave region.

As can be seen, any varying of chemical potential would turn the surface impedance of graphene. The chemical potential of graphene is determined by its carrier density:

$$n_s = \frac{2}{\pi \hbar^2 V_F^2} \int_0^\infty \varepsilon [f_d(\varepsilon) - f_d(\varepsilon + 2U_c)] d\varepsilon \quad (2.5)$$

where $V_F \approx 1 \times 10^6$ m/s and $f_d = 1/(1 + e^{(\varepsilon - U_c)/k_B T})$ is the Fermi distribution

function. Thanks to the field-effect structure, the changes in chemical potential can be achieved by turning the gate voltage [15]. The carrier density n_s is determined by external electric field V_{DC} :

$$n_s = \varepsilon_0 \varepsilon_r V_{DC} / t e \quad (2.6)$$

where ε_0 is free space permittivity, ε_r is relative permittivity of insulator, t is the thickness of insulator and e is the electron charge. The relationship between external voltage and chemical potential is illustrated in Figure 2-2.

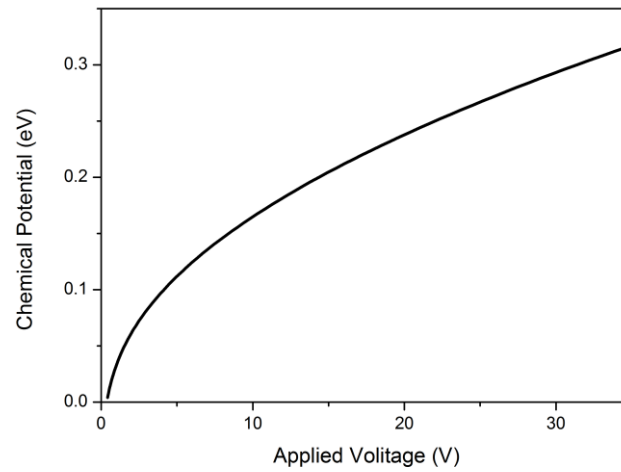


Figure 2-2: The relationship between applied voltage and chemical potential [16].

For the better demonstration of the tunability of graphene in microwave region, a coplanar waveguide (CPW) tunable transmission line with back-gated graphene structure was simulated by applying Kubo model [16]. The simulation model is demonstrated in Figure 2-3. The structure is built on 350 μm thick undoped high resistive silicon substrate (Resistivity: 20 $\text{k}\Omega\cdot\text{cm}$). The thin 90 nm silicon dioxide reduces the external voltage lower than 30 V. 70 nm gold was evaporated on the top. The external voltage is applied between the gold and undoped silicon substrate.

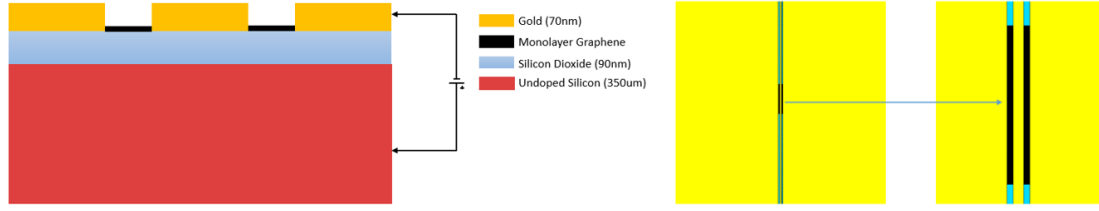


Figure 2-3: The structure of the constructed CPW graphene switch in vertical cross view (left) and top view (right) [16].

In the ‘on’ state of the graphene transmission line, there is no external voltage applied. The signal is divided to graphene sheet and another port. In the ‘off’ state, the external voltage is applied to graphene which forces the conductivity increasing. Signal path is shorted and reflected. There are no signal passes through the transmission line. Simulated transmission coefficient (S_{21}) is shown in Figure 2-4. The effects of chemical potentials on the S_{21} can be clearly observed, corresponding well with above analysis.

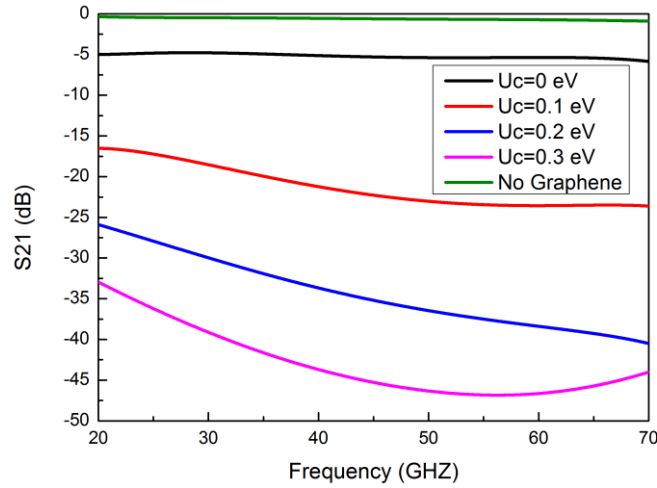


Figure 2-4: The magnitude of measured transmission S_{21} over the frequency range 0–110 GHz respectively [16].

However, pure mono-layer graphene flakes are quite difficult to be obtained. The low-cost approaches are using sonication [17], shear exfoliation [18]. The final products

would be few-layer graphene (<3 nm) or graphene nano pellets (> 3 nm). Their mobility and conductivity would be degraded due to the increased interlayer channels [19]. The electrical behaviors are more close to graphite structure. Therefore, for such printed (inkjet or screen printing) graphene thin layer laminates can be modeled as an ohmic sheet because its thickness is thinner than skin depth in microwave region and the dimensions of voids are orders shorter than wavelength.

2.2 Basic theories

2.2.1 Sheet resistance

Although conductivity (σ) or resistivity (ρ) is an essential property for all materials. It is not practical in design or simulation for uniform thin films. The more convenient way is using sheet resistance. It is expressed as Ω/sq [20]. In the conventional 3-D conductive materials, the resistance is:

$$R = \rho \frac{L}{Wt} \quad (2.7)$$

where ρ is the resistivity, L is the length, W and t are the width and thickness of cross-section, respectively. By combining the resistivity and thickness:

$$R = R_s \frac{L}{W} \quad (2.8)$$

$$R_s = \frac{\rho}{t} \quad (2.9)$$

where R_s is sheet resistance.

2.2.2 Skin depth and surface resistance

In the real world, a perfect conductor does not exist. A good conductor such as

metals, the conductive current is orders higher than the displacement current. Therefore the propagation constant of a plane wave can be approximated by ignoring displacement current and the skin depth can be expressed as [21]:

$$\delta_s = \sqrt{\frac{2}{\omega\mu\sigma}} \quad (2.7)$$

where ω is angular frequency, μ is permeability of the conductor and σ is conductivity. The magnitude of currents in the conductor decreased by 36.8% after traveling each skin depth. In microwave regions, the skin depth of metal conductors usually is less than micrometers. However, for the higher loss of printed graphene laminates and thin, monolayer graphene, the skin depth issue must be considered for low loss microwave components.

In real microwave applications, the conductor loss must be considered. The surface resistance can be written as [21]:

$$R_s = \frac{1}{\sigma\delta_s} = \frac{\rho}{\delta_s} = \sqrt{\frac{\omega\mu}{2\sigma}} \quad (2.8)$$

The expression of the surface resistance and DC sheet resistance is similar in formula expressions.

2.2.3 Antenna gain measurement

For the gain and radiation pattern measurement of antennas, the electromagnetic illumination source must generate uniform plane wave. To satisfy this requirement, the source antenna and receiving antenna must be in the far-field zones of each other. The minimum distance of two antennas can be calculated as [22]:

$$R_{min} = 2D_{max}^2/\lambda \quad (2.9)$$

where D_{max} is the maximum length of the source antenna.

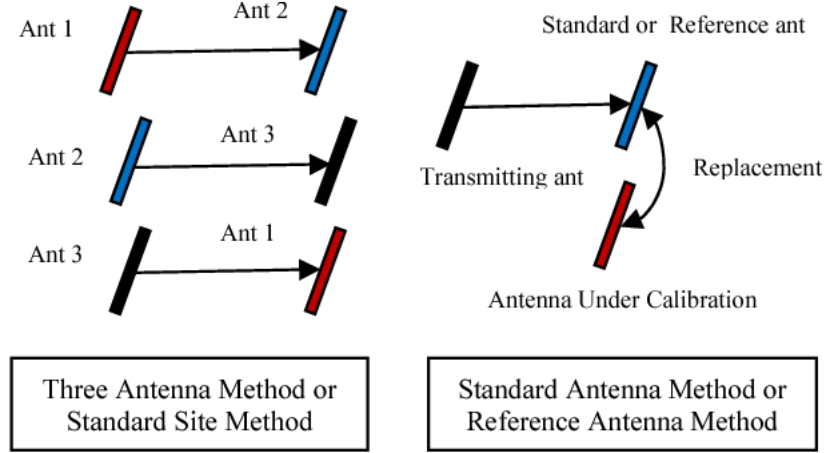


Figure 2-5: Antenna measurement methods [23].

The most commonly used antenna measurement methods are standard antenna method and three-antenna method. Expensive standard antennas are required for the standard antenna method because the measurement accuracy depends on these antennas. In this thesis, the three-antenna method is used for all gain and radiation pattern measurement. In Figure 2-5, all three antennas are measured as a pair (transmitting and receiving). Assuming the polarization and matching are perfect, Friis transmission equation can be used to calculate antenna gain:

$$\frac{P_r}{P_t} = \left(\frac{\lambda}{4\pi R}\right)^2 G_t G_r \quad (2.10)$$

where P_t is the power that transmitted from the source antenna; P_r is the power that received from receiver antenna; λ is wavelength; R is the distance between two antennas; G_t, G_r are the gain of transmitting and receiving antennas. This equation can be rewritten in decibel format as:

$$G_{t(dB)} + G_{r(dB)} = 20 \log_{10} \left(\frac{4\pi R}{\lambda} \right) + 10 \log_{10} \left(\frac{P_r}{P_t} \right) \quad (2.11)$$

Combine the results of three pair's measurement (antenna 1 & 2, antenna 1 & 3 and

antenna 2 & 3). Equ. (2.11) can be expended as:

$$G_{1(dB)} + G_{2(dB)} = 20 \log_{10} \left(\frac{4\pi R}{\lambda} \right) + 10 \log_{10} \left(\frac{P_1}{P_2} \right) \quad (2.12)$$

$$G_{1(dB)} + G_{3(dB)} = 20 \log_{10} \left(\frac{4\pi R}{\lambda} \right) + 10 \log_{10} \left(\frac{P_1}{P_3} \right) \quad (2.13)$$

$$G_{2(dB)} + G_{3(dB)} = 20 \log_{10} \left(\frac{4\pi R}{\lambda} \right) + 10 \log_{10} \left(\frac{P_2}{P_3} \right) \quad (2.14)$$

Then simplified as:

$$G_{1(dB)} + G_{2(dB)} = A \quad (2.15)$$

$$G_{1(dB)} + G_{3(dB)} = B \quad (2.16)$$

$$G_{2(dB)} + G_{3(dB)} = C \quad (2.17)$$

In final, the gains of the three antennas can be obtained simultaneously:

$$G_{1(dB)} = \frac{A+B-C}{2} \quad (2.18)$$

$$G_{2(dB)} = \frac{A-B+C}{2} \quad (2.19)$$

$$G_{3(dB)} = \frac{B+C-A}{2} \quad (2.20)$$

2.2.4 Permittivity and permeability measurement (Nicolson-Ross-Weir (NRW) method)

In this thesis, graphene loaded conductive sponges were fabricated in chapter 4 and their electrical permittivity and permeability in X-band were measured by standard waveguide NRW method [24]. The reflection coefficient Γ is calculated by S-parameters [24] that obtained from the waveguide:

$$\Gamma = \frac{Z_s - Z_0}{Z_s + Z_0} = \frac{\sqrt{\frac{\mu_r}{\epsilon_r}} - 1}{\sqrt{\frac{\mu_r}{\epsilon_r}} + 1} \quad (2.21)$$

The transmission coefficient T is given by [24]:

$$T = e^{-\frac{j\omega}{c} \sqrt{\mu_r \epsilon_r} d} \quad (2.22)$$

where c is the speed of light in vacuum; d is the thickness of the sample in X-band waveguide. In the meantime, the reflection and transmission coefficient can be written as:

$$\Gamma = X \pm \sqrt{X^2 - 1} \quad (2.23)$$

$$T = \frac{S_{11} + S_{21} - \Gamma}{1 - (S_{11} + S_{21})\Gamma} \quad (2.24)$$

Where

$$X = \frac{S_{11}^2 - S_{21}^2 + 1}{2S_{11}} \quad (2.25)$$

From Equ. (2.21~2.24), we could combine them as:

$$x = \frac{\mu_r}{\varepsilon_r} = \left(\frac{1+\Gamma}{1-\Gamma} \right)^2 \quad (2.26)$$

$$y = \mu_r \varepsilon_r = - \left[\frac{c}{\omega d} \ln \frac{1}{T} \right]^2 \quad (2.27)$$

It should be noticed that T is a complex number and the solution of $\ln \frac{1}{T}$ would have complex results plus $2\pi n$, where n is the integral of $\left(\frac{d}{\lambda} \right)$. Therefore, a thin sample (wavelength in the sample $\lambda >$ sample thickness d) or time domain techniques [24] must be involved to get correct results. Then the relative permittivity ε_r and permeability μ_r can be simplified as:

$$\varepsilon_r = \sqrt{\frac{y}{x}} \quad (2.28)$$

$$\mu_r = \sqrt{xy} \quad (2.29)$$

In final, μ_r can be calculated as [24]:

$$\mu_r = \frac{1+\Gamma}{\Lambda(1-\Gamma) \sqrt{\frac{1}{\lambda_0^2} - \frac{1}{\lambda_c^2}}} \quad (2.30)$$

and ε_r can be obtained as:

$$\varepsilon_r = \frac{(\frac{1}{\Lambda^2} + \frac{1}{\lambda_c^2})\lambda_0^2}{\mu_r} \quad (2.31)$$

For the waveguide measurement with sample holder [25]:

$$\frac{1}{\Lambda^2} = (\frac{\varepsilon_r \mu_r}{\lambda_0^2} - \frac{1}{\lambda_c^2}) \quad (2.32)$$

where λ_0 is the corresponded wavelength of free space and λ_c is the cutoff wavelength of the X-band waveguide. From Equ. (2.30) and (2.31), both permittivity and permeability are frequency dependent. A Labview program and Keysight N9918A vector network analyzer (VNA) are used in this thesis.

References

- [1] Novoselov KS, Geim AK, Morozov S V, Jiang D, Zhang Y, Dubonos S V, et al. Electric field effect in atomically thin carbon films. *Science* (80-) 2004;306:666–9.
- [2] Novoselov KS, Geim AK, Morozov Sv, Jiang D, Katsnelson MI, Grigorieva Iv, et al. Two-dimensional gas of massless Dirac fermions in graphene. *Nature* 2005;438:197.
- [3] Lemme MC. Current status of graphene transistors. *Solid State Phenom.*, vol. 156, Trans Tech Publ; 2010, p. 499–509.
- [4] Chen J-H, Jang C, Xiao S, Ishigami M, Fuhrer MS. Intrinsic and extrinsic performance limits of graphene devices on SiO₂. *Nat Nanotechnol* 2008;3:206.
- [5] SHIN YOUNG JUN. Electronic transport of graphene devices 2012.
- [6] Bolotin KI, Sikes KJ, Jiang Z, Klima M, Fudenberg G, Hone J, et al. Ultrahigh electron mobility in suspended graphene. *Solid State Commun* 2008;146:351–5.
- [7] Fang T, Konar A, Xing H, Jena D. Mobility in semiconducting graphene nanoribbons: Phonon, impurity, and edge roughness scattering. *Phys Rev B* 2008;78:205403.
- [8] Bae S, Kim H, Lee Y, Xu X, Park J-S, Zheng Y, et al. Roll-to-roll production of 30-inch graphene films for transparent electrodes. *Nat Nanotechnol* 2010;5:574.
- [9] Hanson GW. Erratum:“Dyadic Green’s functions and guided surface waves for a surface conductivity model of graphene”[*J. Appl. Phys.* 103, 064302 (2008)]. *J Appl Phys* 2013;113:29902.
- [10] Deligeorgis G, Dragoman M, Neculoiu D, Dragoman D, Konstantinidis G, Cismaru A, et al. Microwave propagation in graphene. *Appl Phys Lett* 2009;95:73107. doi:10.1063/1.3202413.
- [11] Tamagnone M, Gomez-Diaz JS, Mosig JR, Perruisseau-Carrier J. Reconfigurable terahertz plasmonic antenna concept using a graphene stack. *Appl Phys Lett* 2012;101:214102.
- [12] Correias-Serrano D, Gomez-Diaz JS, Perruisseau-Carrier J, Alvarez-Melcon A. Graphene-based plasmonic tunable low-pass filters in the terahertz band. *IEEE Trans Nanotechnol* 2014;13:1145–53.
- [13] Wu B, Hu Y, Zhao YT, Lu WB, Zhang W. Large angle beam steering THz antenna using active frequency selective surface based on hybrid graphene-gold structure. *Opt Express* 2018;26:15353–61.
- [14] Huang X, Hu Z, Liu P. Graphene based tunable fractal Hilbert curve array broadband radar absorbing screen for radar cross section reduction. *Aip Adv* 2014;4:117103.
- [15] Sensale-Rodriguez B, Yan R, Kelly MM, Fang T, Tahy K, Hwang WS, et al. Broadband graphene terahertz modulators enabled by intraband transitions. *Nat Commun* 2012;3:780.
- [16] Pan K, Leng T, Zhang X, Hu Z. Design and modeling of back gated graphene based RF switch with CPW transmission line on a high resistivity silicon substrate. 2017 10th UK-Europe-China Work. Millimetre Waves Terahertz Technol., IEEE; 2017, p. 1–2.
- [17] Ciesielski A, Samorì P. Graphene via sonication assisted liquid-phase exfoliation. *Chem Soc Rev* 2014;43:381–98.
- [18] Paton KR, Varrla E, Backes C, Smith RJ, Khan U, O’Neill A, et al. Scalable production of large quantities of defect-free few-layer graphene by shear exfoliation in liquids. *Nat Mater* 2014;13:624.
- [19] Fang X-Y, Yu X-X, Zheng H-M, Jin H-B, Wang L, Cao M-S. Temperature-and thickness-dependent electrical conductivity of few-layer graphene and graphene nanosheets. *Phys Lett A* 2015;379:2245–51.

- [20] Nulman J. Film sheet resistance measurement 1997.
- [21] Pozar DM. Microwave engineering. John Wiley & Sons; 2009.
- [22] Balanis CA. Antenna theory: analysis and design. John wiley & sons; 2016.
- [23] Park J, Mun G, Yu D, Lee B, Kim WN. Proposal of simple Reference Antenna Method for EMI antenna calibration. 2011 IEEE Int. Symp. Electromagn. Compat., IEEE; 2011, p. 90–5.
- [24] Nicolson AM, Ross GF. Measurement of the intrinsic properties of materials by time-domain techniques. IEEE Trans Instrum Meas 1970;19:377–82.
- [25] Weir WB. Automatic measurement of complex dielectric constant and permeability at microwave frequencies. Proc IEEE 1974;62:33–6.

3 Sustainable production of highly conductive multilayer graphene ink for wireless connectivity and IoT applications

Kewen Pan, Yangyang Fan, Ting Leng, Jiashen Li, Zhiying Xin, Jiawei Zhang, Ling Hao, John Gallop, Kostya S. Novoselov & Zhirun Hu

NATURE COMMUNICATIONS | (2018) 9:519

My contributions:

I have prepared graphene inks designed and fabricated all devices, performed most of the ink characterization except AFM. I also performed all microwave parameters measurement, analyzed all the data, and drew all the graphs.

Abstract

Printed electronics offer a breakthrough in the penetration of information technology into everyday life. The possibility of printing electronic circuits will further promote the spread of the Internet of Things applications. Inks based on graphene have a chance to dominate this technology, as they potentially can be low cost and applied directly on materials like textile and paper. Here we report the environmentally sustainable route of production of graphene ink suitable for screen-printing technology. The use of non-toxic solvent Dihydrolevoglucosenone (Cyrene) significantly speeds up and reduces the cost of the liquid phase exfoliation of graphite. Printing with our ink results in very high conductivity ($7.13 \times 10^4 \text{ S m}^{-1}$) devices, which allows us to produce wireless connectivity antenna operational from MHz to tens of GHz, which can be used for wireless data communication and energy harvesting, which brings us very close to the ubiquitous use of printed graphene technology for such applications.

3.1 Introduction

Development of printed conductive inks for electronic applications has grown rapidly due to widening applications in transistors [1], sensors [2], antennas [3,4], radio frequency identification (RFID) [5–7] tags, wearable electronics [8], etc. As conductor is the core component in printed electronics, efforts have been mainly focused on providing highly conductive metal nanoparticle inks, especially using silver nanoparticles [9]. Silver nanoparticle inks are widely used because of their high

conductivity and good levelling property. However, silver is too expensive to be employed for low cost applications [10]. Other metal nanoparticles such as copper or aluminium are much cheaper but can be easily oxidized. To avoid oxidation, a sintering process is necessary after printing [11,12]. However, in the case of heat sensitive substrates (paper, plastic, etc), sintering can't be applied. Conductive polymers can also be fabricated as conductive film. This technique is however both chemically and thermally unstable [13]. Carbon nanotubes (CNTs) were once seen as an alternative for metal nanoparticles. The extremely high junction resistance between CNTs results in lower surface conductivity and hinders their applications [14]. The printed electronics industry has long been crying out for low cost highly conductive inks.

Graphene ink, a dispersion of graphene flakes in solvents, can be easily patterned via spraying [15], screen printing [16], inkjet-printing [17,18] and doctor-blading [19] techniques. For antenna printing applications, spraying is a less reported method, suffering from lacking of flatness in films. Inkjet-printing and doctor blading methods are complementary, the former having high accuracy and cost, in contrast to the latter. In addition, inkjet-printing has to print many cycles [20] to achieve low sheet resistance, which costs time and is not economically viable for mass production. Considering costs, printing accuracy and surface conductivity, screen printing technique is the best candidate for industrial scale production. However, few screen-printed graphene devices have been reported including electrodes [13,21,22], electronic circuits [23] and antennas [16,19,24]. Most graphene ink processes use organic solvents such as N-Methyl-2-pyrrolidone (NMP) and dimethylformamide (DMF). They are toxic, with low

concentrations, and unsustainable, preventing them from using for industrial scale production.

Here we report the use of a cellulose derived solvent, Dihydrolevoglucosenone (Cyrene), which is not only non-toxic, environmentally friendly and sustainable but also can provide higher concentration of graphene ink, resulting in significant cost reduction for large-scale production. In this work, low cost, environmentally friendly and sustainable, highly conductive graphene ink (10 mg mL^{-1}) has been developed and was further concentrated to 70 mg mL^{-1} for screen printing. More importantly, we have demonstrated that printed graphene antennas, ranging from high frequency band (a few tens of MHz) to microwave band (a few tens of GHz), can be applied across the entire RF spectrum. As critical demonstrations, a printed graphene enabled battery-free wireless body temperature sensor, RFID tags and RF energy harvesting system for powering battery-free devices that are capable of sensing resistive and capacitive sensors are presented, illustrating the potential of low cost, screen printed graphene enabled wearables for IoT applications such as healthcare and wellbeing monitoring, also embodying sustainability and disposability, all of these are critical factors to enter the mass-produced market.

3.2 Results

3.2.1 Ink characterization.

Conductive graphene ink has been researched for a number of years. It is now possible to obtain defect free, less oxidized and stable graphene flakes by liquid phase

exfoliation [25,26] which can be deposited on different substrates. Many organic solvents with specified surface energy [27] have been verified for graphene exfoliation under bath sonication treatment with low residual and better stability such as NMP and DMF [27,28]. However, low concentrations, environmentally harmful and toxic properties of these organic solvents have prevented their applications from industrial scale graphene ink production [29]. Alternative method is to exfoliate graphene in low cost aqueous-based solutions with surfactants [30–32]. A recent work [33] proposed ultra-high concentration (50 mg mL^{-1}) graphene slurry in water, but oxidization on the edge of graphene flakes still degrades its conductivity.

Bio-based Cyrene (CAS: 53716-82-8) was first identified as a high-performance solvent for graphene dispersion in 2017 [29]. The solvent not only has appropriate polarity [29,34] and surface tension [27,29,35] which are especially suitable for graphene ink preparation, but also the concentration of dispersion where graphene can exist stably is at least an order higher than other organic solvents [29]. Moreover, Cyrene is non-toxic and easily extracted from cellulose which is abundant on Earth, has a great potential for low cost, environmentally friendly and sustainable industrial scale graphene ink production. However, for printed electronic applications, the most crucial property, electrical conductivity of Cyrene based graphene ink, has not been reported, nor have its electronic applications.

In this work, expanded graphite was added into Cyrene and NMP (as comparison). Graphene flakes were produced during sonication treatment. Firstly, the sonication time for exfoliation was investigated as it is of significance for large-scale ink production.

Samples were extracted at different sonication time. It is easy to remove unexfoliated graphite particles in extracted samples via centrifugation and filtration (see **3.4 Methods**). It has been noticed that long sonication period also affects the quality of graphene flakes and degrades the conductivity of graphene [36]. For wireless connectivity applications, the conductivity of the printed graphene pattern is crucially significant. Thin graphene flakes allow for the best stacking; however, they end up with the maximum number of interfaces, which potentially can increase the resistance. Thick graphene flakes allow one to reduce the number of interfaces between the flakes, but they do not guarantee good stacking and result in a number of voids when printed. The conductivity can be maximized by selecting flake thickness, otherwise low conductivity increases connection loss and jeopardises the ink applications. To evaluate conductivity, the sheet resistance variations of the graphene laminate under different sonication time in both NMP and Cyrene solvents were plotted in Figure 3-1. As it can be seen, the sheet resistance of the graphene laminate decreases rapidly within the first 8 hours ultrasonic exfoliation in Cyrene whereas it takes 20 hours in NMP to reach the similar sheet resistance. The rate of decreasing of sheet resistance with Cyrene ink is significantly faster than that of NMP ink (red and black dash lines), which exceeds $0.6 \Omega \text{ sq}^{-1} \text{ h}^{-1}$ between 4 to 8 hours. The minimum sheet resistance of Cyrene ink is $0.78 \Omega \text{ sq}^{-1}$, which happens at 8 hours sonication. After that, the sheet resistance rises as sonication time further increases because the longer sonication time leads to smaller flake sizes as well as damages sp^2 network of graphene flakes [36], affecting the graphene flake's electrical conductivity, which is not recoverable. For NMP solvent, the

decreasing rate of sheet resistance is slower. The minimum sheet resistance is $0.77 \Omega \text{ sq}^{-1}$, happens at 48 hours sonication. That said, although the physical properties of both solvents are quite similar [29], the best sonication time for NMP is 6 times longer than that for Cyrene, which indicates that Cyrene has better exfoliation efficiency compared to NMP, providing an advantage in time saving and cost reduction for large-scale graphene ink production.

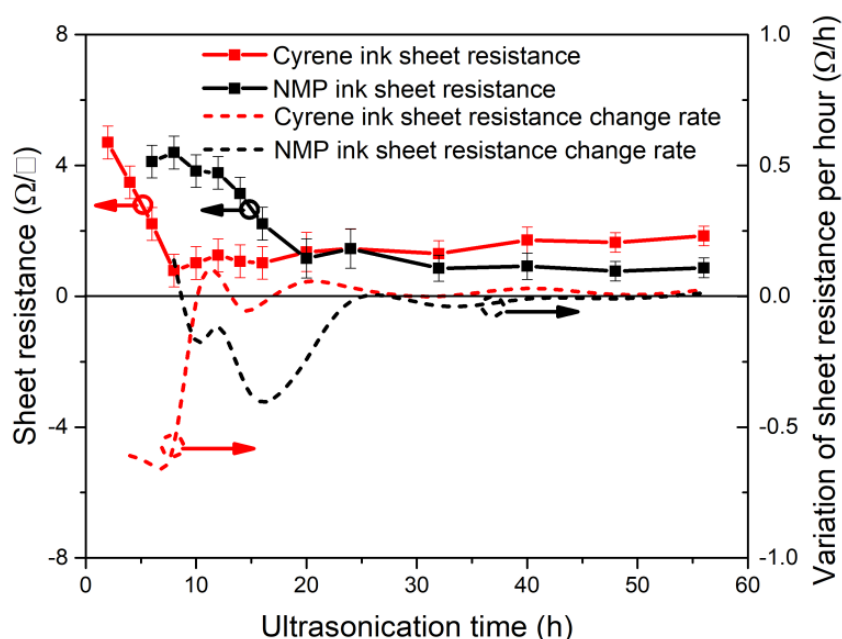


Figure 3-1: Quality of exfoliated graphene flakes in Cyrene: Measured average sheet resistance values (left axis, measured 5 times per point) and variation (right axis) of sheet resistance as function of sonication time (black line: NMP, red line: Cyrene).

The electrical conductivity of dried and compressed graphene laminate (8 hours exfoliated in Cyrene, see in **3.4 Methods**) is $7.13 \times 10^4 \text{ S m}^{-1}$, higher than any work reported so far [37–39], confirming that Cyrene is an excellent solvent with higher exfoliation efficiency and less defects on graphene flakes for replacing traditional toxic organic solvents.

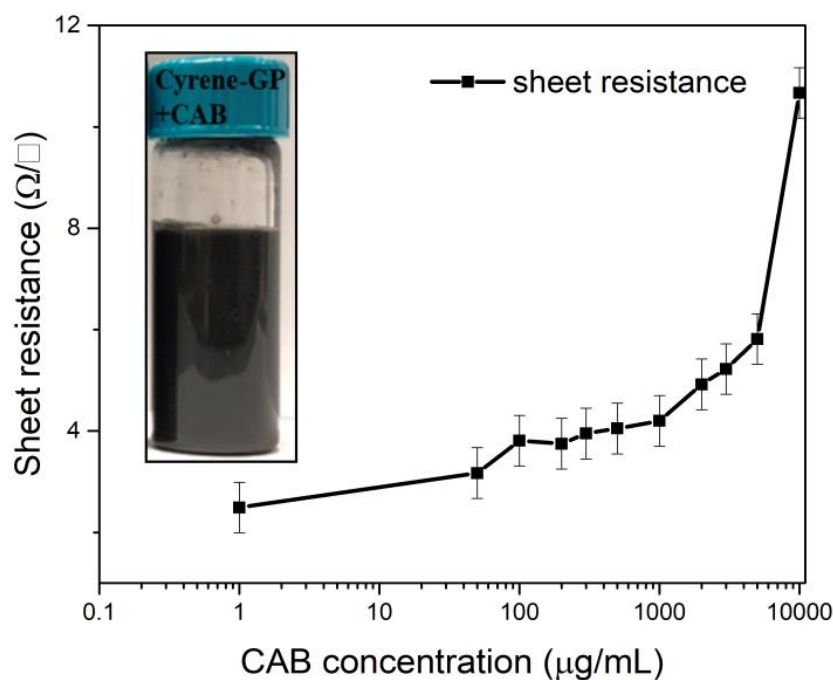


Figure 3-2: Sheet resistance variation (measured 5 times per point) with different CAB concentration and the insert sample of 10 mg mL⁻¹ graphene ink with 1 mg mL⁻¹ CAB.

Binder-free graphene ink and its applications have been reported [16,40]. However, the adhesion was less impressive. For practical applications, adhesive materials are normally added in the ink. The drawback for adding adhesive materials is that it will significantly degrade the ink electrical conductivity. In this work, cellulose acetate butyrate (CAB) was added into the Cyrene graphene ink, acting as a polymer assisted agent. CAB can stabilize the ink because the electrostatic repulsion between CAB molecules prevents graphene flakes from restacking and aggregation [41], also enhances adhesion and anti-scratching performance of the printed pattern. However, addition of CAB to the ink decreases its conductivity dramatically. In order to understand the relationship between CAB concentration and sheet resistance, 0.05, 0.1, 0.2, 0.3, 0.4, 0.5, 1, 2, 3, 5 and 10 mg CAB was dissolved into 1 mL of pristine graphene ink (10 mg mL⁻¹, exfoliated in Cyrene for 8 hours) with a short period of sonication

treatment. As can be observed in Figure 3-2, the sheet resistance of the graphene/CAB laminate rises relatively rapidly when CAB concentration is less than $100\text{ }\mu\text{g mL}^{-1}$ but slowly increases while the CAB concentration is between $100\text{ }\mu\text{g mL}^{-1}$ to mg mL^{-1} . The sheet resistance is about two times higher than that of pristine graphene laminate when the concentration of CAB is 1 mg mL^{-1} . The sheet resistance increases logarithmically for CAB concentration over 1 mg mL^{-1} . To achieve good conductivity as well as printing quality, 1 mg mL^{-1} CAB concentration was applied in this work. The insert in Figure 3-2 shows the ink sample.

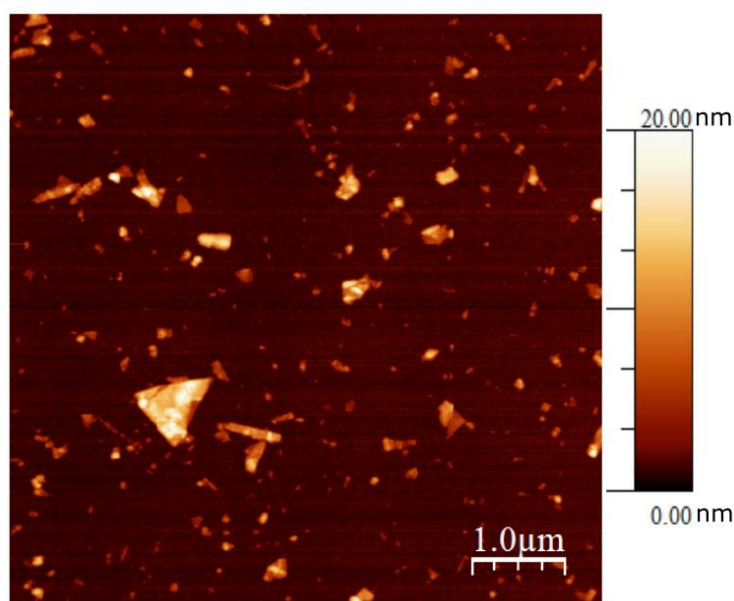


Figure 3-3: AFM image of graphene flakes on silicon substrate; scale bar is $1\text{ }\mu\text{m}$.

Atomic Force Microscopy (AFM) was used to characterise graphene flakes (prepared from graphene/CAB ink, 10 mg mL^{-1} with 8 hours sonication). Clear graphene flakes are shown in Figure 3-3 with lateral area of $6\times 6\text{ }\mu\text{m}$, which confirms the stable existence of few-layers graphene nanoflakes in the high concentration ink (AFM image of a single graphene nanoflake profile can be seen in Supplementary Figure 3-20).

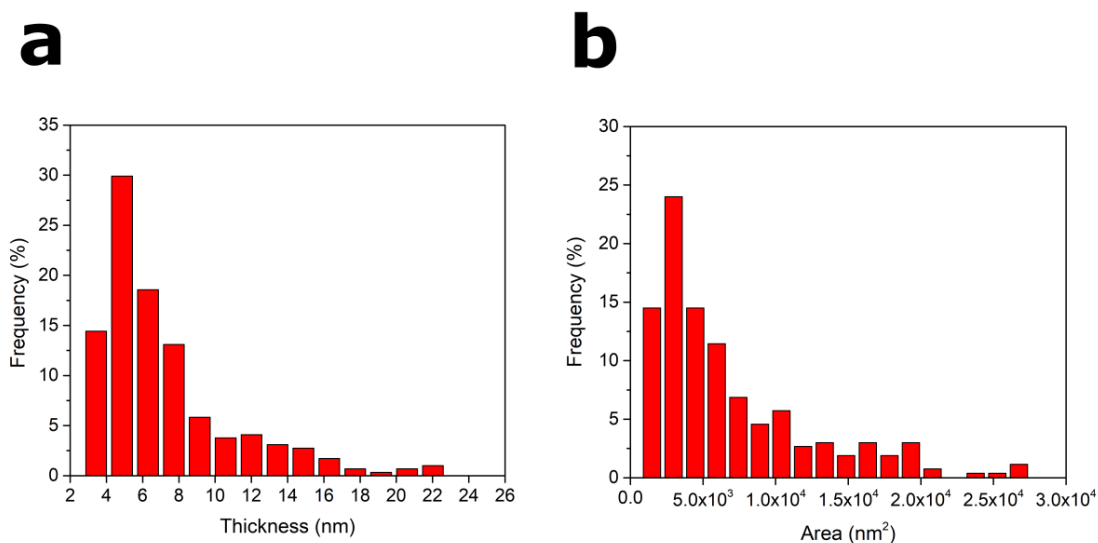


Figure 3-4: (a) Thickness histograms and (b) flake size.

The measured flake thickness and size distribution (291 flakes were counted) are peaked at 5 nm (Figure 3-4a) and $2.5 \times 10^3 \text{ nm}^2$ (Figure 3-4b), respectively. It is worth noticing that the statistics follow lognormal distribution of high power sonication of 2D materials as expected [42].

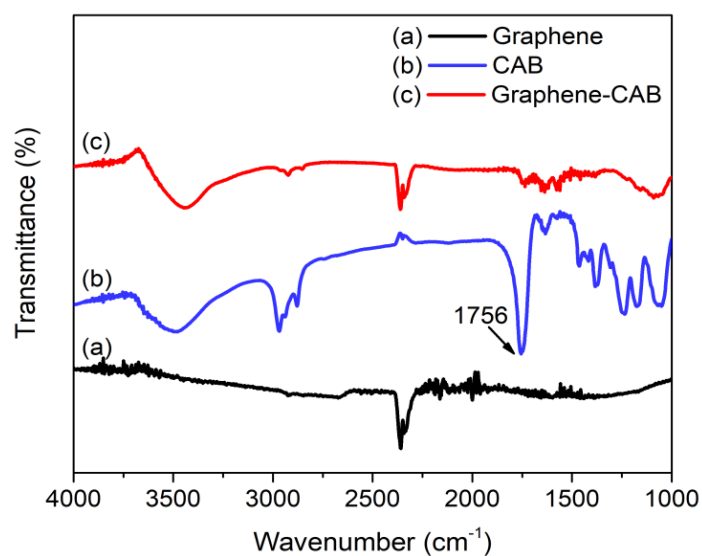


Figure 3-5: FTIR characterization of Cyrene graphene ink with and without CAB.

FTIR and Raman spectroscopy were used to investigate the quality of exfoliated

graphene flakes. Figure 3-5 illustrates the FTIR spectra of pure exfoliated graphene, exfoliated graphene with CAB assisted and CAB itself. Compared to reduced graphene oxide (rGO) or chemically derived graphene, it is worth noticing that no peaks associated with -OH ($\sim 1340\text{ cm}^{-1}$) and -COOH ($\sim 1710\text{--}1720\text{ cm}^{-1}$) groups are detected for the exfoliated graphene [43] (black line in Figure 3-5). The absence of peaks is evidence that the graphene flakes is composed of largely defect-free material. CAB is a polymer that has been partially esterified but still has large numbers of hydroxyl groups which have broad OH absorption located at 3490 cm^{-1} (blue line). A characteristic peak is seen at 1756 cm^{-1} attributed to CAB (C=O stretch) which can also be observed on graphene/CAB (red line).

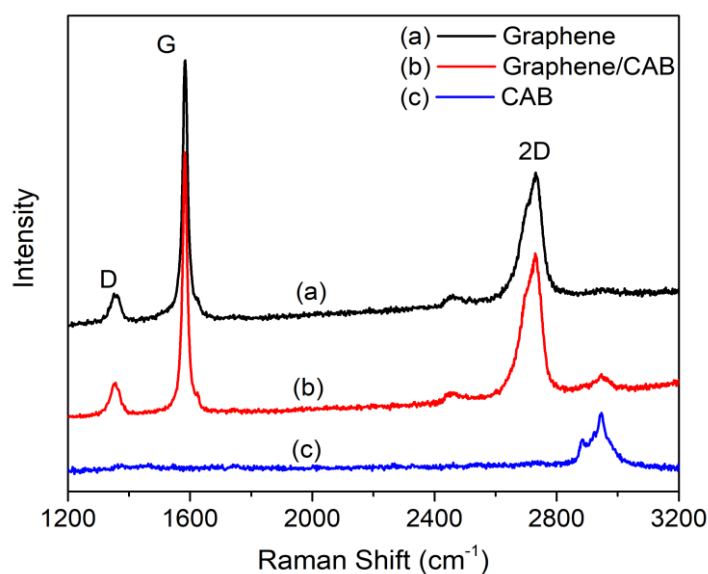


Figure 3-6: Raman spectra of Cyrene graphene ink with and without CAB.

Raman spectroscopy of exfoliated graphene is shown in Figure 3-6, featuring the breathing mode of sp^2 carbon atoms at D -band (1355 cm^{-1}), G -band (1583 cm^{-1}), associated with in-phase vibrations of the graphite lattice, the relatively wide $2D$ -band

at 2731 cm^{-1} and an overtone of the *D*-band [27,44]. Low *D/G* ratio indicates fewer defects on graphene flakes [45], which is significant for electron flow and no structure change of graphene flakes can be detected by Raman in the graphene/CAB sample.

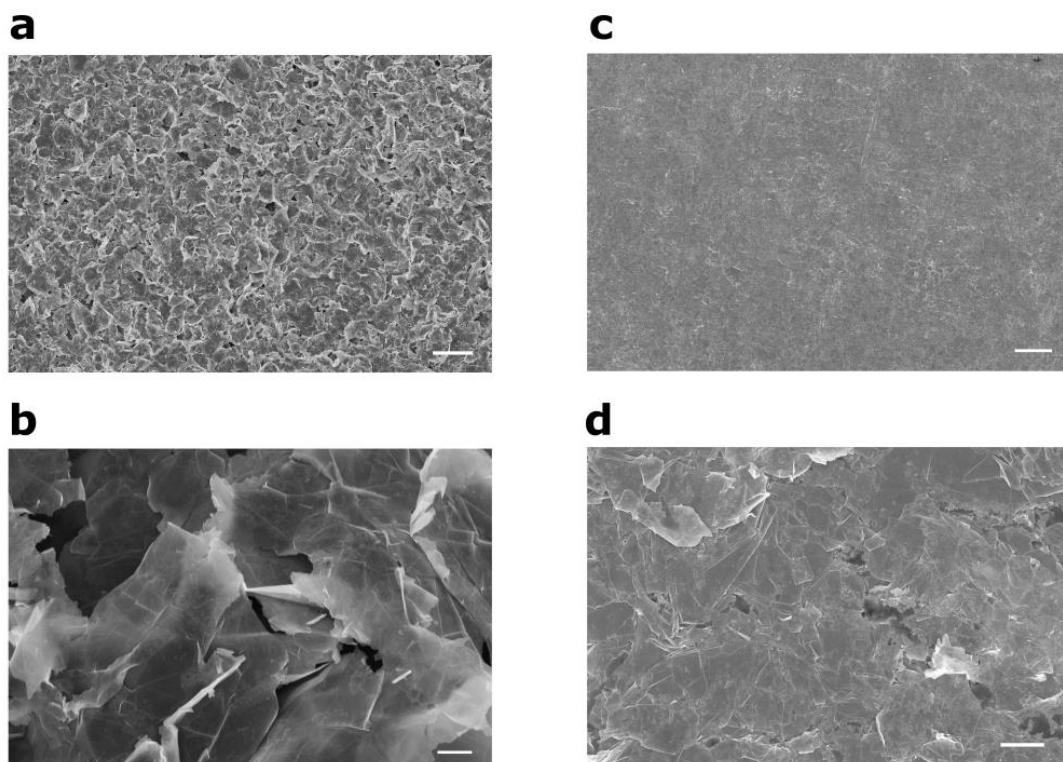


Figure 3-7: SEM images of screen printed graphene on paper (**a** Uncompressed and **c** Compressed screen-printed graphene laminates with 300X magnification; scale bar is $30\text{ }\mu\text{m}$, **b** Uncompressed and **d** Compressed screen-printed graphene laminates with 10kX magnification; scale bar is $1\text{ }\mu\text{m}$.)

Morphological features of graphene/CAB laminate were investigated by using SEM. Graphene flakes can be clearly seen at Figure 3-7a,b. Uncompressed graphene is curly and has poor adhesion between flakes. It is obvious that graphene flakes were randomly stacked to each other. There are gaps (dark holes) between the flakes, severely degrading the contact quality. Around the gaps, electron flow between the graphene flakes appears between the edges and tips of the flakes, which results in a relatively large sheet resistance ($37\text{ }\Omega\text{ sq}^{-1}$). Hence, the following compression process is

significant for improving sheet resistance. A paper rolling machine (Agile F130 Manual Mill) was used to compress the printed patterns. As it can be seen in Figure 3-7e,f, the surface is no longer coarse after compressing, graphene flakes are piled sequentially with face-to-face contacts, dramatically reducing the sheet resistance. The sheet resistance of compressed patterns was measured to be $1.2 \Omega \text{ sq}^{-1}$ on average, 30 times smaller than uncompressed patterns.

3.2.2 Antennas design and fabrication.

A commercial manual screen printer was used in this work. Figure 3-9a, b, c demonstrate the straightforward steps of graphene antenna screen-printing: **a** graphene ink is uniformly added on the exposed screen with negative antenna patterns and a squeegee is moved from one side to another, transferring the ink on to the substrate, **b** thermal annealing and **c** compression.

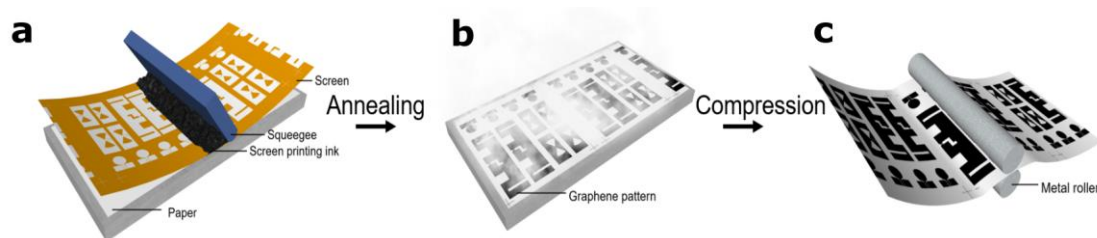


Figure 3-8: Graphene antenna fabrication using screen printing technology. Screen-printing steps: **a** Patterning graphene ink via exposed screen and squeegee, **b** Annealing printed patterns and **c** Compressing dried pattern with steel rolling machine.

Ultrahigh graphene concentration (70 mg mL^{-1}) screen-printing ink was achieved via rotary evaporation from 10 mg mL^{-1} graphene/CAB ink, as seen in Figure 3-10 (the viscosity data can be found in Supplementary Figure 3-21).

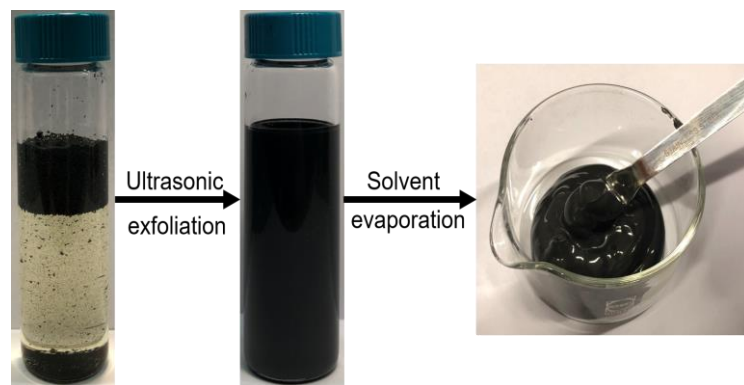


Figure 3-9: Cyrene based graphene ink and high concentrated (70 mg mL^{-1}) screen printing ink.

The screen printer and printed graphene antenna patterns are illustrated in Figure 3-10a. The resolution of our screen printed patterns is 0.4 mm. A cross-section view of the screen-printed graphene/CAB laminate on paper is shown in Figure 3-10b. There is no obvious boundary between graphene and paper, revealing good adhesion.

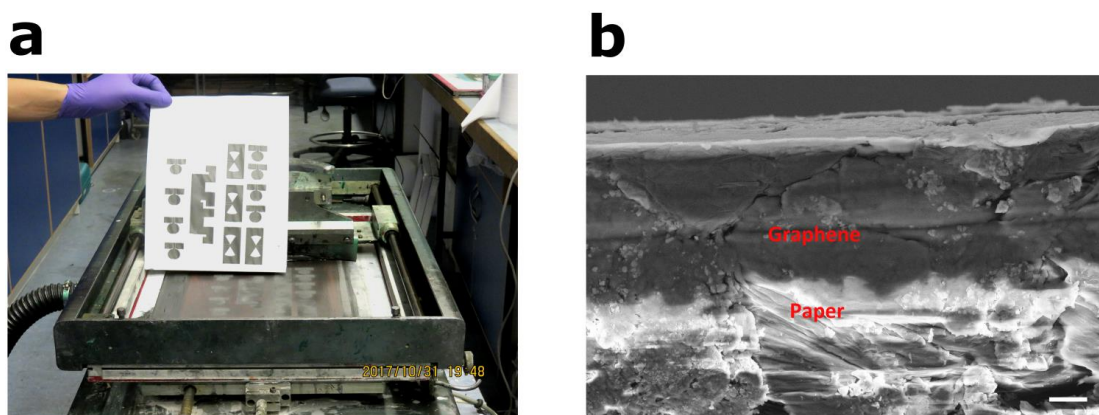


Figure 3-10: **a** Demonstration of printed antennas on A4 paper. **b** SEM cross-section view of the printed graphene antenna; scale bar is $1 \mu\text{m}$.

The printed patterns have excellent mechanical flexibility, as shown in Figure 3-11. Such flexible property has a great potential in wearable, deformable IoT applications [46]. The average thickness of screen-printed graphene laminate is $7.8 \mu\text{m}$ and conductivity can therefore be calculated as $3.7 \times 10^4 \text{ S m}^{-1}$ which is approximately about half of that of the pristine graphene ink (without CAB) but still has about the

same conductivity as recently reported work [47] which however requires high temperature (350°C) annealing. Additional bending and adhesion performance of the printed graphene/CAB pattern were tested. Low residual blue tape (BT-150E-KL) was used to test adhesion performance by sticking and peeling off from printed pattern repeatedly⁴⁷. The sheet resistance of pristine graphene pattern doubled after first cycle. In the meantime, the sheet resistance of graphene/CAB pattern increased 5%. After 10 cycles, the sheet resistance of graphene/CAB pattern increased 40% whereas pristine graphene pattern was peeled off from paper completely and its sheet resistance became too large to be measured ($>20 \text{ M}\Omega \text{ sq}^{-1}$) at cycle 7. In a bending test, a 3 cm \times 1 cm rectangular pattern was printed and compressed. The pattern was bent from 0° to 90° for 2000 cycles while its resistance only increased 5%, which is comparable to other published works [48].

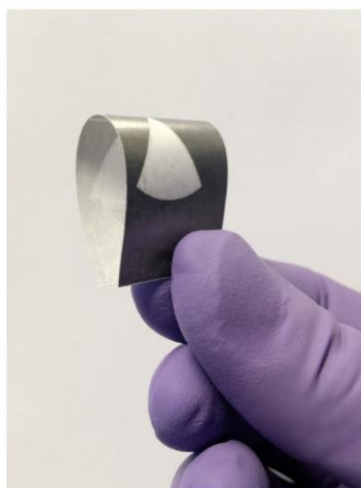


Figure 3-11: Flexibility of the printed graphene antenna.

Three different types of antennas were printed, ranging from Near Field Communication (NFC, Figure 3-12a), Ultra High Frequency (UHF, Figure 3-12b) Radio Frequency Identification (RFID) to C-X-K_u ultra-wideband slot antennas (Figure 3-12c). These antennas were designed for low cost, flexible and disposable wireless

applications. For instance, the environmentally friendly printed graphene NFC antenna can replace traditional metal NFC antenna for access card applications. The wideband slot antenna can replace metal antennas for ultra-wideband (UWB) data communication with conformability and lower cost. All antennas were designed and simulated by using commercial full-wave electromagnetic simulation software CST. In the simulation, the printed graphene/CAB laminate was modelled as ohmic sheets because the laminate thickness is much smaller than its skin depth. One of the beauties of using graphene ink to print antennas is that the sheet resistance can be controlled from one to tens of ohms per square. This provides extra design freedom depending on the antenna applications. For high gain, high efficiency antennas, lower sheet resistance will be required. For wideband antennas, however, relatively higher sheet resistance ink can be used if the radiation efficiency is not critical. The geometrical dimensions of the antennas are all illustrated in Figure 3-12a-c (sheet resistance details can be found in Supplementary Figure 3-22). The inner line and gap width of coplanar waveguide (CPW) transmission line applied on wideband slot antenna is 3 mm and 0.4 mm respectively.

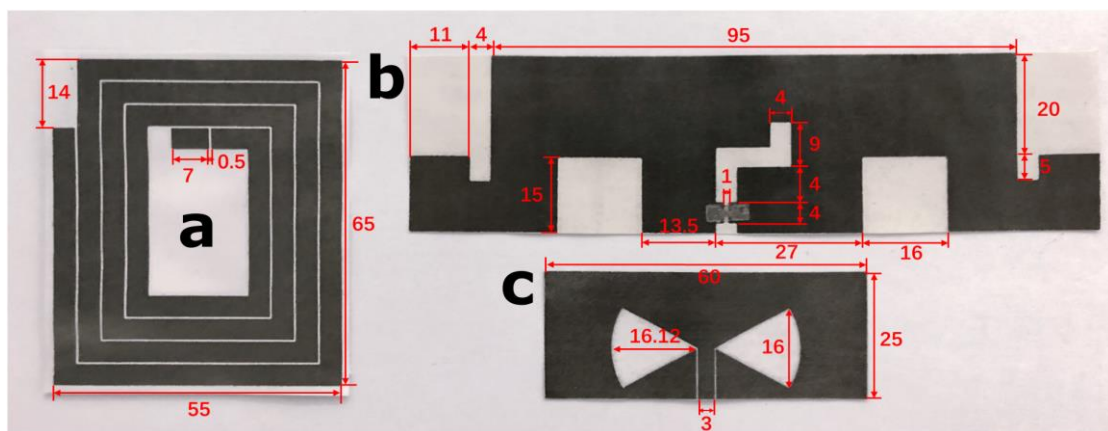


Figure 3-12: **a-c** Printed graphene antennas' geometric parameters (mm): **a** NFC antenna (without NFC chip and jumper), **b** UHF RFID antenna, **c** wideband slot antenna.

3.2.3 NFC battery-free temperature sensor.

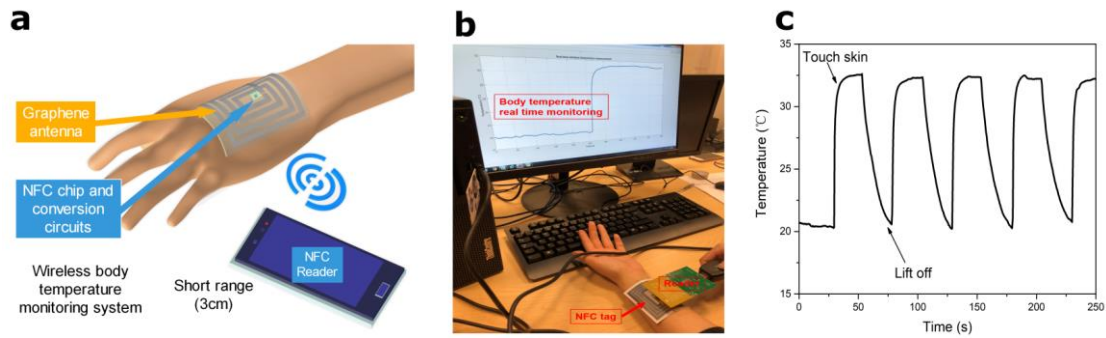


Figure 3-13: **a-c** Healthcare applications (**a** Illustration of graphene printed NFC temperature sensing system, **b** Demonstration of measurement and **c** recorded data of body temperature).

NFC technology plays an increasingly important role with the development of IoT technology. It not only can be applied for access or ID cards but can also be used for other near field wireless monitoring applications, such as wireless healthcare and wellbeing monitoring. In this work, a wireless body temperature monitoring system has been designed and demonstrated. The sensor tag consists of disposable graphene printed planar coil antenna, temperature sensor (NTHS0603N17N2003JE, VISHAY) and functional NFC chip (RF430FRL152H, Texas Instruments), as shown in Figure 3-13a (more information can be found in Supplementary Figure 3-23 and Supplementary Note 1). The printed graphene NFC antenna harvests RF power for the chips and provides data communication when activated by the reader. The real-time temperature monitoring is illustrated in Figure 3-13b at the distance of 2.5 cm between tag and reader. The near field reader (TRF7970AEVM, Texas Instruments) communicates with the sensor tag for continuously recording body temperature and uploads data to a designated terminal. Figure 3-13c illustrates a data frame that was transmitted from the

near field temperature sensor. There is no transmission error in 250 s measurement period. A clear, repeatable high and low temperature variation can be observed when the near field sensor is placed on the human skin and removed from it. This can be very useful for wireless monitoring patients' temperature in hospital wards and even at home. The data can then be relayed to the cloud and analysed by professional health workers remotely.

3.2.4 Long read range UHF RFID antenna.

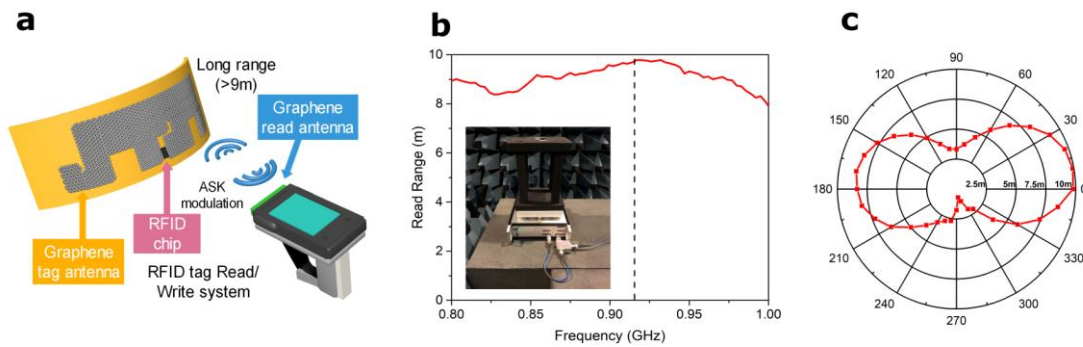


Figure 3-14: **a-c** UHF RFID tag applications demonstration (**a** Illustration of printed graphene RFID antenna system, **b** Read range and **c** radiation pattern (E-field, at 915 MHz)).

In order to further demonstrate the potential of printed graphene antennas, a UHF RFID antenna has been designed, optimized and printed for long read range communication, as shown in Figure 3-14a. The antenna tag consists of a radiator (printed graphene), T-matching network (printed graphene) and an RFID chip (Impinj Monza R6). One of the most important technical merits for a UHF RFID antenna tag is its read range r , which can be calculated by [49]:

$$r = \frac{\lambda}{4\pi} \sqrt{\frac{P_t G_t G_r \tau}{P_{th}}} \quad (3.1)$$

where λ is the wavelength, P_t is the transmitted power from the reader antenna, G_t is the gain of the reader antenna, G_r is the gain of tag antenna, P_{th} is the minimum threshold of the power needed to activate the RFID chip and τ is the matching factor, which varies from 0 to 1 and is given by [50]:

$$\tau = \frac{4R_c R_a}{|Z_c + Z_a|^2} \quad (3.2)$$

where Z_c, Z_a represent chip impedance and antenna input impedance, respectively.

R_c, R_a are the real parts of the chip and antenna impedance. Conjugate impedance matching is required between the RFID antenna and the chip in order to maximize the matching factor, resulting in maximal read range. The maximum read range of the printed graphene UHF RFID antenna versus frequency is illustrated in Figure 3-14b, which shows that a 9.8 m read range at 917 MHz was achieved and the tag has long read range of over 9 m from 854 MHz to 971 MHz, covering the whole UHF RFID band (860 MHz~960 MHz). This is a very useful property as it provides enough frequency shift redundancy for printing tolerance and different application environments. This result, doubling the read range of the nearest work in printed graphene RFID [19], rival to aluminium etched commercial RFID antennas and silver ink printed RFID ones [51]. For a more intuitive demonstration, the radiation pattern in the E-plane at 915 MHz was plotted against maximum read range instead of antenna gain and the data was recorded for every 10° rotation, as shown in Figure 3-14c. A typical dipole pattern can be seen from the radiation pattern where the maximum reading range occurs at 0° and 360°, the minimum read range happens at 90° and 270°.

3.2.5 Ultra-wideband antenna and energy harvesting applications.

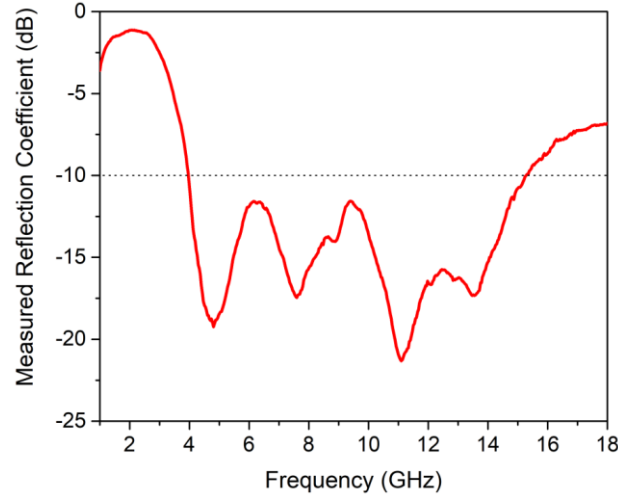


Figure 3-15: Measured reflection coefficient (S_{11}) of the graphene printed slot antenna.

Figure 3-15 shows the reflection coefficient (S_{11}) of the printed graphene ultra-wideband slot antenna. The 10 dB bandwidth is from 3.8 GHz to 15.5 GHz, achieving more than 120% fractional bandwidth. This wideband characteristic is very useful for upcoming 5G mobile communication and UWB radar applications [52]. The fundamental resonance of the slot antenna is around 5 GHz and low reflection extends close to 9 GHz. Above 9 GHz, the higher resonance modes start to play the major role. The fundamental and higher mode resonances overlapped around 9 GHz, resulting in a wide bandwidth (simulated surface current distributions on the antenna at 9 GHz and 12 GHz can be seen in Supplementary Figure 3-24).

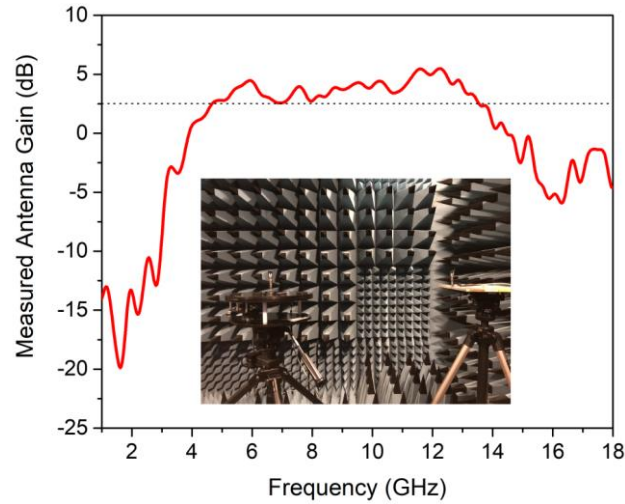


Figure 3-16: Measured slot antenna gain (three-antenna method).

Antenna gain was measured at the maximum gain point and shown in Figure 3-16. The antenna gain varies from 2.5 dB to 6 dB from 4.6 GHz to 13.5 GHz. The radiation patterns for the printed graphene ultra-wideband slot antenna under different frequencies are illustrated in Figure 3-17. All data were plotted with linear form for comparison. As the first two radiation patterns at 4 GHz (Figure 3-17a) and 8 GHz (Figure 3-17b) show a typical symmetrical dipole pattern, this demonstrates that the antenna is working in its fundamental resonance mode. The gain maximum occurs at 0° . The radiation level at the front side is slightly stronger than the back side, probably due to the loss of paper substrate. For the radiation pattern at 12 GHz (Figure 3-17c) and 14 GHz (Figure 3-17d), typical dipole radiation patterns have disappeared, indicating higher mode resonance.

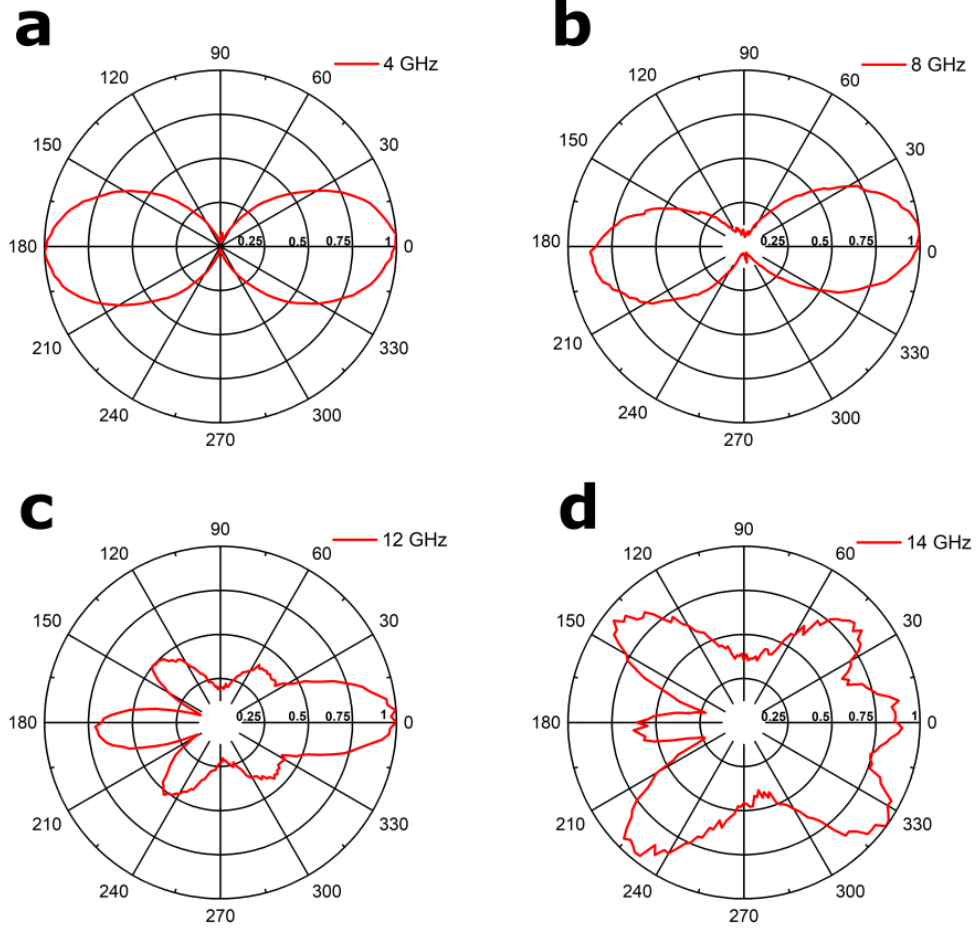


Figure 3-17: **a-d** Measured radiation pattern at **a** 4 GHz, **b** 8 GHz, **c** 12 GHz and **d** 14 GHz.

There are various wireless signals in free space at any moment of time. Such wireless energy can be harvested and stored to power up low-power, battery-free electronic devices intermittently. This strategy is becoming highly desirable due to the fast development of wireless sensor networks (WSNs) and IoT technologies [53,54]. Here we demonstrate a printed graphene-enabled RF energy harvesting system. The harvesting system consists of an ultra-wideband printed graphene slot antenna, low pass filter that can suppress harmonic radiation [54] and rectifier with 4-stage Cockcroft–Walton voltage multiplier which converts the RF to DC power and provides the required output voltage to drive low power CMOS devices, as shown in

Figure 3-18a,b (the reflection coefficient of the conversion circuit can be found in Supplementary Figure 3-23).

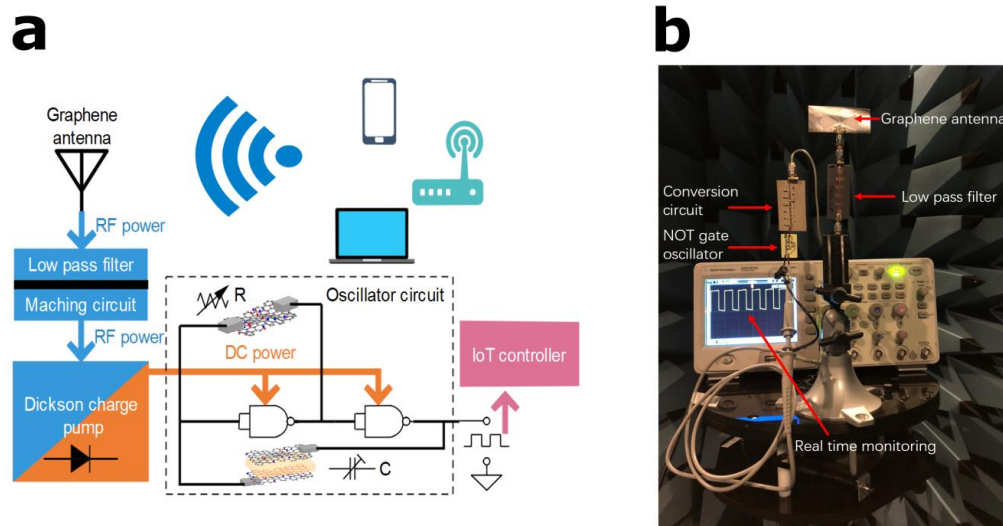


Figure 3-18: **a** Illustration of RF energy harvesting system, **b** Measurement set up.

To measure the conversion efficiency of the harvesting system, an RF signal generator and standard gain horn antenna which provides accurate RF energy and gain were used. The printed graphene antenna and conversion circuit were placed at 2 m away in an anechoic chamber. 5.8 GHz was applied in the measurement because more and more wireless devices (e.g. 5G WiFi, UAVs) are using this free license channel. The antenna total efficiency, circuit conversion efficiency and overall RF-to-DC conversion efficiency of the system were measured and plotted in Figure 3-19.

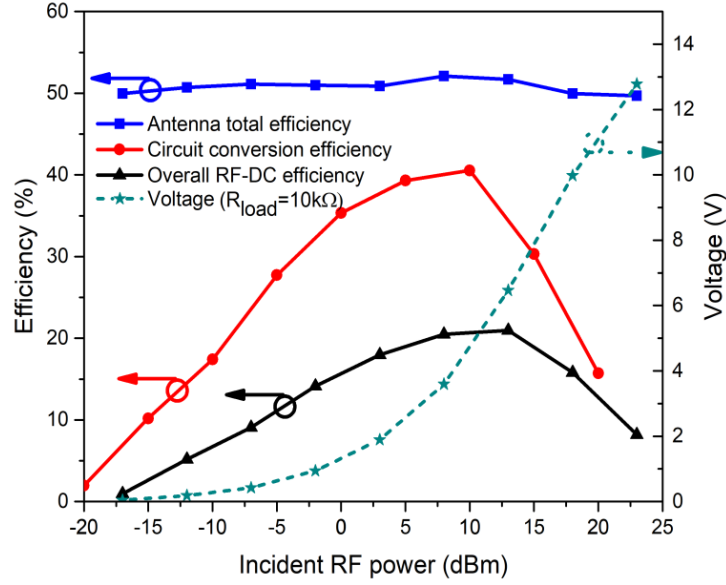


Figure 3-19: Measured efficiencies and output DC voltage as a function of different RF power levels.

It can be observed that the printed graphene antenna has constant efficiency (51%) for different RF power levels since the antenna is a linear device. The overall RF-to-DC conversion efficiency varies with RF power due to the diodes' nonlinearity and reaches its maximum of 22% ($R_{load} = 10\text{ k}\Omega$), which can be further improved by using diodes with lower barrier height in the voltage multiplier. From the view of IoT applications, high quality printed 2D material sensors [55,56] can be embedded into the system with the same printing process. A prototype of RF powered, battery-free low-power square wave oscillator which converts the sensors' analogue outputs to frequency modulated signals is developed and demonstrated here. The oscillator consists of two CMOS NOR gates (SN74AUP1G02), variable resistor (resistive sensor) and variable capacitor (capacitive sensor), as shown in Figure 3-18a, which can be powered wirelessly as long as the incident RF power is over -12 dBm. One of the generated square waveforms by the system with frequency of 5 kHz and peak to

peak voltage of 2 V can be observed from the oscilloscope in Figure 3-18b, experimentally verifying that the printed graphene enabled RF energy harvesting system is fully functional.

3.3 Discussion

Environmentally friendly, sustainable, low cost, highly conductive and concentrated screen printing graphene/CAB ink has been developed. High-quality pristine graphene sheets were exfoliated and dispersed in Cyrene with the concentration of 10 mg mL^{-1} . Using Cyrene has eliminated the use of toxic solvents, significantly simplifying post production treatments, especially propitious for industrial scale manufacturing. Exfoliation times and conductivity of Cyrene graphene ink were measured and compared to those of NMP one. Conductivity of $7.13 \times 10^4 \text{ S m}^{-1}$ has been achieved after compressing, which is the highest reported so far. After adding CAB as stabilizing agent and rotary evaporation, the further concentrated graphene ink (70 mg mL^{-1}) becomes screen printable. The printed graphene/CAB laminate still achieved high conductivity of $3.7 \times 10^4 \text{ S m}^{-1}$. The prototype NFC antenna in the high frequency region, high-performance RFID antenna working in ultra-high frequency band and ultra-wideband antenna operating in microwave bands all provide evidence that printed graphene antennas can replace traditional metal antennas for wireless identification, sensing and data communications for low cost and ubiquitous wireless connectivity. Furthermore, graphene-based NFC temperature sensors for healthcare and wellbeing monitoring and graphene enabled energy harvesting system that can power

battery-free CMOS oscillator have been successfully demonstrated, opening an avenue for low cost, environmentally friendly and sustainable printable devices at upcoming IoT applications.

3.4 Methods

3.4.1 Liquid exfoliation of graphene with high concentration.

Expandable graphite with +50 mesh flake size was purchased from Sigma-Aldrich. Cyrene (Dihydrolevoglucosenone, >99%) was provided by Circa Group Pty Ltd. N-methyl-2-pyrrolidinone (NMP, >99%) was from Alfa Asia. Cellulose acetate butyrate (CAB, butyryl content 35-39%) was from Arcos Organics. Graphene nanoflakes were obtained via the liquid phase exfoliation method. Expandable graphite was placed in a ceramic crucible and then heated in an 800 W commercial microwave oven for 30 s to obtain expanded graphite with fewer layers. The expanded graphite flakes were stirred and washed in deionized water to remove residual acid until the pH is close to 7. Then, the mixture was dried in an oven for 5 hours at 100 °C. Dried expanded graphite was deposited into NMP solvent (10 mg mL⁻¹) and Cyrene (10 mg mL⁻¹) respectively where these organic solvents provide appropriate surface energy for sonication processes. After that, the mixture was sonicated in an ultrasonic bath (SHESTO, UT8061-EUK). Samples were extracted at 0, 2, 4, 6, 8, 10, 12, 14, 16, 20, 24, 32, 40, 48, and 56 sonication hours for sheet resistance measurement.

3.4.2 Screen-printing high concentration graphene ink preparation.

The exfoliated graphene nanoflakes were obtained in the dispersion after sonication. A 300-mesh stainless steel screen filtered the mixture first. After that, unexpanded graphite particles were removed after 5 mins low speed centrifugation (500 rpm). After that, the graphene dispersion was concentrated to 10 mg mL^{-1} with vacuum rotary evaporation (Buchi R-114 Rotavap evaporator). CAB was added into Cyrene as polymer stabilizing agent to increase the stable existence of graphene flakes in Cyrene and improve the printing performance. In order to achieve appropriate viscosity for screen-printing, the graphene concentration of 70 mg mL^{-1} was achieved (mixture of graphene flakes, CAB and Cyrene) by vacuum rotary evaporation. Before printing, the mixture was mechanically agitated for 5 minutes and bubbles inside the ink were removed after a short period of vacuum treatment. The printing screen with 62 mesh was specially fabricated with capillary film (ULANO, EZ50-Orange) to achieve uniform laminate of graphene paste. Then, the sample was dried and annealed in an oven (vacuum) at 100°C for 5 hours (comparison of antenna gains printed with Cyrene based graphene ink (8h sonication time) and NMP based graphene ink (20h sonication time) can be found in Supplementary Figure 3-25).

3.4.3 FTIR.

Both of graphene, CAB and graphene-CAB samples were annealed in an oven (vacuum) at 100°C for 48 hours to ensure dryness and avoid errors of measurement.

They were mixed with potassium bromide (KBr) with 1:20 mass ratio and ground in an agate mortar, respectively. FTIR data were recorded by a Fourier transform infrared spectrometer (Nicolet 5700).

3.4.4 Raman.

Films of exfoliated graphene (without CAB), graphene/CAB ink and CAB were coated on SiO₂/Si substrate. Raman spectra were acquired with a Renishaw System 1000 Raman Spectrometer. Micro-Raman spectrometer at a 50× objective, with an incident power of 2.3 mW. The system has within 1.5 cm⁻¹ spectral resolution at 514 nm.

3.4.5 Atomic force microscopy.

Atomic force microscopy imaging of few layer graphene was measured with a Bruker Dimension Icon in tapping mode. The concentration of graphene/CAB ink is 10 mg mL⁻¹ and 100 µL ink sample was spin-coated (3000 rpm, 1 min) on a clean SiO₂/Si substrate and washed by acetone, distilled water and isopropyl alcohol sequentially. The AFM sample was dried in an oven for 5 hours at 100 °C.

3.4.6 Scanning electron microscopy.

Scanning electron microscopy was performed using a ZEISS Sigma HV. Aperture size is 7 µm. The field emission gun is 5 KV and signal was acquired from InLens. For the cross-section measurement, the paper with printed graphene on top was soaked in liquid nitrogen and cut by scalpel.

3.4.7 Conductivity measurement.

Sheet resistance is used to describe the thin film resistance regardless of film thickness, it can be written as:

$$R_s = \frac{\rho}{t} \quad (3.3)$$

where R_s is sheet resistance, ρ is the resistivity of the film and t represents the thickness of film. For the measurement of sheet resistance variation with different ultrasonic treatment times, the ink was first filtered via a 300-mesh stainless steel screen. Small unexpanded graphite particles were removed after 5 mins low speed centrifugation (500 rpm, 5 mins). To avoid coffee-ring effect, a filter paper (Whatman qualitative filter paper, Grade 5) was held on a glass funnel (140mL Aldrich Buchner funnel) by vacuum. After that, 60 μ L of the filtered sample was dropped on filter paper. The ink was annealed in an oven for 5 hours (100 °C) and compressed with the rolling machine. The sheet resistance was measured using 4-point probe station (Jandel, RM3000) and semiconductor characterization system (Keithley, 4200C).

3.4.8 Antenna reflection coefficient measurement.

For reflection coefficient measurement (S_{11}), the ultra-wideband slot antenna was directly connected to a calibrated Vector Network Analyzer (VNA, Fieldfox N9918A, Keysight).

3.4.9 Radiation pattern measurement.

There are three graphene printed antennas to measure gain by themselves. The

SMA (RS PRO, 526-5763) connector was connected with the antenna using conductive epoxy (Circuit works CW2400). The measurement distance between any two adjacent antennas is 0.6 m, satisfied with far field requirement. The three antennas measurement method does not need a calibrated reference antenna; the gain of the antennas can be solved after measuring S_{21} with different combinations:

$$G_a = \frac{S_{21}^{ab} + S_{21}^{ac} - S_{21}^{bc} - 10 \lg \left(\frac{4\pi d}{\lambda} \right)^2}{2} [dB] \quad (3.4)$$

where G_a is the measured graphene antenna gain, S_{21}^{ab} , S_{21}^{ac} , S_{21}^{bc} are measured S_{21} [in dB] between different antennas (G_a , G_b , G_c : printed graphene antenna). The last term describes free space loss and depends on wavelength λ and distance d between measured antennas.

Radiation patterns of the antenna were recorded using an antenna measurement system (Antenna Measurement Studio 5.5, Diamond Engineering) and N9918A VNA. The data was recorded every 2° rotation. Standard horn antenna was used as transmitting antenna. Different bands of horn antennas were used: C, X bands (Narda, standard gain horn, model 643, 642 and 640) and K_u band (Steatite Q-par Antennas, standard horn, QSH18).

3.4.10 RFID antenna measurement.

Read range and radiation pattern measurement was performed using a professional RFID measurement setup (Voyantic Tagformance measurement system) with EIRP=4 W. Before measurement, the system was calibrated and the effects of receiver antenna gain, cable and free-space loss were eliminated. For read range measurement, the

system sweeps linearly from 800 MHz to 1 GHz with 3 MHz steps. For radiation pattern measurement, the frequency is 915 MHz and data were recorded every 10° rotation.

3.4.11 Antenna efficiency measurement.

The antenna total efficiency was measured by using rotary table, Antenna Measurement Studio 5.5 and N9918A VNA. The circuit conversion efficiency was measured using RF CW source (MARCONI, 6200) and precision multimeter (Agilent, U1251A).

References

- [1] Noh Y-Y, Zhao N, Caironi M, Sirringhaus H. Downscaling of self-aligned, all-printed polymer thin-film transistors. *Nat Nanotechnol* 2007;2:784.
- [2] Dua V, Surwade SP, Ammu S, Agnihotra SR, Jain S, Roberts KE, et al. All-organic vapor sensor using inkjet-printed reduced graphene oxide. *Angew Chemie* 2010;122:2200–3.
- [3] Shaker G, Safavi-Naeini S, Sangary N, Tentzeris MM. Inkjet printing of ultrawideband (UWB) antennas on paper-based substrates. *IEEE Antennas Wirel Propag Lett* 2011;10:111–4.
- [4] Abutarboush HF, Shamim A. Paper-based inkjet-printed tri-band U-slot monopole antenna for wireless applications. *IEEE Antennas Wirel Propag Lett* 2012. doi:10.1109/LAWP.2012.2223751.
- [5] Rida A, Yang L, Vyas R, Tentzeris MM. Conductive inkjet-printed antennas on flexible low-cost paper-based substrates for RFID and WSN applications. *IEEE Antennas Propag Mag* 2009;51.
- [6] Yang L, Rida A, Vyas R, Tentzeris MM. RFID tag and RF structures on a paper substrate using inkjet-printing technology. *IEEE Trans Microw Theory Tech* 2007;55:2894–901.
- [7] Kim Y, Lee B, Yang S, Byun I, Jeong I, Cho SM. Use of copper ink for fabricating conductive electrodes and RFID antenna tags by screen printing. *Curr Appl Phys* 2012;12:473–8.
- [8] Liu H, Qing H, Li Z, Han YL, Lin M, Yang H, et al. A promising material for human-friendly functional wearable electronics. *Mater Sci Eng R Reports* 2017;112:1–22.
- [9] Magdassi S, Bassa A, Vinetsky Y, Kamyshny A. Silver nanoparticles as pigments for water-based ink-jet inks. *Chem Mater* 2003;15:2208–17.
- [10] Li YG, Lu D, Wong CP. Electrical conductive adhesives with nanotechnologies. Springer Science & Business Media; 2009.
- [11] Volkman SK, Yin S, Bakhishev T, Puntambekar K, Subramanian V, Toney MF. Mechanistic studies on sintering of silver nanoparticles. *Chem Mater* 2011;23:4634–40.
- [12] Kamyshny A, Magdassi S. Conductive nanomaterials for printed electronics. *Small* 2014;10:3515–35.
- [13] Cochrane C, Koncar V, Lewandowski M, Dufour C. Design and development of a flexible strain sensor for textile structures based on a conductive polymer composite. *Sensors* 2007;7:473–92.
- [14] Hellstrom SL, Lee HW, Bao Z. Polymer-assisted direct deposition of uniform carbon nanotube bundle networks for high performance transparent electrodes. *ACS Nano* 2009;3:1423–30.
- [15] Huang X, Pan K, Hu Z. Experimental demonstration of printed graphene nano-flakes enabled flexible and conformable wideband radar absorbers. *Sci Rep* 2016;6:38197.
- [16] Huang X, Leng T, Zhang X, Chen JC, Chang KH, Geim AK, et al. Binder-free highly conductive graphene laminate for low cost printed radio frequency applications. *Appl Phys Lett* 2015;106:203105.
- [17] Torrisi F, Hasan T, Wu W, Sun Z, Lombardo A, Kulmala TS, et al. Inkjet-printed graphene electronics. *ACS Nano* 2012;6:2992–3006.
- [18] Li W, Li F, Li H, Su M, Gao M, Li Y, et al. Flexible circuits and soft actuators by printing assembly of graphene. *ACS Appl Mater Interfaces* 2016;8:12369–76.
- [19] Akbari M, Khan MWA, Hasani M, Björninen T, Sydänheimo L, Ukkonen L. Fabrication and

- characterization of graphene antenna for low-cost and environmentally friendly RFID tags. *IEEE Antennas Wirel Propag Lett* 2016;15:1569–72.
- [20] Secor EB, Prabhumirashi PL, Puntambekar K, Geier ML, Hersam MC. Inkjet printing of high conductivity, flexible graphene patterns. *J Phys Chem Lett* 2013;4:1347–51.
- [21] Hyun WJ, Secor EB, Hersam MC, Frisbie CD, Francis LF. High-resolution patterning of graphene by screen printing with a silicon stencil for highly flexible printed electronics. *Adv Mater* 2015;27:109–15.
- [22] Ping J, Wu J, Wang Y, Ying Y. Simultaneous determination of ascorbic acid, dopamine and uric acid using high-performance screen-printed graphene electrode. *Biosens Bioelectron* 2012;34:70–6.
- [23] Hyun WJ, Park OO, Chin BD. Foldable graphene electronic circuits based on paper substrates. *Adv Mater* 2013;25:4729–34.
- [24] Shin K, Hong J, Jang J. Micropatterning of graphene sheets by inkjet printing and its wideband dipole-antenna application. *Adv Mater* 2011;23:2113–8.
- [25] Bonaccorso F, Lombardo A, Hasan T, Sun Z, Colombo L, Ferrari AC. Production and processing of graphene and 2d crystals. *Mater Today* 2012;15:564–89.
- [26] Nicolosi V, Chhowalla M, Kanatzidis MG, Strano MS, Coleman JN. Liquid exfoliation of layered materials. *Science* (80-) 2013;340:1226419.
- [27] Hernandez Y, Nicolosi V, Lotya M, Blighe FM, Sun Z, De S, et al. High-yield production of graphene by liquid-phase exfoliation of graphite. *Nat Nanotechnol* 2008;3:563.
- [28] O'Neill A, Khan U, Nirmalraj PN, Boland J, Coleman JN. Graphene dispersion and exfoliation in low boiling point solvents. *J Phys Chem C* 2011;115:5422–8.
- [29] Salavagione HJ, Sherwood J, Budarin VL, Ellis GJ, Clark JH, Shuttleworth PS. Identification of high performance solvents for the sustainable processing of graphene. *Green Chem* 2017;19:2550–60.
- [30] Lotya M, Hernandez Y, King PJ, Smith RJ, Nicolosi V, Karlsson LS, et al. Liquid phase production of graphene by exfoliation of graphite in surfactant/water solutions. *J Am Chem Soc* 2009;131:3611–20.
- [31] Hasan T, Torrisi F, Sun Z, Popa D, Nicolosi V, Privitera G, et al. Solution-phase exfoliation of graphite for ultrafast photonics. *Phys Status Solidi* 2010;247:2953–7.
- [32] Wang Y, Tong X, Guo X, Wang Y, Jin G, Guo X. Large scale production of highly-qualified graphene by ultrasonic exfoliation of expanded graphite under the promotion of (NH₄)₂CO₃ decomposition. *Nanotechnology* 2013;24:475602.
- [33] Dong L, Chen Z, Zhao X, Ma J, Lin S, Li M, et al. A non-dispersion strategy for large-scale production of ultra-high concentration graphene slurries in water. *Nat Commun* 2018;9:76.
- [34] Hernandez Y, Lotya M, Rickard D, Bergin SD, Coleman JN. Measurement of multicomponent solubility parameters for graphene facilitates solvent discovery. *Langmuir* 2009;26:3208–13.
- [35] Wang S, Zhang Y, Abidi N, Cabrales L. Wettability and surface free energy of graphene films. *Langmuir* 2009;25:11078–81.
- [36] Khan U, O'Neill A, Lotya M, De S, Coleman JN. High-concentration solvent exfoliation of graphene. *Small* 2010;6:864–71.
- [37] Lamminen A, Arapov K, de With G, Haque S, Sandberg HGO, Friedrich H, et al. Graphene-flakes printed wideband elliptical dipole antenna for low-cost wireless communications applications. *IEEE Antennas Wirel Propag Lett* 2017;16:1883–6.

- [38] Jeon GW, An J-E, Jeong YG. High performance cellulose acetate propionate composites reinforced with exfoliated graphene. *Compos Part B Eng* 2012;43:3412–8.
- [39] Karagiannidis PG, Hodge SA, Lombardi L, Tomarchio F, Decorde N, Milana S, et al. Microfluidization of graphite and formulation of graphene-based conductive inks. *ACS Nano* 2017;11:2742–55.
- [40] Huang X, Leng T, Zhu M, Zhang X, Chen J, Chang K, et al. Highly flexible and conductive printed graphene for wireless wearable communications applications. *Sci Rep* 2015;5:18298.
- [41] Ciesielski A, Samorì P. Graphene via sonication assisted liquid-phase exfoliation. *Chem Soc Rev* 2014;43:381–98.
- [42] Kouroupis-Agalou K, Liscio A, Treossi E, Ortolani L, Morandi V, Pugno NM, et al. Fragmentation and exfoliation of 2-dimensional materials: a statistical approach. *Nanoscale* 2014;6:5926–33.
- [43] Guo H-L, Wang X-F, Qian Q-Y, Wang F-B, Xia X-H. A green approach to the synthesis of graphene nanosheets. *ACS Nano* 2009;3:2653–9.
- [44] Paton KR, Varrla E, Backes C, Smith RJ, Khan U, O'Neill A, et al. Scalable production of large quantities of defect-free few-layer graphene by shear exfoliation in liquids. *Nat Mater* 2014;13:624.
- [45] Ferrari AC, Basko DM. Raman spectroscopy as a versatile tool for studying the properties of graphene. *Nat Nanotechnol* 2013;8:235.
- [46] Yamada T, Hayamizu Y, Yamamoto Y, Yomogida Y, Izadi-Najafabadi A, Futaba DN, et al. A stretchable carbon nanotube strain sensor for human-motion detection. *Nat Nanotechnol* 2011;6:296.
- [47] Secor EB, Gao TZ, Islam AE, Rao R, Wallace SG, Zhu J, et al. Enhanced conductivity, adhesion, and environmental stability of printed graphene inks with nitrocellulose. *Chem Mater* 2017;29:2332–40.
- [48] Secor EB, Ahn BY, Gao TZ, Lewis JA, Hersam MC. Rapid and versatile photonic annealing of graphene inks for flexible printed electronics. *Adv Mater* 2015;27:6683–8.
- [49] Pouzin A, Vuong T-P, Tedjini S, Pouyet M, Perdereau J. Determination of the activation range of passive UHF RFID transponders by radar cross-section measurements. *Microw. Conf. 2009. EuMC 2009. Eur., IEEE; 2009, p. 9–12.*
- [50] Marrocco G. The art of UHF RFID antenna design: Impedance-matching and size-reduction techniques. *IEEE Antennas Propag Mag* 2008;50.
- [51] Sipilä E, Virkki J, Sydänheimo L, Ukkonen L. Effect of sintering method on the read range of brush-painted silver nanoparticle UHF RFID tags on wood and polyimide substrates. *RFID Technol. Appl. Conf. (RFID-TA), 2014 IEEE, IEEE; 2014, p. 219–22.*
- [52] Ojaroudi N. Compact UWB monopole antenna with enhanced bandwidth using rotated L-shaped slots and parasitic structures. *Microw Opt Technol Lett* 2014;56:175–8.
- [53] Valenta CR, Durgin GD. Harvesting wireless power: Survey of energy-harvester conversion efficiency in far-field, wireless power transfer systems. *IEEE Microw Mag* 2014;15:108–20.
- [54] McSpadden JO, Fan L, Chang K. Design and experiments of a high-conversion-efficiency 5.8-GHz rectenna. *IEEE Trans Microw Theory Tech* 1998;46:2053–60.
- [55] Shao Y, Wang J, Wu H, Liu J, Aksay IA, Lin Y. Graphene based electrochemical sensors and biosensors: a review. *Electroanal An Int J Devoted to Fundam Pract Asp Electroanal* 2010;22:1027–36.

- [56] Huang X, Leng T, Georgiou T, Abraham J, Nair RR, Novoselov KS, et al. Graphene oxide dielectric permittivity at GHz and its applications for wireless humidity sensing. *Sci Rep* 2018;8:43.

3.5 Supplementary figures

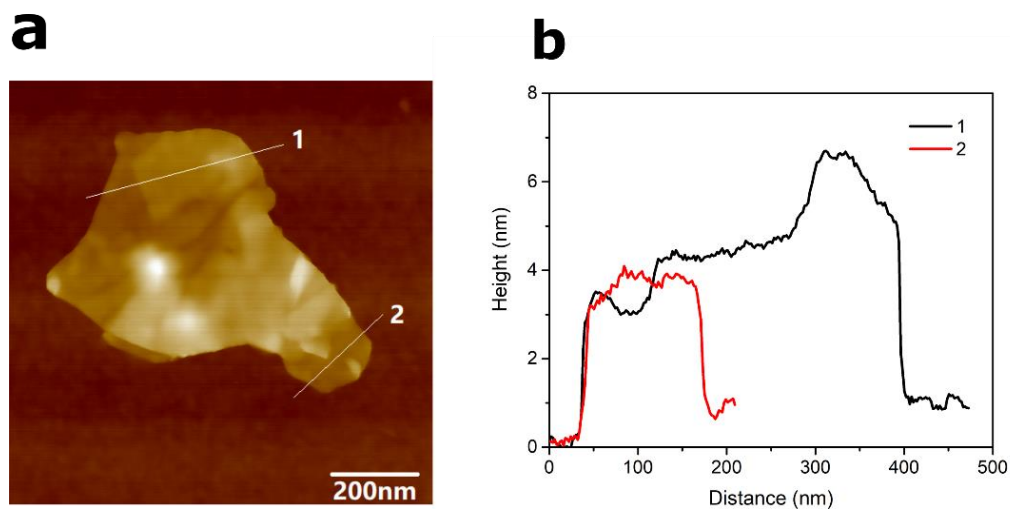


Figure 3-20: A single graphene nanoflake profile measurement. Atomic force microscopy image of a single graphene nanoflake exfoliated in Cyrene **a** and the corresponded cross section heights **b**.

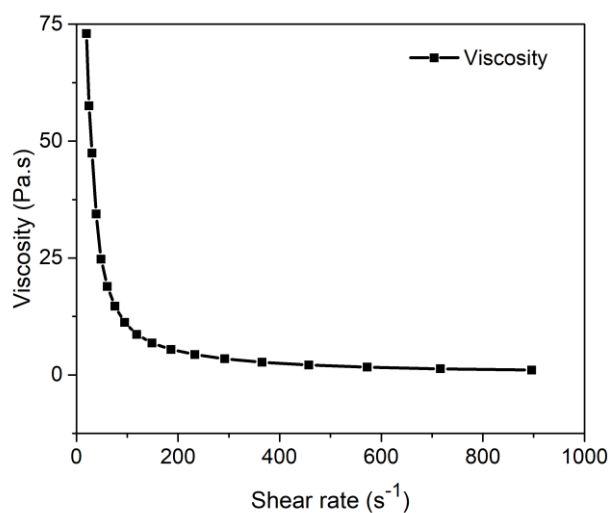


Figure 3-21: Viscosity of the screen printable ink. Measured viscosity data of the screen printable ink with the graphene concentration of 70 mg mL⁻¹ and CAB concentration of 7 mg mL⁻¹.

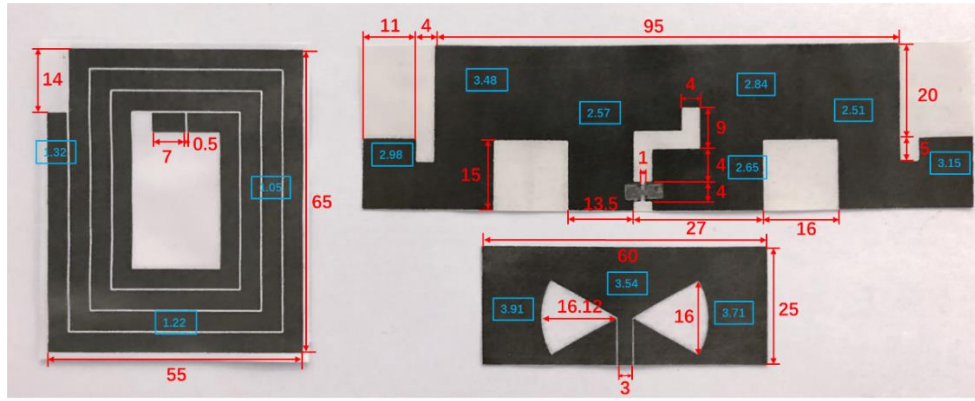
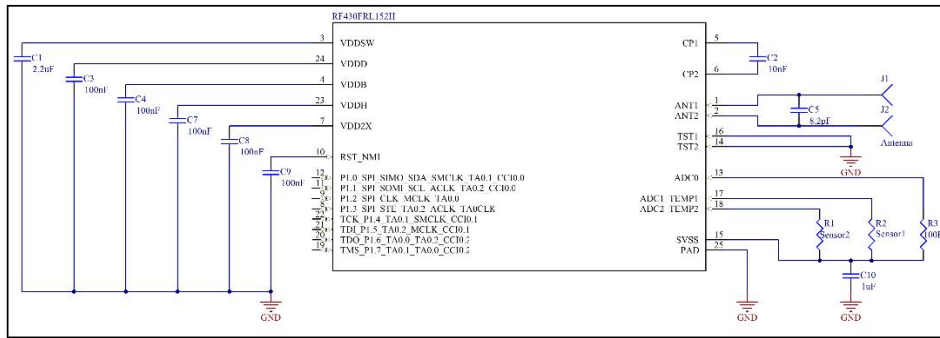
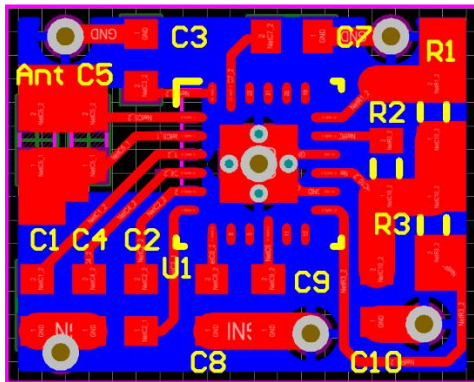


Figure 3-22: Antenna dimensions and sheet resistance. The blue rectangles represent measured sheet resistance at this point. The variation was caused by unflatness of the exposed screen. The average sheet resistance for the nearfield antenna is $1.2 \Omega \text{ sq}^{-1}$; for RFID antenna is $2.88 \Omega \text{ sq}^{-1}$; for wideband slot antenna is $3.72 \Omega \text{ sq}^{-1}$. The red lines indicate specific dimensions (mm).

a



b



c

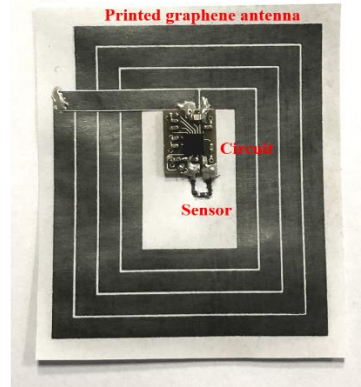


Figure 3-23: Printed graphene temperature monitoring system. Schematic sensing and conversion circuit **a** and PCB **b**. Photo of the entire wireless sensor **c**. The conductive epoxy (CW2400, Circuitworks) was used to connect graphene antenna and the PCB.

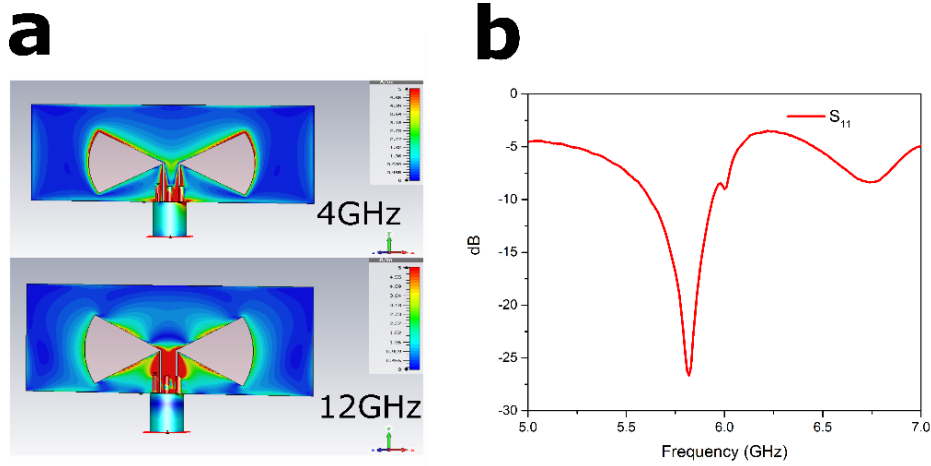


Figure 3-24: Energy harvesting Antenna and circuits. Surface current distributions of the C-X-Ku band wideband antenna at fundamental resonance (4GHz) and harmonic resonance (12GHz) **a**. Reflection coefficient of matched conversion circuit **b**.

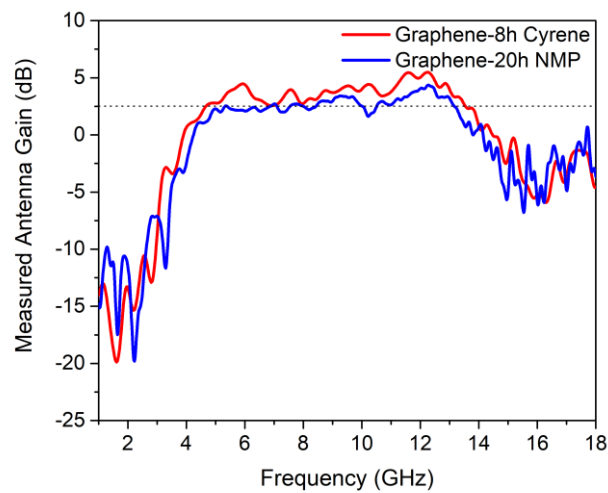


Figure 3-25: Antenna gain based on different graphene inks. Red line: Cyrene based graphene ink (8h ultrasonic treatment). Blue line: NMP based graphene ink (20h ultrasonic treatment). The 8h Cyrene based antenna has slightly higher gain than 20h NMP based antenna because the conductivity of 8h Cyrene printed pattern is slightly higher.

3.6 Supplementary notes

Supplementary Note 1: Temperature monitoring system converting circuits.

In order to demonstrate the functionality of the graphene printed NFC antenna, a commercial NFC chip (RF430FRL152H) which is integrated with NFC module and

microcontroller was connected to the antenna. The capacitor C5 in Supplementary Figure 3-23a together with internal capacitor of the NFC chip constitute an LC resonance circuit which operates in 13.56 MHz. The RTD temperature sensor (NTHS0603N17N2003JE, VISHAY) in Supplementary Figure 3-23a was connected to R1 and R3, which are standard resistors. The absolute measurement accuracy is 0.3% when refresh frequency is 0.5 Hz.

Supplementary Note 2: Temperature monitoring system program.

```

%%%%%%%%%%%%%%%%%%%%%%%%%%%%%%%%%%%%%%%%%%%%%%%%%%%%%%%%%%%%%%%%%%%%%%%%
%Kewen Pan
%TRF7970A EVM testing program for tag2
%6/May/2016
%%%%%%%%%%%%%%%%%%%%%%%%%%%%%%%%%%%%%%%%%%%%%%%%%%%%%%%%%%%%%%%%%%%%%%%%

clear;clc; %Clear
i=1;
j=0;
buffer=zeros(1,50);
delay_time=0.01;

dev_name = 'Silicon Labs CP210x USB to UART Bridge';
[~,res]=system('wmic path Win32_SerialPort');
ind = strfind(res,dev_name);
if (~isempty(ind))
    port_name = res(ind(1)+length(dev_name)+2:ind(1)+length(dev_name)+5);
    fprintf('COM-port is %s\n',port_name);
    try

        s = serial(port_name);
        set(s,'BaudRate',
111700,'DataBits',8,'StopBits',1,'Parity','none','FlowControl','none','terminator','ETX' );

        s.ReadAsyncMode='continuous';
        s.Timeout=0.02
        s.InputBufferSize = 1024;

        s.OutputBufferSize = 1024;

        fopen(s);
        fprintf('%s is opened\n',port_name);
    catch err
        fprintf('%s\n%s\n',err.identifier,err.message);

```

```

        end
    else
        fprintf('COM-port is not find\n');
    end
    fprintf(port_name);
    fprintf(' serial port open success!');
    pause(1);
    %%%%%%%%%%%%%%%
    %s.status    %Serial port status check
    %instrfind   %Specification
    %%%%%%%%%%%%%%%
    fprintf(s,'%s','0108000304FF0000');%find evm broad
    data=fscanf(s);
    if strcmp(data(1),'T');
        fprintf('found TRF7970A\r');
        % pause(delay_time);
    else
        fprintf('cannot found TRF7970A\r');
    end
    %%%%%%%%%%%%%%%
    fprintf(s,'%s','010A0003041001210000');%register write request1
    data=fscanf(s);
    if strcmp(data(1),'R');
        fprintf('register1 write success\r');
        % pause(delay_time);
    else
        fprintf('register write error1\r');
    end
    %%%%%%%%%%%%%%%
    fprintf(s,'%s','010C00030410002101000000');%register write request2
    data=fscanf(s);
    if strcmp(data(1),'R');
        fprintf('register2 write success\r');
        % pause(delay_time);
    else
        fprintf('register write error2\r');
    end
    %%%%%%%%%%%%%%%
    fprintf(s,'%s','0109000304F0000000');%AGC Toggle
    data=fscanf(s);
    if strcmp(data(1),'A');
        fprintf('AGC toggle success\r');
        % pause(delay_time);
    else

```

```

        fprintf('AGC Toggle error\r');
end
%%%%%%%%%%%%%%%%%%%%%%%%%%%%%%%%%%%%%%%%%%%%%%%%%%%%%%%%%%%%%%%%%%%%%%%%%%%%%%
fprintf(s,'%s','0109000304F1FF0000');%AM PM Toggle
data=fscanf(s);
if strcmp(data(1),'A');
    fprintf('AM PM Toggle success\r');
    %   pause(delay_time);
else
    fprintf('AM PM Toggle error\r');
end
while 1
    while 1
        %%%%%%%%%%%%%%%%%%%%%%%%%%%%%%%%%%%%%%%%%%%%%%%%%%%%%%%%%%%%%%%%%%%%%%%%%%%%%%%
        set(s,'terminator','ETX' );
        fprintf(s,'%s','010B000304140401000000');%ISO15693 Inventory Request
        data=fscanf(s);
        if length(data)<35;
            fprintf('ISO15693 Inventory Request error\r');
        else
            fprintf('ISO15693 Inventory Request success\r');
            %   pause(delay_time);
            fprintf(data);
            break;
        end
    end
end
%%%%%%%%%%%%%%%%%%%%%%%%%%%%%%%%%%%%%%%%%%%%%%%%%%%%%%%%%%%%%%%%%%%%%%%%%%%%%%Basic configuration success%%%%%%%%%%%%%%%%%%%%%%%%%%%%%%%%%%%%%%%%%%%%%%%%%%%%%%%%%%%%%%%%%%%%%%%%%%%%%%

%%%%%%%%%%%%%%%%%%%%%%%%%%%%%%%%%%%%%%%%%%%%%%%%%%%%%%%%%%%%%%%%%%%%%%%%%%%%%%Write functional register%%%%%%%%%%%%%%%%%%%%%%%%%%%%%%%%%%%%%%%%%%%%%%%%%%%%%%%%%%%%%%%%%%%%%%%%%%%%%%
fprintf(s,'%s','010F00030418402100010203800000');%Reg 00
data=fscanf(s);
d=data(17);
if strcmp(data(17),'J');
    fprintf('Reset failed\r');
    fprintf("Tag disconnected\r");
    %buffer=zeros(1,50);
    break;
end

fprintf(s,'%s','010F00030418402100010203000000');%Reg 00
data=fscanf(s);
if strcmp(data(1),'R');
    fprintf('Reg00\r');
    fprintf(data,'\r');

```

```

%   pause(delay_time);
    fprintf(data);
else
    fprintf('Write reg 00 failed\r');
end
%%%%%%%%%%%%%%%%%%%%%%%%%%%%%%%%%%%%%%%%%%%%%%%%%%%%%%%%%%%%%%%%%%%%%%%%
fprintf(s,'%s','010F00030418402101010100400000');%Reg01
data=fscanf(s);
if strcmp(data(1),'R');
    fprintf('Reg01\r');
    fprintf(data,'\r');
%   pause(delay_time);
    fprintf(data);
else
    fprintf('Write reg 01 failed\r');
end
%%%%%%%%%%%%%%%%%%%%%%%%%%%%%%%%%%%%%%%%%%%%%%%%%%%%%%%%%%%%%%%%%%%%%%%%
fprintf(s,'%s','010F00030418402102000000000000');%Reg02
data=fscanf(s);
if strcmp(data(1),'R');
    fprintf('Reg02\r');
    fprintf(data,'\r');
%   pause(delay_time);
    fprintf(data);
else
    fprintf('Write reg 02 failed\r');
end
%%%%%%%%%%%%%%%%%%%%%%%%%%%%%%%%%%%%%%%%%%%%%%%%%%%%%%%%%%%%%%%%%%%%%%%%
fprintf(s,'%s','010F00030418402103000000000000');%Reg03
data=fscanf(s);
if strcmp(data(1),'R');
    fprintf('Reg03\r');
    fprintf(data,'\r');
%   pause(delay_time);
    fprintf(data);
else
    fprintf('Write reg 03 failed\r');
end
%%%%%%%%%%%%%%%%%%%%%%%%%%%%%%%%%%%%%%%%%%%%%%%%%%%%%%%%%%%%%%%%%%%%%%%%
fprintf(s,'%s','010F00030418402104191919190000');%Reg04
data=fscanf(s);
if strcmp(data(1),'R');
    fprintf('Reg04\r');

```

```

        fprintf(data, '\r');
%       pause(delay_time);
        fprintf(data);
    else
        fprintf('Write reg 04 failed\r');
    end
%%%%%%%%%%%%%%%%%%%%%%%%%%%%%%%%%%%%%%%%%%%%%%%%%%%%%%%%%%%%%%%%%%%%%%%%%%Config
finished%%%%%%%%%%%%%%%%%%%%%%%%%%%%%%%%%%%%%%%%%%%%%%%%%%%%%%%%%%%%%%%%%%%%%%%%%%
while 1
    set(s, 'terminator', 'I' );
%%%%%%%%%%%%%%%%%%%%%%%%%%%%%%%%%%%%%%%%%%%%%%%%%%%%%%%%%%%%%%%%%%%%%%%%%%Start
sample%%%%%%%%%%%%%%%%%%%%%%%%%%%%%%%%%%%%%%%%%%%%%%%%%%%%%%%%%%%%%%%%%%%%%%%%%%

    fprintf(s, '%s', '010F00030418402100010203000000'); %Reg 00
    data=fscanf(s);
    if strcmp(data(17), 'I');
        fprintf('Write reg 00 failed\r');
        fprintf('Tag disconnected\r');
        %buffer=zeros(1,50);
        break;
    end
%%%%%%%%%%%%%%%%%%%%%%%%%%%%%%%%%%%%%%%%%%%%%%%%%%%%%%%%%%%%%%%%%%%%%%%%%%
%%%%%%%%%%%%%%%%%%%%%%%%%%%%%%%%%%%%%%%%%%%%%%%%%%%%%%%%%%%%%%%%%%%%%%%%%%

%%%%%%%%%%%%%%%%%%%%%%%%%%%%%%%%%%%%%%%%%%%%%%%%%%%%%%%%%%%%%%%%%%%%%%%%%%Start
reading%%%%%%%%%%%%%%%%%%%%%%%%%%%%%%%%%%%%%%%%%%%%%%%%%%%%%%%%%%%%%%%%%%%%%%%%%%
    fprintf(s, '%s', '010B000304180020120000'); %Read reg 0x12
    data=fscanf(s);
    if strcmp(data(19), 'I');
        fprintf('Read reg 0x12 failed\r');
        fprintf('Tag disconnected\r');

        break;
    end

    if strcmp(data(18), 'z');
        fprintf('Read reg 0x12 failed\r');
        fprintf('Tag disconnected\r');

        break;
    end

    Stand_res=[data(23),data(24),data(21),data(22)];

```

```

Sensor_res=[data(27),data(28),data(25),data(26)];

Resistance=(hex2dec(Sensor_res)/hex2dec(Stand_res))*100;%cal sensor R
Temp=-1.27*Resistance+203;%exp curve fitting
if (Temp>=0)&&(Temp<=50)
buffer=[buffer(2:end), buffer(1:1)];%left shift 1 bit
buffer(50)=Temp;%push in
plot(buffer,'Linewidth',3);
set(gca, 'FontWeight', 'bold', 'FontName','Calibri','FontSize',14)
title('Graphene Based Yarn Temperature Sensor');
ylabel('Temperature');
xlabel('Time');
grid on;
drawnow;
pause(0.5);
% else

end

end

end

fclose(s);
delete(s);
clear s
%close all;

```

4 3D graphene/polymer porous spongy for sensing and microwave absorbing applications

Kewen Pan, Ting Leng, Jiashen Li, Kostya S. Novoselov & Zhirun Hu

Submitted to *Advanced functional materials*

My contributions:

I have prepared graphene inks designed and fabricated all devices, performed all materials and sponge characterization. I also performed all microwave parameters measurement, analyzed all the data, and drew all the graphs.

Abstract

In this paper, we have fabricated and characterized a novel graphene loaded highly stretchable and conductive sponge. Conductivity optimized graphite/graphene dispersion has been researched and its conductivity was increased up to $7 \times 10^4 \text{ S}\cdot\text{m}^{-1}$. Due to the outstanding electrical properties, the applications of soft microwave absorbers in X-band (8.2-12.4 GHz) has been demonstrated. A double layer absorber design can achieve effective absorption (above 0.9) in the whole band, with only 4 mm thick. Another four layers of design can absorb effectively when incident microwave angle varies from 0° to 60° . The flexibility of graphene flakes and polymer enables the conformal applications of absorbers. Moreover, a soft, stretchable supercapacitor was fabricated in this paper. It can be stretched up to 200% of its original length, where the capacitance retention stands after 100 cyclic charge-discharge tests. This work not only revealed the possibilities that the novel multi-functional sponge can do on electronic devices but also opened a new door for stretchable and wearable electronics.

4.1 Introduction

As graphene loaded composites have already been well researched for decades, many outstanding progresses have been achieved. However, a severe issue that cannot be solved is that the electrical conductivity of such composites is relative low [1,2]. The consequence is that the measurement of such low conductivity materials (normally $\text{M}\Omega$ level) requires more power and complex circuits. It hindered these composites'

electrical applications. This phenomenon is natural to be explained as all graphene flakes are covered by insulating polymers, where electron flow is difficult. The way to solve this problem is to increase graphene content [3]. However, excessive graphene loading would degrade its mechanical properties [4]. Moreover, the high loading of graphene would raise the cost, and residual in graphene dispersion may affect cross-linking if epoxy was used. Therefore, coating a thin layer of graphene on sponge-based material is another route that can significantly increase graphene flakes density in the coating layer. Due to several advantages of graphene sponges such as three-dimensional graphene networks, high surface area [5], high electro/thermal conductivities [6,7], high chemical/electrochemical stability [8], high flexibility and elasticity [9], extremely high surface hydrophobicity [10], and so on, they have been used to demonstrate a feasibility way for bridging the nano-scale properties of graphene-based materials to practical macro-scale applications. Their practical applications include compositing materials [11], the use as the electrode materials for electrochemical sensors [12], the use as the absorbers for both gases and liquids [13], and the use as electrode materials for devices involved in electrochemical energy storage and conversion [14–16]. Furthermore, with successful implementation, these three-dimensional structures offer a border range of applicability and more exceptional performance than those achieved with two-dimensional graphene.

Several methods have been successfully developed, demonstrating the feasibility in preparing high quality and high-performance graphene sponges [17]. These methods include the templated growth of graphene on nickel sponges [18], direct sponging of

graphene oxide (GO) solutions [19], self-assembly [20] and several others. Among these methods, the CVD growth technique can produce well-defined, large pore size structures with high conductivity, and the material's quality can be primarily controlled by process variables during the CVD growth. However, the high temperature, sacrificial template and multistep processing limit the scalability. The self-assembly technique using the reduction of GO is compatible with the simultaneous growth of other composite materials. The properties and performance of the formed graphene sponges are shown to be strongly dependant on the quality and size of the GO precursor, the type of the reducing agents, cross linkers, doping agents and the pH of synthetic solution. Although the direct freeze drying self-assembly is simple, it is heavily dependent on size and concentration, in which controlling ice crystal formation and cracking on a larger size scale is a challenge. Moreover, most of the sponges reported are on a small lab scale and despite reported flexibility and elasticity, most graphene sponges remain fragile and easily broken or torn without careful handling. Therefore, all of the methods require further development to promote robust, scalable sponges at low cost and with less restacking.

In order to overcome all problems mentioned above, a cost-effective strategy has been developed to fabricate large-scale 3D graphene/elastomer sponge, as shown in Figure 4-1. No hydrothermal assembly process, solvothermal treatment or freeze-drying are required. This method does not require complicated and energy-consuming synthetic steps. The raw materials are commercialized graphene, elastomer, and porogen particles (NaCl in this paper). At initial, NaCl particles are mixed with

graphene dispersion and then filled in a metal mold with constant pressure. After that, the annealing process will evaporate solvents and burn out additional polymer. Then, hardener mixed Ecoflex 00-50 is injected into the mold. Until Ecoflex is completely cross-linked, graphene flakes are bonded, the rest NaCl particles can be dissolved in water.

In this paper, a low cost but high conductive graphite/graphene (Gp&Gr) dispersion was optimized and discussed in advance. Then the porous sponge was fabricated. Detailed fabrication and characterizations are presented. Due to the outstanding electrical performance, Jaumann structured multilayer absorbers which operate in X-band have been proposed, where each layer of the absorber was carefully optimized based on the measured permittivity of sponges. We also demonstrated the design process which can be straight applied to other materials. Thanks for the excellent stretchability of Ecoflex. The application of the sponge is not limited by EM wave absorption. Therefore, a soft, double-layered supercapacitor was fabricated and measured. The two examples revealed the enormous potential of Gp&Gr loaded sponges. More applications such as sensors, microwave shielding and soft electrodes are waiting to be explored.

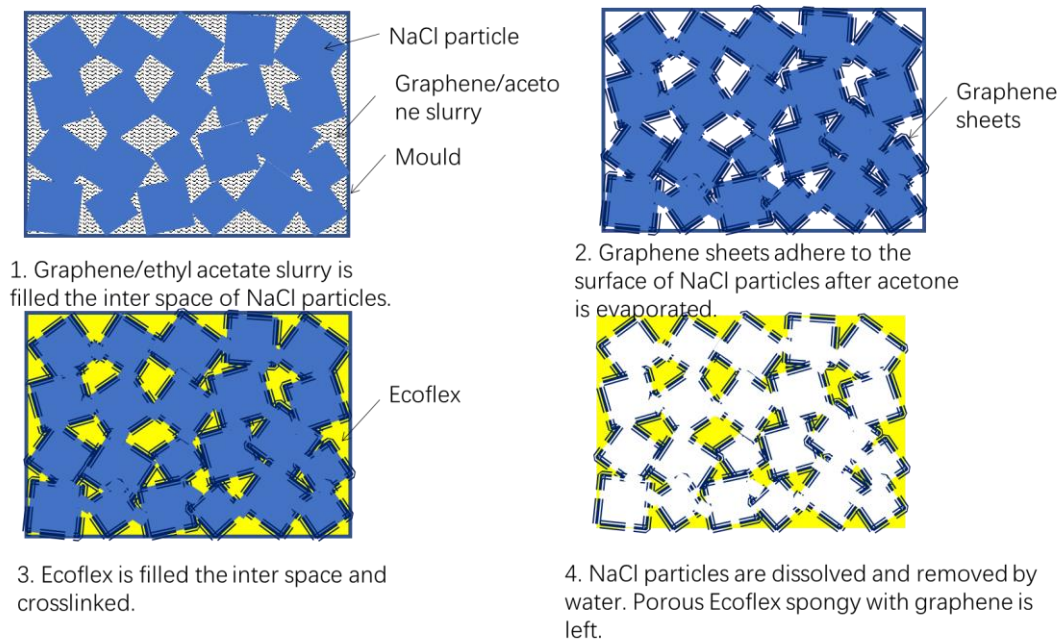


Figure 4-1: Schematic illustration of Gp&Gr loaded high conductive sponge fabrication process.

4.2 Results

As printing electronic technology has been developed for decades, transistors and sensors [21] are now possible to be printed on flexible substrates. The low-cost manufacturing leads IoT and wearable electronics coming to daily life. Conducting materials are the fundamental part of all printed electronic circuits and also accounts on a high percentage within cost. It is significant to select cheap conductive materials in low-cost electronic systems. Unfortunately, silver based conductive inks are still the most commonly used in real products due to its excellent electrical and ink properties [22,23]. In order to reduce cost, cheaper but more reactive metals such as copper and nickel are used for conductive inks. The durability of these inks is not excellent because of oxidation [24]. After that, the organic conducting materials have been developed with high conductivity [25] but still orders lower than metal based inks. Since 2004 [26], the

research of liquid phase exfoliated graphene inks has last for years [27], the better conductivity and lower cost of raw materials nowadays make graphene based ink to be a better alternative choice of conductive ink. At initial, ultrasonic treatment was applied to exfoliate graphite particles with appropriate solvents which have similar surface energies with graphene [28]. On the contrary, low concentration and toxic solvents hindered the ink's application. Polymers and surfactants [29] were added into graphene inks, which can raise concentration and also avoid aggregation problem. The latest research reports [30] that the concentration of ultrasonication assisted graphene ink was raised to 10 mg mL^{-1} and conductivity after compressing was enhanced to $7.13 \times 10^4 \text{ S}\cdot\text{m}^{-1}$. Although the processing steps have been optimized in this report, ultrasonic treatment still requires 8 hrs at least. The development of the shear mixing exfoliation method boosts the production of graphene ink. Comparing with the ultrasonication method, the yield of shear mixing method is an order higher while the energy density keeps the same [31]. Following the significant progress, high concentration inkjet [32] and screen printing [33] graphene inks were produced with different solvents and surfactants [34–36]. However, in spite of the high yield of graphene flakes, the surfactants are barely possible to be removed from the final printed conductive pattern, which severely degrades electrical conductivity. A recent study [37] that using nitrocellulose (NC) as dispersing agent achieved very high conductivity because NC can drastic decompose around $200 \text{ }^{\circ}\text{C}$. However, the yield is still less attractive for scale-up production.

As graphene has been well researched, we know that mono-layer graphene has

super high electrical conductivity [38]. Due to the interlayer channel effect [39], the electrical conductivity of few-layer graphene (FLG) decreases with the increase of thickness. From previous literatures, the contents of mono-layer graphene flakes are very few. FLG (<3nm) and graphene nano pellets (GNP >3nm) are the main ingredients of graphene inks. On the other hand, the centrifugation process separates graphite particles but the conductivity of those inks is limited lower than $10^5 \text{ S}\cdot\text{m}^{-1}$, which is similar to carbon blacks [40]. Therefore, is that meaningful to separate graphene flakes for conductive ink with such low conductivity and yield?

As a matter of fact, the conductivities of graphene inks are affected by many reasons. Our previous research [30] has confirmed that different size and thickness distributions of the flakes plays a significant role. Thinner graphene flakes have higher conductivity. These flakes result in better stacking, but much more interfaces between flakes, which may increase resistance. Thick graphene flakes reduced the number of interfaces, but its poor stacking would lose adhesion, also produce several voids after printing. It is difficult to analyse these parameters quantitatively, but optimizing flake distribution to achieve maximum electrical conductivity and yield is obtainable via adjusting centrifuge speeds.

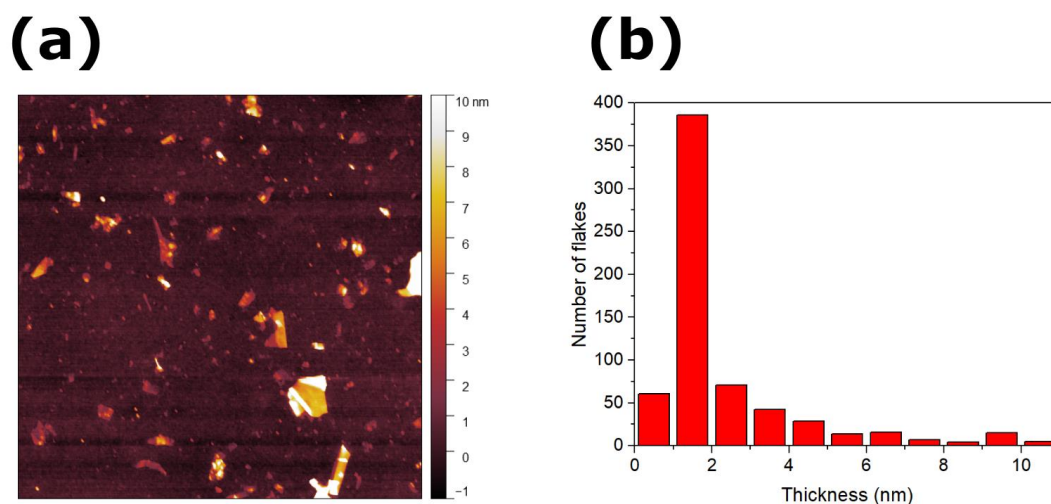


Figure 4-2: High conductive Gp&Gr ink characterization. (a) AFM image of 2K RPM centrifuged Gp&Gr dispersion on silicon dioxide substrate; scale is $5\ \mu\text{m} \times 5\ \mu\text{m}$. (b) Height distribution of flakes.

In this work, graphite flakes and NC were added into ethyl acetate for shear mixing processing (see **4.4 Methods**). The final 2000 RPM centrifuged product was characterized by Atomic force microscopy (AFM). Clear layered graphene flakes are shown in Figure 4-2a with a lateral area of $5 \times 5\ \mu\text{m}$. The measured thickness distribution in Figure 4-2b is peaked at 1.5 nm, which confirmed the existence of graphene flakes. It is worth noticing that the lateral size of graphene flakes in Figure 4-2a is less than 1 μm , consistent with previously reported shear mixing product [37]. AFM can only characterize thin layered graphene but unexfoliated graphite particles in this sample cannot be separated completely due to the low-speed centrifuge.

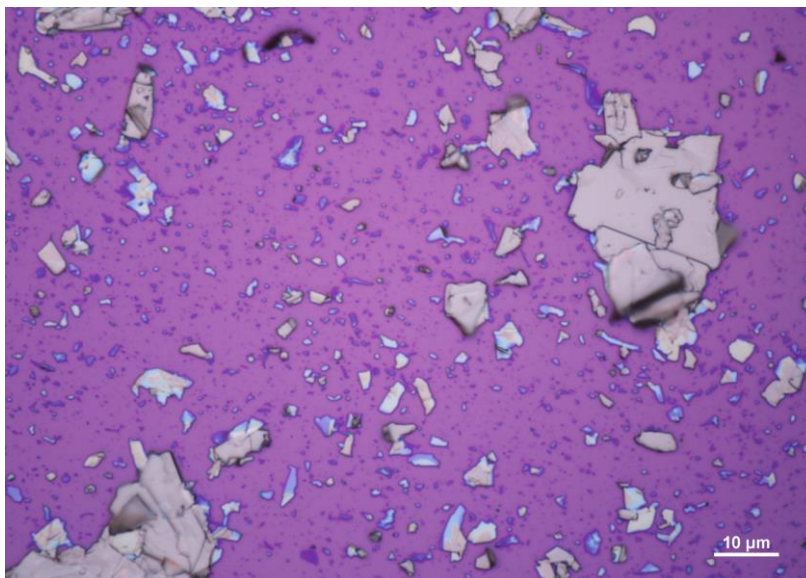


Figure 4-3: Optical image of the AFM sample, scale bar is in the image.

Therefore, microscope image of the sample is shown in Figure 4-3. The blue flakes might be graphene but gold flakes are definitely very thick graphite particles. Comparing with graphene flakes, graphite particles are fewer in the amount but account exceedingly at weight percentage. The effect of size distribution on conductivity will be quantitatively discussed.

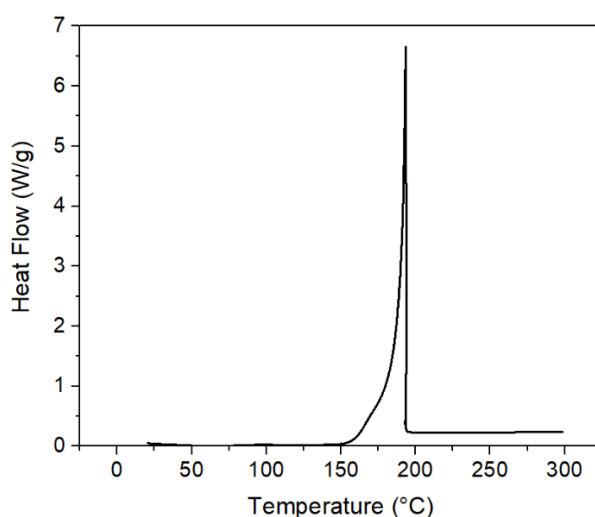


Figure 4-4: DSC analysis of pure NC.

Differential scanning calorimetry (DSC) was used to investigate the decomposition

temperature of NC, as plotted in Figure 4-4. There was no heat flow variation when temperature was below 150 °C, which indicates the stable existence of NC. While temperature was rising, the heat flow increased exponentially, indicating the spontaneous combustion took place. After that, heat flow dropped back to 0.2 W/g when temperature reached 190 °C. According to the literature [41], the primary decomposition process was complete and residual materials kept reacting at higher temperature.

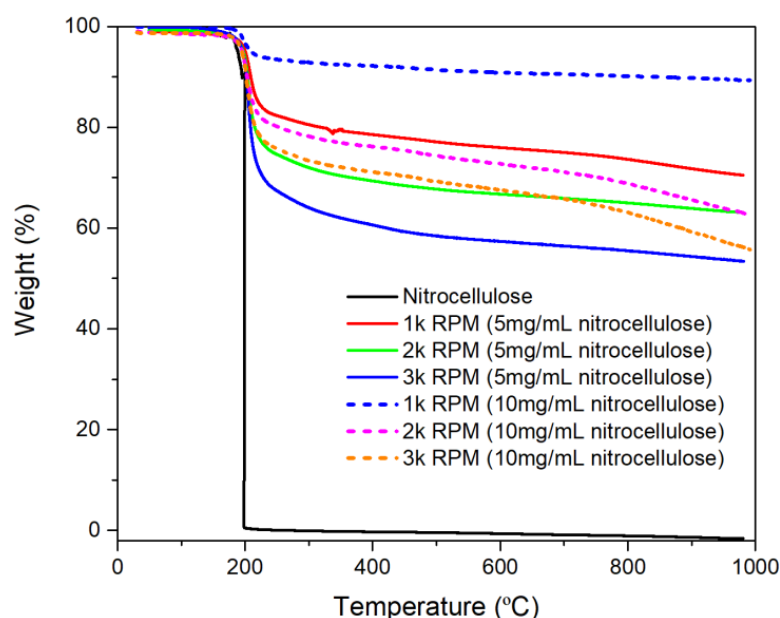


Figure 4-5: TGA results of dried dispersion samples with different centrifuge speed and NC content. The less weight loss at high temperature represents higher Gp&Gr flakes concentration.

Thermo Gravimetric Analysis (TGA) results were plotted in Figure 4-5, samples have little weight variation at initial. Pure NC has a sharp transition of weight percentage around 195 °C. The promising low residual result is not agreed with previous reported [37] because the nitrogen content of NC that we used in this paper is much higher (>13%wt). Benefiting from the low residual characters, it is possible to enhance ink conductivity with low temperature (<240 °C) annealing. For the rest inks,

we can see that inks with higher NC concentration and lower centrifuge speed have less weight drop, which indicates higher Gp&Gr concentration. After calculation, we plotted the Gp&Gr concentration in Figure 4-6.

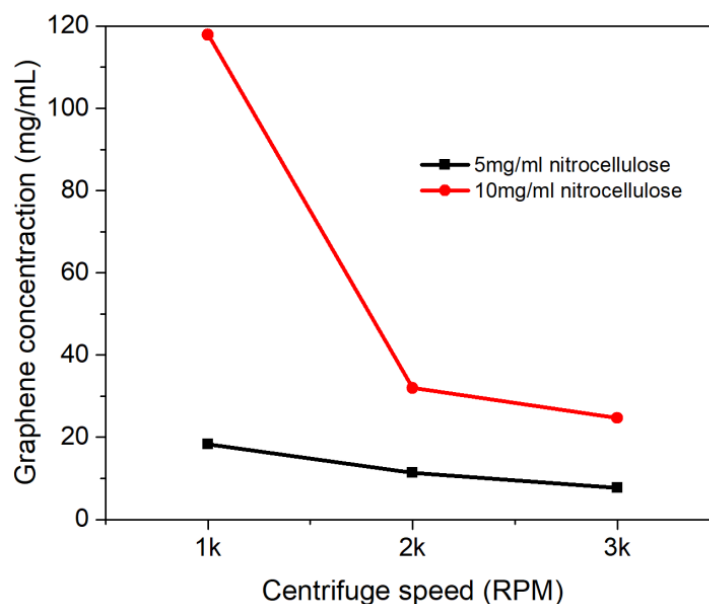


Figure 4-6: Calculated graphene concentration from Figure 4-5.

The concentration dropped linearly for 5 mg/mL NC samples. However, there is a significant drop between 1k and 2k RPM for 10 mg/mL NC samples. For 1k RPM sample, the Gp&Gr concentration is 3.6 times higher than 2k RPM sample. It would be really attractive for industrial production if the conductivity is not much different. Furthermore, both two derivative curves from TGA results in Figure 4-7 show main peaks around 200 °C but the decomposition speed of lower NC concentration sample was faster, which suggested the interaction Gp&Gr flakes only alter the decomposition speed of NC rather than temperature.

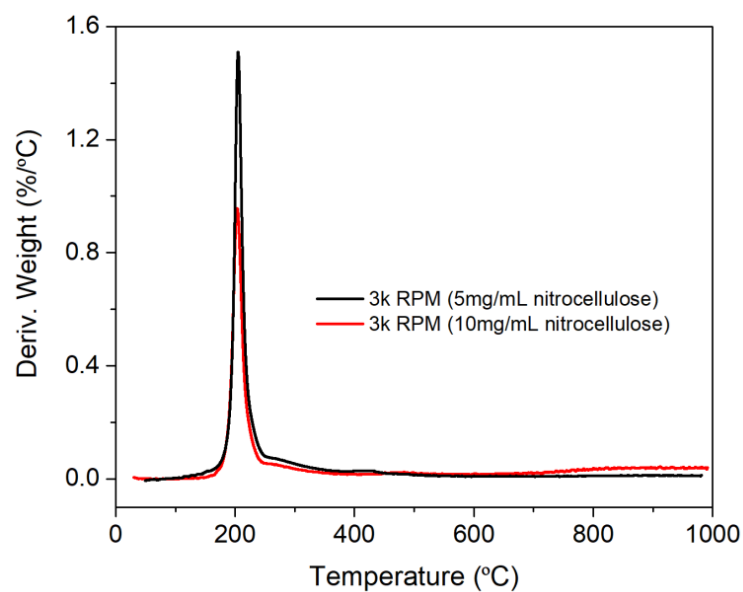


Figure 4-7: The derivative of the 3K RPM TGA results with different NC contents.

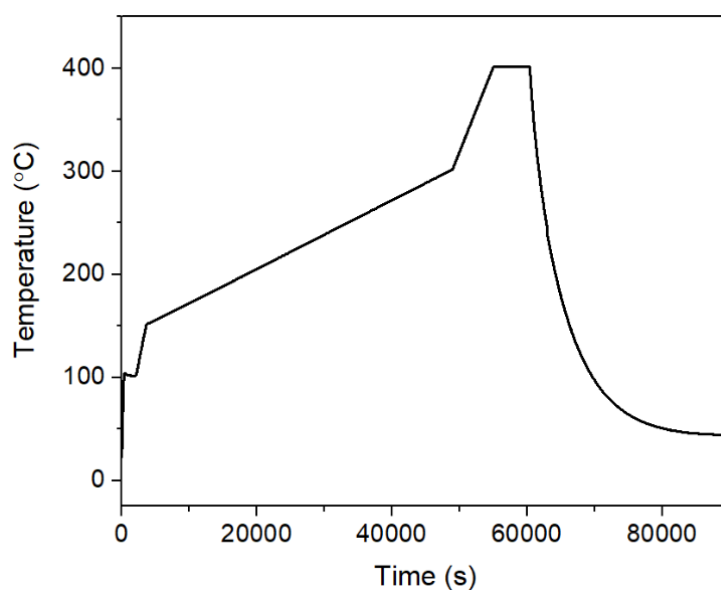


Figure 4-8: Measured temperature ramping in annealing process.

Based on the above analysis, we set and monitored the annealing sequence of dried dispersion, as shown in Figure 4-8. At initial, the sample was heated to 100 °C and kept for 30 min. After that, the temperature ramping rate was set to 2 °C/min because NC would not decompose at low temperatures. Until the temperature reaches 150 °C, the ramping rate was minimized to 0.2 °C/min to ensure uniformly heating. On the other

hand, it can avoid drastic decomposition of NC, which may blow off Gp&Gr flakes. We increased the ramping speed to 1°C/min from 300 °C to 400 °C and then kept for 1.5 hr to ensure full decomposition of residual. Morphological features of the dried laminate were observed by scanning electron microscope (SEM).

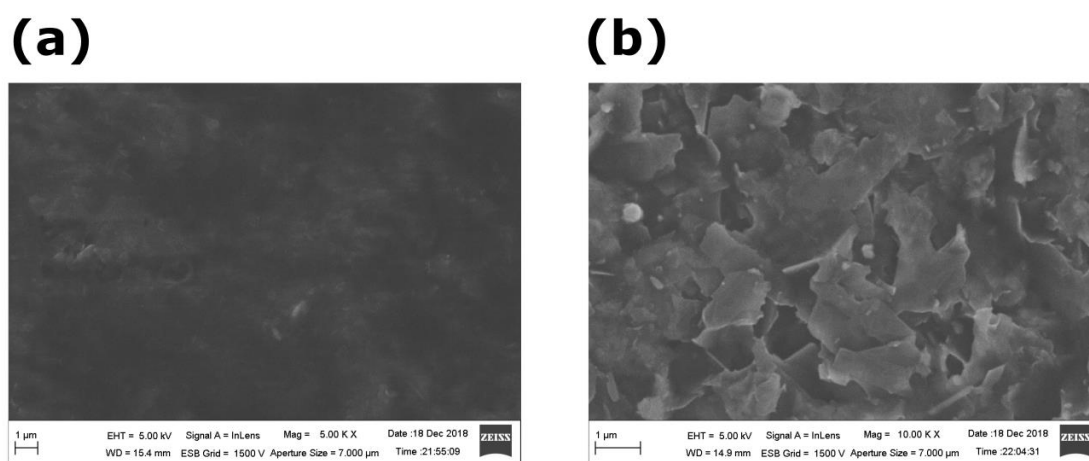


Figure 4-9: Post-processing of the dried conductive laminates and sponges. (a) SEM image of the dried Gp/Gr dispersion. Flakes have been enveloped in NC. (b) SEM image of the annealed sample, NC has been completely removed and graphite fragment can be clearly observed.

Figure 4-9a demonstrated the 2k RPM sample, flakes cannot be observed because of the coverage of NC. After the annealing process, flakes can be clearly seen in Figure 4-9b. The porous stacking structure was formed by the escape of decomposed gas. However, it would severely degrade the contact between flakes, resulting in low conductivity. Based on our previous study [30], mechanical compression forced flakes restacking together, hence conductivity would be improved. The flakes distribution is not practical for real production. We choose centrifuge speed as the main parameter to investigate conductivity variation. The centrifuged inks were dropped on 5cm×5cm glass substrates and then annealed in oven. After cooling down, 20 points on each sample were randomly selected for sheet resistance and height measurement.

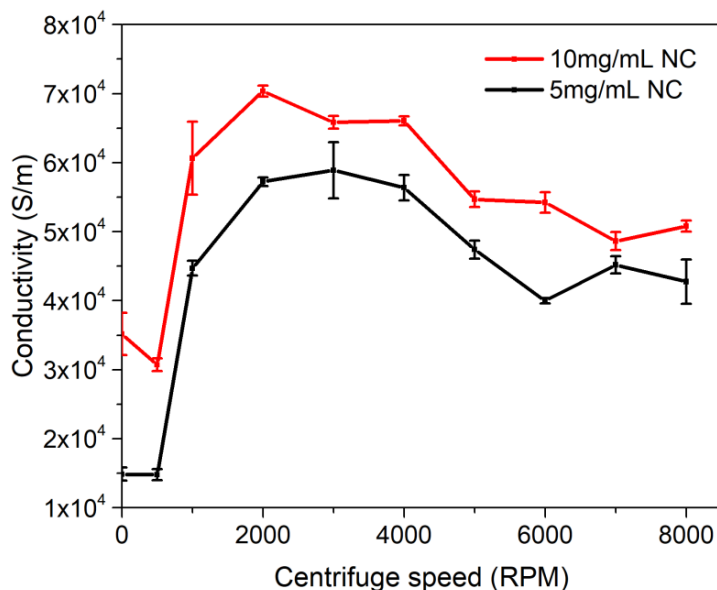


Figure 4-10: Conductivity measurement of the annealed laminates as a function of centrifuge speeds.

As shown in Figure 4-10, inks with high NC concentration generally have better conductivity. The high NC concentration ink (red line) doubled its conductivity at 2k RPM centrifuge speed while low NC concentration ink (black line) almost quadruple. This result confirmed the removal of large graphite flakes would massively increase conductivity. However, it can be observed that both lines decreased gradually after centrifuge speed was higher than 3k RPM, indicating higher contents of small flake graphene would actually decrease conductivity. This unexpected result indicates that blindly pursuing graphene is useless. Those small graphene flakes cannot give better conductivity. In the meantime, the lower graphene concentration due to high-speed centrifuge leads to poor production efficiency. Consequently, the best graphene ink must achieve a balance between concentration and conductivity rather than separating graphene at any cost. In this paper, 2k RPM centrifuged and 10 mg/mL NC loaded graphene ink was selected because of the highest conductivity ($7 \times 10^4 \text{ S} \cdot \text{m}^{-1}$).

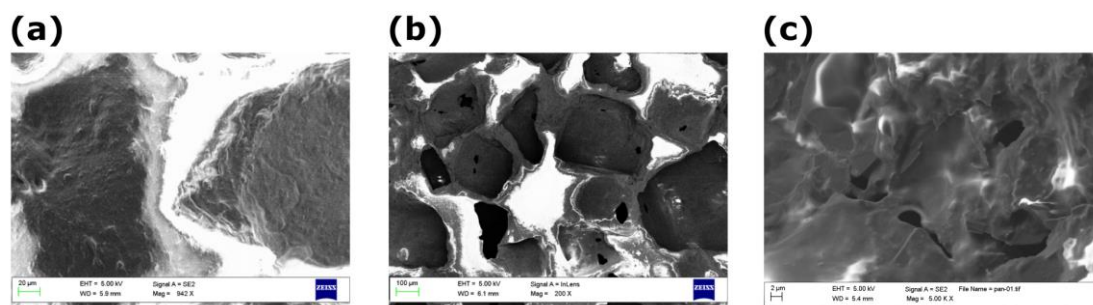


Figure 4-11: (a) Magnified cross-section view of the fabricated sponge, the white part is not conductive (polymer) and the grey part are conductive (Gp&Gr flakes). (b) The cross-section SEM image of the sponge under low magnification, clear cube shaped holes can be seen. (c) The magnified SEM image of the conductive surface, flakes have been well covered by cross-linked Ecoflex polymer.

As the development and problems of porous conductive materials were discussed in the previous section, a conductive and highly stretchable sponge was fabricated in this paper. The fabrication steps can be found in **4.4 Methods**. To demonstrate the structure of sponge, the cross-section view of SEM images were shown in Figure 4-11a,b. The bright white part is insulated material (Ecoflex polymer), and the grey part is conductive. It revealed the bearing part of the sponge is puer Ecoflex which provides its mechanical stretchability. The Gp&Gr flakes were coated on the surface. Comparing with the previously reported work [2], such structure has higher flakes density while the flakes' contents are the same. Therefore, the coated layer provides excellent electrical conductivity. The small holes in Figure 4-11b were formed because of the staked NaCl crystals. It also allows water to go through for NaCl crystals' removal. Nevertheless, Gp&Gr flake structure cannot be observed from the magnified SEM image (Figure 4-11f), which means flakes were clad entirely and immobilized in Ecoflex. Predictably, the electrical properties would be stable and resistance relaxing time would be short when the sponge is deformed. Take a step further, the SEM sample was also observed under microscope, as shown in Figure 4-12a. Black fragments can

be clearly seen at the sides of the polymer wall.

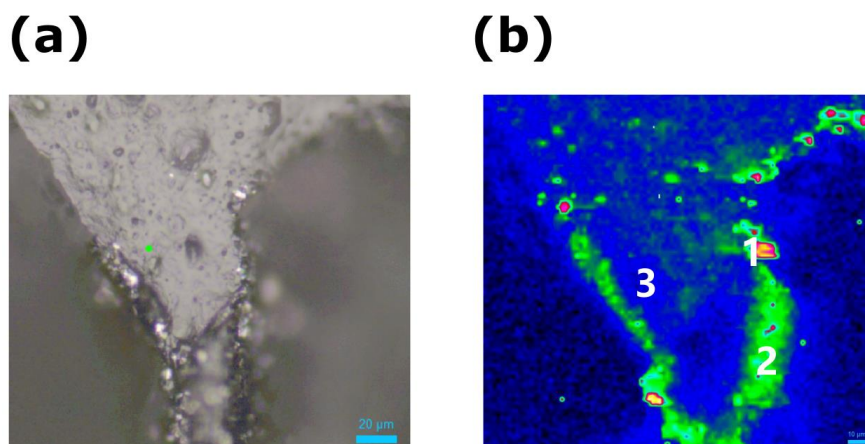


Figure 4-12: (a) The optical image at 50 \times . (b) Mapping of the intensity ratio of 2707 cm^{-1} (Graphene 2D band) and 2896 cm^{-1} (Ecoflex C-H).

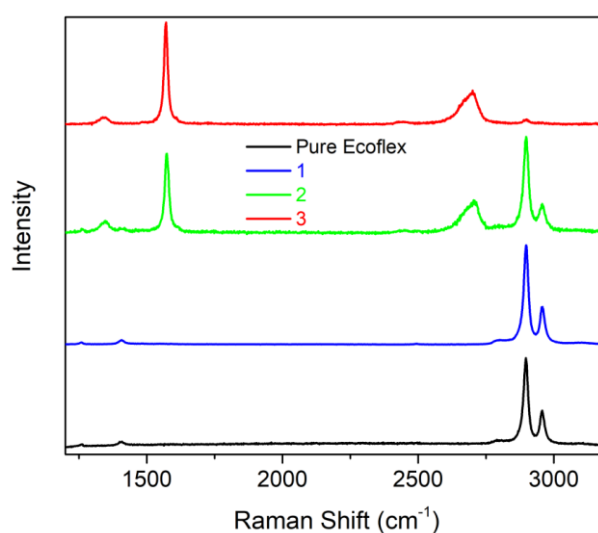


Figure 4-13: Raman results of the sponge cross-section, where mark 1,2 and 3 are corresponded to the area in Figure 4-12b.

Raman spectroscopy was used to identify the sample. We first measured the pure Ecoflex polymer and polymer area in the sample. They are precisely the same (blue and black lines). The main peaks locating around 2896 cm^{-1} are the C-H [42] stretching of Ecoflex. The weaker 2956 cm^{-1} and 1409 cm^{-1} peaks were formed by CH_2 [43]. Secondly, the area with black fragments was measured (area 2 in Figure 4-12b). There is no shift of the polymer peaks or generation of new peaks, indicating no chemical

bond was formed between polymer and flakes. Also, explicit sp^2 carbon atoms breathing mode at D-band (1346 cm^{-1}), G-band (1572 cm^{-1}), associated with the in-phase vibrations of graphite lattice, the relatively wide 2D-band at 2707 cm^{-1} and an overtone of the D-band is observed [31]. In final, we measured the flakes exposed area (area 1 in Figure 4-12b), only shown the graphite peaks and very weak C-H peak. However, none of the samples observed the existence of nitro groups ($-\text{NO}_2$). This is also the evidence that NC was completely decomposed to gas in the annealing step. For intuitive demonstration, the Raman mapping image (2707 cm^{-1} 2D-band/ 2896 cm^{-1} C-H peak) was shown in Figure 4-12b. The green and red areas that surrounded the polymer structure represent higher Gp&Gr content. In contrast, only a few scattered flakes can be seen in polymer.

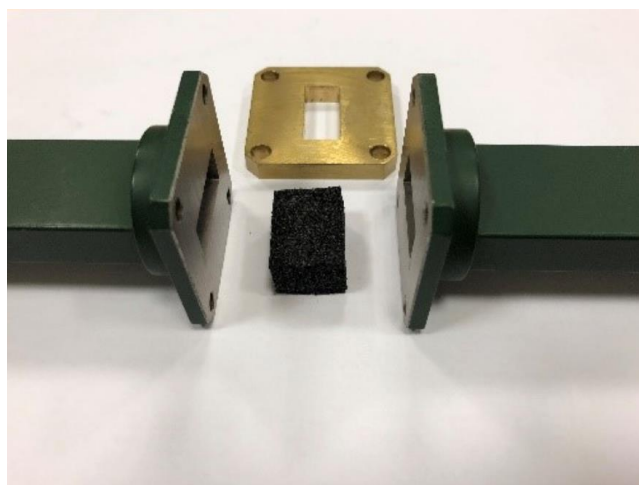


Figure 4-14: X-band sponges' permittivity and permeability measurement set up.

As the fabrication process and material characterization of the porous sponge has been discussed in **4.2 Results**, its microwave properties which are necessary for exploring microwave absorbers will be demonstrated in this section.

For the measurement of microwave permittivity (ϵ_r) and permeability (μ_r), a pair

of X-band waveguide was used and the porous sponges were cut into cuboids that can fit into waveguide spacer, as shown in Figure 4-14.

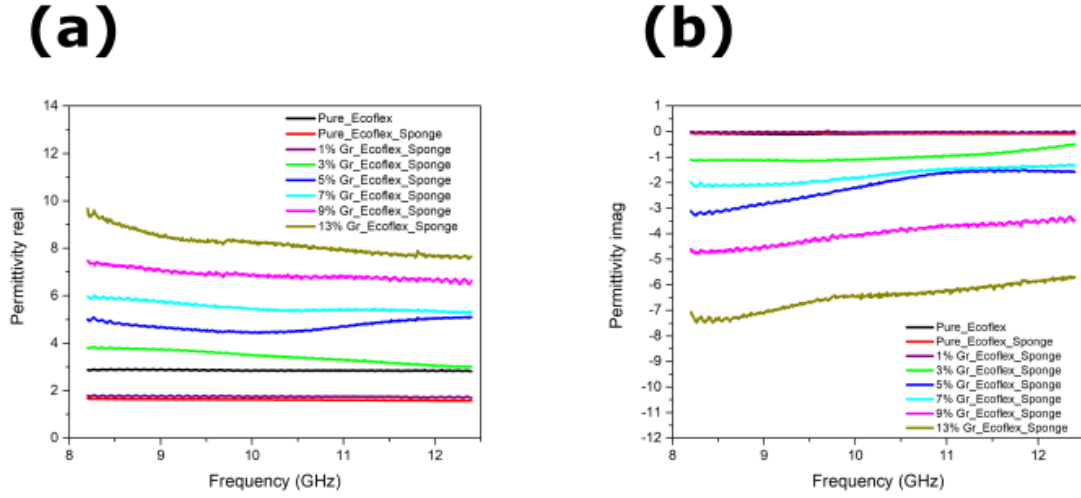


Figure 4-15: Measured real part (a) and imaginary part (b) of permittivity.

S-parameters were measured using a calibrated Vector Network Analyser (VNA, Keysight N9918A). Reflections and transmissions of the sponge were acquired through VNA. Based on these vector data, it is possible to calculate both ϵ_r and μ_r through the waveguide method [44,45]. There are 1024 points for the S-parameter measurement from 8.2 GHz to 12.4 GHz and all points were converted to the corresponding ϵ_r and μ_r . In Figure 4-15 a and b, the real (ϵ'_r) and imaginary (ϵ''_r) parts of the relative permittivity with different Gp&Gr contents were plotted, respectively. The real part permittivity of pure Ecoflex brick is higher than the sponge (black and red lines) but their imaginary parts keep the same. It revealed that Ecoflex is a very good low loss material. As more Gp&Gr flakes were added for higher filler weight percentage, the greater real and absolute imaginary parts were achieved. Also, the results show the shaper increasing of loss tangent ($\tan\delta = |\epsilon''_r/\epsilon'_r|$) with higher flakes' weight

percentage. In the meantime, the materials' magnetic permeability was calculated.

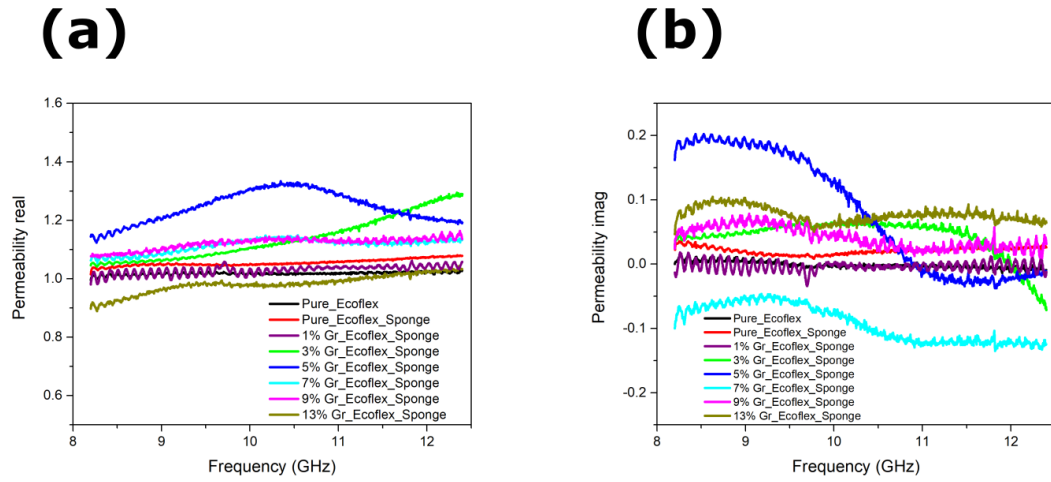


Figure 4-16: (a) and (b) is the real part and imaginary part of permeability, respectively.

Although all materials have responses to magnetic fields but graphite, graphene or Ecoflex are not ferromagnetic nor ferromagnetic materials. Their responses to magnetic fields are negligible [47], in other words, close to free space permeability. Therefore, the real parts of permeability in Figure 4-16a is close to 1, not related to the weight percentage of flakes. The same conclusion can be obtained in Figure 4-16b.

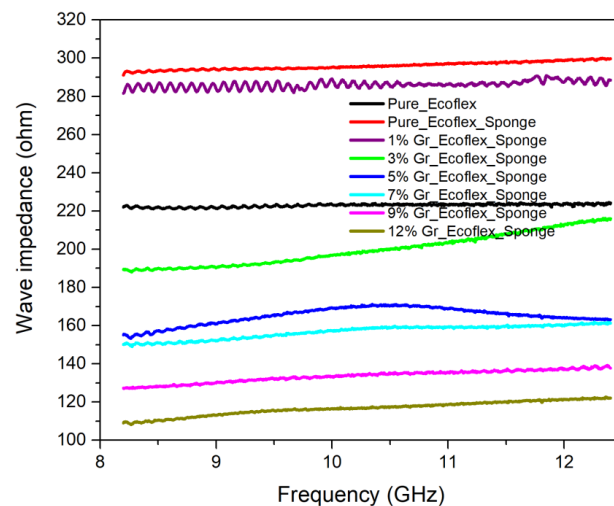


Figure 4-17: Corresponded wave impedance of the sponges with different graphene content.

To start design microwave absorbers, we calculated wave impedance (TEM) of

sponges by the equation:

$$\eta_x = \sqrt{\frac{\mu_0}{\varepsilon_0}} \sqrt{\frac{\mu_r}{\varepsilon' - j\varepsilon''}} \quad (4.1)$$

where μ_0 and ε_0 are the free space permittivity and permeability. From the results in Figure 4-17, we can see the higher Gp&Gr flakes loading would reduce wave impedance; in other words, stronger reflection to an incident electromagnetic wave [48]. Therefore, layered RAM structure absorber can be designed by utilizing the diversity of reflection.

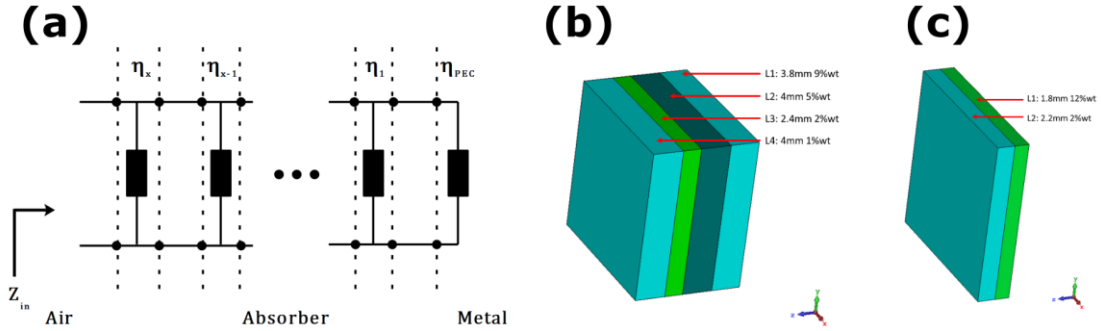


Figure 4-18: (a) Transmission line equivalent circuit model of the microwave absorber. (b), (c) 3D illustration of the proposed four and two layers' microwave absorber. Thickness and Gp&Gr contents are marked.

We suppose a plane TEM wave illuminates on an infinite absorber which is consisted by layered sponges with different flakes content, as depicted in Figure 4-18a. Reflection coefficient (RL) of the absorber is able to be evaluated by the well-known equation:

$$RL = 20 \log_{10} \left| \frac{Z_x - 377}{Z_x + 377} \right| \quad (4.2)$$

Z_x is the input impedance of the top layer (air-absorber interface) and it can be written from transmission line theory:

$$Z_x = \eta_x \frac{Z_{x-1} + j\eta_x \tan(\beta_x l_x)}{\eta_x + jZ_{x-1} \tan(\beta_x l_x)} \quad (4.3)$$

where l_x is the thickness, Z_{x-1} is the input impedance of the last layer and β_x is the

propagation constant that can be expressed as:

$$\beta_x = 2\pi f \sqrt{\mu_0 \varepsilon_0} \sqrt{\mu_x (\varepsilon'_x - j\varepsilon''_x)} \quad (4.4)$$

The equivalent circuit model of the Jaumann absorber is illustrated in Figure 4.2-3d. The black component represents wave impedance of each layer and the last layer is metal where its wave impedance can be approximated to 0. The absorption of the Jaumann absorber is mainly contributed by dielectric losses of the sponges and matching with air. As we have precisely calculated permittivity, the dielectric losses are known, while the matching condition has to consider each layers' permittivity, thickness frequency, etc. Consequently, a Matlab program with transmission line algorithm was provided in the supplementary material to help design the most efficient absorber.

In order to verify the performance of MATLAB designed absorber. Two X-band absorbers with two layers and four layers were designed and then simulated by using commercial software CST MWS. The 3-D view of the absorber structure is demonstrated in Figure 4-18b,c. For the two layers absorber, the first layer towards air has 2%wt flakes content, 2.2 mm thick while the second layer flakes content is 12%wt, 1.8mm thick. For the four layers absorber, flakes content was 1%, 2%, 5% and 9%, respectively. The corresponded thickness of each layer is 4, 2.4, 4 and 3.8 mm. In the simulation, the Gp&Gr flakes loaded sponges were modeled as normal materials with measured permittivity and permeability. Periodic unit cell boundary was used in CST to avoid the edge effect. Because the absorber structure is symmetry in x-y plane, the response is precisely the same for both vertical and horizontal polarized waves.

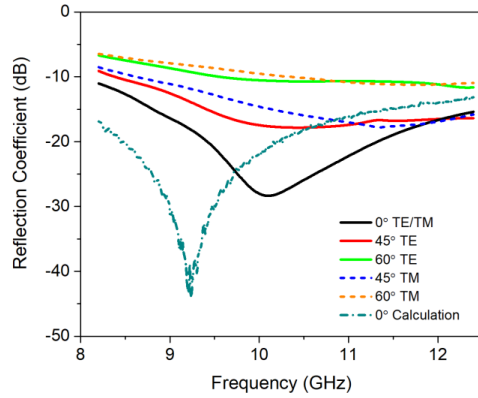
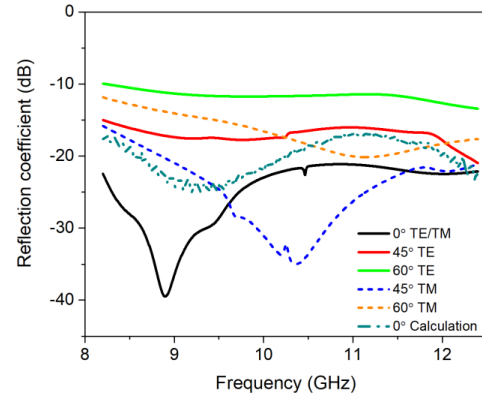
(a)**(b)**

Figure 4-19: (a) Simulated reflection results of four layers absorber at perpendicular and angled incident conditions. (b) Simulation results for two layers absorber with the same incident angles.

The calculated and simulated amplitude of reflection coefficients of two layers absorber have been plotted in Figure 4-19a. It can be seen that the calculated (green dash line) result achieved low reflection (< -10 dB) at whole X-band. The maximum absorption is -44dB which was contributed by the resonance of absorber at 9.25 GHz. The fullwave simulation results (black line) agreed well with calculated results from the equivalent circuit model, although the resonance shifted to 10 GHz. For the thicker four layers absorber in Figure 4-19b, the maximum reflection is better than two layers absorber. Also, the resonance may have moved further down outside X-band, achieving a flat response. In real applications, the incident microwave comes from all angles. Typically, Jaumann structured absorber has its best performance at vertical incidence. Therefore, if an absorber can effectively absorb microwave at higher incident angles, the performance is better. However, the transmission line model cannot calculate the performance while incident wave is not perpendicular to the absorber. In this paper, fullwave simulation was used to evaluate angled incident wave performance. Firstly,

the TE incident wave reflection of two layers absorber with 45° incident angle was simulated and illustrated. Under this situation, -10 dB bandwidth cannot be achieved over X-band because of the stronger reflection from 8.2 to 8.5 GHz. Also, the resonance peak became broadband. For the four layers absorber, the reflection is 10 dB stronger on average. While the incident angle was increased to 60°, the reflections are worse for both absorbers but thanks to the outstanding performance at initial 0°, four layers absorber is still able to maintain its reflection lower than -10 dB. Similar behavior for TM incidence can be observed at two layers absorber. However, the performance of 45° TM incidence is even better at four layers absorber. There is a broad resonance occurred around 10.4 GHz, which probably caused by $\lambda/4$ resonant between the top and bottom layer. Take a step further, the absorbers' performance can be more intuitively expressed by EM absorption:

$$1 - |S_{11}|^2 - |S_{21}|^2 \quad (4.5)$$

where S_{21} is transmission coefficient which is negligible in this case. Results are shown in Figure 4-20.

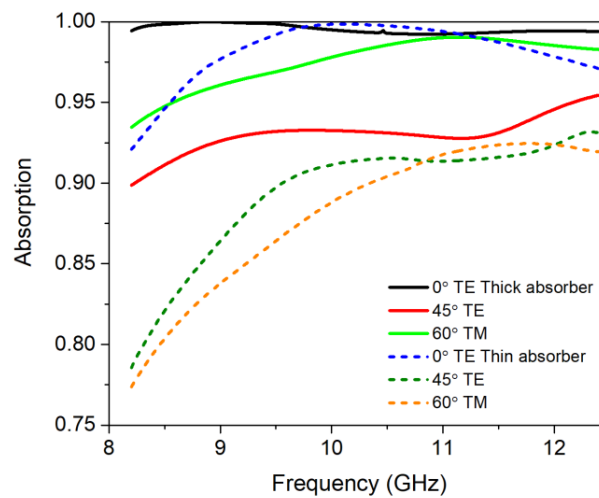


Figure 4-20: Calculated microwave absorptions, effective absorption generally above 0.9.

For a practical absorber, effective absorption is generally above 0.9 [49]. The two layers absorber can only achieve this standard while incidence wave is close to vertical. In the meantime, four layers absorber can effectively absorb microwave from 0° to 60° and the maximum absorption is 0.99998 at 8.89 GHz. In conclusion, the four layers absorber performed better at the expense of thickness (14.2 mm) while the thinner absorber (4 mm) can be applied where the weight and space are sensitive. Moreover, the highly flexible and conformable sponge is not only limited to flat or slightly bent surfaces but suitable to any curved objects, which takes a step forward to our previous work [49].

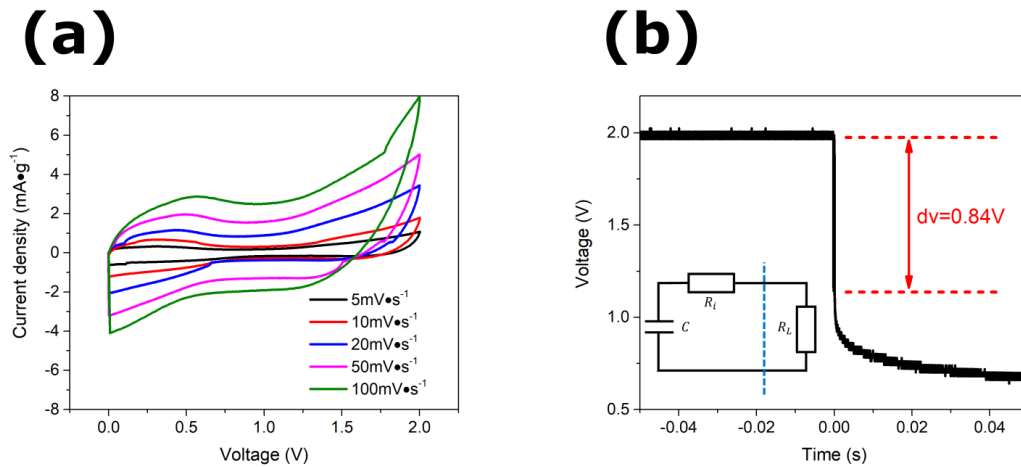


Figure 4-21: (a) Cyclic voltammetry (C-V) curves of the fabricated supercapacitor with varied charge speeds. (b) Measurement of equivalent series resistance (ESR), the small schematic in (b) is the DC equivalent circuit for ESR measurement.

Because of the surprisingly excellent electrical conductivity of Gp&Gr laminates, the applications of the highly stretchable sponge are not limited to microwave absorber. The porous structure and high surface area of graphene flakes make the sponge an alternative selection for soft, deformable supercapacitor. To verify the feasibility, a supercapacitor with soft Ecoflex based shell was fabricated in this section. The

capacitive performance of the Ecoflex-graphene sponge material was evaluated by a two electrodes symmetrical system with Diethylmethyl(2-methoxyethyl)ammonium bis(trifluoromethylsulfonyl)imide (DEMMA-TFSI) ionic electrolyte. The cyclic voltammetry (CV) measurement results in Figure 4-21a. It exhibits a quasi-rectangular curve of a double layer capacitor[50] while the scanning rate of the applied voltage is 5 mV/s. However, under the higher scanning rate, distorted curves can be observed. The slightly tilted shape is caused by charge transfer resistance (leakage current). In addition, the broadband redox reaction peaks appeared (ion insertion or extraction to Gp&Gr/DEMMA-TFSI interface) while the applied voltage is within 0-0.8V. From 10 mV/s to 100 mV/s, the redox peaks shift to higher voltages [51]. Other peaks that appeared around 2 V are proportional to scanning voltage which proved these peaks are not contributed by leakage current. From previously reported papers [52,53], the series DC parasitic resistance (include capacitor resistance and contact resistance between electrode and sponge) together with the capacitance constitutes a low pass filter with a relatively higher time constant, resulting to the deformation of the rectangular shape and these peaks [54–56]. In order to get better understanding of the tilted CV curve, the equivalent series resistance R_i (ESR) was measured by connecting a load resistor $R_L = 10\ \Omega$ (more details illustrated in supplementary materials). The result is demonstrated in Figure 4-21b. In the initial 5 μ s, the supercapacitor can be considered as constant voltage source but the voltage at supercapacitor terminals dropped 0.84 V. Therefore, the calculated R_i is 7.24 Ω which is intensely higher than commercial supercapacitors [57,58] and also leads to a considerably long time constant. This

phenomenon is shown from the round flat discharge CV curves. Fortunately, the contact resistance and sponge resistance in this experiment can be further minimized via doping [59] or conductive coating process[60].

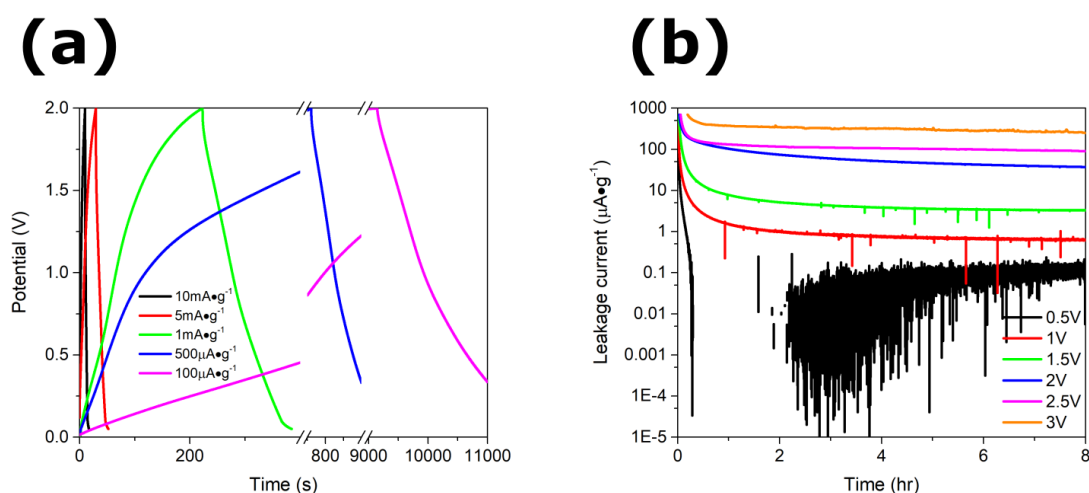


Figure 4-22: (a) Galvanostatic charge-discharge (GCD) profile of the supercapacitor. (b) Measured leakage currents versus applied voltage and time.

The capacitive performance and specific capacitances under different charging speeds were evaluated by galvanostatic charge/discharge (GCD) curve with charging/discharging current from 0.1 to 10 mA/g. All charging processes halt at 2 V and discharging processes halt at 50 mV. The results were measured and plotted in Figure 4-22a and measurement schematic diagram can be found in Supplementary materials. Symmetrical triangular charge/discharge shapes can be observed when current density is 5 or 10 mA/g, revealing a standard behaviour of electric double layer supercapacitor [61]. However, we found the distortion of the charge current curves are worse while the charge current decrease. For instance, the GCD curve under 0.1 mA/g is close to a quadrilateral shape. We suspect the distortion is related to the unfinished ion insertion process and leakage current. Therefore, the supercapacitor was connected

to a precision voltage source and then charged 8 hrs with different voltages for steady-state leakage current measurement. All logged data can be found in Figure 4-22b. The current density at 0.4 hr (turning point of 0.1 mA/g curve) is 151.26 $\mu\text{A/g}$, which is significantly higher than 0.1 mA/g charge current density in GCD measurement. When the applied voltage reaches 2 V (2.52 hrs), the current density is still 65.9 $\mu\text{A/g}$. Apart from the constant leakage current, the low drop rate of the current density is due to the slow ion penetration process from Ecoflex sponge to graphene flakes' surface. That explained the distortions of GCD curves in low charge current densities. After 8hrs, the stable current density can be considered as leakage current density, which is 37.2 $\mu\text{A/g}$.

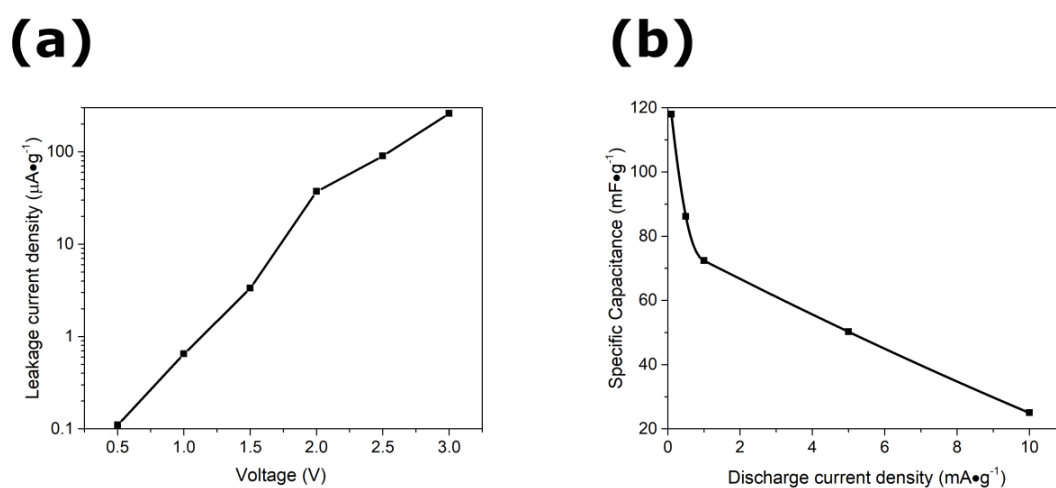


Figure 4-23: (a) Leakage currents after 8 hrs stabilization. (b) Calculated specific capacitance from GCD results.

The steady-state leakage current densities versus different applied voltage were recorded in Figure 4-23a. In lower voltage region, the leakage current is mainly contributed by residues and other ions within electrolyte. The logarithmic relationship also indicates that high voltage may electrolyze the supercapacitor's electrolyte, which is not recoverable. Similar behaviors can be found in [62–64].

From GCD curves, capacitance can be calculated by employing the formula [58]:

$$C_s = \frac{I}{m \cdot dV/dt} \quad (4.6)$$

where dV/dt is the slope of GCD's discharge curve and m is the weight of graphene flakes. In order to ensure the accuracy of capacitance calculation [65,66], the nearly linear parts of discharge curves were selected (0.5 V to 1.5 V). Figure 4-23b presents calculated capacitance under different discharge current densities. At 0.1 mA/g, the supercapacitor exhibits 118 mF/g specific capacitance. In contrast, the specific capacitance drops to 26 mF/g while current density increased to 10 mA/g. Such a difference is resulted by low ion diffusion speed due to large ion size [67], Ecoflex blockage, high viscosity of the ionic liquid [68] and thick separator, which all drag down ion movement speed. It is worth to be noticed that specific capacitance is three orders lower compering with rGO/polymers based supercapacitor [69–72] because the specific surface area of graphite flakes is orders lower than well chemical intercalated graphene oxide. However, the structural defects and unreduced oxygen groups on rGO flakes lead to a less stable electrode interface. During the capacitor retention test in Figure 4-24a, the capacitance only dropped 2% after 5000 times full (2 V) charge/discharge cycles, which shown a better capacitance retention comparing with the above literatures.

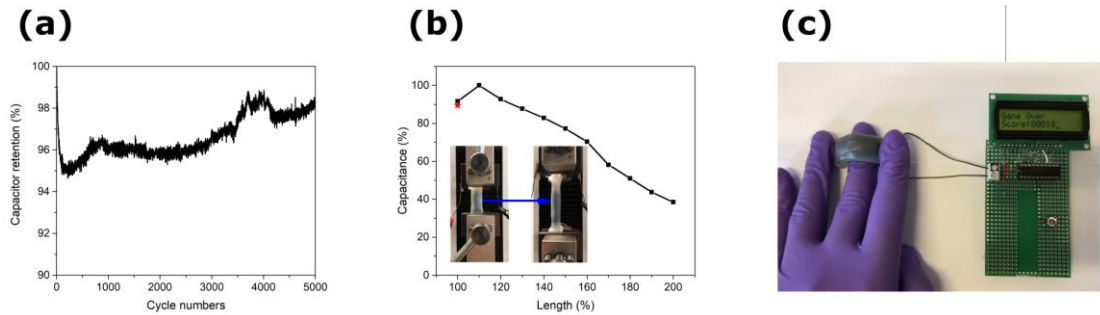


Figure 4-24: (a) Measured capacitor retention with full charge (2 V) and discharge (<50 mV) cycles. (b) Stretch test of the supercapacitor. Only 1.7% capacitance lost after 100 times cyclic test. (c) The

demonstration of a fully charged supercapacitor can work effectively to power up an electric circuit for a short period even though it has been bent.

From the above discussion, the proposed supercapacitor is not comparable to other carbon-based materials in capacity or charging speed. On the other hand, firmly bonded graphite flakes and elastic separator provides excellent stretchability. In Figure 4-24b, the supercapacitor was stretched up to 200% of its original length. The capacitance increased during the initial 10% stretch, then decreased linearly after that. There is still 43% capacitance remaining while the supercapacitor was doubled its original length. Additionally, only 1.7% capacitance lost (red star mark in Figure 4-24b) after 100 times stretching test. The promising stretchability results are compatible with previous reported [59,73,74]. To further demonstrate its stretchability, the supercapacitor was bent and connected to a nano power microcontroller (MSP430G2553) which was running a game. It is capable of supporting the microcontroller running a game for seconds, as demonstrated in Figure 4-24c.

4.3 Conclusion

We have applied the high conductive graphene loaded sponge to radar absorbers and supercapacitors in this paper. Shear exfoliation of graphene has been discussed. The best centrifuge speed which achieved the highest conductivity has been measured. Also, the structure of Gr&Gp/Ecoflex sponges is demonstrated with Raman and SEM characterization. Based on the measured permittivity and permeability of the sponges, two RAM structured radar absorbers have been designed. Both of them can absorb microwave energy effectively in the whole X-band, but the thicker one has better

absorption versus different incident angles, which is more suitable for conformable applications. Moreover, the soft supercapacitor was fabricated with outstanding stretchability. The capacitance retains 98.3% after 100 times of double-length stretch test. In conclusion, this work has demonstrated the potential of massive electronic applications that graphene-based materials can be applied, not limited to one specific area.

4.4 Method

4.4.1 Shear Mixing exfoliation of graphene.

NC was synthesized to assist the exfoliation of graphene. 200 mL 98% sulfuric acid (258105 from Sigma Aldrich) was carefully poured into 100 mL 70% nitric acid (438073 from Sigma Aldrich) with a temperature controller which keeps the temperature around 20 °C. After 5 mins agitation, shredded absorbent cotton fiber was added slowly into the mixture and temperature should be maintained lower than 30 °C. The reaction process lasts 4 hours. We washed the products a few times to remove acids and immersed them in 800 mL 1% hot sulphuric acid solution 10 mins to remove sulfate. The final step is to neutralize residual acids. NC was immersed into 800 mL 0.05% hot sodium carbonate (791768 from Sigma Aldrich) solution for 20 mins and then washed with DI water until PH is close to 7. This step is extremely critical because NC is not stable under acid environments. It would slowly decompose, which may cause fire or explosion. The final neutralized NC was dried completely in vacuum drier and then dissolved in ethyl acetate (270989 Sigma Aldrich) for safer storage.

In order to prepare graphene inks, 100 g natural graphite flakes with +100 mesh flake size (332461 from Sigma Aldrich) were poured into 1000 mL NC/ethyl acetate mixtures (NC concentrations are 5 mg/mL and 10 mg/mL respectively). A water-cooling system keeps the temperature at 20 °C. The modified shear mixer (L4R, Silverson) sheared each sample 4 hours with 8000 RPM. After that, samples were centrifuged three times, 20 mins each.

4.4.2 Preparing Gp&Gr loaded conductive sponge.

In order to prepare the conductive sponge, salt (S9888) from Sigma Aldrich was sieved between 40 (0.42 mm) and 70 (0.21 mm) mesh. Sieved salt was poured into large beakers which contain 2000 RPM centrifuged Gp&Gr mixture. Then, the mixed slurry was heated on a hot plate at 70 °C with mild agitation. This step is to remove excessive ethyl acetate. After that, the semi-solid slurry was poured into sponge mold (more details about the mold can be found in supplementary information). Afterward, the mold was heated in an oven with nitrogen protection. In this step, ethyl acetate and NC were removed sequentially from the mold but with different temperature ramping rates. A high temperature ramping rate would speed up the decomposition process of NC which is really dangerous. While the mold was completely cooled down, Ecoflex 00-50 was mixed and inhaled into the mold via vacuum and salt can be dissolved by water after the cross-linking of Ecoflex. We left the final product in 25 L hot water (80 °C) and changed the water frequently until silver nitrate cannot detect the existence of Cl⁻. In the final, the sponge was placed in an oven to evaporate all moisture.

4.4.3 Atomic force microscopy

Atomic force microscopy imaging of the shear mixed product was measured with Bruker Dimension Fast Scan in peak force mode. 100 μL of 2000 RPM centrifuged Gp&Gr mixture was spin-coated on an O_2 plasma cleaned SiO_2/Si substrate. Until dried, the sample was heated in nitrogen protected oven 5h at 400 $^\circ\text{C}$ to remove NC. After that, the sample was washed by acetone, distilled water and isopropyl alcohol sequentially.

4.4.4 Scanning electron microscopy

Zeiss Ultra 55 was used for scanning electron microscope measurements. The field emission gun is 5 KV. For the cross-section measurement, the sponge samples were soaked in liquid nitrogen and cut by a scalpel.

4.4.5 Raman

Raman spectra were acquired with Horiba Xplora Plus. The single and mapping results were measured under $\times 50$ objective, with an incident power of 5 mW. The wavelength is 532 nm

4.4.6 TGA and DSC

The Gp&Gr mixtures with different centrifuged speeds were completely dried in an oven for 12 hr at 80 $^\circ\text{C}$. 0.1g of each dried sample was placed in a platinum boat and analyzed under nitrogen protection. Temperature ramping rate is 5 $^\circ\text{C}/\text{min}$.

References

- [1] Jia J, Sun X, Lin X, Shen X, Mai Y-W, Kim J-K. Exceptional electrical conductivity and fracture resistance of 3D interconnected graphene foam/epoxy composites. *ACS Nano* 2014;8:5774–83.
- [2] Boland CS, Khan U, Ryan G, Barwich S, Charifou R, Harvey A, et al. Sensitive electromechanical sensors using viscoelastic graphene-polymer nanocomposites. *Science* (80-) 2016;354:1257–60.
- [3] Li M, Gao C, Hu H, Zhao Z. Electrical conductivity of thermally reduced graphene oxide/polymer composites with a segregated structure. *Carbon N Y* 2013;65:371–3.
- [4] Dong B, Liu C, Zhang L, Wu Y. Preparation, fracture, and fatigue of exfoliated graphene oxide/natural rubber composites. *Rsc Adv* 2015;5:17140–8.
- [5] Yang Z, Jin L, Lu G, Xiao Q, Zhang Y, Jing L, et al. Sponge-templated preparation of high surface area graphene with ultrahigh capacitive deionization performance. *Adv Funct Mater* 2014;24:3917–25.
- [6] Li Y, Samad YA, Polychronopoulou K, Alhassan SM, Liao K. Highly electrically conductive nanocomposites based on polymerinfused graphene sponges. *Sci Rep* 2014;4:4652.
- [7] Song SH, Park KH, Kim BH, Choi YW, Jun GH, Lee DJ, et al. Enhanced thermal conductivity of epoxy–graphene composites by using non-oxidized graphene flakes with non-covalent functionalization. *Adv Mater* 2013;25:732–7.
- [8] Xing L-B, Xi K, Li Q, Su Z, Lai C, Zhao X, et al. Nitrogen, sulfur-codoped graphene sponge as electroactive carbon interlayer for high-energy and-power lithium–sulfur batteries. *J Power Sources* 2016;303:22–8.
- [9] Yao H, Ge J, Wang C, Wang X, Hu W, Zheng Z, et al. A flexible and highly pressure-sensitive graphene–polyurethane sponge based on fractured microstructure design. *Adv Mater* 2013;25:6692–8.
- [10] Nguyen DD, Tai N-H, Lee S-B, Kuo W-S. Superhydrophobic and superoleophilic properties of graphene-based sponges fabricated using a facile dip coating method. *Energy Environ Sci* 2012;5:7908–12.
- [11] Lin C, Niu C, Xu X, Li K, Cai Z, Zhang Y, et al. A facile synthesis of three dimensional graphene sponge composited with sulfur nanoparticles for flexible Li–S cathodes. *Phys Chem Chem Phys* 2016;18:22146–53.
- [12] Liu F, Seo TS. A controllable self-assembly method for large-scale synthesis of graphene sponges and free-standing graphene films. *Adv Funct Mater* 2010;20:1930–6.
- [13] Chabot V, Higgins D, Yu A, Xiao X, Chen Z, Zhang J. A review of graphene and graphene oxide sponge: material synthesis and applications to energy and the environment. *Energy Environ Sci* 2014;7:1564–96.
- [14] Dubal DP, Holze R, Gomez-Romero P. Development of hybrid materials based on sponge supported reduced graphene oxide and transition metal hydroxides for hybrid energy storage devices. *Sci Rep* 2014;4:7349.
- [15] Ye S, Zhang Q, Hu D, Feng J. Core–shell-like structured graphene aerogel encapsulating paraffin: shape-stable phase change material for thermal energy storage. *J Mater Chem A* 2015;3:4018–25.
- [16] Wang H, Yuan X, Zeng G, Wu Y, Liu Y, Jiang Q, et al. Three dimensional graphene based materials: Synthesis and applications from energy storage and conversion to electrochemical

- sensor and environmental remediation. *Adv Colloid Interface Sci* 2015;221:41–59.
- [17] Fang Q, Shen Y, Chen B. Synthesis, decoration and properties of three-dimensional graphene-based macrostructures: a review. *Chem Eng J* 2015;264:753–71.
- [18] Lee J-S, Ahn H-J, Yoon J-C, Jang J-H. Three-dimensional nano-foam of few-layer graphene grown by CVD for DSSC. *Phys Chem Chem Phys* 2012;14:7938–43.
- [19] Hu G, Xu C, Sun Z, Wang S, Cheng H, Li F, et al. 3D Graphene-Foam–Reduced-Graphene-Oxide Hybrid Nested Hierarchical Networks for High-Performance Li–S Batteries. *Adv Mater* 2016;28:1603–9.
- [20] Cong H-P, Ren X-C, Wang P, Yu S-H. Macroscopic multifunctional graphene-based hydrogels and aerogels by a metal ion induced self-assembly process. *ACS Nano* 2012;6:2693–703.
- [21] Khan S, Lorenzelli L, Dahiya RS. Technologies for printing sensors and electronics over large flexible substrates: a review. *IEEE Sens J* 2014;15:3164–85.
- [22] Tobjörk D, Österbacka R. Paper electronics. *Adv Mater* 2011;23:1935–61.
- [23] Leenen MAM, Arning V, Thiem H, Steiger J, Anselmann R. Printable electronics: Flexibility for the future. *Phys Status Solidi* 2009;206:588–97.
- [24] Krebs FC. Fabrication and processing of polymer solar cells: A review of printing and coating techniques. *Sol Energy Mater Sol Cells* 2009;93:394–412.
- [25] Choi M-C, Kim Y, Ha C-S. Polymers for flexible displays: From material selection to device applications. *Prog Polym Sci* 2008;33:581–630.
- [26] Novoselov KS, Geim AK, Morozov S V, Jiang D, Zhang Y, Dubonos S V, et al. Electric field effect in atomically thin carbon films. *Science* (80-) 2004;306:666–9.
- [27] Becerril HA, Mao J, Liu Z, Stoltenberg RM, Bao Z, Chen Y. Evaluation of solution-processed reduced graphene oxide films as transparent conductors. *ACS Nano* 2008;2:463–70.
- [28] Hernandez Y, Nicolosi V, Lotya M, Blighe FM, Sun Z, De S, et al. High-yield production of graphene by liquid-phase exfoliation of graphite. *Nat Nanotechnol* 2008;3:563.
- [29] Ciesielski A, Samorì P. Graphene via sonication assisted liquid-phase exfoliation. *Chem Soc Rev* 2014;43:381–98.
- [30] Pan K, Fan Y, Leng T, Li J, Xin Z, Zhang J, et al. Sustainable production of highly conductive multilayer graphene ink for wireless connectivity and IoT applications. *Nat Commun* 2018;9:5197.
- [31] Paton KR, Varrla E, Backes C, Smith RJ, Khan U, O'Neill A, et al. Scalable production of large quantities of defect-free few-layer graphene by shear exfoliation in liquids. *Nat Mater* 2014;13:624.
- [32] Secor EB, Ahn BY, Gao TZ, Lewis JA, Hersam MC. Rapid and versatile photonic annealing of graphene inks for flexible printed electronics. *Adv Mater* 2015;27:6683–8.
- [33] Arapov K, Rubingh E, Abbel R, Laven J, de With G, Friedrich H. Conductive screen printing inks by gelation of graphene dispersions. *Adv Funct Mater* 2016;26:586–93.
- [34] Majee S, Song M, Zhang S-L, Zhang Z-B. Scalable inkjet printing of shear-exfoliated graphene transparent conductive films. *Carbon N Y* 2016;102:51–7.
- [35] Liu L, Shen Z, Yi M, Zhang X, Ma S. A green, rapid and size-controlled production of high-quality graphene sheets by hydrodynamic forces. *Rsc Adv* 2014;4:36464–70.
- [36] Yi M, Shen Z. A review on mechanical exfoliation for the scalable production of graphene. *J Mater Chem A* 2015;3:11700–15.
- [37] Secor EB, Gao TZ, Islam AE, Rao R, Wallace SG, Zhu J, et al. Enhanced conductivity, adhesion,

- and environmental stability of printed graphene inks with nitrocellulose. *Chem Mater* 2017;29:2332–40.
- [38] Geim AK, Novoselov KS. The rise of graphene. *Nanosci. Technol. A Collect. Rev. from Nat. Journals, World Scientific*; 2010, p. 11–9.
- [39] Fang X-Y, Yu X-X, Zheng H-M, Jin H-B, Wang L, Cao M-S. Temperature-and thickness-dependent electrical conductivity of few-layer graphene and graphene nanosheets. *Phys Lett A* 2015;379:2245–51.
- [40] Donnet J-B. Carbon black: science and technology. CRC Press; 1993.
- [41] Luo Q, Ren T, Shen H, Zhang J, Liang D. The thermal properties of nitrocellulose: from thermal decomposition to thermal explosion. *Combust Sci Technol* 2018;190:579–90.
- [42] Howell NK, Arteaga G, Nakai S, Li-Chan ECY. Raman spectral analysis in the C–H stretching region of proteins and amino acids for investigation of hydrophobic interactions. *J Agric Food Chem* 1999;47:924–33.
- [43] Wunder SL, Bell MI, Zerbi G. Band broadening of CH₂ vibrations in the Raman spectra of polymethylene chains. *J Chem Phys* 1986;85:3827–39.
- [44] Baker-Jarvis J, Geyer RG, Grosvenor CA, Holloway CL, Janezic MD, Johk RT, et al. Measuring the permittivity and permeability of lossy materials: Solids, liquids, metals, building materials, and negative-index materials. 2005.
- [45] Nicolson AM, Ross GF. Measurement of the intrinsic properties of materials by time-domain techniques. *IEEE Trans Instrum Meas* 1970;19:377–82.
- [46] Hotta M, Hayashi M, Lanagan MT, Agrawal DK, Nagata K. Complex permittivity of graphite, carbon black and coal powders in the ranges of X-band frequencies (8.2 to 12.4 GHz) and between 1 and 10 GHz. *ISIJ Int* 2011;51:1766–72.
- [47] Chen L-F, Ong CK, Neo CP, Varadan V V, Varadan VK. Microwave electronics: measurement and materials characterization. John Wiley & Sons; 2004.
- [48] Micheli D, Apollo C, Pastore R, Marchetti M. X-Band microwave characterization of carbon-based nanocomposite material, absorption capability comparison and RAS design simulation. *Compos Sci Technol* 2010;70:400–9.
- [49] Huang X, Pan K, Hu Z. Experimental demonstration of printed graphene nano-flakes enabled flexible and conformable wideband radar absorbers. *Sci Rep* 2016;6:38197.
- [50] Simon P, Gogotsi Y, Dunn B. Where do batteries end and supercapacitors begin? *Science* (80-) 2014;343:1210–1.
- [51] Kim TY, Lee HW, Stoller M, Dreyer DR, Bielawski CW, Ruoff RS, et al. High-performance supercapacitors based on poly (ionic liquid)-modified graphene electrodes. *ACS Nano* 2010;5:436–42.
- [52] Samal R, Dash B, Sarangi C, Sanjay K, Subbaiah T, Senanayake G, et al. Influence of synthesis temperature on the growth and surface morphology of Co₃O₄ nanocubes for supercapacitor applications. *Nanomaterials* 2017;7:356.
- [53] Lin J-H, Shi B-W, Chen Z-C. High-performance asymmetric supercapacitors based on the surfactant/ionic liquid complex intercalated reduced graphene oxide composites. *Appl Sci* 2018;8:484.
- [54] Yoon S, Lee J, Hyeon T, Oh SM. Electric double-layer capacitor performance of a new mesoporous carbon. *J Electrochem Soc* 2000;147:2507–12.
- [55] Du M, Yang T, Ma S, Zhao C, Jiao K. Ionic liquid-functionalized graphene as modifier for

- electrochemical and electrocatalytic improvement: comparison of different carbon electrodes. *Anal Chim Acta* 2011;690:169–74.
- [56] Ren J, Ren R-P, Lv Y-K. Stretchable all-solid-state supercapacitors based on highly conductive polypyrrole-coated graphene foam. *Chem Eng J* 2018;349:111–8.
- [57] Zhao D, Wang Y, Zhang Y. High-performance Li-ion batteries and supercapacitors based on prospective 1-D nanomaterials. *Nano-Micro Lett* 2011;3:62–71.
- [58] Wang K, Zhao N, Lei S, Yan R, Tian X, Wang J, et al. Promising biomass-based activated carbons derived from willow catkins for high performance supercapacitors. *Electrochim Acta* 2015;166:1–11.
- [59] Zhang Z, Wang L, Li Y, Wang Y, Zhang J, Guan G, et al. Nitrogen-Doped Core-Sheath Carbon Nanotube Array for Highly Stretchable Supercapacitor. *Adv Energy Mater* 2017;7:1601814.
- [60] Xia T, Zhang X, Zhao J, Li Q, Ao C, Hu R, et al. Flexible and conductive carbonized cotton fabrics coupled with a nanostructured Ni (OH)₂ coating for high performance aqueous symmetric supercapacitors. *ACS Sustain Chem Eng* 2019;7:5231–9.
- [61] Zhang Y, Liu X, Wang S, Li L, Dou S. Bio-Nanotechnology in High-Performance Supercapacitors. *Adv Energy Mater* 2017;7.
- [62] Mishra RK, Choi GJ, Sohn Y, Lee SH, Gwag JS. Reduced Graphene Oxide Based Supercapacitors: Study of Self-Discharge Mechanisms, Leakage Current and Stability via Voltage Holding Tests. *Mater Lett* 2019.
- [63] Sun G, An J, Chua CK, Pang H, Zhang J, Chen P. Layer-by-layer printing of laminated graphene-based interdigitated microelectrodes for flexible planar micro-supercapacitors. *Electrochem Commun* 2015;51:33–6.
- [64] Lehtimäki S, Railanmaa A, Keskinen J, Kujala M, Tuukkanen S, Lupo D. Performance, stability and operation voltage optimization of screen-printed aqueous supercapacitors. *Sci Rep* 2017;7:46001.
- [65] Sevilla M, Ferrero GA, Fuertes AB. Graphene-cellulose tissue composites for high power supercapacitors. *Energy Storage Mater* 2016;5:33–42.
- [66] Stoller MD, Ruoff RS. Best practice methods for determining an electrode material's performance for ultracapacitors. *Energy Environ Sci* 2010;3:1294–301.
- [67] Banda H, Daffos B, Périé S, Chenavier Y, Dubois L, Aradilla D, et al. Ion sieving effects in chemically tuned pillared graphene materials for electrochemical capacitors. *Chem Mater* 2018;30:3040–7.
- [68] Li Z, Gadipelli S, Yang Y, He G, Guo J, Li J, et al. Exceptional supercapacitor performance from optimized oxidation of graphene-oxide. *Energy Storage Mater* 2019;17:12–21.
- [69] Liu Y, Zhang Y, Ma G, Wang Z, Liu K, Liu H. Ethylene glycol reduced graphene oxide/polypyrrole composite for supercapacitor. *Electrochim Acta* 2013;88:519–25.
- [70] Zhang LL, Zhao S, Tian XN, Zhao XS. Layered graphene oxide nanostructures with sandwiched conducting polymers as supercapacitor electrodes. *Langmuir* 2010;26:17624–8.
- [71] Shayeh JS, Ehsani A, Ganjali MR, Norouzi P, Jaleh B. Conductive polymer/reduced graphene oxide/Au nano particles as efficient composite materials in electrochemical supercapacitors. *Appl Surf Sci* 2015;353:594–9.
- [72] Zhang J, Zhao XS. Conducting polymers directly coated on reduced graphene oxide sheets as high-performance supercapacitor electrodes. *J Phys Chem C* 2012;116:5420–6.
- [73] Yu C, Masarapu C, Rong J, Wei B, Jiang H. Stretchable supercapacitors based on buckled single-

- walled carbon-nanotube macrofilms. *Adv Mater* 2009;21:4793–7.
- [74] Lamberti A, Clerici F, Fontana M, Scaltrito L. A Highly Stretchable Supercapacitor Using Laser-Induced Graphene Electrodes onto Elastomeric Substrate. *Adv Energy Mater* 2016;6:1600050.

4.5 Supplementary information

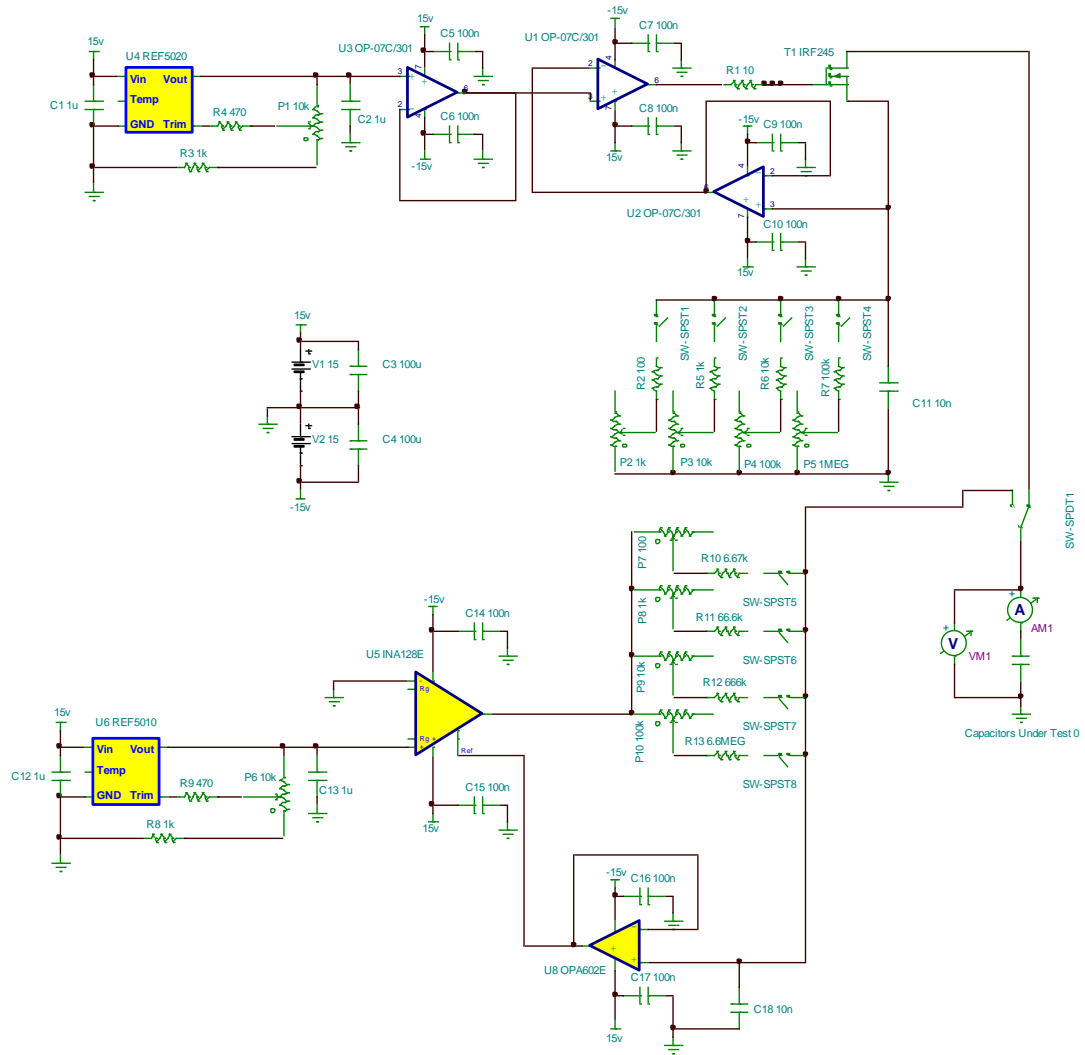


Figure 4-25: Electronic circuit schematic for supercapacitors' GCD measurement.

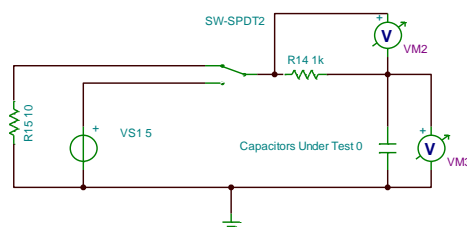


Figure 4-26: Circuit diagram for ESR and leakage current tests.

5 Controlled reduction of graphene oxide laminate and its applications for ultra-wideband microwave absorption

Kewen Pan, Ting Leng, Jun Song, Chengyu Ji, Jiawei Zhang, Jiashen Li, Kostya S.

Novoselov & Zhirun Hu

Carbon Volume 160, 30 April 2020, Pages 307-316.

My contributions:

I did all material characterization except XPS analysis. I have designed and fabricated the proposed absorber, performed all measurements, analysed the data, and prepared all the graphs.

Abstract

In this work, we first screen print thin graphene oxide laminates on Kapton film and then chemically reduce to reduced graphene oxide (rGO) with desired sheet resistance by controlling printing cycles and reduction time. The thin rGO laminates have a wide range of conductivity from $2.8 \text{ S}\cdot\text{m}^{-1}$ up to $1.3 \times 10^4 \text{ S}\cdot\text{m}^{-1}$, exhibiting excellent consistency of electric performance even after 50000 times bending. Commonly used rGO reduction level characterization methods have been compared with the proposed sheet resistance method. It is revealed that the later has high variation with reduction time, providing a new method for reduction monitoring of rGO. Benefiting from the tunability of its sheet resistance, the rGO laminate not only can be used in flexible electronic circuits as conductors or resistors, but also highly efficient to absorb microwave radiations with proper design. Therefore, a printed, three-layer, Jaumann structured microwave absorber has been designed, fabricated and characterised. The maximum microwave absorption rate is up to 99.9997% where the -10 dB fractional bandwidth is more than 153%, which covers L, S and C bands. Moreover, the fabricated absorber can absorb efficiently even when the incident angle is as low as 20° . Full design procedure, simulation and measurement results are presented.

5.1 Introduction

With the fast development of 5G [1] and IoT [2] technologies, the protection for electromagnetic (EM) wave radiation is becoming of significance nowadays. Not only considering the higher EM wave density may have side effects to human, but

commercial wireless communication bands adding with newly developed multiplexing technology (e.g. MIMO) causes strong EM wave interference, which is difficult to be eliminated [3]. One most commonly used EM radiation protection technique is EM shielding, which normally uses metal based [4,5] or carbon based [6–9] films/composites to cover the objects which can reflect the EM waves. Recently, studies on EM shielding functional devices using rGO and rGO composites have been reported, such as rGO composite films [10,11], rGO/SiO₂ [12], rGO coating on foams [13], rGO/carbon fibres [9, 13], rGO/epoxy composite [15], rGO compressed films [16] and doped rGO [17,18]. rGO hybrid structure with magnetic materials have also been investigated [19]. The basic motivation to use graphene based materials for EM shielding is because graphene can have high carrier mobility as well as high electrical conductivity [20]. However, rGO is not graphene [21,22], and the sp^2 structure of graphene is considerably degraded during chemical exfoliation/reduction process and its π - π stacking becomes less stable [8]. The highest reported mobility of rGO is only 320 cm²V⁻¹s⁻¹ [23], resulting in a much lower electrical conductivity. This is the root cause why commercial aluminium foil provides much better shielding effectiveness (SE) than any rGO based shielding materials. In order to achieve better SE, thicker samples or doped rGO films have been investigated. They however still performed much inferior to their metal counterpart.

While EM shielding is very useful to protect human or electronic circuits from unwanted radiation, the reflected wave can act as a new radiating source to promote propagation of EM wave which can cause unwanted effects on human and operation of

electronic equipment that are not protected nearby, i.e. electromagnetic interference (EMI) [24]. In order to alleviate reflected waves, EM absorbing technique has been developed. Different to EM shielding, EM absorbing is able to either convert the incident EM energy to heat [25] or scatter it [26] to various directions by whittling down the EM radiation to have smaller radar cross section (RCS). Decades ago, Dallenbach [27] and Salisbury absorbers [28] were invented for RCS reduction. Jaumann absorber was invented afterwards to provide much wider absorption bandwidth [29]. In the last decades, frequency selective surface (FSS) and metamaterial based ultra-wideband, flexible and low profile absorbers have been reported [30–33].

Lightweight CVD graphene millimetre-wave absorbers with 28% fractional bandwidth at 140 GHz was first reported [34]. After that, multilayer, large area CVD graphene absorber at microwave band [25,35] and electrically tunable CVD graphene-electrolyte structured absorber [36], tunable absorber based on patterned graphene metasurface were also demonstrated [37]. However, the difficulties of the wet transform process (from Cu/Ni to electrolyte or dielectric materials), the costs of large area CVD graphene sheets and varied surface resistance due to unwanted doping during each process have hindered them from low cost, large-scale applications. On the other hand, printed graphene absorbers [30] have been proved to be a promising alternative considering lightweight, low cost, flexibility and wide ranges of applications. However, precisely controlling the sheet resistance of a graphene laminate is still very challenging. Most reported works related to graphene inks have been focusing on enhancing the conductivity via compressing [38–42], photonic annealing [43], etc. In EM wave

absorber design, the absorbance really depends on the matching conditions between the free space and the absorber. The conductivity is of less importance. The higher electric conductivity does not guarantee better absorbance. The surface conductivity of rGO, on the other hand, can be controlled with high precision. Therefore, rGO can prove to be a solution, not only due to its near 100% yield, but also its surface conductivity can be precisely controlled during chemical reduction process which provides wideband and better absorbance. However, rGO based EM wave absorber has been barely reported so far.

In this work, we report a rGO microwave absorber on Kapton [44] film, which covers L, S and C bands. Detailed design and fabrication procedures of the microwave rGO absorber are presented. In order to match the free space characteristic impedance to the absorber for wideband absorption, multi-layered rGO structures have been proposed and the surface resistivity of each layer has been carefully designed and realized. In doing so, we have demonstrated a novel approach to accurately control the surface resistance of rGO laminates. The critical path to the success of rGO wideband absorber is the control of the sheet resistance. The conventional approach to make rGO solution from reduction of graphene oxide (GO) solution is not suitable for precise control of the sheet resistance. In addition, the aggregating issue of rGO flakes are difficult to be eliminated. Instead, GO was first printed on the Kapton film and the reduction process was then followed in this work. It is revealed that the reduction speed of the printed GO laminate is much slower than the reduction of GO solution [45], which enables the control of the sheet resistance much easier and accurate. In the

meantime, the sheet resistance change of rGO laminates during reduction process is wider than any existing reduction monitoring approaches, potentially very useful as an indicator to monitor the relative reduction level of rGO.

5.2 Experimental detail

5.2.1 Material preparation

The expended graphite flakes were purchased from Qingdao Huatai Sealing and Lubrication Co. L-ascorbic acid (255564-100G) was from Sigma-Aldrich. Potassium permanganate was obtained from Alfa Aesar. Sulfuric acid (>95%), hydrochloric acid (32%) and Hydrogen peroxide (>30%) are all from Fisher Scientific.

We used the well-known improved Hummers method to produce GO from graphite. First, 5 g expanded graphite flakes were washed by deionized water twice and dried in oven. The dried powder was poured into 1000 mL concentrated sulfuric acid under mechanical stirring. A temperature controller (JULABO F250) was connected to control temperature around 20 °C. After 30 minutes stirring, 50 g KMnO_4 was slowly added to the mixture where temperature of the mixture was lower than 50 °C. The mixture turned to green because of MnO_3^+ . After 24 hr reaction, 1000 mL deionized water and 250 mL H_2O_2 were added (temperature <50 °C). Until the temperature dropped to 20 °C, 1000 mL 3% HCl solution was added to the golden colour mixture, which removed solid MnO_2 particles. The mixture was stirred for another 24 hr and then centrifuged at 8000 rpm until $\text{PH} \approx 6$. Finally, the GO solution was centrifuged at low speed (500 rpm) for 5 min, repeated three times to remove graphite and impurity

particles.

5.2.2 Preparation of rGO laminates

The GO solution was further concentrated to 25 mg/mL via vacuum rotatory evaporator (Buchi R-114 Rotavap evaporator) with the temperature of 50 °C. The semi-automatic screen-printing machine (YICAI Ltd) was used to print the GO on 50 µm thick Kapton films (RS stock number: 536-3952) which had been pre-cleaned by acetone, deionized water and isopropyl alcohol. The screen is of 250 µm pole size to allow the penetration of large GO flakes. Before printing, the GO solution was mechanically agitated for 5 min and bubbles inside the ink were removed after a short period of vacuum treatment. Before the next printing pass, samples were completely dried in vacuum oven. To acquire different thickness and sheet resistance, we have printed 6 different samples from 1 layer to 6 layers which were labelled as “1” to “6”. In order to reduce GO, we first prepared 1 L fresh L-AA solution (4 mg/mL) and heated to 65 °C, then the printed GO films were immersed into the solution. Samples were extracted after 1, 3, 5, 9, 15, 27 hr reaction.

5.2.3 Characterization

AFM image of GO sheets was measured with a Bruker Dimension Icon in peak-force mode. Scan rate is 0.2 Hz. The concentration of GO solution was diluted to 0.1 mg mL⁻¹ and 100 µL ink sample was spin-coated (3000 rpm, 1 min) on a pre-cleaned SiO₂/Si substrate. For Raman measurement, GO laminates were printed and reduced on

pre-cleaned SiO₂/Si substrate where the processes are exactly the same as that on Kapton film. Raman spectra were acquired with a Renishaw System 1000 Raman Spectrometer at ×50 objective, with an incident power of 2.3 mW. The system has within 1.5 cm⁻¹ spectral resolution at 514 nm. XRD, XPS and TGA use the same Raman samples. For FTIR measurement, potassium bromide (KBr) was annealed in oven at 100 °C for 24 hr to ensure dryness. Samples and KBr were mixed with 1:50 mass ratio and then grounded in an agate mortar. FTIR data were recorded by a Fourier transform infrared spectrometer (Nicolet 5700). For SEM characterization, Zeiss Ultra 100 was used with 20 µm aperture size. The field emission gun is 5 KV. For the cross-section measurement, samples were immersed in liquid nitrogen and cut by a scalpel.

The sheet resistance was measured by 4-point probe station (Jandel, RM3000) and semiconductor characterization system (Keithley, 4200C). Sample thickness was measured by SEM. For absorber measurement, two double-ridged guide antennas (Model 3115, ETS-Lindgren) from 0.75 GHz to 18 GHz were direct connected to a calibrated VNA (Fieldfox N9918A, Keysight).

We built a bending tester with LEGO bricks, as shown in Figure 5.2-3e. Four wires resistance measurement method was used to avoid cable and connector resistance. The bending tester was controlled by custom Labview program and NI-DAQ (USB-6211), resistance data was measured by digital multimeter (NI USB-4065) which operated in 6.5 digits resolution, 100 kΩ range.

5.3 Results and discussion

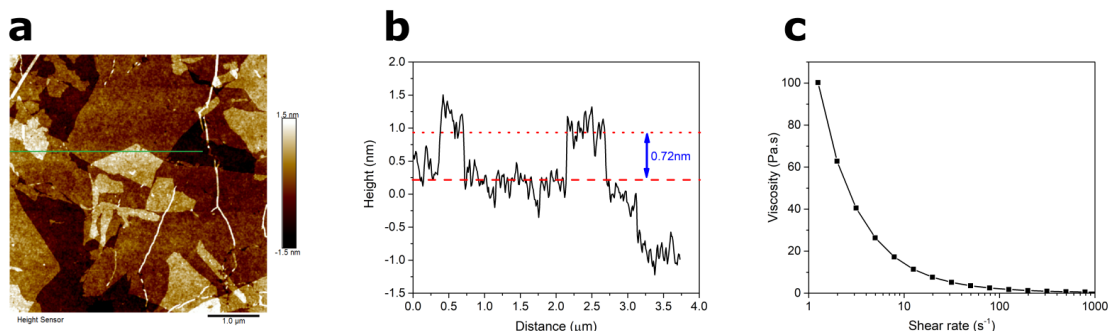


Figure 5-1: (a) AFM image of GO sheets on silicon dioxide substrate; scale bar is 1 μm . (b) Height of GO sheets in AFM image (green line). (c) Measured viscosity of the screen printable GO ink with the concentration of 25 mg mL^{-1} .

Figure 5-1a shows the surface topography of GO sheets. Large, flat GO sheets indicate no aggregation in water [45]. Cracked surface were formed due to the vaporization of water [46]. Comparing with mechanical exfoliated graphene sheet [38], the rugged surface of GO sheets is the evidence of successful oxidation because defects and oxygen functional groups are attached [47]. The surface height variation of GO sheets is approximately 1 nm. Average GO sheet thickness were calculated from overlapped GO sheets, which is 0.72 nm, shown in Figure 5-1b. This result confirms the existence of single layer, moderate oxidized GO sheets [48–50].

Once the GO water dispersion was concentrated to 25 mg/mL (see 2.2), the GO solution turned into dark brown paste and was ready for screen printing. The viscosity was measured and shown in Figure 5-1c. The shear thinning property is capable to achieve appropriate screen printing viscosity at a high shear rate. In this work, we choose the shear rate of 200 S^{-1} where corresponded viscosity is 1.7 $\text{Pa}\cdot\text{S}$ (1~2.5 $\text{Pa}\cdot\text{S}$ is suitable for high speed screen printing [51]).

The GO films (GO laminate + kapton) were soaked in L-AA solution for reduction (see Methods). Reduction progress was characterized by choosing different samples which were reduced with 1, 3, 5, 9, 15 and 27 hr.

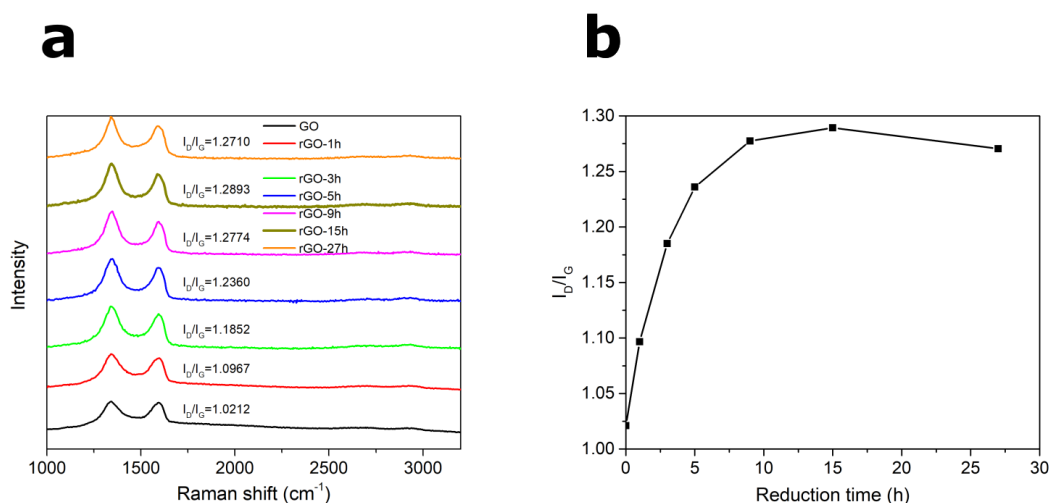


Figure 5-2: (a) Raman spectra of rGO laminate with different reduction times (0 hr, 1 hr, 3 hr, 5 hr, 9 hr, 15 hr and 27 hr). (b) I_D/I_G intensity ratio of Raman spectra in (a).

Raman spectroscopy was used to characterize the reduction level of GO. The two prominent peaks in Figure 5-2a are located at 1340 cm⁻¹ and 1594 cm⁻¹, which are D-band (plane defects of GO) and G-band (first order Raman scattering of graphite structure of GO). Two weak peaks can be found in 2500 cm⁻¹ to 3000 cm⁻¹ region, one is flat G' band at 2680 cm⁻¹, the other one is called D+G mode [52], which again confirmed significant amount of defects in GO. The intensity ratio of D-band and G-band is plotted in Figure 5-2b to estimate the disorder level of rGO [45]. The ratio increases with the reduction time except the last point (27 hr). This inversed phenomenon was probably caused by the formation of the small size of *sp*² structure and the defects of graphene which was formed by removing oxygen functional groups [45,53]. The logarithmically varying relationship indicates that most of the reduction process

finished in the first 5 hr (22% change of I_D/I_G) whereas the following 22 hr reduction only changes 5%. In other studies, the similar relation can be observed but with a much shorter reduction time [45,54]. This is because L-AA molecules have to penetrate into GO sheets before starting reaction with GO.

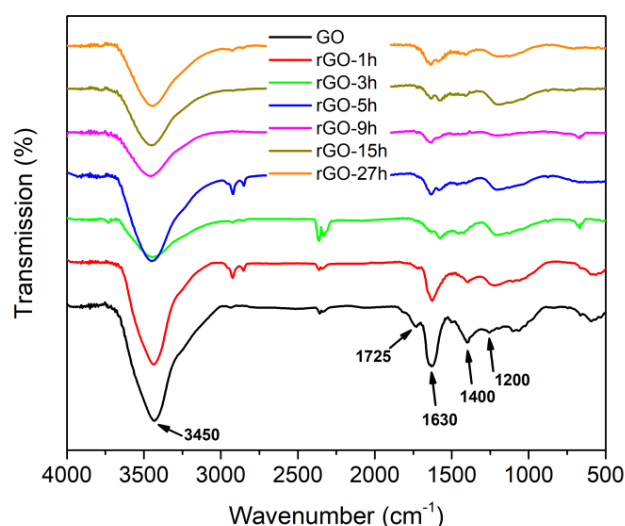


Figure 5-3: FTIR characterization of rGO laminates with different reduction times.

Figure 5-3 shows the Fourier-transform Infrared Spectroscopy (FTIR) spectra of GO and rGO with different reduction times. For GO (black line), all peaks can be clearly observed. First, the broadband water O-H stretching vibrations which centred at 3450 cm^{-1} are mainly contributed by water molecules. A narrower and weak peak located at 1725 cm^{-1} is C=O stretching vibrations from carbonyl and carboxyl groups of GO [55]. It can be noticed that the peak is getting weaker after reduction, not detectable after 5 hr reduction process. The peak at 1630 cm^{-1} represents C=C stretching from non-oxidized graphite structure. The other important peak at 1400 cm^{-1} is –OH vibrations of hydroxyl groups from graphene. The last peak around 1200 cm^{-1} is attributed to C-O (epoxy) group vibration. From the 27 hr reduced graphene oxide, the

peaks located at 1400 cm^{-1} and 1200 cm^{-1} are still detectable, which confirms that the reduction process is not entirely complete [18]. Nevertheless, ascorbic acid has good effect to remove carbonyl and carboxyl groups on graphene oxide.

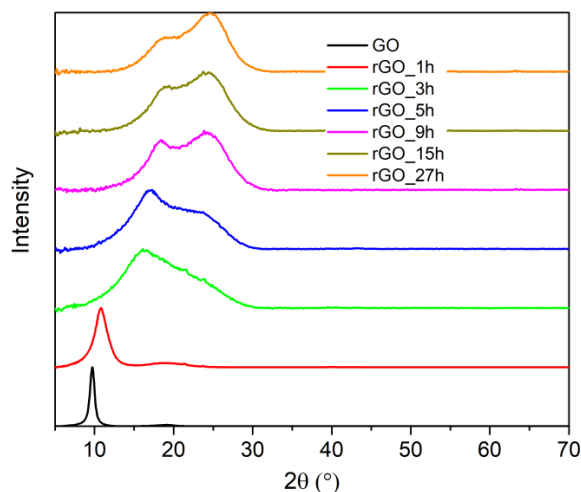


Figure 5-4: XRD spectra of rGO laminate with different reduction times.

The X-Ray Diffraction (XRD) patterns of GO and rGO as a function of reducing time are displayed in Figure 5-4. A sharp and intense peak centered at approximate 9.5° indicates the existence of GO for 0 hr of reducing time. With the increasing in reducing time from 1 hr to 3 hr, the peak has move towards higher diffraction angle and become broadening simultaneously, which demonstrates that the crystal quality has deteriorated because of the removal of oxygen functional groups and the decease of interlayer spacing. With reduction time increasing further, the peak of GO disappears gradually and the peak positioned at around 25° becomes predominant, which shows that C=C bonds have restored. The peak is still highly broad as the crystal structure of rGO has been destroyed. The calculated d-spacing for GO is 0.908 nm. It drops to 0.36 nm on average after 27 hr of reduction which is closed to graphite structure [56]. In general,

the XRD differences of rGO laminates are distinct when the reduction time is lower than 5 hr, but less distinguishable after 5 hr.

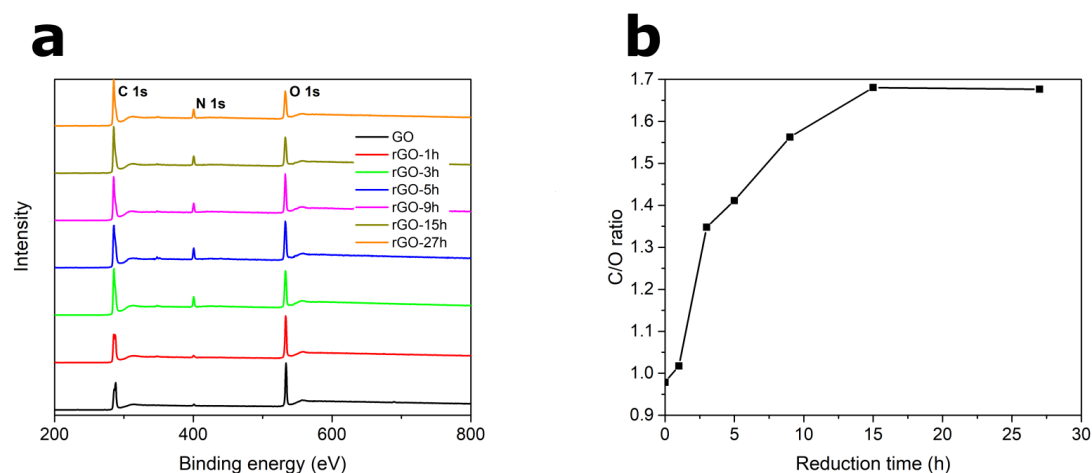


Figure 5-5: (a) Wide scan XPS spectra of rGO laminate with different reduction times. (b) The calculated carbon/oxygen ratio from XPS.

X-Ray Photo-electron Spectrometry (XPS) is an powerful tool to analysis the element surface content [57,58]. In Figure 5-5a, we have plotted XPS results of GO and rGO samples with different treatment time. The peaks of C_{1s}, N_{1s} (residue from the reaction between L-AA and Kapton film) and O_{1s} can be clearly observed, which again confirms the successful oxidation of graphite. To examine the reduction level of rGO, carbon to oxygen ratio (C/O ratio) has been studied and shown in Figure 5-5b. The low C/O ratio of GO represents the high oxidation level [18]. C/O ratio kept rising as reduction time increasing. The increasing rate of first 5 hr is fastest (removal of oxygen functional groups) whereas no obvious change can be seen after 15 hr, which can be interpreted that the L-AA reduction process for GO is almost finished in 15 hr.

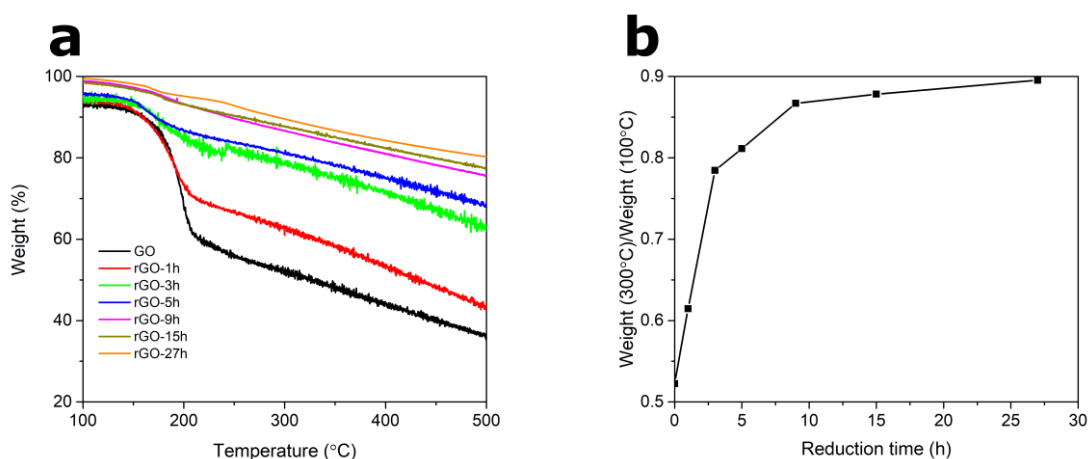


Figure 5-6: (a) TGA results of rGO laminate with different reduction times. The less weight loss at high temperature represents better reduction. (b) Weight ratio of GO and rGO laminates from TGA results at different temperatures (300°C and 100°C).

Thermo Gravimetric Analysis (TGA) results are plotted in Figure 5-6a, samples have different weight percentage at initial 100 °C. The 8 % variation between GO and rGO-27h is attributed to the evaporation of residual water and light thermal reduction [59,60]. In GO and some rGO samples, a significant weight drop occurs around 190 °C because of the decomposition of carboxyl and hydroxyl groups [45]. However, the samples after 9 hr reduction do not have obvious weight loss which indicates the removal process has almost completed. The further decompositions of H atoms bonded to the aromatic ring [61] and more stable function groups (10~15 %wt in each sample) occur mildly with temperature increasing while electrical properties remain [62]. The weight ratio (300 °C and 100 °C) can be used to compare the weight loss between samples and indicate the reduction level, as shown in Figure 5-6b. The GO sample has lost 48% weight whereas only 11% weight has dropped for the rGO after 27 hr reduction. It is worth noticed that the weight ratio has similar behaviour with C/O ratio in Figure 5-5b.

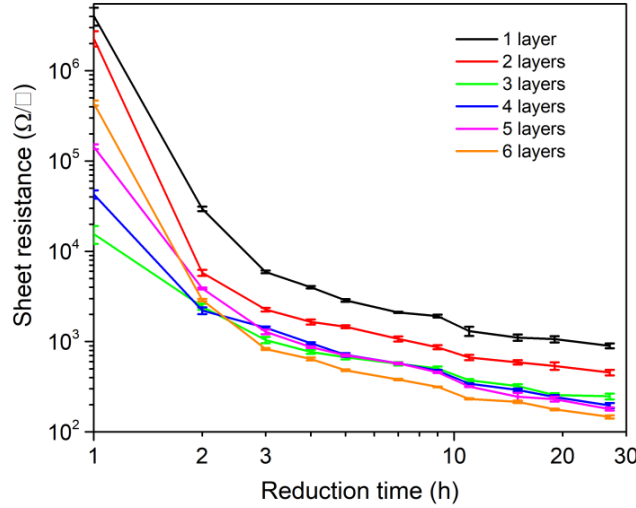


Figure 5-7: Sheet resistance measurement of rGO laminate (from 1 printed layer to 6 printed layers) with different reduction times.

The sheet resistance of the rGO laminates were measured using four point resistance measurement system and the results were shown in Figure 5-7. We printed different layers (1 layer to 6 layers) to obtain desired sheet resistance. 10 points on each sample were selected randomly for four point measurement. From the results, it can be seen that the reduction process produces a wide variation of sheet resistance. Thanks to the semi-automatic printer, the printing speed was constant, resulting in a promising uniform laminate. The variation of sheet resistance at all samples didn't exceed 15%. As it can be seen, the sheet resistance of all layers decreased over an order of magnitudes in the first three hours of reduction and much slower afterwards. The average thickness of 27 hr reduced samples from 1 layer to 6 layers are 86.4 nm, 231.35 nm, 453.2 nm, 625.3 nm, 879.8 nm and 1259 nm, respectively. The corresponded conductivity can be calculated as $1.29 \times 10^4 \text{ S} \cdot \text{m}^{-1}$, $0.95 \times 10^4 \text{ S} \cdot \text{m}^{-1}$, $0.89 \times 10^4 \text{ S} \cdot \text{m}^{-1}$, $0.81 \times 10^4 \text{ S} \cdot \text{m}^{-1}$, $0.63 \times 10^4 \text{ S} \cdot \text{m}^{-1}$ and $0.54 \times 10^4 \text{ S} \cdot \text{m}^{-1}$. Due to the fact that the reduction process is not uniform and the surface of rGO laminate exhibits the highest reduction,

it is not surprising that the samples' conductivities are same, but inversely proportional to thickness. In contrast, Raman and XPS can only characterize the surface reduction level. We further investigated the reduction level of rGO versus reduction time through the first order derivative of Raman [63], XRD, XPS [64], TGA [65] and sheet resistance (measured on the large samples printed on Kapton film), as depicted in Figure 5-8.

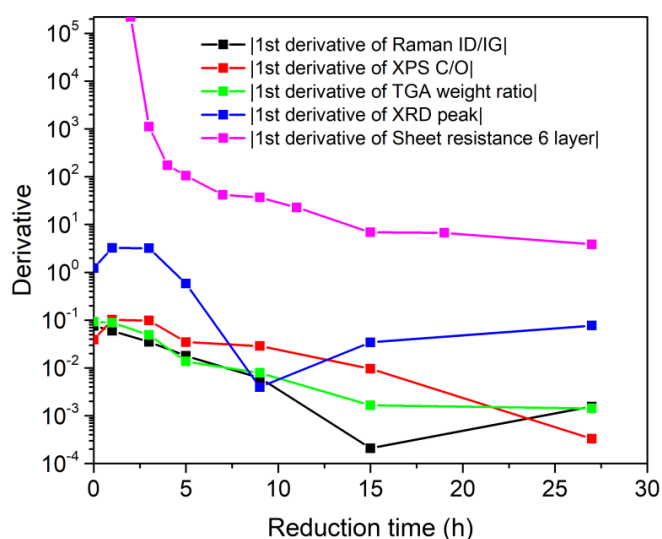


Figure 5-8: 1st derivative of Raman, XPS, XRD and sheet resistance results.

It can be seen that Raman I_D/I_G ratio shows the lowest variation to reduction time. The variation of TGA and XPS are in about the same order. XRD has about two-order higher variation than those of TGA and XPS in the first 5 hr. It can also be observed that the variations of all these characterization techniques are higher in the first few hours of reduction. This phenomenon is explainable because most reduction takes place in the first few hours. In this work, we have introduced sheet resistance for the first time to indicate the reduction level of rGO. Although temperature, different contents of oxygen functional groups and structure defects would affect sheet resistance and conductivity of rGO samples [66], the derivatives of the sheet resistance are at least two-orders

higher than that of XRD, revealing that the removal of oxygen functional groups and restoration of C=C bonds have resulted in a giant variation of the conductivity, especially in the first few hours. Therefore, we believe that sheet resistance can be potentially very useful to characterize the relative reduction level of rGO samples. There is no need of making extra samples on SiO₂/Si substrate. The sheet resistance can be measured directly on any substrates.

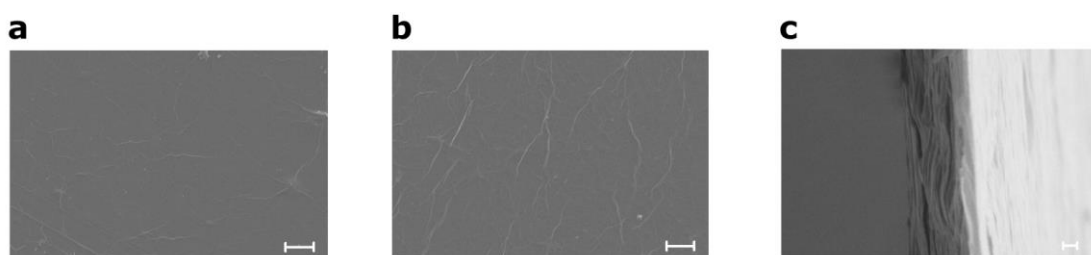


Figure 5-9: (a,b) SEM images of rGO laminates (1 printed layer (a), 6 printed layers (b)), scale bar is 10 μm . (c) SEM cross-sectional view of the rGO laminate with 3 printed layers and scale bar is 100 nm.

Morphological features of 27 hr reduced rGO laminate can be observed under SEM. Figure 5-9a shows the rGO surface with 1 printed layer. Few wrinkles can be observed on the surface, but no folded edges, indicating well re-stacked rGO sheets [67]. More details can be observed from TEM results in supplementary Figure 5-18. The SEM image of rGO laminate with 6 printed layers has more wrinkles on the surface, as shown in Figure 5-9b. More wrinkles will affect the flake stacks, resulting higher contact resistance. This presumably contributes to the aforementioned conductivity drop as the number of printed layer increases. The magnified lateral view in Figure 5-9c demonstrates that the rGO sheets (3 printed layers) are parallel stacked on the substrate (Kapton film).

For a microwave absorber, it would be desirable that the absorber can be flexible

to wrap curved metal components. Therefore, we have investigated the flexibility of the rGO laminate on Kapton film (6 printed layers). The measurement setup for the bending test is illustrated in Figure 5-10a.

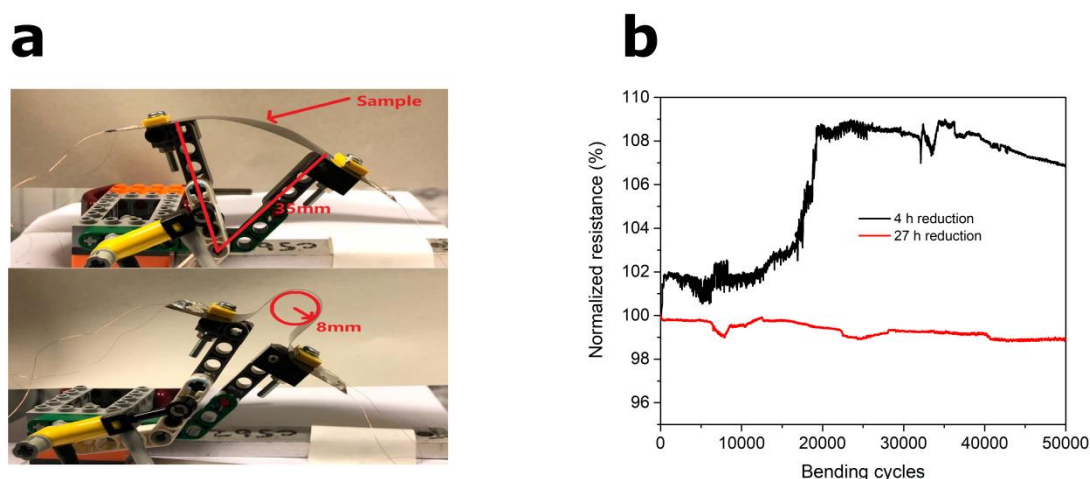


Figure 5-10: (a) Bending test setup (upper: initial state, lower: banded state). (b) Bending test results of the rGO laminate with 6 printed layers.

The system was constructed by LEGO bricks and driven by a pneumatic cylinder. Laminate under test was screw tightened on the top of arms and four thin copper wires were connected to four probe measurement system which eliminates the contact resistance between the wires and sample. At start, the radius of rGO-Kapton laminate was 35 mm. After bending, the radius dropped to 8 mm and bended angle is around 135° . The repeated process was executed 50000 times where the resistance variations of the 4 and 27 hr reduced rGO laminates were recorded, as shown in Figure 5-10b. It can be seen that the 27 hr reduced rGO laminate is very stable, only 1 % drop of its resistance after 50000 times bending. The resistance variation of 4 hr reduced laminate after 50000 times bending are less than 9 %. This is a highly desirable property for conformable and flexible applications, e.g. PDMS [68] and Ecoflex [69].

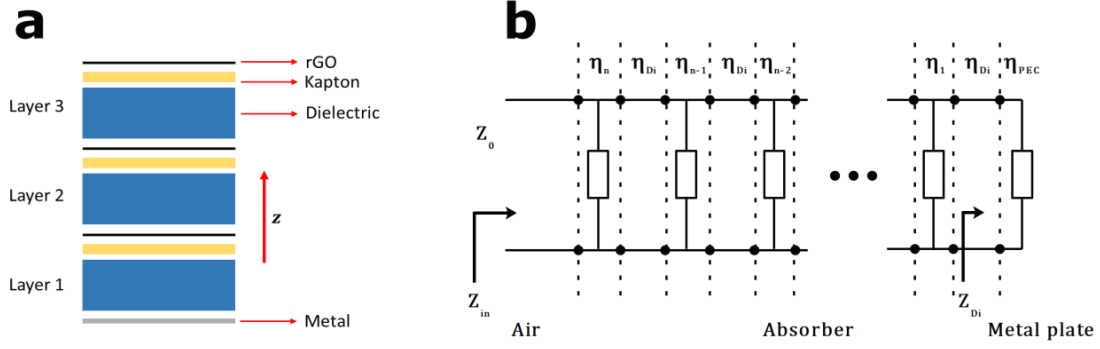


Figure 5-11: Absorber structure and fabrication (a) Cross-section illustration of the proposed three-layer microwave absorber. (b) Transmission line equivalent circuit model of the microwave absorber.

The structure of the proposed microwave absorber (Jaumann layers) is depicted in Figure 5-11a. The black materials on the top and between the gaps are printed rGO laminates. The supporting Kapton film is represented as yellow, the blue parts are dielectric substrate which can be light weight foams or flexible materials depending on applications. The grey line at bottom is metal plate. Microwave propagation direction is $-\vec{z}$. The incident microwave induces current and reflections at rGO laminates. These reflected waves are designed to cancel out each other and the current dissipates as heat.

To design the printed rGO microwave absorber, we start from the complex permittivity that can be expressed as the well-known formula:

$$\varepsilon_r = \varepsilon' - j\varepsilon'' \quad (5.1)$$

where ε' is the dielectric constant of rGO and ε'' represents the loss, mainly contributed by the displacement current on rGO surface. As the thickness of the rGO laminate is far thinner than its skin depth at microwave region, we can consider that the current density is uniform. Therefore, the imaginary part in (1) can be rewritten as:

$$\varepsilon'' = \frac{1}{2\pi f_0 \varepsilon_0 R_s t} \quad (5.2)$$

where f_0 is the frequency of the incident wave, ε_0 is dielectric constant of free space,

R_s is sheet resistance of the rGO laminate where t represents its thickness. The plane wave impedance of the rGO laminate can be written as [70]:

$$\eta_n = \sqrt{\frac{\mu_r \mu_0}{\epsilon' \epsilon_0 - j \frac{1}{2\pi f_0 R_{s,n} t}}} \quad (5.3)$$

rGO is not a ferromagnetic material, hence $\mu_r = 1$. The wave impedance here represents the characteristic impedance of the rGO laminates in the transmission line model (η_n) in Figure 5-11b. The goal of absorber design is to match the free space impedance and input impedance of the absorber at operational frequency band.

The rGO laminates were printed on Kapton films. In the design, the sheet resistance of rGO laminates, thickness and dielectric priorities of dielectric materials can be optimized to realize maximum absorption for a desired bandwidth. The input impedance of the first dielectric layer can be expressed as:

$$Z_{Di} = \eta_{Di} \frac{\eta_{PEC} + j\eta_{Di} \tan(\beta_{Di} L_{Di})}{\eta_{Di} + j\eta_{PEC} \tan(\beta_{Di} L_{Di})} \quad (5.4)$$

where L_{Di} is the thickness of the dielectric material and β_{Di} is its propagation constant. η_{PEC} is the wave impedance of the ground metal plate. For perfect conductor, $\eta_{PEC} = 0$. η_{Di} represents the wave impedance of the dielectric material (Kapton + dielectric). η_n can be calculated from (3).

Similarly, the input impedance Z_{in} of a n -layer rGO laminate can be given by:

$$Z_{in} = Z_n = \eta_n \frac{Z_{n-1} + j\eta_n \tan(\beta_n L_n)}{\eta_n + jZ_{n-1} \tan(\beta_n L_n)} \quad (5.5)$$

The propagation constant is:

$$\beta_n = 2\pi f_0 \sqrt{\mu_0 \epsilon_0} \sqrt{\mu_n \left(\epsilon'_n - j \frac{1}{2\pi f_0 R_{s,n} L_n \epsilon_0} \right)} \quad (5.6)$$

The rGO laminate loss, dielectric material absorption and multiple reflections have been all included in Z_n , the matching between free space and the absorber can be

evaluated by the reflection coefficient Γ :

$$\Gamma = \frac{Z_n - Z_0}{Z_n + Z_0} \quad (5.7)$$

where Z_0 is the free space characteristic impedance. Finally, the absorption A can be simply calculated as:

$$A = 1 - \Gamma^2 \quad (5.8)$$

In order to demonstrate that the equivalent circuit model method can be used to analyse the absorber, two different types of absorbers (broad band and narrowband) with the structure shown in Figure 5-11a were simulated using commercial software CST MWS [71].

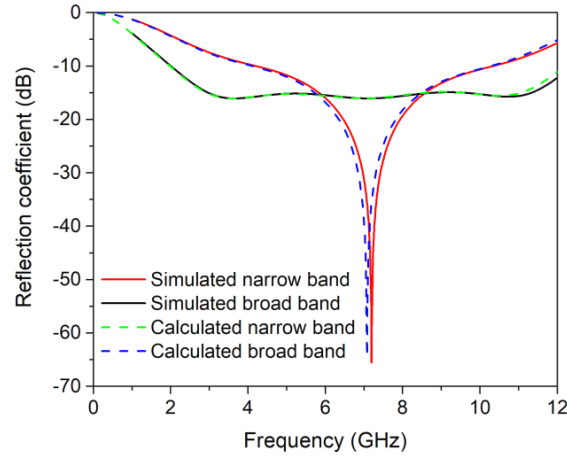


Figure 5-12: Performance comparison of calculated results from Figure 5-11b and simulated ones using full wave simulator CST.

In the simulation, the printed rGO laminates were modeled as ohmic sheets. The Kapton film has dielectric constant of 3.4, dissipation factor of 0.008 with 0.05 mm thick and low loss foam (71-IG-F) has dielectric constant of 1.11 and dissipation factor of 0.0007. The foam is of 10 mm thick. As the structure is symmetry, the response is exactly the same for both vertical and horizontal polarized waves.

The sheet resistance of the rGO films for the broad band absorber, from bottom to top, are $350 \Omega \cdot \text{sq}^{-1}$, $350 \Omega \cdot \text{sq}^{-1}$ and $1870 \Omega \cdot \text{sq}^{-1}$, respectively. The narrowband one has the sheet resistance combination of $381 \Omega \cdot \text{sq}^{-1}$, $6000 \Omega \cdot \text{sq}^{-1}$, and $6000 \Omega \cdot \text{sq}^{-1}$, respectively. The calculated and simulated magnitudes of the reflection coefficient $|\Gamma|$ are plotted in Figure 5-12. It can be seen that the broad band absorber (green dash line) achieves flat absorption from 2.7 GHz to 11 GHz and effective absorption (-10dB bandwidth) from 2 GHz to 12 GHz, which covers S, C and X bands. The full wave simulation results (black line) agreed very well with calculated results from the equivalent circuit model. For narrowband absorber, the centre frequency is 7.1 GHz. The calculated result shows that $|\Gamma|$ achieved -65 dB (blue dash line) which means over 99.9999% of incident RF signal at 7.1 GHz can be absorbed. Likewise, the simulation result (red line) only shifts a little to 7.2 GHz which may be caused by ignoring thin Kapton films in the calculation. It should be noticed that the centre frequency of such absorber structure is determined by dielectric layer permittivity and thickness. The un-patterned rGO laminates can only be optimized to achieve maximum absorption either at single frequency point or maximum bandwidth over the desired bandwidth.

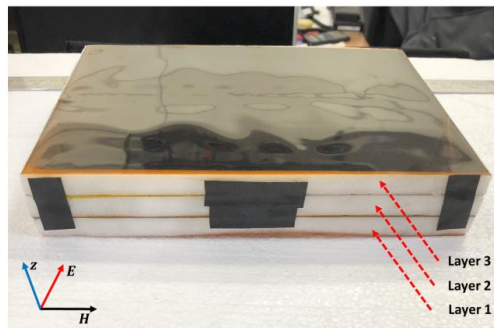


Figure 5-13: Image of the fabricated three-layer microwave absorber.

In order to experimentally verify the design and simulation results, we have fabricated a three-layer wideband microwave absorber, as shown in Figure 5-13. The final sheet resistance of the rGO laminates were measured by 4-probes method where 20 points were randomly picked for each sample. The measured average sheet resistance of layer 3 is $3180 \Omega \cdot \text{sq}^{-1}$ (13.1% error for 20 points), layer 2 is $588 \Omega \cdot \text{sq}^{-1}$ (8.3% error) and the bottom layer is $180 \Omega \cdot \text{sq}^{-1}$ (7.9% error), as shown in Figure 5-14b.

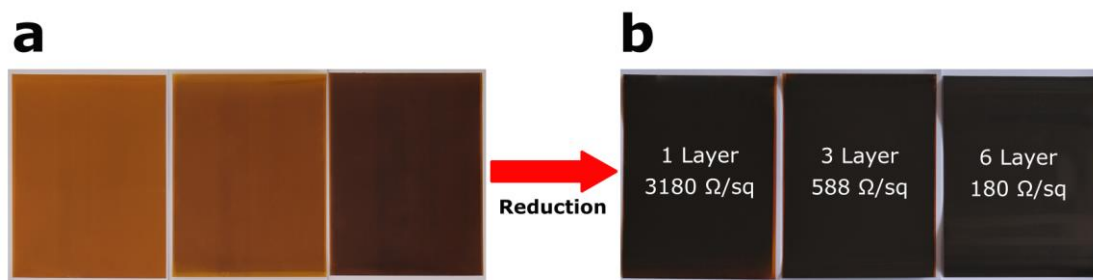


Figure 5-14: (a) Printed GO laminates. (b) L-AA reduced rGO laminates.

A 0.5 mm thick copper plate was stuck at the bottom. Figure 5-15a illustrates the measurement setup in the anechoic chamber. A pair of double-ridged guide antennas (ETS: Model 3115) were acting as transmitting/receiving (T/R) antennas to measure the reflection from the absorber. They are slightly angled to obtain maximum reflection from the absorber. The distance between antennas and absorber is 2 m. The angle between two antennas is less than 2° . The incident angle can be considered to be 90° . A similar setup can be found in Figure 5-15b, where the angle between two antennas is 90° and the incident angle is 45° .

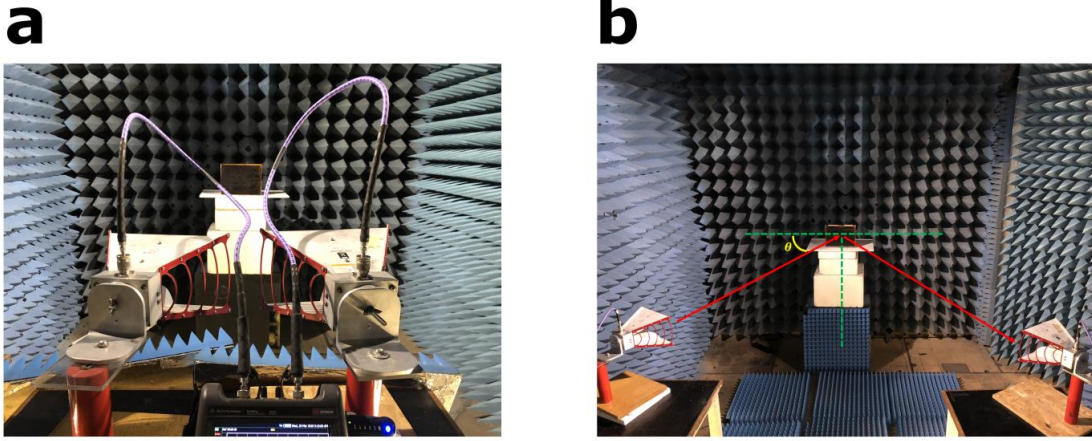


Figure 5-15: (a) Perpendicular incident experiment setup. (b) 45° incident experiment setup (θ represents incident angle).

Measurements were carried out from 1 GHz to 12 GHz for both incident angles. Due to the coupling effect between two antennas and the reflection from anechoic chamber walls (absorption performance of anechoic chamber degrades at lower frequency), the absorption of the sample was completely submerged in noise at low frequencies. Therefore, all RF measurements in this paper used Time Gating technique [72] to eliminate unwanted interference. First, as shown in Figure 5-16a, background noise without absorber was measured. It can be seen that the transmission coefficient between two antennas is less than -60 dB at the whole band, which is acceptable for our purpose. Secondly, the absorber itself was measured, plotted as black line in Figure 5-16a. Last but not the least, an additional copper plate which has the same size as the absorber was measured for comparison and RCS calculation. The results were labelled as ‘metal’. Comparing with ‘metal’, the transmission coefficient of the rGO absorber is much lower from 1 GHz to 9 GHz, revealing that it has absorbed considerable amount of the incident EM energy. From these results, we can obtain the RCS of the absorber. It achieves the minimum of -42 dBsm at 3.5 GHz where the same size copper plate is

8.2 dBsm. In the region from 2 GHz to 6.3 GHz, the absorber can reduce over 90% RCS which again proves its excellent microwave absorption capability. Figure 5-16b shows the calculated, simulated and measured reflection coefficients. The calculated -10 dB bandwidth is about the same as the simulated one. The measured one has a wider bandwidth due to the fact that lower end of the band has moved further down although the higher end has also shifted to the left. The measured reflection coefficients can be obtained after subtracting transmission coefficients of absorber and metal which achieved its minimum -55 dB at 3.5 GHz. It is worth noticed that comparing with calculated and simulated data, the measured reflection is slightly shifted to lower frequencies because of extra air gaps between absorber layers due to surface unflatness and fabrication error. The -10 dB fractional bandwidth for the simulated, calculated and measured reflections are 135%, 139% and 153%, respectively. Compared to previously reported absorbers, this work has much wider measured bandwidth [30,73]. EM absorption can simply be calculated by $1 - |S_{21}^{absorber}/S_{21}^{metal}|^2$, where S_{21} is transmission coefficient. As shown in Figure 5-16b, both absorptions reach their minimum values around 9.5 GHz and then rapidly grow as frequency decreases or increases. The measured absorption of the absorber (blue dash line) covers from 1 GHz to 7.3 GHz where absorption is higher than 0.9 (0.999 absorption from 2.9 GHz to 5.6 GHz), revealing that the absorber provides excellent wideband microwave absorption.

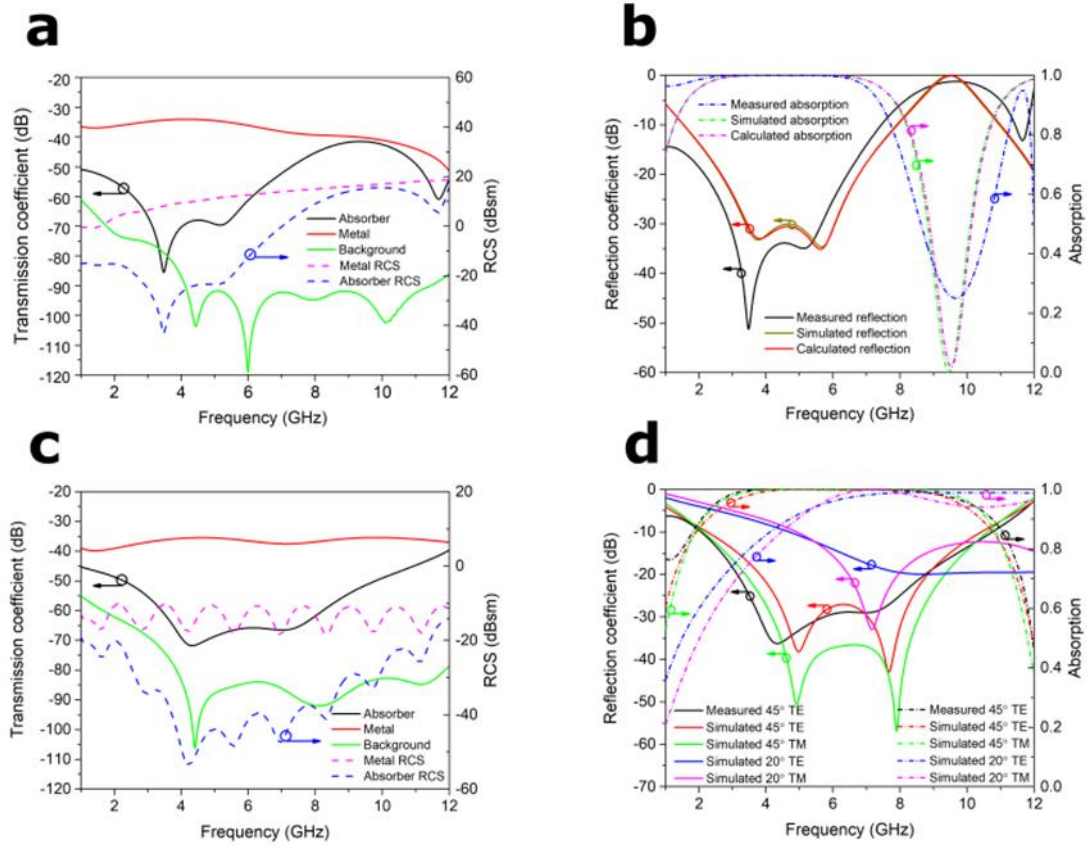


Figure 5-16: Microwave absorber measurement and comparison with simulation. (a) Measured transmission at perpendicular incident (solid lines) and RCS (dash lines). (b) Comparing calculated, simulated and measured reflection coefficients (solid lines) and absorptions (dash lines) at perpendicular incident. (c) Measured transmission TE wave at 45° incident condition (solid lines) and RCS (dash lines). (d) Comparing simulated and measured reflection coefficients (solid lines) and absorptions (dash lines) at different incident angles.

A comparison of non-hybrid microwave absorbers based on graphene/rGO is provided as Table 5-1 in Supplementary data. To further understand the absorption, the simulated surface power densities of the absorber at 1, 3, 5, 9 GHz are illustrated in Figure 5-17. At 1 GHz and 9 GHz, little absorption takes place, most incident energy has reflected. Therefore, the current density is weak, resulting in lower power densities at all three layers. The first and second absorption peaks occur around 3 GHz and 5 GHz. It can be seen that most of the EM power has been absorbed in Layer 2 whereas Layer 3 contributes a bit more absorption at 5 GHz. Consequently, the middle layer is the major

layer to absorb EM energy, the purpose of other two layers (especially layer 3) is to achieve wider bandwidth. Most absorbers reported are related to relatively low incident RF power. In this work, the output power of Vector Network Analyzer (VNA) is 3 dBm. If the incident power is very strong, high thermal conductive materials should be selected for dielectric layers between the rGO laminates to dissipate heat although rGO laminate itself is excellent thermal conducting material [8].

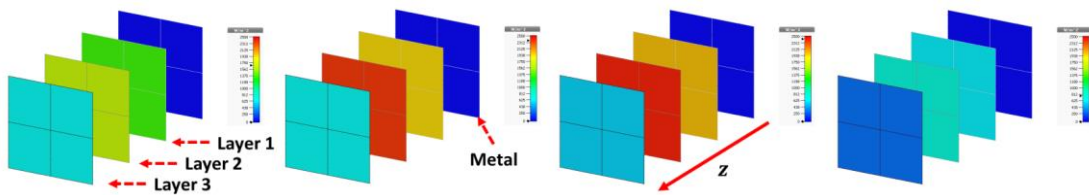


Figure 5-17: Simulated surface power loss density of the absorber in different layers at 1, 3, 5, 9 GHz from left to right respectively.

In practical applications, the incident microwave can come from any angles. If an absorber can effectively absorb microwave at a lower incident angle, it has better performance. It is useful to evaluate absorbers at different incident angles. Unfortunately, the equivalent circuit model cannot predict the performance when the incident wave is not perpendicular to the absorber. Therefore, full wave simulation and measurement have been used to evaluate the performance of the rGO absorber. Firstly, we measured the TE wave reflection where the incident angle θ is 45° . The measurement setup is illustrated in Figure 5-15b and the white holder which supports absorber is made by EM transparent foam (dielectric constant ≈ 1). The procedure for transmission coefficient measurement was exactly the same as aforementioned. Compared with perpendicular incidence, it can be seen in Figure 5-16c that the absorption bandwidth has expanded and achieved better absorption at higher frequency.

The -10 dB absorption bandwidth is from 2 GHz to 10.8 GHz, indicating the absolute bandwidth is wider than 8.8 GHz, i.e., 138% fractional bandwidth. The measured RCS of the absorber is about 20 dB lower than that of metal from 3.5 GHz to 8.5 GHz and 10 dB lower from 2 GHz to 11 GHz. The ripples on the measured data (both dash lines) were caused by edge scattering. We also provided comparisons of RCS reduction of functional absorbers reported in Table. S2 in Supplementary data.

20° incidence condition was also studied numerically. It is found that the reflection at lower frequency increases significantly (blue line in Figure 5-16d), which leads the starting point of -10 dB bandwidth move to 4.8 GHz. Parallel polarized (TM) wave incidence condition was further simulated and compared. It can be seen that the bandwidth of 45° TM incident is close to that of 45° TE one, whereas the reflections of both 20° TE and TM incidents at higher band are less than -10 dB, resulting much wider bandwidths. Even though the reflection in passband is stronger for angled incidence conditions, the 90% absorptions for 45° incident conditions (Both TE and TM) are about from 2.1 GHz to 10.5 GHz. For 20° incident situations, Both TE and TM waves can achieve even wider bandwidth but the 10 dB absorption band shifts to higher frequency, starting from 4.1 GHz. It can be concluded that under the lower incident angles, the absorption and RCS reduction would deteriorate at lower frequency band but enhance at higher frequency band. The wideband and wide angle absorption of the rGO absorber demonstrated in this work can be very useful for flexible and conformal applications.

5.4 Conclusions

In conclusion, we have demonstrated a chemically reduced rGO laminate with precisely controlled sheet resistance and its application for microwave absorption. A more accurate approach of controlling rGO sheet resistance was proposed and verified. The concentrated GO solution was first printed on a substrate (Kapton), dried and then reduced to rGO laminate. The sheet resistance of the rGO laminate was precisely controlled to the designed value by accurately controlling the reduction time and printed passes. The final rGO/Kapton thin film has excellent features of mechanical and electrical properties. Comparing with more commonly reported method (reduce GO solution first and then directly print rGO), the excellent performance of the rGO laminate in this work comes of no surprise because GO disperses quite well in water and has no aggregating problem, resulting in a uniform and cross bonded laminate. Moreover, ultrasonic treatment and extra surfactants [74] are no longer required in the proposed approach. Furthermore, it is experimentally verified that the sheet resistance can be potentially very useful for monitoring the reduction level of rGO due to its large sheet resistance variation with reduction times. The rGO/ Kapton films with different sheet resistance have been fabricated and their application for microwave absorption has been demonstrated, revealing a very good RCS reduction at L, S and C bands. The absorber is not sensitive to the incident modes and has a good tolerance to the incident angles. All these properties are highly desirable for microwave absorption applications. Additionally, the rGO laminate can be easily patterned to provide even better absorption performance, which has the potential to extend the rGO applications to flexible

connectivity and electronic components for wearable wireless communication, energy harvesting and sensing.

References

- [1] T.S. Rappaport, S. Sun, R. Mayzus, H. Zhao, Y. Azar, K. Wang, G.N. Wong, J.K. Schulz, M. Samimi, F. Gutierrez, Millimeter wave mobile communications for 5G cellular: It will work!, *IEEE Access*. 1 (2013) 335–349.
- [2] A. Costanzo, D. Masotti, Energizing 5G: Near-and far-field wireless energy and data trantransfer as an enabling technology for the 5G IoT, *IEEE Microw. Mag.* 18 (2017) 125–136.
- [3] D. Korpi, L. Anttila, M. Valkama, Nonlinear self-interference cancellation in MIMO full-duplex transceivers under crosstalk, *EURASIP J. Wirel. Commun. Netw.* 2017 (2017) 24.
- [4] F. Shahzad, M. Alhabeb, C.B. Hatter, B. Anasori, S.M. Hong, C.M. Koo, Y. Gogotsi, Electromagnetic interference shielding with 2D transition metal carbides (MXenes), *Science* (80-.). 353 (2016) 1137–1140.
- [5] M. Bailleul, Shielding of the electromagnetic field of a coplanar waveguide by a metal film: Implications for broadband ferromagnetic resonance measurements, *Appl. Phys. Lett.* 103 (2013) 192405.
- [6] W.L. Song, M.-S. Cao, M.-M. Lu, S. Bi, C.-Y. Wang, J. Liu, J. Yuan, L.-Z. Fan, Flexible graphene/polymer composite films in sandwich structures for effective electromagnetic interference shielding, *Carbon N. Y.* 66 (2014) 67–76.
- [7] D.D.L. Chung, Electromagnetic interference shielding effectiveness of carbon materials, *Carbon N. Y.* 39 (2001) 279–285.
- [8] P. Kumar, F. Shahzad, S. Yu, S.M. Hong, Y.-H. Kim, C.M. Koo, Large-area reduced graphene oxide thin film with excellent thermal conductivity and electromagnetic interference shielding effectiveness, *Carbon N. Y.* 94 (2015) 494–500.
- [9] M.S. Cao, W.-L. Song, Z.-L. Hou, B. Wen, J. Yuan, The effects of temperature and frequency on the dielectric properties, electromagnetic interference shielding and microwave-absorption of short carbon fiber/silica composites, *Carbon N. Y.* 48 (2010) 788–796.
doi:10.1016/J.CARBON.2009.10.028.
- [10] B. Shen, W. Zhai, W. Zheng, Ultrathin Flexible Graphene Film: An Excellent Thermal Conducting Material with Efficient EMI Shielding, *Adv. Funct. Mater.* 24 (2014) 4542–4548.
doi:10.1002/adfm.201400079.
- [11] D.X. Yan, H. Pang, B. Li, R. Vajtai, L. Xu, P.-G. Ren, J.-H. Wang, Z.-M. Li, Structured Reduced Graphene Oxide/Polymer Composites for Ultra-Efficient Electromagnetic Interference Shielding, *Adv. Funct. Mater.* 25 (2015) 559–566. doi:10.1002/adfm.201403809.
- [12] B. Wen, M. Cao, M. Lu, W. Cao, H. Shi, J. Liu, X. Wang, H. Jin, X. Fang, W. Wang, J. Yuan, Reduced Graphene Oxides: Light-Weight and High-Efficiency Electromagnetic Interference Shielding at Elevated Temperatures, *Adv. Mater.* 26 (2014) 3484–3489.
doi:10.1002/adma.201400108.
- [13] B. Shen, Y. Li, W. Zhai, W. Zheng, Compressible graphene-coated polymer foams with ultralow density for adjustable electromagnetic interference (EMI) shielding, *ACS Appl. Mater. Interfaces*. 8 (2016) 8050–8057.
- [14] J. Chen, D. Zhao, H. Ge, J. Wang, Graphene oxide-deposited carbon fiber/cement composites for electromagnetic interference shielding application, *Constr. Build. Mater.* 84 (2015) 66–72.
- [15] J. Liang, Y. Wang, Y. Huang, Y. Ma, Z. Liu, J. Cai, C. Zhang, H. Gao, Y. Chen,

- Electromagnetic interference shielding of graphene/epoxy composites, *Carbon* N. Y. 47 (2009) 922–925.
- [16] S. Lin, S. Ju, J. Zhang, G. Shi, Y. He, D. Jiang, Ultrathin flexible graphene films with high thermal conductivity and excellent EMI shielding performance using large-sized graphene oxide flakes, *RSC Adv.* 9 (2019) 1419–1427. doi:10.1039/C8RA09376H.
 - [17] F. Shahzad, P. Kumar, S. Yu, S. Lee, Y.-H. Kim, S.M. Hong, C.M. Koo, Sulfur-doped graphene laminates for EMI shielding applications, *J. Mater. Chem. C* 3 (2015) 9802–9810.
 - [18] Y.J. Wan, P.-L. Zhu, S.-H. Yu, R. Sun, C.-P. Wong, W.-H. Liao, Graphene paper for exceptional EMI shielding performance using large-sized graphene oxide sheets and doping strategy, *Carbon* N. Y. 122 (2017) 74–81. doi:10.1016/J.CARBON.2017.06.042.
 - [19] A.P. Singh, P. Garg, F. Alam, K. Singh, R.B. Mathur, R.P. Tandon, A. Chandra, S.K. Dhawan, Phenolic resin-based composite sheets filled with mixtures of reduced graphene oxide, γ -Fe₂O₃ and carbon fibers for excellent electromagnetic interference shielding in the X-band, *Carbon* N. Y. 50 (2012) 3868–3875. doi:10.1016/J.CARBON.2012.04.030.
 - [20] Y. Liu, Z. Xu, J. Zhan, P. Li, C. Gao, Superb electrically conductive graphene fibers via doping strategy, *Adv. Mater.* 28 (2016) 7941–7947.
 - [21] X.-Y. Fang, X.-X. Yu, H.-M. Zheng, H.-B. Jin, L. Wang, M.-S. Cao, Temperature-and thickness-dependent electrical conductivity of few-layer graphene and graphene nanosheets, *Phys. Lett. A* 379 (2015) 2245–2251.
 - [22] P.N. Nirmalraj, T. Lutz, S. Kumar, G.S. Duesberg, J.J. Boland, Nanoscale mapping of electrical resistivity and connectivity in graphene strips and networks, *Nano Lett.* 11 (2010) 16–22.
 - [23] Y. Wang, Y. Chen, S.D. Lacey, L. Xu, H. Xie, T. Li, V.A. Danner, L. Hu, Reduced graphene oxide film with record-high conductivity and mobility, *Mater. Today* 21 (2018) 186–192.
 - [24] S. Loyka, EMC/EMI analysis in wireless communication networks, in: 2001 IEEE EMC Int. Symp. Symp. Rec. Int. Symp. Electromagn. Compat. (Cat. No. 01CH37161), IEEE, 2001: pp. 100–105.
 - [25] H. Chen, W.B. Lu, Z.G. Liu, J. Zhang, A.Q. Zhang, B. Wu, Experimental demonstration of microwave absorber using large-area multilayer graphene-based frequency selective surface, *IEEE Trans. Microw. Theory Tech.* 66 (2018) 3807–3816.
 - [26] S. Sui, H. Ma, J. Wang, M. Feng, Y. Pang, J. Zhang, Z. Xu, S. Qu, Synthetic design for a microwave absorber and antireflection to achieve wideband scattering reduction, *J. Phys. D: Appl. Phys.* 52 (2018) 35103.
 - [27] W. Dallenbach, W. Kleinstieber, Reflection and absorption of decimeter-waves by plane dielectric layers, *Hochfreq. u. Elektroak.* 51 (1938) 152–156.
 - [28] W.W. Salisbury, US Patent, Absorbent body for electromagnetic waves, (1952).
 - [29] K. Naishadham, P.K. Kadaba, Measurement of the microwave conductivity of a polymeric material with potential applications in absorbers and shielding, *IEEE Trans. Microw. Theory Tech.* 39 (1991) 1158–1164.
 - [30] X. Huang, K. Pan, Z. Hu, Experimental demonstration of printed graphene nano-flakes enabled flexible and conformable wideband radar absorbers, *Sci. Rep.* 6 (2016) 38197.
 - [31] Y. Liu, S. Gu, C. Luo, X. Zhao, Ultra-thin broadband metamaterial absorber, *Appl. Phys. A* 108 (2012) 19–24.
 - [32] S. Ghosh, S. Bhattacharyya, Y. Kaiprath, K. Vaibhav Srivastava, Bandwidth-enhanced

- polarization-insensitive microwave metamaterial absorber and its equivalent circuit model, *J. Appl. Phys.* 115 (2014) 104503.
- [33] M. Yoo, S. Lim, Polarization-independent and ultrawideband metamaterial absorber using a hexagonal artificial impedance surface and a resistor-capacitor layer, *IEEE Trans. Antennas Propag.* 62 (2014) 2652–2658.
 - [34] B. Wu, H.M. Tuncer, M. Naeem, B. Yang, M.T. Cole, W.I. Milne, Y. Hao, Experimental demonstration of a transparent graphene millimetre wave absorber with 28% fractional bandwidth at 140 GHz, *Sci. Rep.* 4 (2014) 4130.
 - [35] B. Wu, H.M. Tuncer, A. Katsounaros, W. Wu, M.T. Cole, K. Ying, L. Zhang, W.I. Milne, Y. Hao, Microwave absorption and radiation from large-area multilayer CVD graphene, *Carbon* N. Y. 77 (2014) 814–822.
 - [36] O. Balci, E.O. Polat, N. Kakenov, C. Kocabas, Graphene-enabled electrically switchable radar-absorbing surfaces, *Nat. Commun.* 6 (2015) 6628.
 - [37] D. Yi, X.C. Wei, Y.L. Xu, Tunable Microwave Absorber Based on Patterned Graphene, *IEEE Trans. Microw. Theory Tech.* 65 (2017) 2819–2826. doi:10.1109/TMTT.2017.2678501.
 - [38] K. Pan, Y. Fan, T. Leng, J. Li, Z. Xin, J. Zhang, L. Hao, J. Gallop, K.S. Novoselov, Z. Hu, Sustainable production of highly conductive multilayer graphene ink for wireless connectivity and IoT applications, *Nat. Commun.* 9 (2018) 5197.
 - [39] T. Leng, X. Huang, K. Chang, J. Chen, M.A. Abdalla, Z. Hu, Graphene Nanoflakes Printed Flexible Meandered-Line Dipole Antenna on Paper Substrate for Low-Cost RFID and Sensing Applications, *IEEE Antennas Wirel. Propag. Lett.* 15 (2016) 1565–1568. doi:10.1109/LAWP.2016.2518746.
 - [40] X. Huang, T. Leng, M. Zhu, X. Zhang, J. Chen, K. Chang, M. Aqeeli, A.K. Geim, K.S. Novoselov, Z. Hu, Highly Flexible and Conductive Printed Graphene for Wireless Wearable Communications Applications, *Sci. Rep.* 5 (2016) 18298. doi:10.1038/srep18298.
 - [41] X. Huang, T. Leng, X. Zhang, J.C. Chen, K.H. Chang, A.K. Geim, K.S. Novoselov, Z. Hu, Binder-free highly conductive graphene laminate for low cost printed radio frequency applications, *Appl. Phys. Lett.* 106 (2015) 203105.
 - [42] T. Leng, K. Pan, Y. Zhang, J. Li, S. Afroj, K.S. Novoselov, Z. Hu, Screen-Printed Graphite Nanoplate Conductive Ink for Machine Learning Enabled Wireless Radiofrequency-Identification Sensors, *ACS Appl. Nano Mater.* 2 (2019) 6197–6208. doi:10.1021/acsanm.9b01034.
 - [43] E.B. Secor, T.Z. Gao, M.H. Dos Santos, S.G. Wallace, K.W. Putz, M.C. Hersam, Combustion-Assisted Photonic Annealing of Printable Graphene Inks via Exothermic Binders, *ACS Appl. Mater. Interfaces.* 9 (2017) 29418–29423. doi:10.1021/acsami.7b07189.
 - [44] D.Y.W. Yu, F. Spaepen, The yield strength of thin copper films on Kapton, *J. Appl. Phys.* 95 (2004) 2991–2997.
 - [45] K.K.H. De Silva, H.-H. Huang, M. Yoshimura, Progress of reduction of graphene oxide by ascorbic acid, *Appl. Surf. Sci.* 447 (2018) 338–346.
 - [46] D.K. Pandey, T.F. Chung, G. Prakash, R. Piner, Y.P. Chen, R. Reifengerger, Folding and cracking of graphene oxide sheets upon deposition, *Surf. Sci.* 605 (2011) 1669–1675.
 - [47] H.C. Hsu, I. Shown, H.Y. Wei, Y.C. Chang, H.Y. Du, Y.G. Lin, C.A. Tseng, C.-H. Wang, L.C. Chen, Y.-C. Lin, Graphene oxide as a promising photocatalyst for CO₂ to methanol conversion, *Nanoscale.* 5 (2013) 262–268.

- [48] A. Liscio, G.P. Veronese, E. Treossi, F. Suriano, F. Rossella, V. Bellani, R. Rizzoli, P. Samorì, V. Palermo, Charge transport in graphene–polythiophene blends as studied by Kelvin Probe Force Microscopy and transistor characterization, *J. Mater. Chem.* 21 (2011) 2924–2931.
- [49] E. Treossi, M. Melucci, A. Liscio, M. Gazzano, P. Samorì, V. Palermo, High-contrast visualization of graphene oxide on dye-sensitized glass, quartz, and silicon by fluorescence quenching, *J. Am. Chem. Soc.* 131 (2009) 15576–15577.
- [50] S. Gilje, S. Han, M. Wang, K.L. Wang, R.B. Kaner, A chemical route to graphene for device applications, *Nano Lett.* 7 (2007) 3394–3398.
- [51] H.W. Lin, C.P. Chang, W.H. Hwu, M.D. Ger, The rheological behaviors of screen-printing pastes, *J. Mater. Process. Technol.* 197 (2008) 284–291.
- [52] A. Kaniyoor, S. Ramaprabhu, A Raman spectroscopic investigation of graphite oxide derived graphene, *Aip Adv.* 2 (2012) 32183.
- [53] M. Fathy, A. Gomaa, F.A. Taher, M.M. El-Fass, A.E.-H.B. Kashyout, Optimizing the preparation parameters of GO and rGO for large-scale production, *J. Mater. Sci.* 51 (2016) 5664–5675.
- [54] J. Zhang, H. Yang, G. Shen, P. Cheng, J. Zhang, S. Guo, Reduction of graphene oxide via L-ascorbic acid, *Chem. Commun.* 46 (2010) 1112–1114.
- [55] M.J. Fernández-Merino, L. Guardia, J.I. Paredes, S. Villar-Rodil, P. Solís-Fernández, A. Martínez-Alonso, J.M.D. Tascón, Vitamin C is an ideal substitute for hydrazine in the reduction of graphene oxide suspensions, *J. Phys. Chem. C.* 114 (2010) 6426–6432.
- [56] A.K. Mishra, S. Ramaprabhu, Carbon dioxide adsorption in graphene sheets, *AIP Adv.* 1 (2011) 32152.
- [57] J. Zhang, Y. Xu, Z. Liu, W. Yang, J. Liu, A highly conductive porous graphene electrode prepared via in situ reduction of graphene oxide using Cu nanoparticles for the fabrication of high performance supercapacitors, *RSC Adv.* 5 (2015) 54275–54282.
- [58] H.C. Schniepp, J.L. Li, M.J. McAllister, H. Sai, M. Herrera-Alonso, D.H. Adamson, R.K. Prud'homme, R. Car, D.A. Saville, I.A. Aksay, Functionalized single graphene sheets derived from splitting graphite oxide, *J. Phys. Chem. B.* 110 (2006) 8535–8539.
- [59] O.M. Slobodian, P.M. Lytvyn, A.S. Nikolenko, V.M. Naseka, O.Y. Khyzhun, A. V Vasin, S. V Sevostianov, A.N. Nazarov, Low-Temperature Reduction of Graphene Oxide: Electrical Conductance and Scanning Kelvin Probe Force Microscopy, *Nanoscale Res. Lett.* 13 (2018) 139.
- [60] H. Xian, T. Peng, H. Sun, J. Wang, Preparation of graphene nanosheets from microcrystalline graphite by low-temperature exfoliated method and their supercapacitive behavior, *J. Mater. Sci.* 50 (2015) 4025–4033.
- [61] P.-G. Ren, D.-X. Yan, X. Ji, T. Chen, Z.-M. Li, Temperature dependence of graphene oxide reduced by hydrazine hydrate, *Nanotechnology.* 22 (2010) 55705.
- [62] T. Kuila, A.K. Mishra, P. Khanra, N.H. Kim, J.H. Lee, Recent advances in the efficient reduction of graphene oxide and its application as energy storage electrode materials, *Nanoscale.* 5 (2013) 52–71.
- [63] F. Yin, S. Wu, Y. Wang, L. Wu, P. Yuan, X. Wang, Self-assembly of mildly reduced graphene oxide monolayer for enhanced Raman scattering, *J. Solid State Chem.* 237 (2016) 57–63.
- [64] H.H. Huang, K.K.H. De Silva, G.R.A. Kumara, M. Yoshimura, Structural evolution of hydrothermally derived reduced graphene oxide, *Sci. Rep.* 8 (2018) 6849.

- [65] Y.J. Oh, J.J. Yoo, Y. Il Kim, J.K. Yoon, H.N. Yoon, J.-H. Kim, S. Bin Park, Oxygen functional groups and electrochemical capacitive behavior of incompletely reduced graphene oxides as a thin-film electrode of supercapacitor, *Electrochim. Acta.* 116 (2014) 118–128.
- [66] M. Cao, X. Wang, W. Cao, X. Fang, B. Wen, J. Yuan, Thermally driven transport and relaxation switching self-powered electromagnetic energy conversion, *Small.* 14 (2018) 1800987.
- [67] M.A. Velasco-Soto, S.A. Pérez-García, J. Alvarez-Quintana, Y. Cao, L. Nyborg, L. Licea-Jiménez, Selective band gap manipulation of graphene oxide by its reduction with mild reagents, *Carbon N. Y.* 93 (2015) 967–973.
- [68] J. Tang, H. Guo, M. Zhao, J. Yang, D. Tsoukalas, B. Zhang, J. Liu, C. Xue, W. Zhang, Highly stretchable electrodes on wrinkled polydimethylsiloxane substrates, *Sci. Rep.* 5 (2015) 16527.
- [69] K. Pan, L. Teng, L. Ting, Z. Xinyao, A.A. Stokes, Z. Hu, Soft Wireless Battery-free UHF RFID Stretchable Sensor based on Microfluidic Technology, *IEEE J. Radio Freq. Identif.* (2019).
- [70] D. Micheli, C. Apollo, R. Pastore, M. Marchetti, X-Band microwave characterization of carbon-based nanocomposite material, absorption capability comparison and RAS design simulation, *Compos. Sci. Technol.* 70 (2010) 400–409.
- [71] M. Studio, Cst-computer simulation technology, *Bad Nuheimer Str.* 19 (2008) 64289.
- [72] J. Tian, L. Zhang, N. Li, W. Chen, Time-gating method for V/UHF antenna pattern measurement inside an anechoic chamber, in: 2008 Int. Conf. Microw. Millim. Wave Technol., IEEE, 2008: pp. 942–945.
- [73] P. Saville, T. Huber, D. Makeiff, Fabrication of Organic Radar Absorbing Materials: A Report on the TIF Project, DEFENCE RESEARCH AND DEVELOPMENT ATLANTIC DARTMOUTH (CANADA), 2005.
- [74] A. Tyagi, K.M. Tripathi, R.K. Gupta, Recent progress in micro-scale energy storage devices and future aspects, *J. Mater. Chem. A.* 3 (2015) 22507–22541.

5.5 Supplementary figures

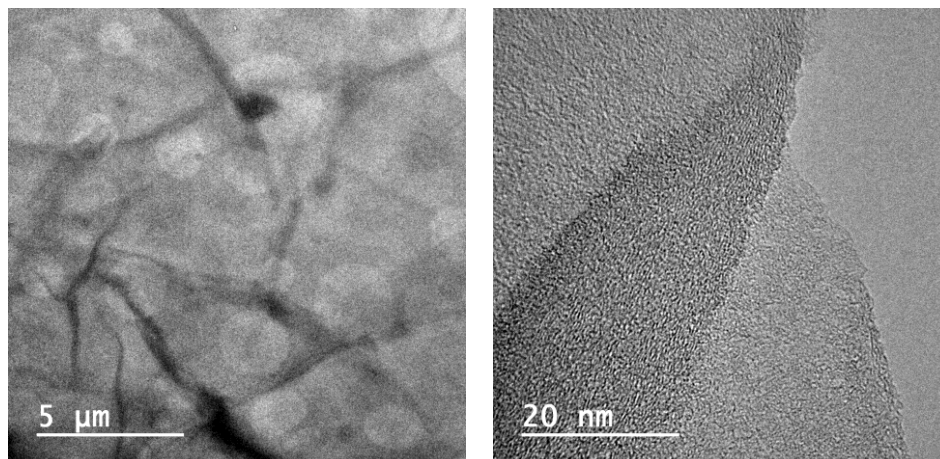


Figure 5-18: (a) TEM image of 1-layer printed sample under low magnification, wrinkles of rGO sheets can be observed. (b) TEM image under high magnification.

5.6 Supplementary tables

Table 5-1: Comparison between non-hybrid microwave absorbers based on graphene/rGO as absorption material.

| Type | Frequency (GHz) | Bandwidth (GHz) | Absorption | Ref |
|--|-----------------|-----------------|-----------------------|-----|
| Printed graphene resistive pattern | 10.4 to 19.7 | 9.3 | 0.9 | [1] |
| CVD-grown patterned graphene | 10.3 to 20 | 9.7 | >0.8 | [2] |
| monolayer graphene on FTO glass | 13 to 16 | 3 | >0.8 | [3] |
| graphene/PET film | 12 to 15 | 3 | >0.8 and 0.9 @12.6GHz | [4] |
| HNO ₃ doped patterned graphen | 5 to 16 | 11 | >0.8 | [5] |
| This work | 1 to 7.3 | 6.3 | >0.9 | |

Table 5-2: RCS Comparison between reported functional radar absorbers.

| Type | Frequency (GHz) | Bandwidth (GHz) | RCS reduction(dB) | Ref |
|--------------------------------------|-----------------|-----------------|-------------------|------|
| Coding Diffusion Metasurface | 8.6 to 22.5 | 13.9 | 9.5 | [6] |
| FSS on paper | 9.65 to 10.42 | 0.77 | 10.2 | [7] |
| capacitive circuit absorbers | 5.3 to 11.2 | -5.9 | 10 | [8] |
| Carbon fiber /glass fabric composite | 8.7 to 19.2 | 10.5 | 10 | [9] |
| Chessboard AMC structure | 15.75 to 41.3 | 25.55 | 10 | [10] |
| absorptive coding metasurface | 6.5 to 20 | 13.5 | 10 | [11] |
| This work | 3.5 to 8.5 | 5 | 20 | |

Supplementary reference

- [1] Huang X, Pan K, Hu Z. Experimental demonstration of printed graphene nano-flakes enabled flexible and conformable wideband radar absorbers. *Sci Rep* 2016;6:38197.
- [2] Chen H, Lu W-B, Liu Z-G, Zhang J, Zhang A-Q, Wu B. Experimental demonstration of microwave absorber using large-area multilayer graphene-based frequency selective surface. *IEEE Trans Microw Theory Tech* 2018;66:3807–16.
- [3] Yi D, Wei X, Xu Y. Experimental demonstration of transparent microwave absorber based on graphene. 2016 IEEE MTT-S Int. Wirel. Symp., IEEE; 2016, p. 1–4. doi:10.1109/IEEE-IWS.2016.7585411.
- [4] Yi D, Wei X-C, Xu Y-L. Transparent Microwave Absorber Based on Patterned Graphene: Design, Measurement, and Enhancement. *IEEE Trans Nanotechnol* 2017;16:484–90. doi:10.1109/TNANO.2017.2688415.
- [5] Lu WB, Wang JW, Zhang J, Liu ZG, Chen H, Song WJ, et al. Flexible and optically transparent microwave absorber with wide bandwidth based on graphene. *Carbon N Y* 2019;152:70–6. doi:10.1016/J.CARBON.2019.06.011.
- [6] Zhang H, Lu Y, Su J, Li Z, Liu J, Yang Y (Lamar). Coding diffusion metasurface for ultra-wideband RCS reduction. *Electron Lett* 2017;53:187–9. doi:10.1049/el.2016.3956.
- [7] Shinozaki Y, Arai H. Microwave Absorber by FSS Using Paper Instead of Dielectric Substrate. 2018 IEEE Int. Work. Electromagn. Student Innov. Compet., IEEE; 2018, p. 1–2. doi:10.1109/iWEM.2018.8536722.
- [8] Kundu D, Mohan A, Chakrabarty A. Single-Layer Wideband Microwave Absorber Using Array of Crossed Dipoles. *IEEE Antennas Wirel Propag Lett* 2016;15:1589–92. doi:10.1109/LAWP.2016.2517663.
- [9] Pang Y, Li Y, Wang J, Yan M, Chen H, Sun L, et al. Carbon fiber assisted glass fabric composite materials for broadband radar cross section reduction. *Compos Sci Technol* 2018;158:19–25. doi:10.1016/J.COMPOSITECH.2018.02.001.
- [10] Ameri E, Esmali SH, Sedighy SH. Wide band radar cross section reduction by thin AMC structure. *AEU - Int J Electron Commun* 2018;93:150–3. doi:10.1016/J.AEUE.2018.06.007.
- [11] Sui S, Ma H, Wang J, Pang Y, Feng M, Xu Z, et al. Absorptive coding metasurface for further radar cross section reduction. *J Phys D Appl Phys* 2018;51:065603. doi:10.1088/1361-6463/aaa3be.

5.7 Supplementary Matlab program for absorber optimization

```
clc;
clear all;
u0=4*pi*10^(-7);
e0=8.854187817*10^(-12);
eg=12; %graphite permittivity
t=10*10^(-6); %film thickness (m)
L=15*10^(-3); %broad thickness (m)
freq=0.1*10^9:10^8:10*10^9; % 91 points
Wair=377; % dielectric broad wave impedance
Wbroad=sqrt(u0/e0)*sqrt(1/(1.1-1i*0.00121));
Bair=2.*pi.*freq.*sqrt(u0.*e0); %wavenumber of dielectric broad
Bbroad=2.*pi.*freq.*sqrt(u0.*e0).*sqrt(1.1-1i*0.00121);
temp=0;
R3=[];
R2=[];
R1=[];
S11_threshold_outer=-10;
S11_threshold_inner=-40;

for Rs3=10:20:4000
    for Rs2=10:20:3000
        for Rs1=10:20:2000

            W3=sqrt(u0./e0).*sqrt(1./(eg+(1./(1i.*Rs3.*t.*2.*pi.*freq.*e0))));
            W2=sqrt(u0./e0).*sqrt(1./(eg+(1./(1i.*Rs2.*t.*2.*pi.*freq.*e0))));
            W1=sqrt(u0./e0).*sqrt(1./(eg+(1./(1i.*Rs1.*t.*2.*pi.*freq.*e0))));
            B3=2.*pi.*freq.*sqrt(u0*e0).*sqrt(eg+(1./(1i.*Rs3.*t.*2.*pi.*freq.*e0
            )));
            B2=2.*pi.*freq.*sqrt(u0*e0).*sqrt(eg+(1./(1i.*Rs2.*t.*2.*pi.*freq.*e0
            )));
            B1=2.*pi.*freq.*sqrt(u0*e0).*sqrt(eg+(1./(1i.*Rs1.*t.*2.*pi.*freq.*e0
            )));
            %wave impedance and number calculation complete
            %start Z calculation
            Zi1=Wbroad.*((0+1i.*Wbroad.*tan(L.*Bbroad))./(Wbroad));
            Zi2=W1.*((Zi1+1i.*W1.*tan(B1.*t))./(W1+1i.*Zi1.*tan(B1.*t)));
            Zi3=Wbroad.*((Zi2+1i.*Wbroad.*tan(Bbroad.*L))./(Wbroad+1i.*Zi2.*tan(B
            broad.*L)));
            Zi4=W2.*((Zi3+1i.*W2.*tan(B2.*t))./(W2+1i.*Zi3.*tan(B2.*t)));
```

```

Zi5=Wbroad.*((Zi4+1i.*Wbroad.*tan(Bbroad.*L))./(Wbroad+1i.*Zi4.*tan(B
broad.*L)));

Zi6=W3.*((Zi5+1i.*W3.*tan(B3.*t))./(W3+1i.*Zi5.*tan(B3.*t)));
S11=20.*log10(abs((Zi6-377)./(Zi6+377)));
start_freq=2*10^9;
end_frequency=7*10^9;
start_point=round((start_freq-0.1*10^9)/10^8)+1;
end_point=round((end_frequency-0.1*10^9)/10^8)+1;
mid_point=round((start_point+end_point)/2);
mid_front_point=round((start_point+mid_point)/2);
mid_end_point=round((end_point+mid_point)/2);
    if((S11(start_point)<S11_threshold_outer)&&
(S11(end_point)<S11_threshold_outer)&&
(S11(mid_point)<S11_threshold_inner)&&
(S11(mid_front_point)<S11_threshold_inner)&&
(S11(mid_end_point)<S11_threshold_inner))
        temp=temp+1;
        plot(freq,S11);
        hold on
        R3(temp)=Rs3;
        R2(temp)=Rs2;
        R1(temp)=Rs1;
    end
end
end
end
for i=1:3
    Txt=actxserver('SAPI.SpVoice');
    Txt.Speak('program finished');
end

```

6 Soft wireless battery-free UHF RFID stretchable sensor based on microfluidic technology

Kewen Pan, Lijun Teng, Leng Ting, Zhou Xinyao, Adam A. Stokes and Zhirun Hu

IEEE Journal of Radio Frequency Identification DOI: 10.1109/JRFID.2019.2912959

My contributions:

This is a joint paper, Kewen and Lijun contributed equally to this work. I proposed this work, designed and simulated this device, performed all RF measurements, analyzed the data, and prepared all the graphs.

© 2019 IEEE. Reprinted, with permission, from Kewen Pan, Lijun Teng, Leng Ting, Zhou Xinyao, Adam A. Stokes and Zhirun Hu, Soft wireless battery-free UHF RFID stretchable sensor based on microfluidic technology, *IEEE Journal of Radio Frequency Identification*, April/2019.

Abstract

Stretchable microfluidic sensors have recently been developed and employed in many sensing applications. However, they are still in their early stage of development and facing considerable challenges, such as practical system integration due to the limitation of costs, wired connections and sensitivity. In this work, we present a compact soft wireless battery-free RFID stretchable sensor based on microfluidic technology. The proposed RFID sensor has high sensitivity and is able to be stretched to 160% of its original size. Moreover, the sensor is completely wireless powered and battery-free. It can be fully embedded into sensor carriers such as robots to eliminate wires, reduce the weight and increase the agility. Difference to known received signal strength indicator (RSSI) techniques for RFID sensing monitoring, resonance frequency shift is used in this work, significantly increasing the measurement accuracy, usefulness and reliability for many practical applications.

6.1 Introduction

Passive RFID technology in UHF band (860MHz-960MHz) utilizes RF signals to detect and identify specific objects [1]. Nowadays there is a growing interest in exploring the use of RFID technologies in sensing and monitoring [2]. Stretch monitoring using passive RFID technology was first demonstrated in [3] and further developed in [4], [5]. However, the deformable metal wire RFID tags in [5] have very limited lifetime and poor repeatability due to the fatigue of metal wire. E-textile works in [4] overcome the metal fatigue problem by using stretchable conductive polymers. However, the measurement depends on the received signal strength indicator (RSSI) which is not only affected by the antenna gain, but also varies with distance between the RFID tag and the reader antenna. Therefore, an additional reference tag located in a specific position is required to calibrate the distance effect. Furthermore, coupling and polarization effects between sensor and the reference tag have to be considered because they are not constant, especially when tags are bended or twisted.

Benefiting from the development of microfluidic technology and the discovery of non-toxic, room-temperature liquid alloys made with gallium, indium (eGaIn) and tin (Galinstan), researchers have successfully fabricated liquid conductors and antennas without metal fatigue problem, e.g. [22] and [23]. Impressive works on deformable soft antennas, such as stretchable microfluidic antennas made with liquid metal and hybrid silicone [8], microfluidic serpentine antennas with reversible stretchability and mechanical frequency modulation ability [9] have been demonstrated. As the fabrication process becomes mature, mechanically tunable soft antenna was first

reported using soft lithographic and rapid prototyping methods in [10]. After that, meandered dipole based stretchable RFID sensor has been reported in [11] and [12], where the measurement of stretch is based on RSSI and reference tag is still be required. In [13], a wireless stretchable RFID sensor which successfully converted the tensile elongation to frequency shift rather than signal strength was reported, significantly advanced the measurement reliability because the distance and angle between the tag and reader antennas are no longer relevant to the measurement accuracy. However, the antenna in [13] is a foot away from practical applications because of its lower Q factor, less sensitivity and nonlinearity.

In this work, the antenna structure is evolved from metamaterial inspired split ring resonator (SRR), operating at its second electric resonant mode [14], which overcomes the disadvantages of meandered dipoles as stretching sensing antennas in [11-13]. A T-matching network [15] was connected for conjugate matching with the RFID chip (Impinj Monza R6). The antenna has the size of $3.3 \times 3.5 \times 0.23 \text{ cm}^3$ and the detection range of 6.7 m with the standard 3.28 W Equivalent Isotropic Radiated Power (EIRP). Antenna design, fabrication process and measurement results will be presented in Section II, III and IV respectively, followed by discussions on the tests of antenna bending and rolling effects. Finally, a soft actuator monitoring system will be demonstrated.

6.2 Design of metamaterial inspired liquid metal soft antenna

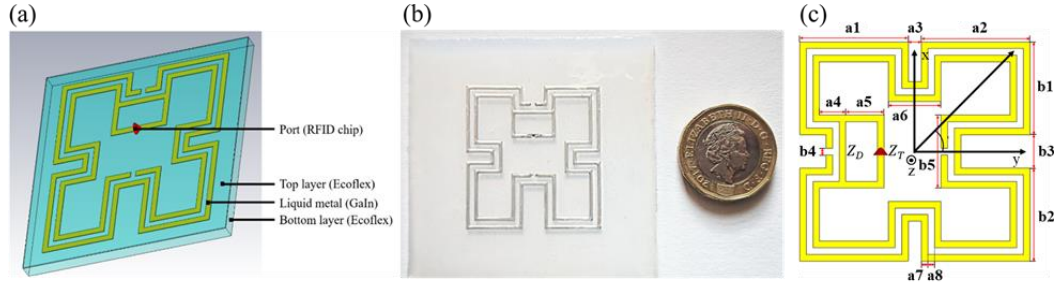


Figure 6-1: Meandered SRR RFID sensor. (a) Antenna structure (red corn is feed port). (b) Fabricated device (3.3cm×3.5cm). (c) Geometry parameters.

SRR is one of the most commonly used metamaterial structures and was first proposed in 1999 [16]. The strong coupling effects between the rings make the structure very sensitive to the change of the ring length and gap width. Such characteristics provide higher sensitivity compared with those of the meandered line antennas [5]. A SRR inspired antenna can have multimode resonances. Its fundamental resonance mode has been proved having low radiation efficiency [14], [17-19] because the radii of the rings are much smaller than the corresponding free space wavelength, which leads to low radiation resistance and efficiency [18-20]. Therefore, second resonance mode was chosen in this work. The antenna consisted of an SRR radiator, T-matching network and a RFID chip, as shown in Figure 6-1a,b. The antenna and matching network were designed and simulated using commercial EM simulation software CST MWS [26]. In the simulation, the liquid alloy was modelled as metal with a conductivity of 2.3×10^6 S/m [20]. The geometrical parameters of the antenna are illustrated in Figure 6-1c (c): $a_1=a_2=16.5$ mm, $a_3=2$ mm, $a_4=4$ mm, $a_5=5.8$ mm, $a_6=8$ mm, $a_7=a_8=1$

mm, $b_1=b_2=14$ mm, $b_3=5$ mm, $b_4=1$ mm, $b_5=11$ mm. The thickness of bottom layer is 2.3 mm with 0.1 mm thick liquid channel. The upper layer is 0.2 mm thick for sealing purpose. The second resonance mode of the SRR antenna has been studied [21]. The radiation resistance in this resonance mode is approximately 7 times higher than a same length half wave dipole. However, the input impedance of the commercial RFID chip (Impinj, Monza R6) is $12-j120\Omega$ at 915MHz. The T-matching network, which connects the chip to the inner ring of the SRR antenna, is required to provide a conjugate matching between the chip and antenna for maximum power efficiency. The input impedance of the antenna is [15]:

$$Z_{in} = \frac{2Z_t n^2 Z_a}{2Z_t + n^2 Z_a} \quad (6.1)$$

where Z_a is the input impedance of the SRR antenna itself, Z_t is the input impedance of T-matching network, n is current ratio between two arms. The overall input impedance Z_{in} can therefore be designed for conjugate matching with the RFID chip.

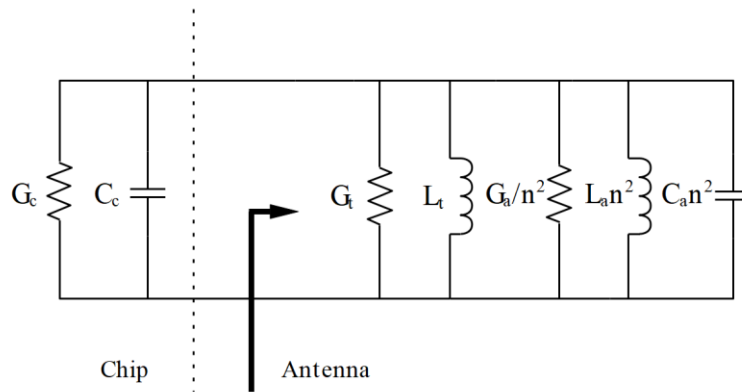


Figure 6-2: Antenna equivalent circuit model (Left is RFID chip side and right is antenna side).

In second resonance mode of SRR structure, the surface current distributions in both rings are of opposite directions [14] and phase. The resonance condition can still be analysed by using equivalent circuit model [19]. To illustrate the relationship between

the resonance frequency and antenna structure, we plotted equivalent circuit model for the whole RFID tag in Figure 6-2. G_c , G_t , and G_n are the conductance of RFID chip, T-matching network loss and SRR antenna (caused by loss and radiation) respectively. C_c and C_a represent the RFID chip input capacitor and SSR antenna parasitic capacitor where $C_a = \pi L_x C_{pul}$ [19] (L_x is the side length of antenna, C_{pul} is per unit length capacitor). L_t and L_a are the T-matching shorter arm equivalent inductor and antenna inductor. Resonance frequency f_0 can be expressed as:

$$f_0 = \frac{1}{2\pi\sqrt{L_{total}C_{total}}} \quad (6.2)$$

where $L_{total} = \frac{L_t L_a n^2}{L_a n^2 - L_t}$ and $C_{total} = C_c + C_a n^2$. It is easy to find out that the resonance frequency degrades significantly due to the transformation of T-matching network and RFID chip capacitor. Therefore, both T-matching network and SRR antenna behave inductively. Under stretched condition, L_t and L_a increase because of longer current path, resulting the resonance frequency move down to lower frequencies. The measurement results between different stretching levels and frequency shifts are discussed in the following sections.

6.3 Soft antenna fabrication

Galinstan is a generic name of a series of room-temperature eutectic liquid alloys which consist of gallium (Ga), indium (In), and tin (Sn). Galinstan has desirable properties such as low toxicity and low reactivity of its component metals. Therefore, Galinstan is an excellent substitution for some conventional conductive liquid, such as toxic mercury and reactive sodium-potassium alloy. Galinstan used in this work has a

typical composition of 68.5% Ga, 21.5% In, and 10% Sn with the electrical conductivity of 2.3×10^6 S/m. It also has a large surface tension and great wetting properties on the surface of Ecoflex or other silicone rubber materials. Galinstan, therefore, can afford stable and reliable connections in the elastic channels [10] as it tends to hold their position even when a device is twisted, stretched, or severely folded.

Ecoflex is one of the most commonly used substrate materials in fluidic devices due to its attractive high elasticity, uncomplicated fabrication, easy casting properties and excellent biocompatibility. In this work, we used Ecoflex type 00-50 to make elastic substrate of the SRR antenna. The elongation at break of Ecoflex 00-50 in tensile strength test with ASTM D412 system is 980% (defined as the percentage change in length or $\left(\frac{l-l_0}{l_0}\right) \times 100\%$, [22]).

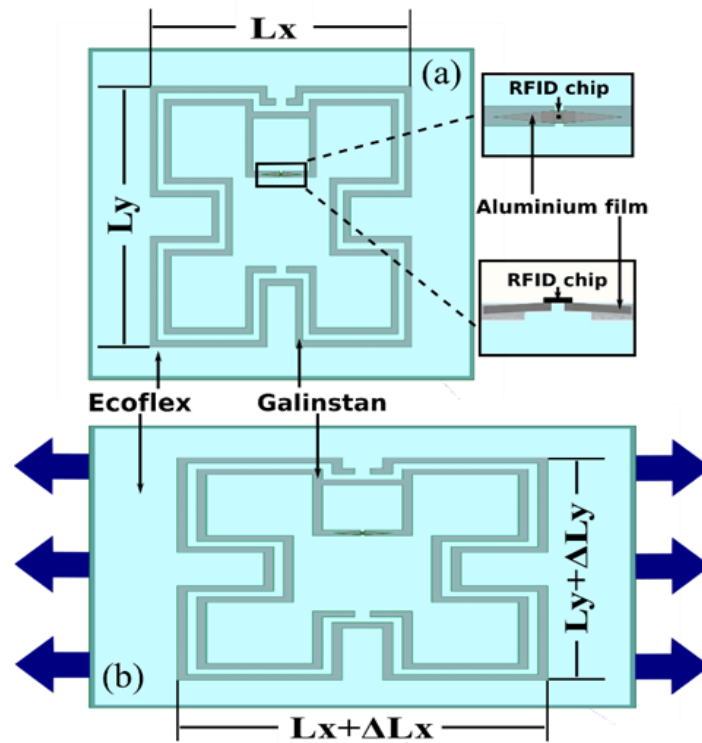


Figure 6-3: (a) Top view of the Ecoflex liquid metal SRR antenna with detailed cross-section drawing of the RFID chip insertion. The initial length, width and thickness of the antenna are $L_x=33$ mm, $L_y=35$ mm and $L_z=2.5$ mm respectively. The channels with filled Galinstan in the Ecoflex substrate are 1 mm in the

width. The RFID chip was bonded on an aluminum film then inserted in the fluidic channels to connect with Galinstan; (b) when the antenna is under stretching, the length in X direction, the width in Y direction and the thickness in Z direction become $L_x + \Delta L_x$, $L_y + \Delta L_y$ and $L_z + \Delta L_z$ respectively.

Figure 6-3a,b show the structure of the antenna without and with stretching respectively. Deformation of the antenna under stretch is significantly influenced by Poisson's effect. For example, when the antenna is stretched in one direction, it becomes narrower and thinner in other directions. Such phenomenon changes the thickness of the antenna substrate and also affects its resonance frequency. The Poisson's ratio (ν) of Ecoflex 00-50 is 0.49 which means this material is a nearly incompressible material which deforms elastically even under a very small strain. In Figure 6-3a, the original length, width and thickness of the antenna are represented by L_x , L_y and L_z respectively. When the antenna is stretched in X direction ($L_x + \Delta L_x$), as shown in Figure 6-3b, the thickness and width change to $L_y + \Delta L_y$ and $L_z + \Delta L_z$. Eq. (3) shows the relationship between $\Delta L_y/L_y$, $\Delta L_z/L_z$ and $L_x + \Delta L_x$ [22]:

$$\frac{\Delta L_y}{L_y} = \frac{\Delta L_z}{L_z} = \left(1 + \frac{\Delta L_x}{L_x}\right)^{-\nu} - 1 \quad (6.3)$$

It should be noticed when the length varies in X direction (L_x), not only the width in Y direction, but the thickness will also change simultaneously.

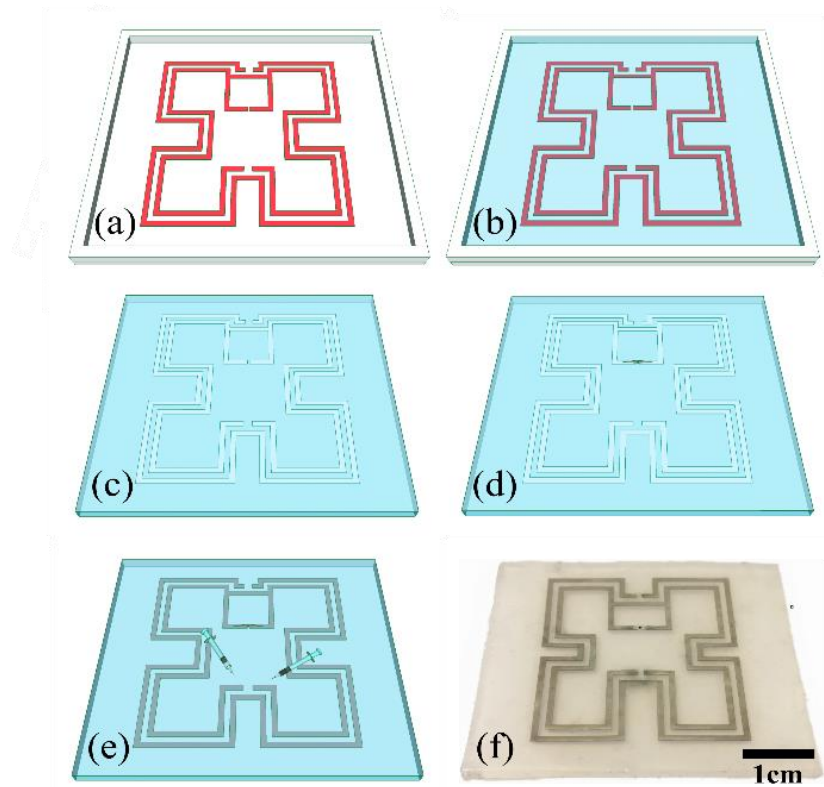


Figure 6-4: Schematic illustration of the fabrication process and photograph of the stretchable fluidic antenna; (a) the soft-lithography mold made with 0.15 mm vinyl film (red) and 2 mm Acrylic substrate and frame (white); (b) uncured Ecoflex with height of 2 mm was poured into the soft-lithography mold; (c) the casted piece of Ecoflex was sealed with another 0.2 mm Ecoflex film; (d) the RFID chip bonded on an aluminum film was inserted into the channels in Ecoflex substrate; (e) two needles were used to inject Galinstan into the channels. (f) Photograph of the final prototype.

Figure 6-4 (a)-(e) illustrate the fabrication process of the stretchable sensor: (i) A soft-lithography mold to cast uncured Ecoflex with a 2 mm Acrylic board (Acrylic Cast, AMARI) and a piece of 0.15 mm self-adhesive vinyl film (CRAFTRKZO, d-c-fix®) were prepared. The Acrylic material, which was shaped with a laser cutter (Epilog Fusion), was used as the substrate and the frame in the mold. The vinyl film was used to form the structure of the channels in the mold. The profile of the antenna structure was cut on the vinyl film with a laser micro-machining system (Protolaser U3, LPKF) which contains an error rate less than 5%. (ii) Part A and part B of Ecoflex (type 00-50, Reynolds Advanced materials) were mixed at the ratio of 1:1. The uncured Ecoflex with

a controlled height of 2 mm was degassed under vacuum for five minutes and then poured into the soft-lithography mold. In order to fasten the curing, the mold was put into a convection oven at 65 °C for 20 mins. (iii) The channels were sealed in the casted 2 mm Ecoflex layer with a piece of 0.2 mm Ecoflex film made with a spin coater. (iv) An RFID chip (Monza R6, Impinj) was bonded on an aluminum film then inserted in the channels. (v) Two 0.3 mm-diameter needles were used to inject Galinstan into the channels through positive pressure. (vi) In the end, a very thin film of uncured Ecoflex was coated on the surface of this antenna to seal all the holes.

6.4 Antenna measurement

Voyantic Tagformance measurement system was used for the RFID tag measurement as shown in Figure 6-5. The RFID reader contains a signal generator, transmitter, power detector and receiver. The RFID antenna receives the signal and power from the reader and activates its chip which in turn modulates and backscatters the signal to the reader antenna.

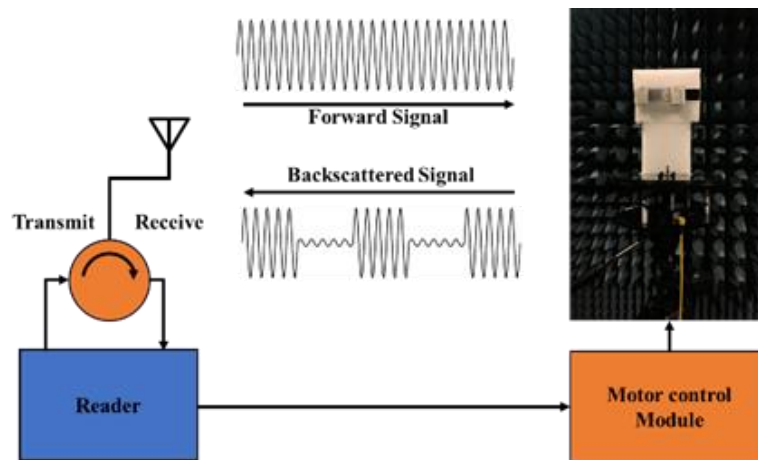


Figure 6-5: RFID measurement set up with Voyantic Tagformance.

The minimum power that the RFID tag requires can be expressed as:

$$P_{tag} = \frac{P_{th}}{\tau G_{tag}} = [P_t - L_{cable} + G_t - FSPL]_{dB} \quad (6.4)$$

where P_t , G_t are the minimum transmitted power and gain of the reader antenna, L_{cable} and $FSPL$ represent cable loss and free space loss which can be calibrated by using a standard tag before measurement. P_{th} is the minimum threshold of the power required to activate the RFID chip, G_{tag} is the gain of the tag antenna. τ is the matching factor, which describes the conjugate impedance matching between the antenna and RFID chip.

P_{th} and τ are constant for a specific frequency, the minimum power that can power on the chip is inverse proportional to the antenna gain G_{tag} , which can be derived from measured P_t :

$$G_{tag} = [P_{th} - P_t + L_{cable} - G_t + FSPL]_{dB} \quad (6.5)$$

Considering the detection distance requirements in real applications, theoretical read range R_{max} can be calculated for given EIRP as:

$$R_{max} = \sqrt{\frac{P_{max,EIRP}}{P_{tag}}} \cdot \frac{c}{4\pi f} \quad (6.6)$$

where $P_{max,EIRP} = 3.28W$, c is light speed and f is the corresponded frequency.

6.5 Results and discussions

The simulated antenna impedance variation with stretching is shown in Figure 6-6a. It can be seen that the peak values of both real and imaginary parts of the impedance shift to lower frequency when increasing the stretching, resulting in the decrease of resonance frequency.

The RFID antenna performance was measured in anechoic chamber. To measure the gain and resonance frequency of the antenna, the reader sweeps linearly from 800 MHz to 1 GHz with a 3 MHz step. The theoretical reading range is calculated using Eq. (6) and plotted in Figure 6-6b. It can be found that the resonance frequency without stretching is 938 MHz with 6.7 m read range and it drops to 818 MHz at 60% strain. Therefore, the sensitivity is 5.71 MHz/mm, doubled the previous result [13] (2.65 MHz/mm). When the antenna is stretched, its resonance frequency decreases whereas the read range increases due to longer electric length of the antenna and higher gain.

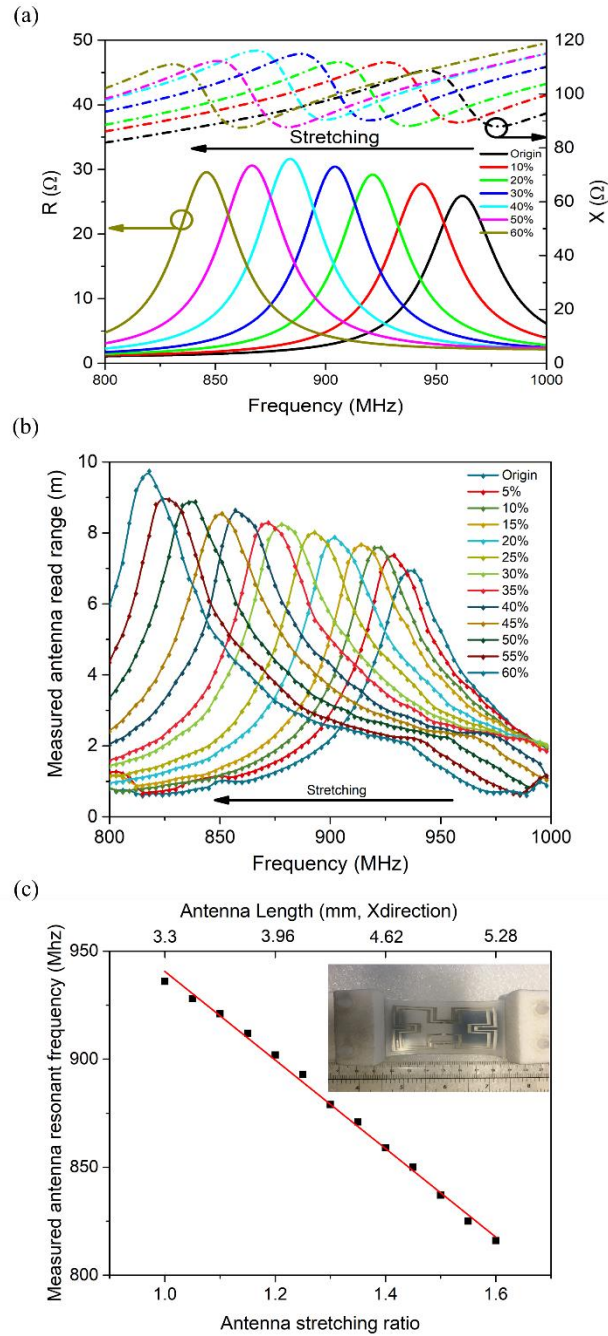


Figure 6-6: (a) Simulated antenna impedance under different stretch conditions. (b) Measurement results of RFID tag read range and resonance frequency under different stretching conditions. (c) Antenna resonance frequency versus antenna stretching ratio (stretched length/ original length), the red line is linear fits of scatters.

Figure 6-6c illustrates the relationship between the resonance frequency and antenna stretching ratio. Two holders, which consist of low permittivity and low loss foam (71 IG-F, MK), were used to hold and stretch the antenna in Y-axis (inset Figure 6-6c). The

distance between the RFID sensor antenna and reader antenna is 80 cm. To eliminate the influence of foam holders, calibration was performed every time when antenna length was changed. High stretchability up to 160% of the antenna length was tested with 5% per step. The antenna operates properly when being stretched to 160% and could be further stretched, yet, its resonance frequency will run out of the lowest allocated RFID frequency spectrum.

From Figure 6-6c, linear relationship between the resonance frequency and stretching length can be observed. Fitted formula of the relationship can be expressed as:

$$f_r = -205 \times r + 1145.6 \quad (6.7)$$

Therefore, it is now possible to use Eq. (7) to convert the stretching ratio r directly from the measured resonance frequency.

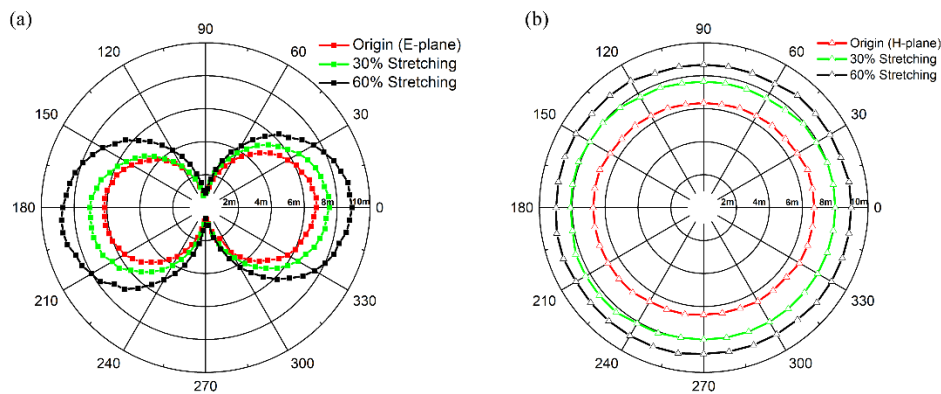


Figure 6-7: Measured RFID antenna radiation pattern under different stretching length in E-plane (a) and H-plane (b) (0%, 30% and 60%).

The radiation patterns of the RFID antenna under different stretching conditions were measured in both E-plane and H-plane (Antenna Measurement Studio 5.5, Diamond

Engineering). For more intuitionistic demonstration, the read range was plotted instead of antenna gain. The data were recorded every 5 degrees rotation, as shown in Figure 6-7. The measured radiation pattern is similar with dipole antenna which means the antenna is omnidirectional at H-plane and weakly directional at E plane. It can receive signals from any positions without dark zone. The maximum read range is approximately 6.7 m, 7.4 m and 9 m with 0%, 30% and 60% stretching, respectively. Except the read range, there is no significant distortion of radiation pattern under stretching.

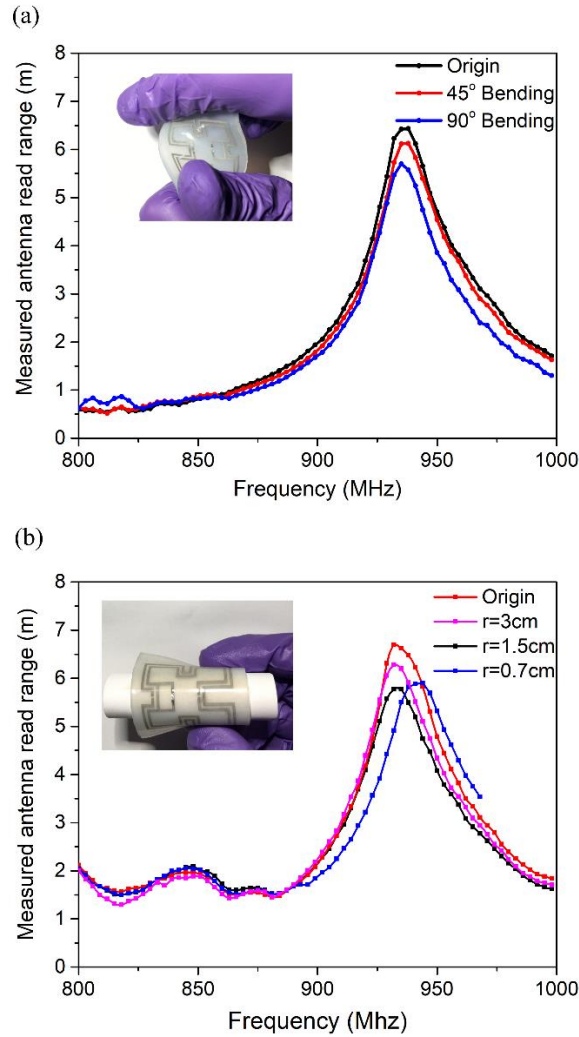


Figure 6-8: (a) Antenna resonance frequency variation with different bending angle (0° , 45° , 90°). (b) Antenna resonance variation under rolling ($r=0.7$, 1.5 , 3 , ∞).

Having demonstrated the relationship between stretching length and resonance frequency of the RFID stretch sensor, we go further to investigate the effects of bending and rolling to the RFID sensor antenna resonance because most applications not only have plane stretching, but also get distortion and deformation in other directions. In Figure 6-8a, the antenna was bended from 0° to 90° (fixed by foam holders with different angles), the strong coupling between the inner and outer rings makes the antenna being less sensitive to the bending, no obvious frequency shift can be observed during bending. However, the maximum read range decreases by 1 metre when the antenna is bended to 90° . This is because the bending distorts the antenna's radiation pattern, i.e., the gain reduces. The same conclusion can be drawn from the rolling test in Figure 6-8b, only when the radius is smaller than 1.5 cm, the resonance frequency starts to shift. It increases by only 15 MHz when the rolling radius reduces to 0.7 cm. At this point, the antenna touches itself from end to end. These experimental data verify that bending and rolling have little effects on the resonance frequency as the electric length of the antenna barely varies.

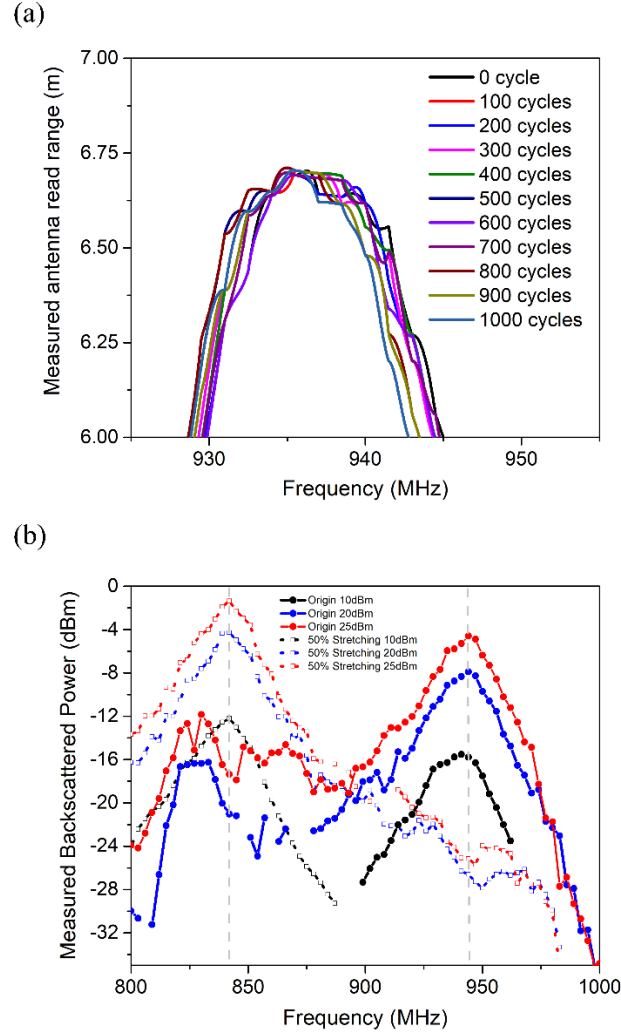


Figure 6-9: (a) Cyclability test of the RFID stretchable sensor. The sensor was stretched from its initial state to 200% of the original length (X direction) with 1000 cycles. (b) Demonstration of the measured backscattered power where the RFID stretchable sensor is placed in normal office environment with a fixed distance.

As the cyclability is another important criterion to evaluate stretchable sensor performance, the RFID sensor was stretched ($2L_x$) and released (L_x) 1000 cycles. Its resonance frequency was recorded every 100 cycles and plotted in Figure 6-9 (a). The resonance frequency is rather stable in the first 500 cycles and starts to decrease from 600 cycles. There is approximately 2 MHz frequency shift after 1000 cycles. Based on Eq. (7), the calculated distance error is 0.032 mm which confirms that the RFID

sensor has an excellent cyclability.

In order to demonstrate that the proposed sensor can be used in practical environment, we moved the whole measurement set to office environment with tables, computers and people moving around. The measurement results are plotted in Figure 6-9 (b). In the original state, the peak value of the backscattered power varies with different radiating power whereas the resonance frequency has kept constant. After stretching the sensor of 50%, all peak values shift from 944 MHz to 842 MHz, indicating that the sensor works well under practical multipath interference environment.

Taking a step further to real applications, we have integrated the RFID stretchable sensor into a soft chamber which is made of silicone materials with pneumatic channels based on the structure described in [23] since it is compatible with soft lithography [24] technology. In the fabricated soft chamber, a series of pneumatic channels were embedded in an extensible Ecoflex layer and bonded to a relatively less extensible PDMS layer (Young's Modulus of Ecoflex is 69 kPa [13] whereas PDMS is 0.8-3MPa [25]). When compressed air is injected into the chamber, the chamber inflates like balloons. The difference in strain between the Ecoflex layer and the PDMS layer causes the structure to bend.



Figure 6-10: Soft pneumatic actuator with RFID stretchable sensor attached on the Ecoflex side.

In Figure 6-10, the fabricated actuator is flat and the RFID stretchable sensor antenna operates in its original state when air pressure is zero. Its resonance frequency is 917 MHz (this is lower than that of the antenna shown in Figure 6-6b because of the increment of substrate thickness). With increasing air pressure, the Ecoflex grooves start to expand. However, the expansion rate of relatively rigid PDMS layer is much smaller. The different expansion rates lead to bending action of the actuator. Under such condition, the RFID stretchable sensor was stretched at both X and Y directions and bended from 0° to 90° . The resonance frequency with different bending angle is shown in Figure 6-11. It can be seen that the average resonance frequency shift rate is >1.4 MHz/ $^{\circ}$ at $0^{\circ}\sim 30^{\circ}$ and >2 MHz/ $^{\circ}$ at $30^{\circ}\sim 60^{\circ}$ (exceed measurement range when bended over 60°).

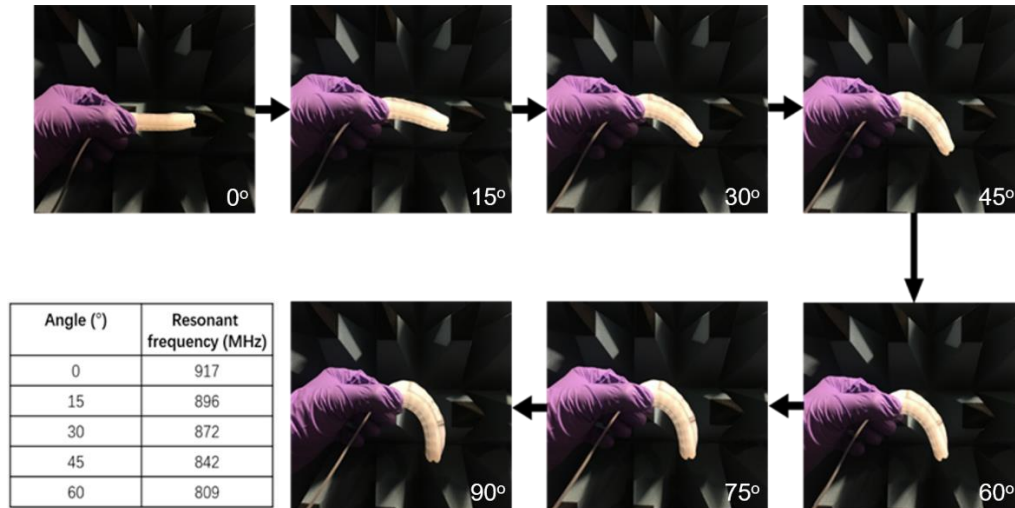


Figure 6-11: Soft pneumatic actuator bending process when air pressure increasing (0°, 15°, 30°, 45°, 60°, 75° and 90°) and corresponded measured RFID antenna resonance frequencies.

6.6 Conclusion

In this paper, we have demonstrated a metamaterial inspired soft wireless battery-free UHF RFID liquid metal stretchable sensor. The operation principle is based on the resonance frequency detection of the RFID sensor antenna, which can convert physical parameter variations to its resonance frequencies. This technique has advantages over the RSSI: it doesn't need reference antenna and has high sensitivity. First a compact SRR UHF RFID antenna which is highly sensitive to the mechanical stretch has been designed and fabricated. Secondly the performance of the RFID sensor under different stretching length, including backscattered powers, read ranges and radiation patterns, has been measured, verifying that the resonance frequency of the RFID antenna can be altered efficiently during stretching. Thirdly, bending and rolling of the antenna have been tested and discussed. Fourthly, the reliability test reveals that the sensor maintains good performance up to 1000 stretching cycles. Finally, a prototype of RFID stretching

sensor enabled soft pneumatic actuator has been fabricated and demonstrated, illustrating the potential applications of the reported soft wireless battery-free UHF RFID stretchable sensor.

References

- [1] H. Stockman, "Communication by means of reflected power," *Proc. IRE*, vol. 36, no. 10, pp. 1196–1204, 1948.
- [2] J. Landt, "The history of RFID," *IEEE potentials*, vol. 24, no. 4, pp. 8–11, 2005.
- [3] S. Merilampi, P. Ruuskanen, T. Björninen, L. Ukkonen, and L. Sydänheimo, "Printed passive UHF RFID tags as wearable strain sensors," in *Applied Sciences in Biomedical and Communication Technologies (ISABEL), 2010 3rd International Symposium on*, 2010, pp. 1–5.
- [4] X. Chen, L. Ukkonen, and T. Björninen, "Passive e-textile uhf rfid-based wireless strain sensors with integrated references," *IEEE Sens. J.*, vol. 16, no. 22, pp. 7835–7836, 2016.
- [5] C. Occhiuzzi, C. Paggi, and G. Marrocco, "Passive RFID strain-sensor based on meander-line antennas," *IEEE Trans. Antennas Propag.*, vol. 59, no. 12, pp. 4836–4840, 2011.
- [6] Y. Lin, C. Cooper, M. Wang, J. J. Adams, J. Genzer, and M. D. Dickey, "Handwritten, soft circuit boards and antennas using liquid metal nanoparticles," *Small*, vol. 11, no. 48, pp. 6397–6403, 2015.
- [7] M. D. Dickey, "Emerging applications of liquid metals featuring surface oxides," *ACS Appl. Mater. Interfaces*, vol. 6, no. 21, pp. 18369–18379, 2014.
- [8] M. Kubo *et al.*, "Stretchable microfluidic radiofrequency antennas," *Adv. Mater.*, vol. 22, no. 25, pp. 2749–2752, 2010.
- [9] Y. Huang, Y. Wang, L. Xiao, H. Liu, W. Dong, and Z. Yin, "Microfluidic serpentine antennas with designed mechanical tunability," *Lab Chip*, vol. 14, no. 21, pp. 4205–4212, 2014.
- [10] J. So, J. Thelen, A. Qusba, G. J. Hayes, G. Lazzi, and M. D. Dickey, "Reversibly deformable and mechanically tunable fluidic antennas," *Adv. Funct. Mater.*, vol. 19, no. 22, pp. 3632–3637, 2009.
- [11] S. H. Jeong, A. Hagman, K. Hjort, M. Jobs, J. Sundqvist, and Z. Wu, "Liquid alloy printing of microfluidic stretchable electronics," *Lab Chip*, vol. 12, no. 22, pp. 4657–4664, 2012.
- [12] S. H. Jeong, K. Hjort, and Z. Wu, "Tape transfer printing of a liquid metal alloy for stretchable RF electronics," *Sensors*, vol. 14, no. 9, pp. 16311–16321, 2014.
- [13] L. Teng, K. Pan, M. P. Nemitz, R. Song, Z. Hu, and A. A. Stokes, "Soft Radio-Frequency Identification Sensors: Wireless Long-Range Strain Sensors Using Radio-Frequency Identification," *Soft Robot.*, 2018.
- [14] J. García-García, F. Martín, J. D. Baena, R. Marques, and L. Jelinek, "On the resonances and polarizabilities of split ring resonators," *J. Appl. Phys.*, vol. 98, no. 3, p. 33103, 2005.
- [15] J. Choo, J. Ryoo, J. Hong, H. Jeon, C. Choi, and M. M. Tentzeris, "T-matching networks for the efficient matching of practical RFID tags," in *Microwave Conference, 2009. EuMC 2009. European*, 2009, pp. 5–8.
- [16] J. B. Pendry, A. J. Holden, D. J. Robbins, and W. J. Stewart, "Magnetism from conductors and enhanced nonlinear phenomena," *IEEE Trans. Microw. Theory Tech.*, vol. 47, no. 11, pp. 2075–2084, 1999.
- [17] R. Marqués, F. Mesa, J. Martel, and F. Medina, "Comparative analysis of edge-and broadside-coupled split ring resonators for metamaterial design-theory and experiments," *IEEE Trans. Antennas Propag.*, vol. 51, no. 10, pp. 2572–2581, 2003.
- [18] B. Sauviac, C. R. Simovski, and S. A. Tretyakov, "Double split-ring resonators: Analytical modeling and numerical simulations," *Electromagnetics*, vol. 24, no. 5, pp. 317–338, 2004.

- [19] R. Marqués, F. Medina, and R. Rafii-El-Idrissi, “Role of bianisotropy in negative permeability and left-handed metamaterials,” *Phys. Rev. B*, vol. 65, no. 14, p. 144440, 2002.
- [20] T. Liu, P. Sen, and C.-J. Kim, “Characterization of nontoxic liquid-metal alloy galinstan for applications in microdevices,” *J. Microelectromechanical Syst.*, vol. 21, no. 2, pp. 443–450, 2012.
- [21] S. Zuffanelli, G. Zamora, P. Aguilà, F. Paredes, F. Martín, and J. Bonache, “On the radiation properties of split-ring resonators (SRRs) at the second resonance,” *IEEE Trans. Microw. Theory Tech.*, vol. 63, no. 7, pp. 2133–2141, 2015.
- [22] J.-B. Chossat, Y.-L. Park, R. J. Wood, and V. Duchaine, “A soft strain sensor based on ionic and metal liquids,” *IEEE Sens. J.*, vol. 13, no. 9, pp. 3405–3414, 2013.
- [23] F. Ilievski, A. D. Mazzeo, R. F. Shepherd, X. Chen, and G. M. Whitesides, “Soft robotics for chemists,” *Angew. Chemie*, vol. 123, no. 8, pp. 1930–1935, 2011.
- [24] D. Qin, Y. Xia, and G. M. Whitesides, “Soft lithography for micro-and nanoscale patterning,” *Nat. Protoc.*, vol. 5, no. 3, p. 491, 2010.
- [25] Y. Fouillet *et al.*, “Stretchable Material for Microfluidic Applications,” in *Multidisciplinary Digital Publishing Institute Proceedings*, 2017, vol. 1, no. 4, p. 501.
- [26] CST (Computer Simulation Technology). <https://www.cst.com/>

7 Soft radio-frequency identification sensors: wireless long-range strain sensors using radio-frequency identification

Lijun Teng, **Kewen Pan**, Markus P. Nemitz, Rui Song, Zhirun Hu, and Adam A. Stokes

Soft robotics, 6(1), 82-94.

My contributions:

This is a joint paper. Kewen and Lijun contributed equally to this work. To use the full paper in this thesis was granted by Dr. Lijun Teng. I have designed and simulated this devices, performed all RF measurements, analyzed the data, and prepared the graphs.

Abstract

Increasing amounts of attention are being paid to the study of *Soft Sensors* and *Soft Systems*. *Soft Robotic Systems* require input from advances in the field of *Soft Sensors*. Soft sensors can help a soft robot to perceive and to act upon its immediate environment. The concept of integrating sensing capabilities into soft robotic systems is becoming increasingly important. One challenge is that most of the existing soft sensors have a requirement to be hardwired to power supplies, or external data-processing equipment. This requirement hinders the ability of a system designer to integrate soft sensors into soft robotic systems.

In this paper we design, fabricate, and characterize a new soft sensor which benefits from a combination of RFID tag design and microfluidic sensor fabrication technologies. We designed this sensor using the working principle of an RFID transporter antenna, but one whose resonant frequency changes in response to an applied strain. This new microfluidic sensor is *intrinsically stretchable* and can be reversibly strained. This sensor is a *passive* and *wireless* device and as such, it does not require a power supply, and is capable of transporting data without a wired connection.

This strain sensor is best understood as an RFID tag antenna; it shows a resonant frequency change from 860 MHz to 800 MHz upon an applied strain change from 0% to 50%. Within the operating frequency, the sensor shows a stand-off reading range of over 7.5 metres (at the resonant frequency). We characterise, experimentally, the electrical performance and the reliability of the fabrication process. We demonstrate a pneumatic soft robot that has four microfluidic sensors embedded in four of its legs,

and we describe the implementation circuit to show that we can obtain movement information from the soft robot using our wireless soft sensors.

7.1 Introduction

7.1.1 Soft sensors

Soft Sensors is an application-driven research field and has received much attention in recent decades. A soft sensor is a measuring tool that is made of a single polymer or a mixture of soft polymers. These soft polymers are usually *softer* than the materials they interact with which make them inherently safe. One prominent example is electronic skin. Electronic skin is also called ‘second skin’ referring to its softness; electronic skin is *softer* than human skin and makes it to an ideal substructure for sensor arrays [1]. A close relative of the field *Soft Sensors* is the field of *Soft Robotics*. One motivating factor for using *Soft Robotics* is the fact that the materials of the robots are *softer* than the environments with which they interact, and this compliance makes them ideal for applications involving human-robot interaction [2-4].

Autonomous agents that *perceive* and act upon their immediate environment (robots) are influenced by sensor research. Sensor research impacts a robots’ sensor modalities, sensor accuracy or measurement range besides others. The concept of integrating sensing capabilities at low cost has also become increasingly important, especially for certain subgroups in robotics, namely soft robotics, modular robotics and swarm robotics. In such cases, lower cost systems are motivated by *design for manufacturability* allowing one to commercialize or to scale a robot system. In the last

decade, the community has started to make soft robotic actuators, such as: i) ionic actuators, [5-7] ii) pneumatic actuators, [8-11] or iii) dielectric actuators [12-14] to just name a few. These actuators can benefit from soft sensors from feedback force control.

Rogers et al. have proposed a stretchable sensor that is made of curvilinear silicon ribbons in an elastic substrate [15]. This novel work allows high-precision complex active electronics to be densely integrated over a few square centimeters area, while achieving high degrees of stretchability, bendability, and twistability. Park et al. designed a soft artificial skin [16] with multiple layers of micro-scale liquid metal channels embedded in an elastomeric substrate to detect multi-axial strain and normal pressure. Single-core copper wire were used in the above researches as interconnect to an external data-logger. Other research work, such as (Vogt et al. 2013), [17] (Tabatabai et al. 2013), [18] (Y. L. Park et al. 2012), [19] and (Majidi et al. 2011) [20] have also used similar connection methods.

Although the soft sensors mentioned above show a promising future for stretchable electronics, they are active sensors that require a power supply and signal processing capabilities such as a microcontroller with analogue-digital converters. As reported in (Teng et al. 2018), [21] each of these sensing systems may has drawbacks in the interconnection to other devices, and these limitations hinder the uptake of the soft-sensor devices into integrated systems. Embedding several such sensors in an untethered soft robotic system is difficult due to power consumption and practical considerations in wiring.

Stretchable antennas which have great potential to be used as wireless soft sensors

have been reported in recent years. Stretchable liquid metal antennas have been presented by (Wu et al.), [22,23] (Whitesides et al.), [24] and (Dickey et al.). [25] Although these antennas have shown fascinating electronic and mechanic properties, they require coaxial RF connector or hardwiring to connect to external data processing equipment, which limits their capability of being implemented in sensing applications such as movement monitoring. (Huang et al.) [26] mentioned the idea of integrating a measurement chip in stretchable antennas, but the researchers didn't provide the solution of integration. Rogers et al. demonstrated epidermal electronics using near field communication; [27] this wireless sensor is biocompatible and achieves sensor reading ranges of a few centimetres. Wu et al. also proposed a reversibly stretchable, large-area wireless strain sensor [28] which can work wirelessly over 5m with a strain limitation of 15%. These studies pave the way for making wireless stretchable antennas that can be used as soft sensors in soft robotic systems.

7.1.2 Design of a new soft RFID sensor

In this paper we present the design, fabrication, and characterisation of a long-range monitoring wireless strain sensor, which is capable of remotely detecting high tensile dynamic strain up to 50% at over 7.5 metres. This sensor benefits from a combination of RFID (Radio Frequency Identification) technology and microfluidic electronics fabrication technology. The proposed sensor is also a configurable RFID tag antenna. The RFID IC chip we integrated in the proposed sensor has very small dimensions (0.4 mm×0.4 mm×0.2 mm), so it won't affect the deformability of the sensor. The electronic

properties of this antenna are highly sensitive to mechanical strains at the frequency of operation (800MHz-860MHz). This sensor can withstand repeated mechanical strain whilst retaining electrical functionality, and can return to its original state after stretching. In comparison to existing stretchable sensors, our sensor is a completely passive and wireless device. The feature of wireless power extends the lifetime of the device, removing the need for changing batteries, or integrating an energy harvesting system.

Additionally, most of existing gallium-based liquid alloy sensors were designed based on measuring the resistance change of the liquid metal, but the long-time stability of these sensors will be affected by the oxidation of gallium (gallium-based liquid alloy is easily oxidized). Our proposed RFID strain sensor was designed based on resonant frequency change upon strain. Benefiting from the high electrical conductivity of Galinstan, the skin depth (a measure of how closely electric current flows along the surface of a material) of Galinstan under 800MHz-860MHz is only a few micrometres. Even though the Galinstan in the channels has a thin oxide layer at the surface, the oxide won't have a large effect on the resonant frequency of the sensor. This RFID sensor can be embedded into soft robots without requiring any power consumption from the original robotic device.

In this work we describe the potential of integrating the proposed RFID sensor into soft robots which have pneumatic actuators. Most of the existing soft sensors have a requirement to be hardwired to power supplies or to signal-processing equipment. This dependence on electrical tethers limits the practical use of soft sensors in many

promising applications in real-world conditions. Although, recently, researchers have presented some fully untethered soft robotic systems, [29-32] most of them require bulky on-board components such as batteries, microprocessors, pumps or motors. These on-board components add additional weight on the soft systems and thereby the systems need to carry more powerful actuators. In this work, we intended to develop untethered soft sensors which can work wirelessly by dispensing, entirely, with the need for onboard power and processors. The proposed sensor can be fully embedded into soft robots without adding any other devices or additional electrical tethers, so that one can eliminate the wire and weight pressures on soft robotic systems. The relatively long measurement working range can allow the soft robots to move freely in a reasonably large area.

7.1.3 RFID technology

Radio Frequency Identification (RFID) is a low-cost technology that allows the passive wireless communication of data. In recent decades, RFIDs have been used in many projects such as in robot motion sensors, [33] indoor localization, [34] and distributed sensor networks. [35] An RFID system usually consists of a transponder (sometimes called RFID tag) and the reader. The reader transmits electromagnetic waves to reach out to the RFID tag; if the RFID tag is within the operating range, it utilizes the energy of the incoming electromagnetic wave to transmit a new electromagnetic wave that contains RFID tag specific information. The information usually contains a unique serial number. The reader receives and visualizes the

information. RFIDs can be operated in different frequency bands. While the LF (125-134KHz) and HF (13.56MHz) bands use magnetic flux coupling, the UHF (300MHz-3GHz) band uses electromagnetic wave coupling. The communication distance of the UHF band is over 16m, which outperforms the LF and HF bands. In this work, the proposed antenna operates in the UHF band.

7.1.4 Sensor constitutes

The sensor we present in this work consists of an RFID chip and a half-dipole antenna. The antenna consists of eutectic liquid alloy filled microfluidic channels in an elastic silicone substrate. The eutectic alloy we used is Galinstan. Galinstan [36] is a family of room temperature liquid eutectic alloys consisting of gallium (Ga), indium (In), and tin (Sn, stannum in Latin). Gallium-based room temperature liquid alloy has previously been used in strain, [16, 37-39] pressure, [16,37,40] curvature, [20,41] and shear [42] sensors. It can be easily injected into channels of soft structures. The resistance of a channel can be approximated by $R = \frac{\rho}{A} * l$ (ρ is resistivity of the liquid metal, A and l are cross-section area and length of the channel respectively); so the channel resistance changes through deformation. The Galinstan we made consists of 68.5% Ga, 21.5% In, and 10% Sn; its melting temperature is -19 °C; and its electrical conductivity is $3.46 \times 10^6 \text{ S}\cdot\text{m}^{-1}$. [36] Galinstan indicates favourable properties as channel conductor. We observed reliable liquid distributions in the antenna channels despite extreme twisting, stretching and folding.

We used Ecoflex as the elastic silicone substrate. This silicone material has a

Young's modulus of ~ 69 kPa.[43] We chose Ecoflex to be the substrate due to its favourable properties, it is: easy to synthesise, easy to handle, low cost, and biocompatible. [44] In tensile tests with the ASTM D412 system, the maximum elongation of Ecoflex 00-50 (type 00-50) is 980% (defined as the percentage change in length or $((l - l_0)/l_0) \times 100\%$).

7.2 Working principles

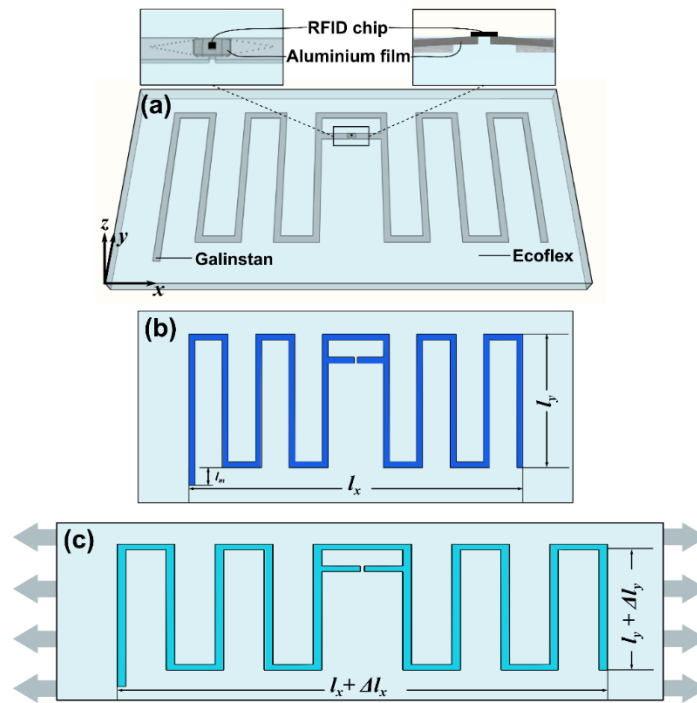


Figure 7-1: (a) Schematic diagram of the stretchable microfluidic sensor. Galinstan is enclosed in Ecoflex substrate while an RFID chip is bonded on a piece of aluminium foil which is inserted in the channels. Detailed and cross-section figures of the part near RFID chip are presented. Directions of x , y , and z axis are indicated; (b) Initial state of the antenna when it's not stretched. The effective antenna length on x -direction and y -direction is defined as l_x and l_y respectively. Notice: The electrical length of the entire antenna is $l_x + 10l_y + l_m$. The non-symmetric part, l_m is used for fine impedance matching between the antenna and the RFID chip; (c) When the soft antenna is stretched, the effective antenna length on x -direction and y -direction is defined as $l_x + \Delta l_x$ and $l_y + \Delta l_y$ respectively.

Figure 7-1a depicts a stretchable meandered half-wave dipole antenna. We embedded an RFID chip into the antenna design. The RFID chip is bonded on

aluminum pads and inserted in between two Galinstan channels. The RFID chip consumes power from received signals and backscatters them without requiring an external power supply depicting a wireless *passive* soft sensor.

Figure 7-1 b and c indicate how deformation of an antenna can change its dimensions. If the channel dimensions change, the channel resistances change and therefore the entire antenna and its parameters change. The RFID chip backscatters signals with varying amplitude and phase based on the degree of stretching.

7.3 Implementation in soft robotics

Figure 7-2 shows the schematic diagram of our soft RFID sensor implementation. The implementation comprises a pneumatic soft robot with four embedded soft RFID tags, one tag on each robot leg, and the electronic circuitry to transceiver data. The *Controller* uses the *Signal Generator* to generate a high frequency carrier signal. An *Amplitude Shift Keying* (ASK) module modulates the amplitude of the carrier signal to decode information. A binary “one” consists of a fixed amplitude and frequency; a binary “zero” is a zero-voltage output. The modulated signal is passed through a power amplifier preparing the signal for transmission. The signal lies on port 1 of a circulator circuit. Port 2 of the circulator outputs the signal to an antenna, therefore broadcasting the signal. The soft RFID tags receive the signal, utilize its energy and transmit a new signal that incorporates their unique IDs. The antenna receives the signals from the soft RFID tags and outputs them to port 3 of the circulator. The circulator ensures that outgoing and incoming signals do not interfere with one another. The incoming signals

from the soft RFID tags pass a low-noise filter, an ASK demodulator and are ultimately inserted into an analogue-to-digital converter. The controller analyses the various signals (distinguishable through their IDs) with regard to their amplitude and phase.

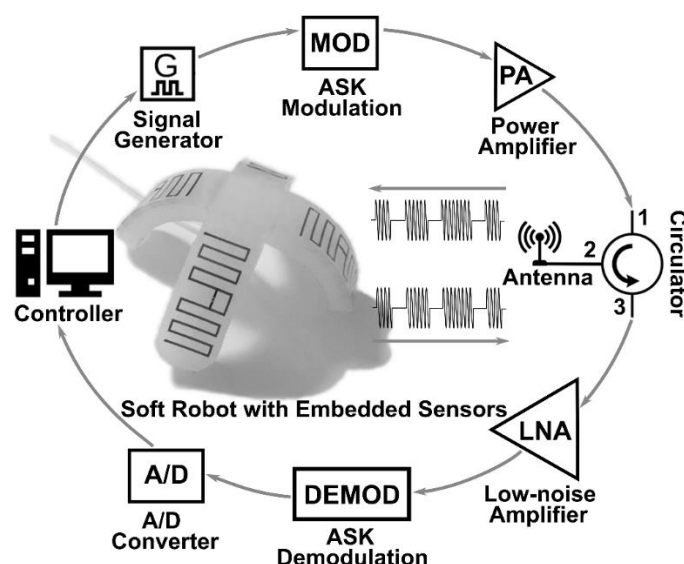


Figure 7-2: The electronic system for measuring data from a pneumatic soft robot that contains four embedded microfluidic strain sensors.

7.4 Antenna design

7.4.1 Selection and design of the antenna

The antenna design of our soft RFID sensor is different from other antenna designs because of power and size requirements. The antenna powers the RFID chip with incoming signals; we do not require a power supply. We decided to design the soft RFID sensor as small as possible to attach the RFID tags to even small objects making our sensor more applicable. Since the soft RFID sensors can be attached in any arbitrary orientation, we ensured 360 degree or *omnidirectional* readouts by using a half-wave dipole antenna design. The effective electrical length of a half-wave dipole antenna is

half the wavelength of the operating frequency of the system. This antenna design is commonly used in Radio Frequency (RF) systems with omnidirectional radiation patterns perpendicular to the antenna axis.

In previous work, small antenna sizes were accomplished by using micro-strips. [45] However, they suffered directional read-out constraints and low efficiency. Our design uses a Meander Line Antenna (MDA) to achieve long reading ranges and small antenna size. MDA is a derivative of the dipole antenna and achieves high efficiencies [46] for small antenna sizes. [47,48]

Stretching the soft half-wave dipole antenna as illustrated in Figure 7-1b causes a change in the dimensions of the antenna in both the x- and y-directions. An increase in strain in the x-direction decreases the thickness of the soft polymer, due to the Poisson effect, and also decreases its height by Δl_y . Therefore, stretching the soft RFID tag changes the electric length of the antenna; each infinitely small change in electric length shifts the resonant frequency. Now, if we send signals to RFID tags, the frequency of the carrier signal can be changed to the specific resonant frequency of the antenna's current electric length. The backscattered signals from the RFID tags will indicate phase and amplitude changes due to the resonant frequency.

7.4.2 Antenna matching

As mentioned in the previous section, the RFID antenna utilizes power from the incoming electromagnetic waves to supply power to the RFID chip. *Impedance matching* between the RFID chip and the antenna is paramount in RFID antenna design

because it affects how much power the antenna is able to reflect, hence determines the antenna's operational range.

Figure 7-3 indicates how to match impedances; The best impedance matching for maximum power transmission is conjugate impedance matching, which means $R_a = R_c$ while $X_a = -X_c$. The RFID chip we used (Monza R6, Impinj) possesses an impedance of $Z_c = (13.5 - j 126)\Omega$ at 860MHz. Therefore, we designed the transporter antenna to match the impedance of this RFID chip.

The theoretical impedance of a half wave dipole antenna in free space is $73+j42.5$ Ohms [49] which makes it impossible to match the impedance of the RFID chip. Therefore, we used the T-match method [50] to match the impedance between transporter antenna and RFID chip. Figure 7-3 b and c indicate that a half-wave dipole antenna can be changed through a centred short-circuit stub. The antenna *source* is connected to a small dipole of length $a \leq l$ and is placed at a close distance b from the first and larger dipole. The electric current distributes along the two main radiators according to the size of their transverse sections. The impedance Z_a at the source points is given by Equation 7.1:

$$Z_a = \frac{2Z_t(1+\alpha)^2 Z'_a}{2Z_t + (1+\alpha)^2 Z'_a} \quad (7.1)$$

In Equation 7.1, Z'_a is the original dipole impedance taken at its centre in the absence of a T-match connection, whereas Z_t is the impedance created by the matching stubs. α is the current division factor between the two connectors, $\alpha = \ln(b/re') / \ln(b/re)$. re and re' are the equivalent radii of the initial dipole and the matching stub.

We performed impedance calculation with finite element method (FEM)

simulations with Computer Simulation Technology Microwave Studio (CST Microwave Studio). FEM includes the use of mesh generation techniques for dividing a complex structure into a large number of small elements. Calculations are made for every single element and combining the individual results can give us the conclusive results of the structure. We modified the edge of the antenna to be asymmetric, so that created l_m in Figure 7-1b, for a final fine matching step.

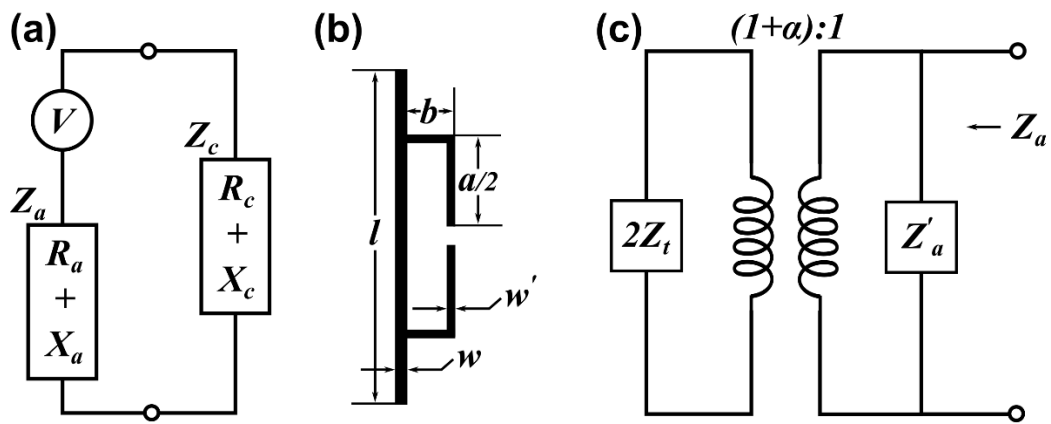


Figure 7-3: (a) Equavialent circuit of the RFID chip and the transporter antenna. Z_a is the total impedance of the transport antenna whereas Z_c is impedance of the RFID chip; (b) Schematic diagram of T-matching for a dipole antenna. The l represents length of the original dipole antenna. This antenna is connected at the centre to a short second dipole. The close distance between matching stub and the original antenna is b , whereas w and w' are the widths of the original dipole antenna and the mating stub respectively; (c) Equivalent circuit at the source point of the dipole antenna after T-matching. Z'_a is the impedance of the first dipole antenna without T-matching while Z_t is the impedance that the matching stub created. The α in the ratio is the current division factor between the two connectors.

7.4.3 Materials and Fabrication Methods

Figure 7-4 shows the soft-lithography fabrication process of our stretchable antenna. We designed and fabricated an antenna mould with a laser micromachining system (Protolaser U3, LPKF) and a self-adhesive vinyl film (CRAFTRKZO, d-c-fix®)

as shown in Figure 7-4a. A piece of vinyl film was attached to an Acrylic substrate (2mm Acrylic Cast, AMARI). The channel profiles were cut with the LPKF laser system. We peeled the vinyl residuals (negative) from the substrate and laid a 2mm-thick acrylic frame along the mould edges as indicated in Figure 7-4b. We synthesized Ecoflex 00-50 (Reynolds Advanced Materials, 1:1 ratio), degassed it in a vacuum chamber and poured the soft polymer into the mould as illustrated in Figure 7-4c. We put the mould into a convection oven at 65°C for 20 minutes, then removed the soft structure from the mould and flipped it over. A 150µm thin Ecoflex 00-50 layer were fabricated with spin coater to seal the unfolded channels in Figure 7-4d. We made small incisions in the centre of the thin Ecoflex layer to embed the RFID chip; the RFID chip (Monza R6, Impinj) was bonded on an Aluminum film with a bonding machine (FB-300 manual RFID wrapping machine) and inserted in the channels. During the bonding process, the chip was aligned to the substrate with a vacuum sucker, microscopes and cameras in the bonding machine, an adhesive material was dispensed between the chip and the aluminum film, then the chip was firmly bonded on the aluminum film with hot-pressing for 10 seconds. We inserted two injection needles into the soft structure as illustrated in Figure 7-4e. One needle was used to inject the Galinstan into the channel, the other needle was used to release air pressure. The Galinstan made contact with the Aluminum pads of the RFID chip without leaking to the surface. At the end, we applied a thin film of uncured Ecoflex on top of the device to seal the open holes created by chip insert and liquid metal injection.

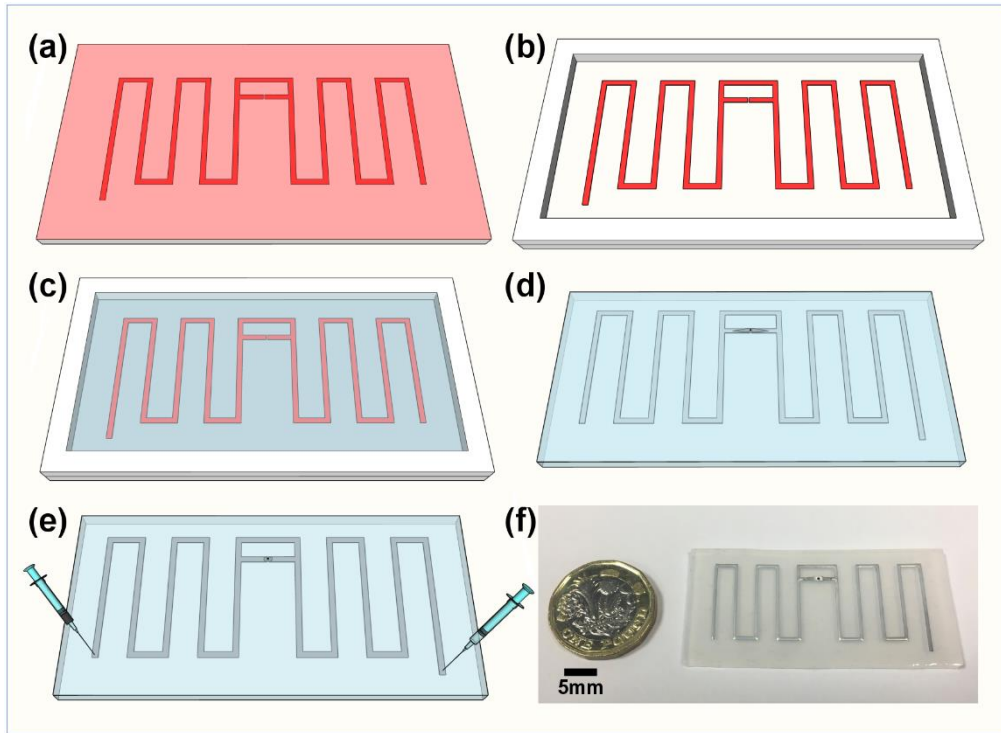


Figure 7-4: Fabrication process and prototype of the stretchable microfluidic sensor (RFID tag antenna). (a) cut the sensor profile on a piece of self-adhesive vinyl attached on an Acrylic substrate. Notice: the red and pink parts are a same piece of vinyl. Two different colours are used here to show the laser-cut profile clearer; (b) the unwanted part of vinyl was peel off, a 2 mm-thick Acrylic frame was stuck on the substrate to form a soft-lithography mould; (c) uncured Ecoflex with a controlled height of 2 mm was poured into the soft-lithography mould; (d) the casted piece of Ecoflex was sealed with another 0.15 mm Ecoflex film and the RFID chip bonded on aluminium film was inserted into the channels; (e) two needles were used to inject Galinstan into the channel; (f) Photograph of the final prototype.

7.4.4 Experimental Design

The permittivity of Ecoflex 00-50 and the resistivity of Galinstan are parameters that are required to simulate S_{11} ; S_{11} is the input reflection coefficient or input return loss. S_{11} indicates the radiation efficiency of the antenna and reaches its maximum value at resonant frequency. We used an Agilent 85070E dielectric probe kit to measure the permittivity variations of Ecoflex 00-50 in a frequency range from 200 MHz to 1.2 GHz as shown in Figure 7-5b. We simulated changes in resonant frequency and radiation

efficiency under strain variations between 0% to 50% and a step size of 5%.

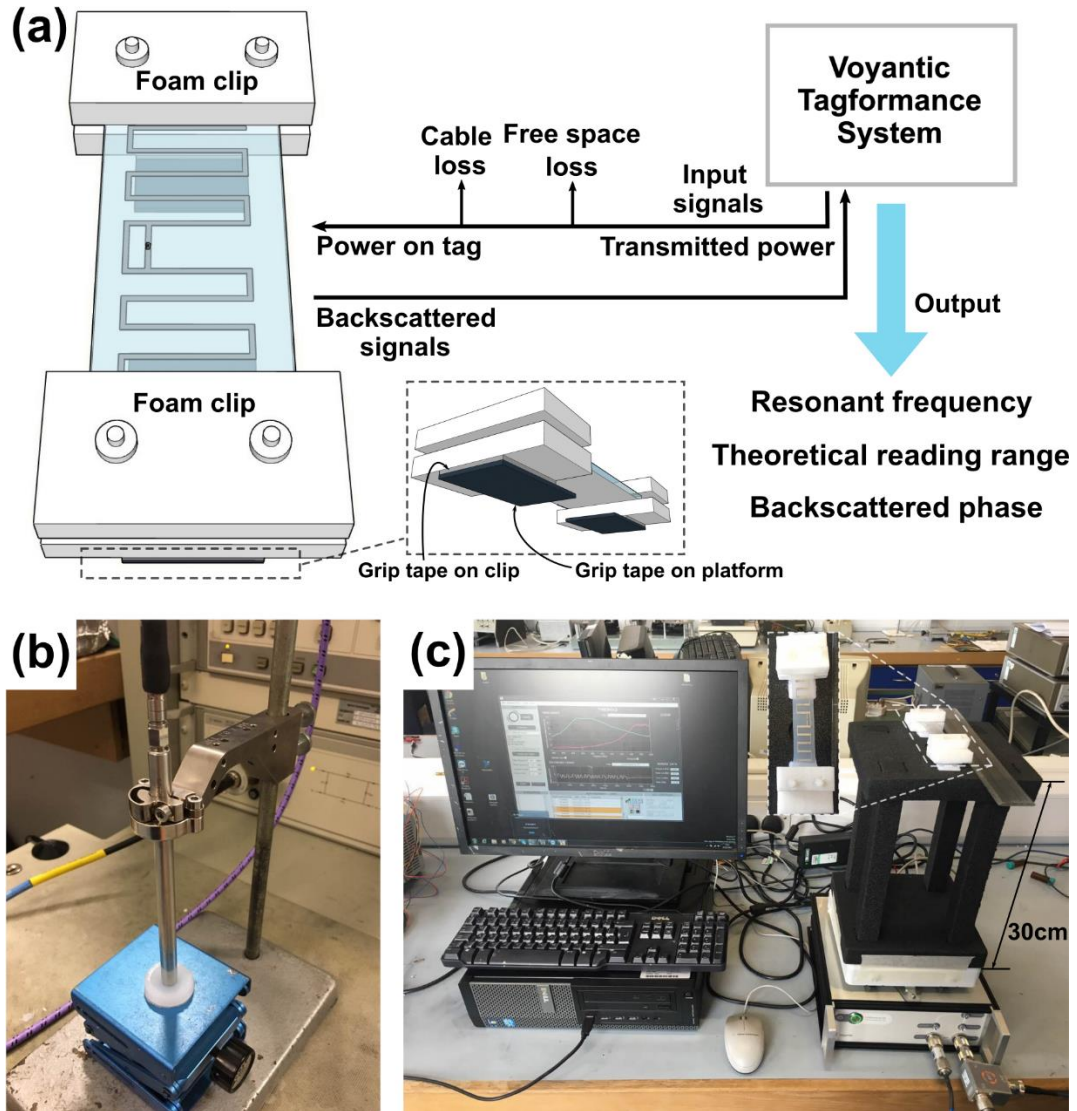


Figure 7-5: (a) We used Voyantic Tagformance system to measure characteristics of the proposed antenna. This measurement system sends input signals to the tag antenna with transmitted power. The power received on tag is the transmitted power minus cable loss and free space loss. RFID chip in the tag antenna receives the input signals, absorbs energy in the signals, and then sends backscattered signals back to the measurement system. According to the results of the measurement system, we can know the resonant frequency and the theoretical reading range of the tag antenna, as well as the phase of the backscattered signals. We affixed the two edges of the tag antenna with clips made of rigid foam. In order to stretch the tag antenna and hold its position for measurement, we stuck grip tape on the surface of the foam clips, and on the measurement platform. (b) Experimental setup for measurement of the permittivity of Ecoflex 00-50 with the Agilent 85070E dielectric probe kit system. (c) Photograph of the experimental setup of the soft antenna and the Voyantic Tagformance system.

We used a Voyantic Tagformance system to measure the characteristics of our antenna design; namely, the frequency modulation of our soft RFID sensor due to strain variations as indicated in Figure 7-5a and c. This setup allowed us to determine the resonant frequency, the theoretical RFID reading range, and the phase changes of the backscattered signals for every applied strain in the range from 0% to 50% with a step size of 5%. We repeated each measurement seven times to indicate the soft polymer's reversibility. We fabricated three sensor samples to enable us to evaluate the repeatability of our fabrication process. We did a cyclic stretching test to prove the reliability of the proposed sensor when it is stretched to 50% for 240 times. It is worth mentioning that we calculated the strain value in all the experiments with $((\frac{\Delta l_x}{l_x}) \times 100\%)$, l_x and Δl_x are as shown in Figure 7-1c. The length we used in calculation is the effective antenna length in x-direction, not the distance between the foam clips. We also tested the soft RFID sensors when we applied twists of 0°, 45°, and 90°.

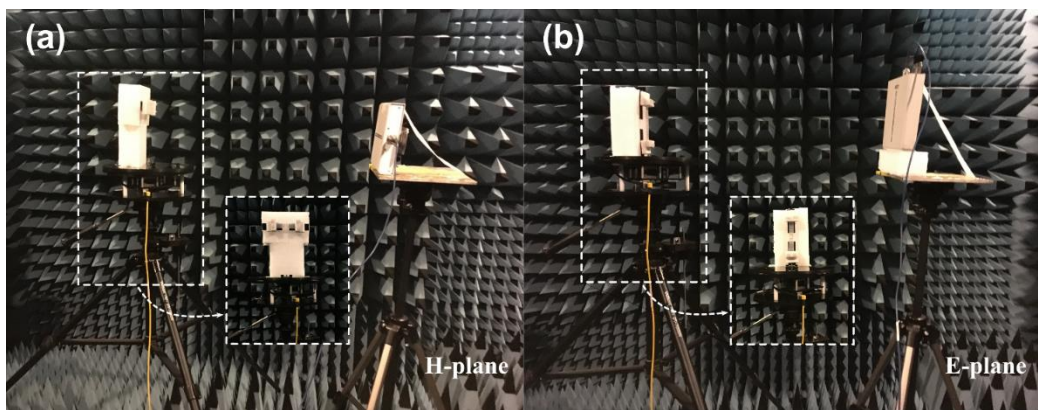


Figure 7-6: Radiation pattern measurement in H-plane and E-plane in an anechoic room with Diamond Engineering Automated measurement system and an automatic turntable. In the measurement, the reader antenna holds its position while the strain sensor (transporter antenna) turn with the turntable.

We used a diamond engineering automated measurement system and an automatic

turning table in an anechoic room to measure the radiation patterns of our soft RFID sensor in the H- and E-plane. An anechoic room absorbs reflections from acoustic and electromagnetic waves. We analysed the directivity of the antenna (in the H- and E-planes) when subjected to strains of 0%, 25%, and 50%.

7.5 Results

7.5.1 Permittivity of Ecoflex 00-50

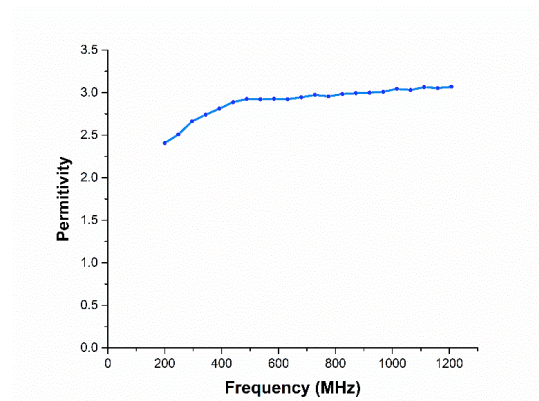


Figure 7-7: Permittivity of Ecoflex type 00-50 in the frequency range of 200 MHz~1.2 GHz. Measured with Agilent 85070E dielectric probe kit system.

According to the results in Figure 7-7, the relative permittivity (ϵ_r) of Ecoflex 00-50 is nearly stable at 3 in the range of 500 MHz-1.2 GHz. The operating frequency range of our sensor is 800 MHz to 860 MHz, which is covered in this stable range; Thus, we can take ϵ_r of Ecoflex as a constant in calculation and simulation.

7.5.2 Simulation of antenna efficiency

When our soft RFID sensor is stretched, its antenna parameters such as resonant frequency and radiation efficiency change. Below we analyze, analytically, the antenna parameters due to strain variations and we apply an ideal folded half-wave dipole

antenna model.

The resonant frequency of a half-wave dipole antenna [51] is given by

$$f_r = \frac{c}{2l_e\sqrt{\varepsilon_e}} \times r \quad (7.2)$$

l_e is the effective electrical length of the antenna; f_r is the resonant frequency; ε_e is the effective permittivity of the antenna substrate; and r is the correction factor of a folded half-wave dipole antenna. We can estimate the effective relative permittivity through [52]

$$\varepsilon_e = 1 + \left(\frac{\varepsilon_r - 1}{2}\right) \frac{K_1}{K_2} \quad (7.3)$$

ε_r is the relative permittivity of Ecoflex, which is considered as a constant here; $K_1 = \frac{K(k_1)}{K'(k_1)}$ and $K_2 = \frac{K(k_2)}{K'(k_2)}$ while $K(k)$ is a complete elliptic function of the first kind and $K(k')$ is its complimentary function. In the K function, $k_1 = \frac{l_e}{l_e + 2s}$ and $k_2 = e^{-\frac{\pi s}{2h}}$ whereas l_e is effective electrical length of the antenna, s is the gap at the feed point, and h is height of substrate of the antenna. According to formula (2) and (3), resonant frequency of a half-wave dipole antenna will change when its effective electrical length or its substrate height changes.

Equations 7.2 shows the resonant frequency of a half-wave dipole antenna changes with its effective electrical length, while Equation 7.3 indicates that the resonant frequency also changes with the substrate height of the antenna.

Rigid antennas possess a fixed effective electrical length, whereas our soft antenna's effective electrical length changes due to strain. Due to the Poisson effect, our antenna physically changes according to

$$\frac{\Delta l_y}{l_y} = 1 - \left(1 + \frac{\Delta l_x}{l_x}\right)^{-\nu} \quad (7.4)$$

l_x is the antenna length; Δl_x describes a change in antenna length; l_y is the antenna width; Δl_y describes a change in antenna width; and the initial (not stretched) electrical length of our antenna is $l_x + 10l_y + l_m$. Since $l_m \ll l_x + 10l_y$, we neglect the effect of l_m here.

We insert Equations 7.3 and 7.4 in Equation 7.2 and receive a new formulation for the resonant frequency for our soft antenna

$$f_r = \frac{c}{2(l_x(1+\frac{\Delta l_x}{l_x})+10l_y(2-(1+\frac{\Delta l_x}{l_x})^{-\nu})) \times \sqrt{1+(\frac{\epsilon_r-1}{2})^{\frac{K_1}{K_2}}}} \times k \quad (7.5)$$

ν is the Poisson ratio of Ecoflex type 00-50.

We performed an electromagnetic finite element simulation using Computer Simulation Technology (CST) to determine S_{11} , the input return loss, under a variety of strains. S_{11} 's maximum indicates the antenna's resonant frequency. Figure 7-8 indicates the simulation results; the soft antenna has been strained from 0% to 50% with a step size of 5%; the S_{11} peak values are all below -20 dB at resonance frequency for each strain condition indicating that 99% of the power from the input signal is scattered back from the soft RFID sensor. We successfully matched antenna to RFID chip resistance.

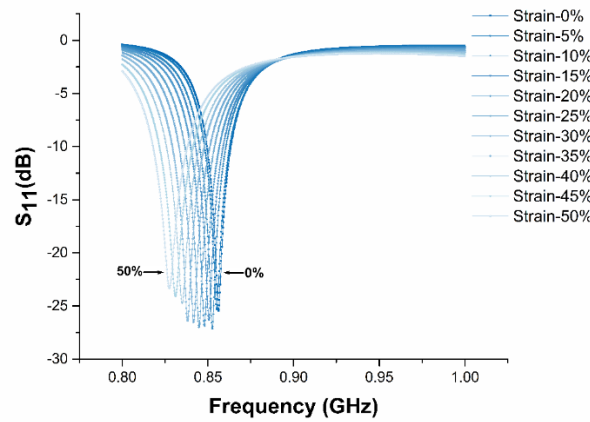


Figure 7-8: Finite elements simulation results. Under 0% strain condition, simulated resonant frequency of the antenna is 856 MHz. The simulated resonant frequency continuously goes down to 827 MHz when

the antenna is under 50% strain.

7.5.3 Resonant frequency upon strain

The Voyantic Tagformance measurement system controls the power of the signal that we transmit to the soft RFID sensor. First, we set the initial signal power to 25 dB. Second, we gradually decreased the signal power until we could not detect the backscattered signal from the soft RFID sensor anymore. Power of the input signal was recorded as Transmitted Power (P_t). We repeated this process for each sampling frequency in the frequency band of 800-880 MHz, with a step of 1 MHz.

As indicated in Figure 7-5a, the power received by the soft RFID tag antenna (P_{tag}) can be calculated as

$$P_{tag} = P_t - L_c + G_t - FSPL \quad (7.6)$$

L_c are cable losses; G_t is the Gain of the Voyantic Tagformance's transmitter antenna; and $FSPL$ are losses due to free space transmissions. $L_c, G_t, FSPL$ can be determined by calibrating the Voyantic Tagformance.

Figure 7-9a shows the minimum transmitted power (P_t) for each sample frequency to result in a detectable backscattered signal from the soft RFID sensor. Figure 7-9b indicates the power received on tag antenna (Power on tag, P_{tag}) corresponding to the minimum P_t for each sample frequency.

The theoretical measurement reading range of the soft RFID sensor is frequency dependent and can be calculated by

$$R_r = \sqrt{\frac{P_{max,EIRP}}{P_{tag}}} \times \frac{c}{4\pi f} \quad (7.7)$$

$P_{max,EIRP}$ is the maximum signal power of the Voyantic Tagformance (default: 3.28 W).

P_{tag} in this formula is related to the minimum transmitted power. Figure 7-9c depicts the reading ranges calculated with formula (7) for the various frequencies; our soft RFID sensor has a reading range of approximately 7.5 meters, whereas this range increases if the soft sensor is under strain. The reading range of the sensor increases to 10 meters under a strain of 50%. The resonant frequency decreases from 862 MHz in idle state (no strain) to around 802 MHz under 50% strain. Figure 7-9d illustrates the backscattered signals from the soft RFID sensor under different strain conditions.

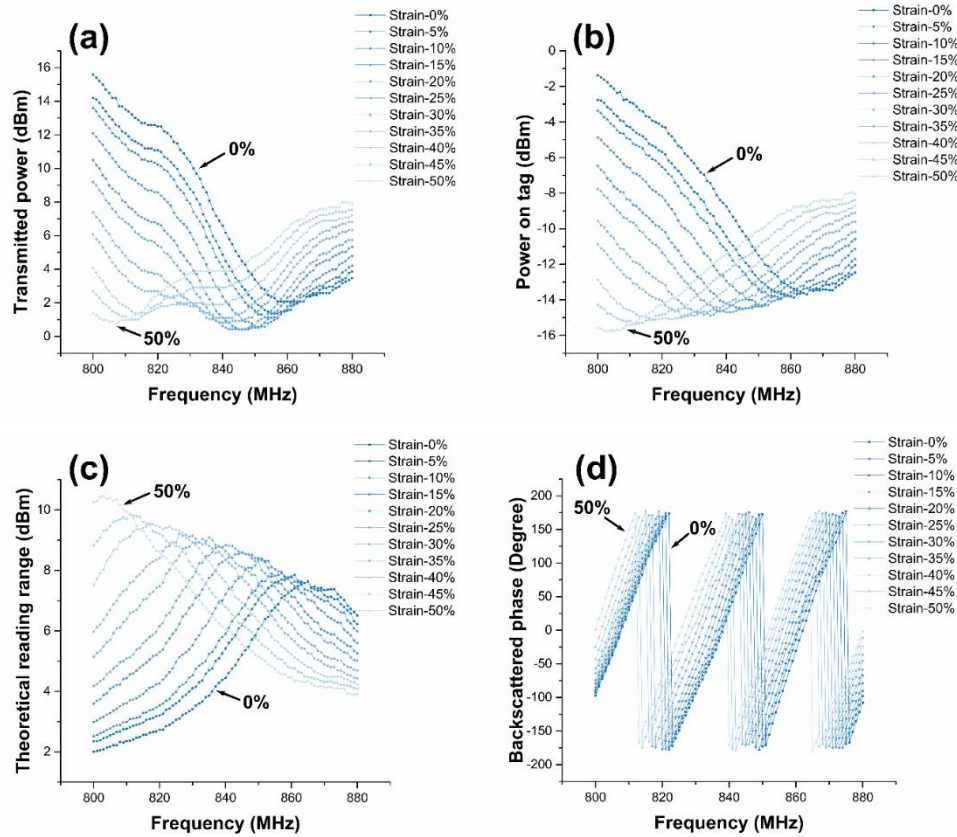


Figure 7-9: (a) Transmitted power. The minimum transmitted power recorded for the sensor under 0% - 50% strain, with a step of 5%. (b) The power received on tag, which was calculated based on the transmitted power and cable and free space loss. (c) Theoretical reading range forward, which was calculated based on the power received on tag. (d) Backscattered phase in the frequency band of 800-880MHz (with a step of 1 MHz) when the sensor was under 0% - 50% strain, with a step of 5%.

7.5.4 Repeatability and reliability test

We tested the reliability of our soft RFID sensor by performing seven strain experiments. We measured the resonant frequency under 0% to 50% strain with a step size of 5%. Figure 7-10a shows the average value and standard deviation of the resonant frequency for each strain. The resonant frequency dropped approximately 61 MHz (from 861 MHz to 800 MHz) from 0% to 50% strain, whereas the maximum standard deviation did not exceed 2.6 MHz. We performed a similar experiment in Figure 7-10c; once we reached 50% strain, we left the device stretched for 24 hours in the laboratory before we gradually released the device to 0% strain. We also involved the simulation results of resonant frequency upon strain in Figure 7-10a as a comparison with the measurement results. In the simulation, the resonant frequency changed 29 MHz in total (from 856 MHz to 827 MHz) from 0% to 50% strain, which is smaller than the measurement results.

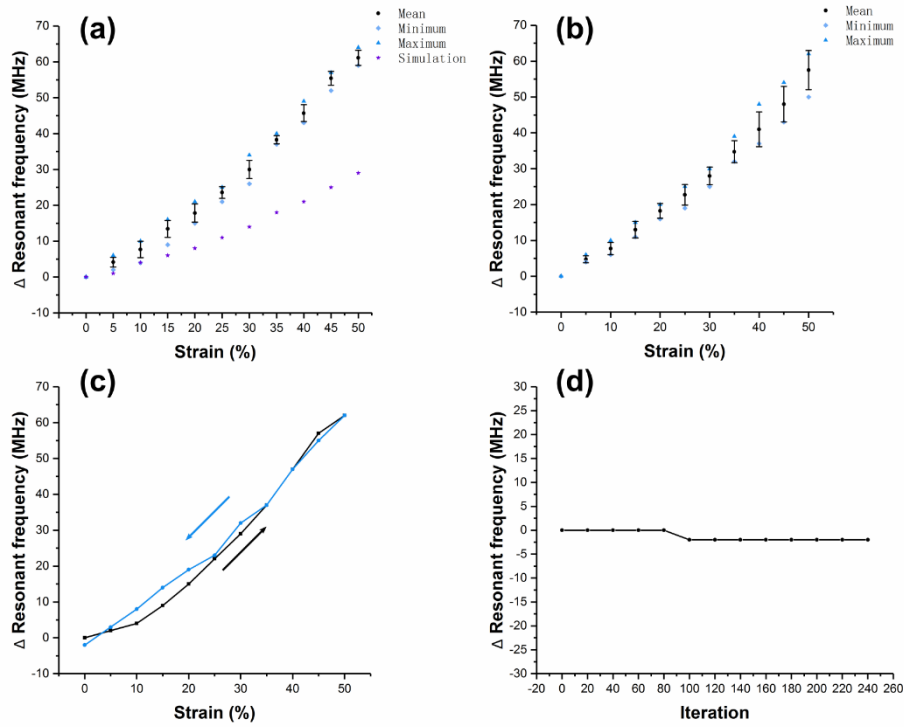


Figure 7-10: (a) Resonant frequency change upon different strain conditions. In the experiment, we did 7 tests on the same prototype. Error bars represent standard deviation. (b) Resonant frequency change upon different strain conditions. In the experiment, we did one test on 3 different prototypes with same design and same fabrication method. Error bars represent standard deviation. (c) Hysteresis test. A prototype was tested from 0% to 50% of strain, leave for 24 hours, then from 50% back to 0%. (d) Cyclic stretching test. The sample was stretched to 50% of strain then back to 0% for 240 times. Resonant frequency of the sample was measured each 20 times of stretching.

We fabricated another three prototypes of the same sensor design and again performed strain-resonant-frequency tests. Average value and standard deviation of the resonant frequency for each prototype are shown by Figure 7-10b. Figure 7-10b shows similar results than Figure 7-10a. Figure 7-10d depicts a cyclic stretching test to prove the reliability of the proposed sensor when it is stretched 240 times. As shown in the results, resonant frequency of the sensor remains stable in the test (only dropped 2 MHz between 80 and 100 of iteration). We also measured resonant frequency response of a soft RFID sensor due to twist rather than strain and put the results in the supplemental

information. According to the results, the electrical characteristics of our soft RFID sensor at frequency of operation are highly sensitive to mechanical strain while having no response to twisting.

7.5.5 Radiation pattern

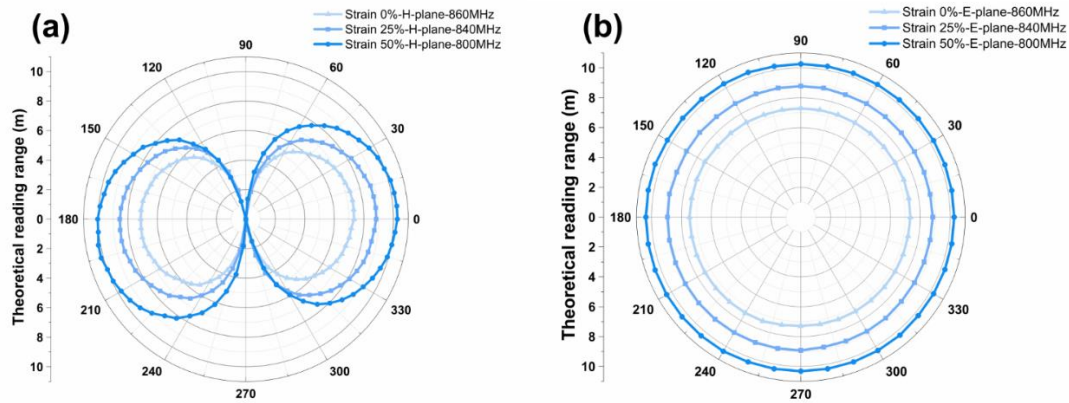


Figure 7-11: Theoretical reading range of the antenna in H-plane (left) and E-plane (right) with 0%, 25% and 50% length stretching in x-direction. The data were recorded for every 5-degree rotation in H-plane and every 10-degree rotation in E-plane.

We measured the theoretical reading range from our soft RFID sensor in the H- and E-plane with an antenna measurement system consisting of antenna measurement studio 5.5 and Diamond Engineering. The right subfigure of Figure 7-11 shows that omnidirectional radiation patterns were measured in the H-plane. The left subfigure of Figure 7-11 indicates that the antenna is constrained in directions that are parallel to the sensor's x-axis ($60^\circ + n\pi < \theta < 120^\circ + n\pi$; n is an arbitrary integer). This constraint might have to be considered in certain applications. The different strain conditions have an impact on our soft RFID sensor's reading range *radius*; if strain is applied, the reading range radius increases.

7.6 Discussion

The results show that our soft RFID sensor changes its resonant frequency and the phase of its backscattered signal as function of strain.

Our measurements correlate with our simulations, the initial resonant frequency of all our sensor prototypes lies in the region of 860 MHz. In our simulation, the resonant frequency did not decrease as much under strain as in our experiments. This mismatch could be caused by the simplified model that we used for the Poisson effect or a potentially emerging resistance between the Galinstan channels and the RFID chip that might occur under strain.

We matched the resistances of the RFID chip and the antenna under 0% strain. Once we apply strain, the resistance of the antenna changes, hence the resistances of the RFID chip and antenna do not perfectly match anymore. Therefore, we expected a decrease in the measurement reading range with an increase in strain. However, the measurement reading range increased with an increase of strain. One explanation could be that a folded dipole antenna consists of conductors with opposite current flows; the opposing magnetic fields that are evoked through the currents might cancel each other out. Now, if we stretch the soft antenna, the conductors are being further separated and the magnetic fields might be too far away to interfere with one another enhancing the antenna's radiation efficiency. An increase of the radiation efficiency might outperform an imperfectly matched antenna-RFID chip.

In this study we investigated the resonant frequency response of stretchable soft RFID sensors due to strain. Future work might focus on the design of soft RFID sensors

based on phase shift differences that occur in backscattered signals. We also want to increase the initial resonant frequency of our soft RFID sensors to increase the strain range. RFIDs usually operate in the range of 800 MHz to 1 GHz; whereas, currently, our system operates in the 800-860 MHz range.

7.7 Conclusion

In this work, we designed and fabricated a stretchable strain sensor (soft RFID sensor) and tested a variety of its characteristics. The soft RFID sensor is a deformable folded half-wave dipole antenna. Its resonant frequency and backscattered signal phase changes under strain. We showed that our soft sensor is stable, reliable and manufacturable. Our sensor consists of Ecoflex 00-50 and Galinstan, materials that are stretchable and withstand permanent deformation. The soft RFID sensor can be easily applied to for applications including wearable strain sensors or as part of soft robotic systems, as demonstrated in this study. The sensor does not require a power supply, indicates long measurement reading ranges (above 7.5 m), and shows omni-directivity.

References

1. Yeo WH, Kim YS, Lee J, et al. Multifunctional epidermal electronics printed directly onto the skin. *Adv Mater.* 2013;25(20):2773-2778. doi:10.1002/adma.201204426
2. Shademan A, Decker RS, Opfermann JD, Leonard S, Krieger A, Kim PCW. Supervised autonomous robotic soft tissue surgery. *Sci Transl Med.* 2016;8(337). doi:10.1126/scitranslmed.aad9398
3. Polygerinos P, Wang Z, Galloway KC, Wood RJ, Walsh CJ. Soft robotic glove for combined assistance and at-home rehabilitation. In: *Robotics and Autonomous Systems*. Vol 73. ; 2015:135-143. doi:10.1016/j.robot.2014.08.014
4. Alspach A, Kim J, Yamane K. Design of a soft upper body robot for physical human-robot interaction. In: *IEEE-RAS International Conference on Humanoid Robots*. Vol 2015-Decem. ; 2015:290-296. doi:10.1109/HUMANOIDS.2015.7363557
5. Bahramzadeh Y, Shahinpoor M. A Review of Ionic Polymeric Soft Actuators and Sensors. *Soft Robot.* 2014;1(1):38-52. doi:10.1089/soro.2013.0006
6. Wei W, Guo S. A novel PDMS diaphragm micropump based on ICPF actuator. In: *2010 IEEE International Conference on Robotics and Biomimetics, ROBIO 2010.* ; 2010:1577-1583. doi:10.1109/ROBIO.2010.5723565
7. Cho MS, Seo HJ, Nam JD, Choi HR, Koo JC, Lee Y. An electroactive conducting polymer actuator based on NBR/RTIL solid polymer electrolyte. *Smart Mater Struct.* 2007;16(2). doi:10.1088/0964-1726/16/2/S06
8. Shepherd RF, Ilievski F, Choi W, et al. Multigait soft robot. *Proc Natl Acad Sci.* 2011;108(51):20400-20403. doi:10.1073/pnas.1116564108
9. Wei T, Stokes A, Webb B. A soft pneumatic maggot robot. In: *Lecture Notes in Computer Science (Including Subseries Lecture Notes in Artificial Intelligence and Lecture Notes in Bioinformatics)*. Vol 9793. ; 2016:375-386. doi:10.1007/978-3-319-42417-0_34
10. Suzumori K, Endo S, Kanda T, Kato N, Suzuki H. A bending pneumatic rubber actuator realizing soft-bodied manta swimming robot. In: *Proceedings - IEEE International Conference on Robotics and Automation.* ; 2007:4975-4980. doi:10.1109/ROBOT.2007.364246
11. Ilievski F, Mazzeo AD, Shepherd RF, Chen X, Whitesides GM. Soft robotics for chemists. *Angew Chemie - Int Ed.* 2011;50(8):1890-1895. doi:10.1002/anie.201006464
12. Cianchetti M, Mattoli V, Mazzolai B, Laschi C, Dario P. A new design methodology of electrostrictive actuators for bio-inspired robotics. *Sensors Actuators, B Chem.* 2009;142(1):288-297. doi:10.1016/j.snb.2009.08.039
13. Pelrine R. Dielectric elastomer artificial muscle actuators: toward biomimetic motion. *Proc SPIE.* 2002;4695(3):126-137. doi:10.1117/12.475157
14. Madden J.D.W, Vandesteeg N.A AP., Madden JDW, Vandesteeg N a., et al. Artificial muscle technology:Physical principles and Naval prospects. *IEEE J Ocean Eng.* 2004;29(3):29,3, 7006-28. doi:10.1109/JOE.2004.833135
15. Kim DH, Ghaffari R, Lu N, Rogers J a. Flexible and Stretchable Electronics for Biointegrated Devices. *Annu Rev Biomed Eng.* 2012;14(1):113-128. doi:10.1146/annurev-bioeng-071811-150018
16. Park YL, Chen B, Wood RJ. Design and Fabrication of Soft Artificial Skin using Embedded

- Microchannels and Liquid Conductors. *IEEE Sens J.* 2012;12(8):2711-2718.
doi:10.1109/JSEN.2012.2200790
17. Vogt D, Menguc Y, Park Y, Wehner M. Progress in Soft, Flexible, and Stretchable Sensing Systems. *BioroboticsHarvardEdu.* 2013:0-1.
http://biorobotics.harvard.edu/pubs/2013/contrib/DVogt_2013ICRA.pdf.
 18. Tabatabai A, Fassler A, Usiak C, Majidi C. Liquid-phase gallium-indium alloy electronics with microcontact printing. *Langmuir Acs J Surfaces Colloids.* 2013;29(20):6194-6200.
doi:10.1021/la401245d@proofing
 19. Park YL, Chen B, Majidi C, Wood RJ. Active modular elastomer sleeve for soft wearable assistance robots. 2012.
 20. Majidi C, Kramer R, Wood RJ. A non-differential elastomer curvature sensor for softer-than-skin electronics. *Smart Mater Struct.* 2011;20(10). doi:10.1088/0964-1726/20/10/105017
 21. Teng L, Jeronimo K, Wei T, Nemitz MP, Lyu G, Stokes A. Integrating Soft Sensor Systems Using Conductive Thread. *J Micromechanics Microengineering.* 2018.
 22. Cheng S, Rydberg A, Hjort K, Wu Z. Liquid metal stretchable unbalanced loop antenna. *Appl Phys Lett.* 2009;94(14). doi:10.1063/1.3114381
 23. Cheng S, Wu Z, Hallbjörner P, Hjort K, Rydberg A. Foldable and stretchable liquid metal planar inverted cone antenna. *IEEE Trans Antennas Propag.* 2009;57(12):3765-3771.
doi:10.1109/TAP.2009.2024560
 24. Kubo M, Li X, Kim C, et al. Stretchable microfluidic radiofrequency antennas. *Adv Mater.* 2010;22(25):2749-2752. doi:10.1002/adma.200904201
 25. So JH, Thelen J, Qusba A, Hayes GJ, Lazzi G, Dickey MD. Reversibly deformable and mechanically tunable fluidic antennas. *Adv Funct Mater.* 2009;19(22):3632-3637.
doi:10.1002/adfm.200900604
 26. Huang Y, Wang Y, Xiao L, Liu H, Dong W, Yin Z. Microfluidic serpentine antennas with designed mechanical tunability. *Lab Chip.* 2014;14(21):4205-4212. doi:10.1039/C4LC00762J
 27. Kim J, Banks A, Cheng H, et al. Epidermal electronics with advanced capabilities in near-field communication. *Small.* 2015;11(8):906-912. doi:10.1002/sml.201402495
 28. Cheng S, Wu Z. A microfluidic, reversibly stretchable, large-area wireless strain sensor. *Adv Funct Mater.* 2011;21(12):2282-2290. doi:10.1002/adfm.201002508
 29. Tolley MT, Shepherd RF, Mosadegh B, et al. A Resilient, Untethered Soft Robot. *Soft Robot.* 2014. doi:10.1089/soro.2014.0008
 30. Marchese AD, Katzschmann RK, Rus D. A Recipe for Soft Fluidic Elastomer Robots. *Soft Robot.* 2015. doi:10.1089/soro.2014.0022
 31. Bartlett NW, Tolley MT, Overvelde JTB, et al. A 3D-printed, functionally graded soft robot powered by combustion. *Science (80-).* 2015. doi:10.1126/science.aab0129
 32. Wehner M, Truby RL, Fitzgerald DJ, et al. An integrated design and fabrication strategy for entirely soft, autonomous robots. *Nature.* 2016. doi:10.1038/nature19100
 33. Liu R, Huskic G, Zell A. Dynamic objects tracking with a mobile robot using passive UHF RFID tags. In: *2014 IEEE/RSJ International Conference on Intelligent Robots and Systems.* ; 2014:4247-4252. doi:10.1109/IROS.2014.6943161
 34. Sanpechuda T, Kovavisaruch L. A review of RFID localization: Applications and techniques. In: *5th International Conference on Electrical Engineering/Electronics, Computer, Telecommunications and Information Technology, ECTI-CON 2008.* Vol 2. ; 2008:769-772.

- doi:10.1109/ECTICON.2008.4600544
35. Choi BS, Lee JW, Lee JJ. Distributed Sensor Network Based on RFID System for Localization of Multiple Mobile Agents. *Wirel Sens Netw.* 2011;03(01):1-9. doi:10.4236/wsn.2011.31001
 36. Liu T, Sen P, Kim CJ. Characterization of nontoxic liquid-metal alloy galinstan for applications in microdevices. *J Microelectromechanical Syst.* 2012;21(2):443-450. doi:10.1109/JMEMS.2011.2174421
 37. Park YL, Majidi C, Kramer R, Brard P, Wood RJ. Hyperelastic pressure sensing with a liquid-embedded elastomer. *J Micromechanics Microengineering.* 2010;20(12). doi:10.1088/0960-1317/20/12/125029
 38. Chossat JB, Park YL, Wood RJ, Duchaine V. A soft strain sensor based on ionic and metal liquids. *IEEE Sens J.* 2013;13(9):3405-3414. doi:10.1109/JSEN.2013.2263797
 39. Adam Bilodeau R, White EL, Kramer RK. Monolithic fabrication of sensors and actuators in a soft robotic gripper. *IEEE Int Conf Intell Robot Syst.* 2015;2015-Decem:2324-2329. doi:10.1109/IROS.2015.7353690
 40. Kramer RK, Majidi C, Wood RJ. Wearable tactile keypad with stretchable artificial skin. In: *Proceedings - IEEE International Conference on Robotics and Automation.* ; 2011:1103-1107. doi:10.1109/ICRA.2011.5980082
 41. Kramer RK, Majidi C, Sahai R, Wood RJ. Soft curvature sensors for joint angle proprioception. *IEEE Int Conf Intell Robot Syst.* 2011:1919-1926. doi:10.1109/IROS.2011.6048270
 42. Vogt D, Park YL, Wood RJ. A soft multi-axis force sensor. In: *Proceedings of IEEE Sensors.* ; 2012. doi:10.1109/ICSENS.2012.6411573
 43. Case JC, White EL, Kramer RK. Soft Material Characterization for Robotic Applications. *Soft Robot.* 2015;2(2):80-87. doi:10.1089/soro.2015.0002
 44. Cheng S, Wu Z. Microfluidic electronics. *Lab Chip.* 2012;12(16):2782. doi:10.1039/c2lc21176a
 45. Ukkonen L, Schaffrath M, Engels DW, Sydänheimo L, Kivikoski M. Operability of folded microstrip patch-type tag antenna in the UHF RFID bands within 865-928 MHz. *IEEE Antennas Wirel Propag Lett.* 2006;5(1):414-417. doi:10.1109/LAWP.2006.883085
 46. Takiguchi M, Yamada Y. Improvement of Radiation Efficiencies by Applying Folded Configurations to Very Small Meander Line Antennas. 2003:96-97.
 47. Hu Z, Cole PH, Zhang L. A method for calculating the resonant frequency of meander-line dipole antenna. *2009 4th IEEE Conf Ind Electron Appl ICIEA 2009.* 2009:1783-1786. doi:10.1109/ICIEA.2009.5138503
 48. Esa M. High-Temperature Superconducting Y-Ba-Cu-O Meander Dipole Antennas for Space-Limited Applications. 1996;(August).
 49. Balanis C a. Antenna Theory: Analysis and Design. Electronics and Power. doi:10.1049/ep.1982.0113
 50. Antennas I, Magazine P, Politecnico V. The art of UHF RFID antenna design : impedance matching and size-reduction techniques. *Methods.* 2008;50(1):1-21. doi:Antennas and Propagation Magazine, Vol.50, No.1, february 2008
 51. Abbosh A. Accurate effective permittivity calculation of printed center-fed dipoles and its application to quasi yagi-uda antennas. *IEEE Trans Antennas Propag.* 2013;61(4):2297-2300. doi:10.1109/TAP.2012.2231925

52. Jackson DR, Alexopoulos NG. Analysis of Planar Strip Geometries in a Substrate-Superstrate Configuration. *IEEE Trans Antennas Propag*. 1986;34(12):1430-1438.
doi:10.1109/TAP.1986.1143784

8 Conclusions and future works

This thesis focused on the study of printed graphene and graphene oxide based electrical and microwave components. An environmentally friendly, low cost, and high conductive screen printing graphene/CAB ink has been developed in chapter 3. After the mechanical compressing process, the conductivity of the dried graphene laminate raised to $7.13 \times 10^4 \text{ S m}^{-1}$. In order to achieve the viscosity requirements of screen printing, the high concentration Cyrene based graphene dispersion was further concentrated to 70 mg mL^{-1} and CAB was added as a binder material but the conductivity still remain as $3.7 \times 10^4 \text{ S m}^{-1}$. A high frequency NFC coil antenna has been designed and proved to be able to provide sufficient power to power up a microcontroller and temperature sensor. A conformable, long-range UHF RFID was proposed afterward, which has long reading distance fitting well for practical IoT and logistics applications. Moreover, an ultra-wideband antenna that operates in several microwave bands has the efficiency over 50%, indicating the printed graphene based antenna is not only limited to signal transmitting or receiving but also capable of the higher power applications. Chapter 3 redesigned, optimized and printed antennas based on the properties of graphene ink, digged out the potential of printed graphene, pointed out a direction for graphene inks from labs to real industry.

In chapter 4, the shear exfoliation of graphene was discussed. This method is more efficiently and high-yield comparing with the last chapter. The best centrifuge speed which achieved the highest conductivity has been measured. However, the polymer

removal process requires high temperatures, which cannot be applied to normal flexible substrates. The applications of high conductive graphene loaded sponge to radar absorbers and supercapacitors have been demonstrated in this chapter. Based on the measured permittivity and permeability of the fabricated sponges, two RAM structured radar absorbers have been designed. Both of them can absorb microwave energy effectively in the entire X-band, but the thicker one has better absorption versus different incident angles, which is more suitable for conformable applications. Moreover, the soft supercapacitor was fabricated with outstanding stretchability. The capacitance retains 98.3% after 100 times of double-length stretch test. In conclusion, this work in chapter 4 has demonstrated the potential of massive electronic applications that graphene-based materials can be applied, not limited to one specific area.

The work in Chapter 5 extends the applications of screen printed GO to printed electronic components and light-weight radar absorber. Firstly, the concentrated GO solution was first printed on a substrate (Kapton), dried and then reduced to rGO laminate. The sheet resistance of the rGO laminate was precisely controlled to the designed value by accurately controlling the reduction time. The final rGO/Kapton thin film has excellent features of mechanical and electrical properties. Moreover, it is experimentally verified that the sheet resistance can be potentially beneficial for monitoring the reduction level of rGO due to its considerable sheet resistance variation with reduction times. The rGO/ Kapton films with different sheet resistance have been fabricated and their radar absorption application has been demonstrated, revealing an excellent RCS reduction performance at L, S and C bands. The absorber is not sensitive

to the incident modes and has good tolerance to the incident angles. Additionally, the rGO laminate can be easily patterned to provide even better absorption performance, which has the potential to extend the rGO applications to flexible connectivity and electronic components for wearable wireless communication, energy harvesting and sensing.

A metamaterial based RFID stretchable sensor has been demonstrated in Chapter 6 and a similar meandered dipole based RFID sensor has been presented in Chapter 7. Galinstan is injected into the antennas as the conductor. Its liquid property keeps the continuity of antennas. The sensing principle of the sensor relies on its resonant frequency shift of antennas, which converts stretching variation to antenna's resonance frequency. This technique is superior to existing measuring techniques. The detection range is orders further than NFC technology. Comparing with commercial active sensors, the complete passive property makes the sensor maintains-free. Secondly, the RFID sensors have been fully evaluated in Chapter 6 and 7, including read ranges, radiation patterns, scattered powers, bending and reliability, etc. In final, a complete wireless measurement system was constructed, demonstrating the RFID sensors has excellent tolerance to scattered signal and interference.

In summary, this thesis extended the newly developed graphene and galinstan's applications in the field of NFC, long-range RFID, microwave absorbers, wireless sensors, wireless energy collection and storage devices, etc. The successful applications prove these two novel materials have great potential in the field of electromagnetics.

There are a lot more that can be further researched are listed below.

1. The modeling and simulation of monolayer graphene in Chapter 2 can be extended to multi-layer graphene. The electromagnetic properties of manual exfoliated graphene, CVD growth graphene, ultrasonic exfoliation graphene, shear exfoliated graphene and reduced graphene oxide should be measured through transmission line or resonator methods. The electric and magnetic tunability should be measured and compared as well because edge shape, doping and defects would have significant effects on graphene's mobility and conductivity.
2. The ultrasonic exfoliated graphene ink in Chapter 2 still has a big space to get improved. The concentration can be further increased by carefully adjusting the Hansen Solubility Parameters of solvents with surfactants and polymers. The conductivity of the dried laminate can get further improved through low temperature annealing. The performance of bent or rolled antennas should be measured and discussed. The printing technique should not be limited to screen printing; other printing methods should be evaluated. It is also essential to research how to direct print antennas on curved objects.
3. The mechanical and chemical produced graphene and printed rGO materials in Chapter 4 and 5 have shown excellent advantages on conformal, thin and light-weight radar absorbers. The ultra-wideband radar absorber which covers from hundreds of MHz to tens of GHz would be the most interest topic for the following research. Metamaterial structures can be printed on the top to reduce thickness further but increase effective bandwidth in the meantime. Also, the uniformity of printed laminate should be researched. The pattern printing with varied sheet

resistance would have amazing results for absorbers.